

Design and Development of a Powder mixing Device used in the deposition of high velocity oxy-fuel (HVOF) Thermal Spray Functionally Graded coatings

A Thesis submitted to the Faculty of Engineering and Computing, School of Mechanical
and Manufacturing Engineering, Dublin City University
For the Degree of Masters of Engineering

By

Md. Kabir Al Mamun

Materials Processing Research Centre and
National Centre for Plasma Science & Technology
Dublin City University, Ireland

DCU

Research Supervisors

Professor M. S. J. Hashmi (Ph. D., D. Sc., CEng., FIMechE., FIEI, MASME)

Dr. Joseph Stokes (BA, BAI, Ph.D., MIEI)

DECLARATION

I hereby certify this material, which I now submit for assessment on the programme of study leading to the award of M.Eng in Engineering, is entirely my own work and has not been taken from the work of others save and the extent that such work has been cited and acknowledged within the text of my work.

Signed:  _____

Md. Kabir Al Mamun

I.D. Number: 53157745

Date: 28.09.2007

ACKNOWLEDGMENTS

There are many individuals who have assisted me during the present work. I would like to thank you all.

In particular, I would like to acknowledge the contributions of Dr. Joseph Stokes of the School of Mechanical and Manufacturing Engineering in Dublin City University, for his unceasing enthusiasm, interest, constructive criticism and practical hand on assistance with HVOF thermal spray system and for putting up with me over the years. His expertise, availability to discuss ideas and willingness to give his knowledge were instrumental in the completion of this thesis. I owe him much gratitude.

I will be forever indebted to Professor M. S. J. Hashmi (Head of School) who not only funded my project but also supported and supervised me unstintingly. Without his support and encouragement this research would not have been done.

I would like to thank the academic staff for any help they gave me over the course of my work, especial thanks to Dr. Dermot Brabazon. I am especially grateful to Michael Tyrrell, Liam Domnican, Keith Hickey, Jim Barry, Eoin Touhy, Alan Meehan, Michael May and Chris Crouch for their technical support, inspiration and discussions throughout this work, and the secretarial staff for their help. I wish to thank all of my fellow postgraduate students within Dublin City University and elsewhere, for their support and friendship; especial thanks to Dr. Mahbub Hasan.

I am grateful to School of Mechanical and Manufacturing Engineering, DCU, without whose support this project would not have been made possible.

Special thanks are due to my parents and family for their endless support during my studies, without which I may not come at this stage. My sincere thanks to Halima Akter, for her love, care and encouragement during the last few years; it has been much appreciated.

ABSTRACT

DESIGN AND DEVELOPMENT OF A POWDER MIXING DEVICE USED IN THE DEPOSITION OF HIGH VELOCITY OXY-FUEL (HVOF) THERMAL SPRAY FUNCTIONALLY GRADED COATINGS

MD. KABIR AL MAMUN

The application of Functionally Graded Materials (FGMs) is quite difficult, but thermal spray processes like Plasma spray have demonstrated their unique potential in producing graded deposits, where researchers have used twin powder feed systems to mix different proportions of powders. However the HVOF (High Velocity Oxy-Fuel) process does not possess this feature. FGMs vary in composition and/or microstructure from one boundary (substrate) to another (top service surface), and innovative characteristics result from the gradient from metals to ceramics or non-metallic to metals. The present study investigates an innovative modification of a HVOF thermal spray process to produce functionally graded thick coatings. In order to deposit thick coatings, certain problems have to be overcome. Graded coatings enable gradual variation of the coating composition and/or microstructure, which offers the possibility of reducing residual stress build-up with in coatings.

In order to spray such a coating, modification to a commercial powder feed hopper was required to enable it to deposit two powders simultaneously which allows deposition of different layers of coating with changing chemical compositions, without interruption to the spraying process. Various concepts for this modification were identified and one design was selected, having been validated through use of a process model, developed using ANSYS Flotran Finite Element Analysis. Post modelling the design was manufactured and tested experimentally for functionality. In the current research the mixing of different proportions of powders was controlled by a computer using Lab VIEW software and hardware, which allowed the control and repeatability of the microstructure when producing functionally graded coatings.

TABLE OF CONTENTS

DECLARATION	I
ACKNOWLEDGMENTS	II
ABSTRACT	IV
TABLE OF CONTENTS	V
LIST OF FIGURES	X
LIST OF TABLES	XVIII

CHAPTER 1	INTRODUCTION	I
-----------	--------------	---

1.1 INTRODUCTION	2
------------------	---

CHAPTER 2	LITERATURE SURVEY	5
-----------	-------------------	---

2.1 INTRODUCTION	6
------------------	---

2.2 SUMMARY OF COATING TECHNIQUES	7
-----------------------------------	---

2.3 THERMAL SPRAY TECHNIQUES	9
------------------------------	---

2.4 HVOF THERMAL SPRAY PROCESS	12
--------------------------------	----

2.4.1 HVOF Gun Design	14
-----------------------	----

2.5 COMBUSTION AND GAS DYNAMICS OF THE HVOF SYSTEM	17
--	----

2.5.1 Features and Benefits of the HVOF Coating	18
---	----

2.5.2 Limitation of the HVOF System	20
-------------------------------------	----

2.6 THERMALLY SPRAYED COATINGS	21
--------------------------------	----

2.6.1 Powder Description	21
--------------------------	----

2.6.2 Coating Deposition, Solidification and Build-Up	22
---	----

2.6.3 Residual Stress	24
-----------------------	----

2.6.4 Coating Structure and Properties	28
--	----

2.7 FUNCTIONALLY GRADED MATERIALS (FGM)	30
---	----

2.8 FUNCTIONALLY GRADED COATINGS	31
----------------------------------	----

2.8.1 Different Techniques Producing Functionally Graded Coatings	32
---	----

2.8.2 Characteristics and Properties of Functionally Graded Coatings	34
--	----

2.8.3 Applications of Functionally Graded Coatings	40
--	----

CHAPTER 3	HVOF EXPERIMENTAL EQUIPMENT AND PROCEDURES	47
<hr/>		
3.1	INTRODUCTION	48
3.2	HVOF THERMAL SPRAYING SYSTEM	49
3.2.1	Diamond Jet (DJ) Gun	50
3.2.2	Powder Feed Unit	52
3.2.3	Gas Supply and Flow Meter Unit	55
3.3	SUPPORT SYSTEM	58
3.3.1	Vaporiser Unit	58
3.3.2	Grit blasting unit	61
3.3.3	Gun Traverse unit	62
3.3.4	Spray Booth and Exhaust System	63
3.3.5	Facility Isolation	64
3.3.6	Cooling System	64
3.3.7	Furnace	64
3.3.8	Safety Equipment	65
3.4	HVOF SPRAYING PROCESS	67
3.4.1	Surface Preparation	67
3.4.2	Pre-Heat Treatment	67
3.4.3	Spraying Process	67
3.4.4	Post-Heat Surface Treatment	70
3.5	COATING CHARACTERIZATION TECHNIQUES	70
3.5.1	Microscopy	71

CHAPTER 4	PRODUCT DESIGN, VERIFICATION AND OPERATING PROCEDURES	73
------------------	--	-----------

4.1 INTRODUCTION	74
4.2 DESIGN SPECIFICATION FOR AUTOMATED HVOF SPRAYING EQUIPMENT (Dual Powder Feed Unit System)	75
4.2.1 Design Brief and Investigation of Possible Solutions	75
4.2.2 Existing Products or Methods	75
4.2.3 Design Concepts and Possible Solutions	76
4.2.4 Concepts Evaluation and Description of the Final Solution	80
4.2.5 Detailed Drawings of the Chosen Solution	82
4.2.6 Design of the Motor Holder	84
4.2.7 Needle Material Selection	86
4.2.8 Re-design of the Bottom Part of the Dual Powder Feed unit System	88
4.2.9 The Control System and Two Axis Integration Problem	91
4.2.10 Software and I/O Solution	94
4.2.11 Electronic Design	95
4.3 REALISATION	98
4.3.1 Component Selection and Purchasing	98
4.3.2 Manufacture of Unique Parts	99
4.3.3 Mechanical and Electronic Assembled Components Integration with Existing Equipment	99
4.3.4 Software Design	103
4.3.5 Control Software Reference Guide	113
4.4 DESIGN CALIBRATIONS AND TEST	119

CHAPTER 5	MODELLING	122
5.1 INTRODUCTION		123
5.2 THE F.E.A PROCESS		123
5.2.1 Pre-processing		124
5.2.2 Solution Phase		126
5.2.3 Post –Processing		128
5.3 Summary		128
CHAPTER 6	RESULTS AND DISCUSSION	129
6.1 INTRODUCTION		130
6.2 SIMULATION RESULTS		131
6.2.1 Results		133
6.2.2 Conclusion of the ANSYS Simulation Results		141
6.3 BENCH TEST RESULTS ON THE NEWLY DESIGNED AND DEVELOPED AUTOMATED POWDER FEED UNIT SYSTEM		142
6.3.1 Difference between Material Particles		151
6.3.2 Conclusion of the Powder flow Bench Test Results		156
6.3.2 Experimental sprayed functionally graded coatings results		158
CHAPTER 7	CONCLUSIONS AND RECOMENDATIONS	167
7.1 CONCLUSIONS		168
7.2 RECOMMENDATIONS FOR FUTURE WORK		170
PUBLICATIONS ARISED FROM THIS RESEARCH		171
REFERANCES		172

APPENDICES

Appendix A	i
Appendix B	xii
Appendix C	lvi
Appendix D	lxiii
Appendix E	lxxviii
Appendix F	lxxxii

LIST OF FIGURES

Figure 2.1: Coating Deposition Techniques adapted form [24].	8
Figure 2.2: Schematic diagram of thermally sprayed spherical particle impinged onto a flat substrate [1]	9
Figure 2.3: Schematic Diagram of Thermal Spray Metal Coating [1]	10
Figure 2.4: A typical microstructure of a metallic thermally sprayed coating. The lamellar structure is interspersed with oxide inclusions and porosity. [1]	10
Figure 2.5: Sulzer Metco HVOF Diamond Jet Gun used in DCU.	13
Figure 2.6: Schematic of cross-section of a Diamond Jet spray gun [23].	14
Figure 2.7: Schematic of a chamber combustion burner HVOF gun.	15
Figure 2.8: Theoretical flame temperature against oxygen/fuel ratio	18
Adopted from [36].	18
Figure 2.9: Cross-section of a columnar structure (single lamella) formed after solidification [49].	23
Figure 2.10: Schematic of quenching stresses adopted from [23].	25
Figure 2.11: Schematic of cooling stresses adopted from [23].	27
Figure 2.12: Schematic section of a spray deposit.	28
Figure 2.13: Schematic of Functionally graded coating of material R and S.	31
Figure 2.14: Schematic of Corrosion of steel under a droplet of water [106].	35
Figure 2.15: Nickel-Chromium Phase Diagram [115].	45
Figure 2.16. A corrosion-resistant 316 stainless steel pump [181].	46

Figure 3.1: Schematic of the HVOF Thermal spray system [30].	49
Figure 3.2: The Sulzer METCO Air-Cooled HVOF type Diamond Jet (DJ) gun [30].	51
Figure 3.3: Schematic of the HVOF DJ gun front-end hardware [30].	52
Figure 3.4: The DJP powder feed unit used in the HVOF process [30].	54
Figure 3.5: Schematic cross section of the hopper assembly on the DJP powder feed unit [30].	55
Figure 3.6: Type DJF Diamond Jet gas flow meter unit used in the HVOF process [30]	57
Figure 3.7: A schematic diagram of vaporiser and its initial set up [185].	59
Figure 3.8: A schematic diagram of the connection of vaporiser unit [185].	60
Figure 3.9: Photo of the grit-blasting unit used to prepare samples for coating deposition.	62
Figure 3.10: Various planes and directions relevant to the linear traverse unit [23].	63
Figure 3.11: Sample substrate (Stainless Steel) onto a substrate holder.	70
Figure 3.12: Sample specimen of a functionally graded coated (Diamalloy 1003 and Diamalloy 1005) Stainless Steel substrate.	72
Figure 4.1: Sectional assembly drawing of the needle shaped bolt, the top plate, the individual powder holders, the base plate, the inlet pressure tube, the powder flow tubes and the powder feed hopper [49].	76
Figure 4.2: Schematic diagram of concept 1.	77
Figure 4.3: Schematic diagram of concept 2.	79
Figure 4.4: Schematic diagram of the Motor Holder and bearing cover.	85
Figure 4.5: Schematic of a needle shape bolt for design calculation.	87
Figure 4.6: Geometry of the model Designed by Previous researcher [49].	89
Figure 4.7: Cross sectional Diagram of Flow Tube (a) and powder Mixing Zone (b)	

and Cross-sectional (assembly) view of the Geometry of the model.	90
Figure 4.8: Schematic diagram of computer controlled Powder feed system.	91
Figure 4.9: Open loop control system, adapted from [195].	92
Figure 4.10: Close loop control system, adapted from [195].	92
Figure 4.11: Non Inverting amplifier, adapted from [199].	96
Figure 4.12: Full two input amplification circuit.	97
Figure 4.13: Digital picture of the newly designed dual powder feed device.	100
Figure 4.14: Digital picture of the entire set up after assemble with the existing powder hopper in HVOF Lab.	101
Figure 4.15: Assembled enclosure for stepper driver and amplifiers with power supply unit.	102
Figure 4.16: DAQ connection board wired with limit switch and stepper drivers.	103
Figure 4.17: Lab VIEW Block Diagram for linear actuators control used in current research.	105
Figure 4.18: Section of the Lab VIEW Block Diagram, which generate clock pulse.	106
Figure 4.19: Lab View Code used which will act as a distance converter to move per step.	107
Figure 4.20: AUTOMATION.PRG, the command sequence used to control the linear motion of the spray gun.	109
Figure 4.21: Counting Loop of the Lab VIEW program.	111
Figure 4.22: Connection between Counting Loop and Linear Actuator Control.	112
Figure 4.23: Block Diagram for Manual Control.	113
Figure 4.24: Control Panel for linear actuators 'A' and 'B'.	115

Figure 5.1: Schematic of the geometry of the powder flow and mixing component.	124
Figure 5.2: Schematic diagram of the applied boundary condition.	126
Figure 6.1: Dual powder feed unit with fine mesh in the mixing zone and homogeneous mesh in rest of the modelling.	133
Figure 6.2: Vector plot showing the path of the velocity particles.	136
Figure 6.3: Pressure plot from nodal solution.	137
Figure 6.4: Velocity plot of the model from the nodal solution at a 2.25:1 pressure ratio.	138
Figure 6.5: Velocity profile at outlet at 2.25:1 pressure ratio (left VX and right VY).	138
Figure 6.6: VSUM at the outlet when the pressure ratio is 2.25:1.	139
Figure 6.7: Particle flow lines for the nitrogen gas and powders for a pressure ratio of 2.25:1.	140
Figure 6.8: particle flow lines for the nitrogen gas and powders for a pressure ratio of 10:1 [49].	141
Figure 6.9: Average mass of stainless steel (Diamalloy 1003) powder flow with vertical increment of the needle shaped bolt controlled via LabVIEW programming.	144
Figure 6.10: Average mass of nickel base alloy ¹ (Diamalloy 1005) powder flow with vertical increment of the needle shaped bolt controlled via Lab VIEW programming.	146
Figure 6.11: Average mass of nickel base alloy ² (Diamalloy 2001) powder flow with vertical increment of the needle shaped bolt controlled via LabVIEW programming.	148
Figure 6.12: Comparison of average mass of stainless steel (Diamalloy 1003), nickel base alloy ¹ (Diamalloy 1005) and nickel base alloy ² (Diamalloy 2001) powder flow against vertical increment of the needle shaped bolt controlled via LabVIEW programming for both Chambers (A and B).	149
Figure 6.13: Comparison of Average mass of powder flow for vertical movement	

(Opening and Closing) of needle shaped bolt from 100% powder flow at 4 mm vertical increment to 0% at 0 mm position. Data obtained from Table 6.4, 6.5, 6.6, D4, D5 and D6 respectively (Appendix D).	150
Figure 6.14: Optical microscope image of Diamalloy 1003.	154
Figure 6.15: Optical microscope image of Diamalloy 1005.	155
Figure 6.16: Optical microscope image of Diamalloy 2001.	155
Figure 6.17: A SEM image of the functionally graded coating sample specimen (Diamalloy 1003 and Diamalloy 2001).	158
Figure 6.18: Chemical composition of first layer or Bond Coat.	159
Figure 6.19: Chemical composition of the middle layer or Middle of the Coat.	159
Figure 6.20: Chemical composition of the final layer or the Top Coat/Service Coat.	160
Figure 6.21: A SEM image of the functionally graded coating sample specimen (Diamalloy 1003 and Diamalloy 1005).	161
Figure 6.22: Chemical composition of the first coat or the Bond Coat.	162
Figure 6.23: Chemical composition of the middle layer or Middle of the Coat.	162
Figure 6.24: Chemical composition of the final coat or the Top Coat/Service Coat.	163

APPENDIX FIGURES

Figure A1: Schematic drawing of the motor holder and bush cover.	ii
Figure A2: Schematic drawing of the needle shaped bolt.	iii
Figure A3: Schematic drawing of the top Plate of the powder holder.	iv
Figure A4: Schematic drawing of the cover plate or base plate of the motor mounting.	v
Figure A5: Schematic of the individual powder holder [49].	vi
Figure A6: Schematic of the base plate [49].	vii
Figure A7: Sectional assembly drawing of the base plate, the top plate and the individual powder holders [49].	viii
Figure A8: Schematic drawing of the top part of the funnel shaped powder flow path.	ix
Figure A9: Schematic drawing of the bottom part of the funnel shaped mixing zone.	x
Figure A10: Schematic assembly drawing of the bottom funnel shape design.	xi

- Figure C1: Vector plot showing the path of the velocity particles at 1:1 nitrogen gas pressure ratio on the inlet pressure tube to pick up shaft (obtain from pressure plot of ANSYS result). lvii
- Figure C2: Pressure plot from nodal solution shows the pressure of inlet tube and pick up shaft inlet are same means 1:1. lvii
- Figure C3: Velocity plot of the modelling from the nodal solution at 1:1 pressure ratio. lviii
- Figure C4: Velocity profile at outlet at 1:1 pressure ratio (left VX and right VY). Velocity values are in m/s. lviii
- Figure C5: VSUM at outlet when pressure ratio is 1:1. Velocity values are in m/s. lix
- Figure C6: Particle flow lines for nitrogen gas and powders for a pressure ratio of 1:1. lix
- Figure C7: Vector plot showing the path of the velocity particles at 1.8:1 nitrogen gas pressure ratio on the inlet pressure tube to pick up shaft (obtain from pressure plot of ANSYS result). lx
- Figure C8: Pressure plot from nodal solution shows the pressure of inlet tube and pick up shaft inlet are same means 1.8:1. lx
- Figure C9: Velocity plot of the modelling from the nodal solution at 1.8:1 pressure ratio. lxi
- Figure C10: VSUM at outlet when pressure ratio is 1:1. Velocity values are in m/s. lxi
- Figure C11: Particle flow lines for nitrogen gas and powders for a pressure ratio of 1.8:1. lxii

Figure D1: Average mass of stainless steel (Diamalloy 1003) powder flow with vertical increment of the needle shaped bolt controlled via Lab VIEW programming and data obtained from Table D1. lxv

Figure D2: Average mass of nickel base alloy1 (Diamalloy 1005) powder flow with vertical increment of the needle shaped bolt controlled via Lab VIEW programming and data obtained from Table D2. lxvii

Figure D3: Average mass of nickel base alloy2 (Diamalloy 2001) powder flow with vertical increment of the needle shaped bolt controlled via Lab VIEW programming and data obtained from Table D3. lxix

Figure D4: Comparison of average mass of stainless steel (Diamalloy 1003), nickel base alloy¹ (Diamalloy 1005) and nickel base alloy² (Diamalloy 2001) powder flow with vertical increment of the needle shaped bolt controlled via Lab VIEW programming. The combine graphical representation of figure D1, D2 and D3 and data obtained from Table D1, D2 and D3 respectively. lxix

Figure D5: Comparison of average mass of stainless steel (Diamalloy 1003), nickel base alloy¹ (Diamalloy 1005) and nickel base alloy² (Diamalloy 2001) powder flow from Chamber 'A' with vertical decrement of the needle shaped bolt controlled via LabVIEW programming. Data obtained from Table D4, D5 and D6 respectively. lxxiii

Figure D6: Comparison of average mass of stainless steel (Diamalloy 1003), nickel base alloy¹ (Diamalloy 1005) and nickel base alloy² (Diamalloy 2001) powder flow from Chamber 'B' with vertical decrement of the needle shaped bolt controlled via LabVIEW programming. Data obtained from Table D7, D8 and D9 respectively. lxxvii

Figure F3: Chemical composition of the final coat or the Top Coat/Service Coat of Sample 1 (3 rd set of point analysis).	lxxxiv
Figure F4: Chemical composition of the middle layer or Middle of the Coat of Sample 1 (2 nd set of point analysis).	lxxxiv
Figure F5: Chemical composition of the middle layer or Middle of the Coat of Sample 1 (3 rd set of point analysis).	lxxxv
Figure F6: Chemical composition of the first coat or the Bond coat of Sample 1 (2 nd set of point analysis).	lxxxv
Figure F7: Chemical composition of the first coat or the Bond coat of Sample 1 (3 rd set of point analysis).	lxxxvi
Figure F8: A SEM image of the functionally graded coating sample 2 (Diamalloy 1003 and Diamalloy 1005) (Represent of Figure 6.21 for the 2 nd and 3 rd set of point analysis).	lxxxvi
Figure F10: Chemical composition of the final coat or the Top Coat/Service Coat of Sample 2 (3 rd set of point analysis).	lxxxvii
Figure F11: Chemical composition of the middle layer or Middle of the Coat of Sample 2 (2 nd set of point analysis).	lxxxviii
Figure F12: Chemical composition of the middle layer or Middle of the Coat of Sample 2 (3 rd set of point analysis).	lxxxviii
Figure F13: Chemical composition of the first coat or the Bond coat of Sample 2 (2 nd set of point analysis).	lxxxix
Figure F14: Chemical composition of the first coat or the Bond coat of Sample 2 (3 rd set of point analysis).	lxxxix

LIST OF TABLES

Table 2.1: Electrical Heating and Flame Heating Process	11
Table 2.2: Characteristics of different thermal spray techniques [31, 50].	16
Table 2.3: Variation of properties of 86WC/10Co/4Cr, produced by different fuel gases [54].	17
Table 2.4: Benefits of using the HVOF coatings [23].	19
Table 2.5: Detail information of the nickel base alloy and stainless steel powder [61, 62].	21
Table 2.6: Names and classifications of different types of FGM manufacturing processes.	31
Table 2.7: Coating porosity in various Diamond Jet HVOF coatings [62,135].	39
Table 2.8: Typical applications of stainless steel/nickel base alloy powder [61, 65, 179]	43
Table 3.1: Gun settings and spray parameters for Stainless steel and Nickel base alloy coating material [188]	69
Table 4.1: Weight analysis table for the proposed three concepts	81
Table 4.2: Hypothesis of the two different powder flows controlled by the vertical movement of the linear actuators 'A' & 'B'.	119

Table 6.1: Pressure ratio for different velocity input of nitrogen gas	131
Table 6.2: Difference of velocity plot and pressure plot between three different models.	134
Table 6.3: Difference of particle flow plot between three different models.	135
Table 6.4: Weight of stainless steel (Diamalloy 1003) from chamber 'A' for various increments of its associated Needle.	143
Table 6.5: Weight of Nickel alloy ¹ (Diamalloy 1005) from chamber 'A' for various increments of its associated Needle.	145
Table 6.6: Weight of Nickel alloy ² (Diamalloy 2001) from chamber 'A' for various increments of its associated Needle.	147
Table 6.7: Different densities of three different powders (Diamalloy 1003, Diamalloy 1005 and Diamalloy 2001).	152
Table 6.8: Results of standard test method for flow rate of metal powders.	153
Table 6.9: vertical increment or decrement composition of needle shaped bolt with different powders.	157
Table 6.10: Chemical composition compared for FGM coatings.	165

APPENDIX TABLES

Table D1: Weight of stainless steel (Diamalloy 1003) from Chamber 'B' for various increments of its associated Needle.	lxiv
Table D2: Weight of Nickel alloy ¹ (Diamalloy 1005) from Chamber 'B' for various increments of its associated Needle.	lxvi
Table D3: Weight of Nickel alloy ² (Diamalloy 2001) from Chamber 'B' for various increments of its associated Needle.	lxviii
Table D4: Weight of stainless steel (Diamalloy 1003) from Chamber 'A' for various decrements of its associated Needle.	lxx
Table D5: Weight of Nickel alloy ¹ (Diamalloy 1005) from Chamber 'A' for various decrements of its associated Needle.	lxxi
Table D6: Weight of Nickel alloy ² (Diamalloy 2001) from Chamber 'A' for various decrements of its associated Needle.	lxxii
Table D7: Weight of stainless steel (Diamalloy 1003) from Chamber 'B' for various decrements of its associated Needle.	lxxiv
Table D8: Weight of Nickel alloy ¹ (Diamalloy 1005) from Chamber 'B' for various decrements of its associated Needle.	lxxv
Table D9: Weight of Nickel alloy ² (Diamalloy 2001) from Chamber 'B' for various decrements of its associated Needle.	lxxvi

CHAPTER 1

INTRODUCTION

1.1 INTRODUCTION

Thermal spraying can be described as a process in which molten or semi molten particles are applied by impact onto a substrate [1]. Functionally Graded Materials (FGMs) are a growing application area with significant promise for the future production of; (a) improved materials and devices for use in applications subjected to large thermal gradients, (b) lower-cost clad materials for combinations of corrosion and strength or wear resistance, and (c) improved electronic material structures for batteries, fuel cells, and thermoelectric energy conversion devices and (d) biomedical implant devices for enhanced bone-tissue attachment. The most immediate application of FGMs is as Thermal Barrier Coatings (TBCs), where large thermal stresses can be minimised. Component lifetimes are improved by tailoring the coefficients of thermal expansion, thermal conductivity, and oxidation resistance.

The application of FGMs is quite difficult; however thermal spray processes like Plasma spray have demonstrated their unique potential in producing graded deposits, where researchers have used twin powder feed systems to mix different proportions of powders. The produced FGM has a continuously varying composition and/or microstructure from one boundary (substrate) to another (top service surface), and innovative characteristics result from the gradient from metals to ceramics or non-metals to metals. To date the Plasma spray process has produced superior coatings for numerous applications, however the HVOF process provides even superior deposits compared to Plasma techniques; with lower porosity, higher bond strength and low residual stress build up due to its high kinetic energy and low combustion temperature design. There exist a large range of materials, which have the potential to benefit from graded structures yet to be researched. The current study aims to contribute new knowledge in these areas by depositing nickel base alloy/stainless steel functionally graded coatings on steel substrates using the HVOF process. Nickel base alloy/Stainless steel graded coatings are used in the automotive and marine industry not only to increase the strength of the coated system but also for corrosion prevention applications. Presently, thermal spraying can be used to produce inter layers of FGM coatings by two methods; Using premixed powders to produce each different layer and secondly Co-injecting two different powders and varying their relative proportions during deposition. Most researchers [2-6] have used the former method while producing functionally graded coatings. The latter method is proposed in this project, however the HVOF does not possess a twin powder feed system, hence such a system was designed to fulfil this application. This research

will discuss the potential of using the HVOF thermal spray process to produce FGMs. In this current research the mixing of different proportions of powders will be controlled by a computer using National Instrument software and hardware which will allow the control and repeatability of the results when producing functionally graded coatings.

The rest of the report is divided into a number of chapters. Chapter two is a review of literature relevant to the study. Initially it describes a brief description of different coating techniques then various HVOF thermal spray processes are examined, followed by a description of how the thermal sprayed coating is built-up and also considering their advantages and disadvantages. Properties of different types of coating powders are then detailed. Then FGM are explained with their advantages and manufacturing techniques. Finally this chapter presents the properties and field of applications for functionally graded coatings.

Chapter three describes the equipment used in present study: the HVOF Diamond Jet process. This chapter includes a brief description on the HVOF experimental equipment and procedures associated with the tests conducted during the research.

Chapter four describes different design concepts and possible solutions for the newly designed automated HVOF spraying equipment (Dual powder feed unit system). Then the design of modification including addition of some newly design parts to the commercial powder feed hopper are detailed. Next this chapter includes details of mechanical and electrical equipments assembly procedure and integration with the existing process. Then it describes the software design and user guide of that software which will control the newly designed automated powder feed unit system. Finally this chapter includes the design calibration and test procedure to validate the newly designed automated powder feed unit system, which produces functionally graded coatings (the aim of this current study).

In chapter five the FLOTTRAN CFD ANSYS Finite Element package is described in relation to the nitrogen gas-powder flow model, which was used to predict the usefulness of the design.

Chapter six includes the results and discussion for the present study experiment. This chapter initially describes the ANSYS simulation results then includes the results of the bench test for

the newly designed and developed Automated Graded Powder Feed Unit System. Finally it presents the experimental coating results of the functionally graded coatings.

Finally chapter seven summarises the major conclusions from the results of the current research, and presents recommendations for future work in this area.

CHAPTER 2

LITERATURE SURVEY

2.1 INTRODUCTION

The surface of an engineered component is its primary defence against the attack of chemical or microbial corrosion, and for many years engineers have had to design coatings to protect these surfaces from these harsh environments. The behaviour of a material is greatly dependent upon its surface, the environment and its operating conditions. Surface engineering can be defined as the branch of science, which deals with methods for achieving, desired surface requirements and behaviour in service for engineering components [7].

The surface of any constituent may be selected on the basis of texture and colour, but engineering components commonly expect a lot more than this. Engineering components have to execute certain functions entirely and effectively under various circumstances, and most probably in hostile environments. Recent process environments, which contribute to wear, can be very complex, involving a combination of chemical and physical degradation. Surface properties of the component used in service have to be designed with that environment in mind. Surface engineering in today's production world embraces the design, assessment and performance in service of a component starting at the substrate, through to the interface, then onto the surface of a coating [8].

Coatings can be applied to surfaces to develop the surface characteristics over those of the bulk properties and are widely used in tribological applications either to reduce wear and/or friction during sliding contact. Welding or electroplating has been traditionally used to deposit corrosion resistant coatings, but these applications have been restricted by metallurgical incompatibility between the overlay and the substrate. One of the foremost coating methods for combating wear is thermal spraying, however despite its widespread industrial use [9-12], little is known about the vital friction behaviour and the mechanisms by which such coatings wear. Thus, most thermal spray wear coating applications and developments are based on empirical results. In many instances values for friction and wear resistance of thermally sprayed coatings have been reported in the literature [13-17]. Thermal spraying can also deposit functional graded coatings, but the porous nature of thermally sprayed coatings limits its application in corrosive environments. The HVOF and the High-Velocity Air Fuel (HVOF) techniques are comparatively new thermal spraying methods, which can produce high quality and low porosity coatings well bonded to the substrate compared to other thermal spray techniques such as atmospheric Plasma technique [18-20].

However Plasma Spray has demonstrated its technique for applying FGM, but unfortunately no such technique is available for the HVOF or HVAF Process. Thus this research will identify the usefulness of FGM's and the design of a device used to produce FGM's using the HVOF Process.

2.2 SUMMARY OF COATING TECHNIQUES

A coating may be defined as a layer of viscous material applied to the base material into which granules or other surfacing are implanted. The selection of a particular deposition process depends on several factors, including [21, 22]:

- i. Chemical, process and mechanical compatibility of the coating material with the substrate
- ii. Requirement of deposition rate
- iii. The ability of the substrate to withstand the required processing
- iv. Limitation imposed by the substrate (for example max. allowable deposition temp.)
- v. Process energy
- vi. Adhesion of the deposited material to the substrate
- vii. Purity of the target material
- viii. Requirement and availability of the apparatus
- ix. Cost
- x. Ecological considerations

There are many coating deposition techniques on offer; therefore a synopsis is given in Figure 2.1. Further information on these techniques is detailed by Stokes [23]. Thermal spraying is of the most importance in this research; hence the following section concentrates on this technique.

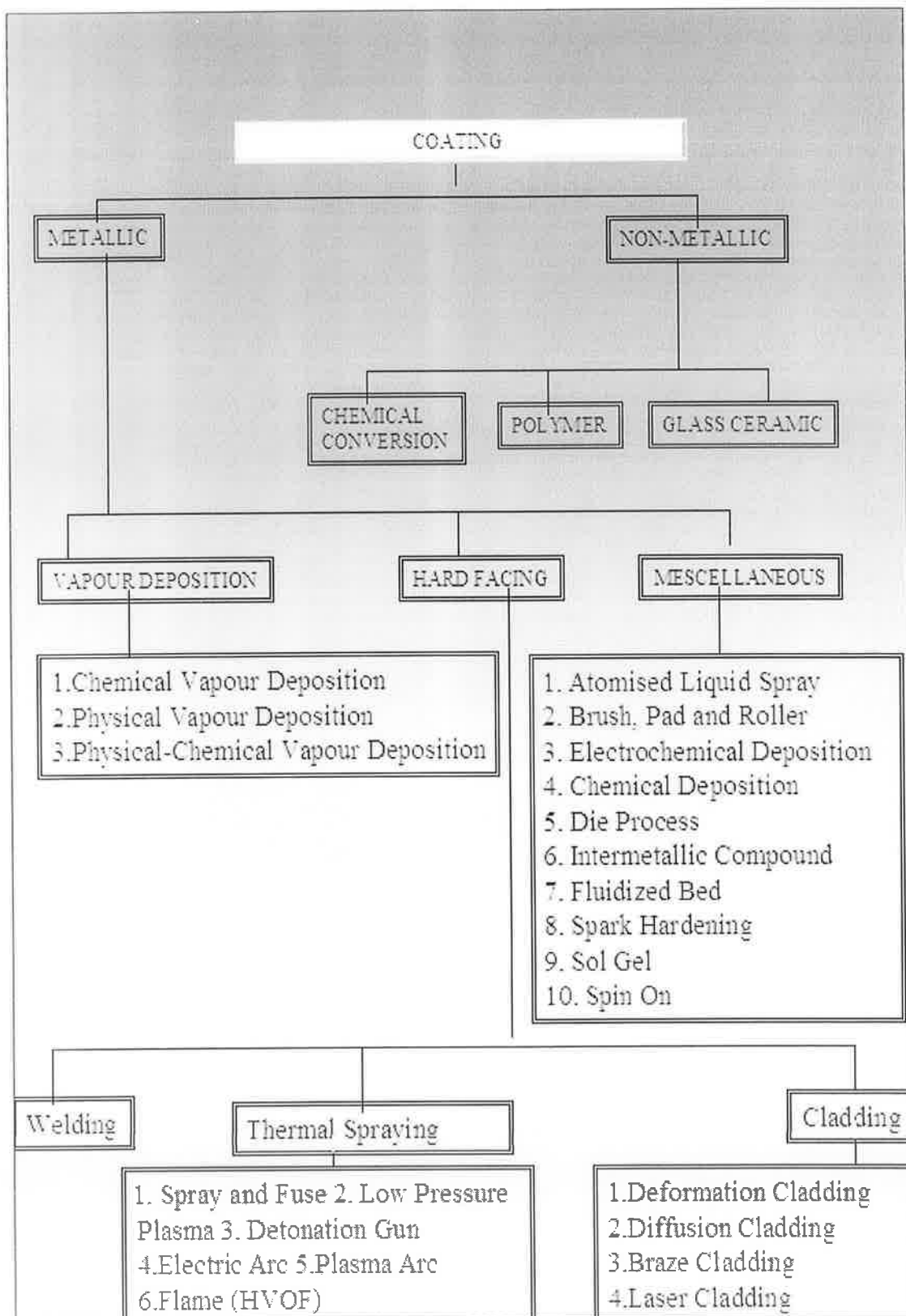


Figure 2.1: Coating Deposition Techniques adapted form [24].

2.3 THERMAL SPRAY TECHNIQUES

Following numerous patents in 1882 and 1899, Dr. Max Schoop first applied tin and lead coatings to metal surfaces by flame spraying [25]. The rate of evolution was sluggish after the techniques commencement by Schoop; but then it increased at high rate until the 1950s. At that time a variety of what then was identified as modern plasmatrons appeared, which boosted the expansion significantly [26]. In particular, the D-gun coatings, developed by Praxair Surface Technology found an approachable market in the aerospace industry and a large proportion of consequent technological growth was due to plasma based thermal barrier coatings [26]. The subsequent growth occurred in the 1980s with the development of vacuum plasma spraying, low pressure plasma spraying and the Jet Kote HVOF technique. The Jet Kote system was manufactured by Browning Engineering, in the USA [26]. Sulzer METCO introduced the Diamond Jet HVOF system in 1988, which is the process under investigation in the existing research and which is described in detail later in this report.

Thermal spraying can be described as a process which coats molten or semi molten particles by impact onto a substrate [1] (Figures 2.2 and 2.3). A common feature of all thermal spray coatings is their lenticular or lamellar grain structure (Figure 2.4) resulting from the rapid solidification of small globules, flattened from striking a cold surface at high velocities [1].

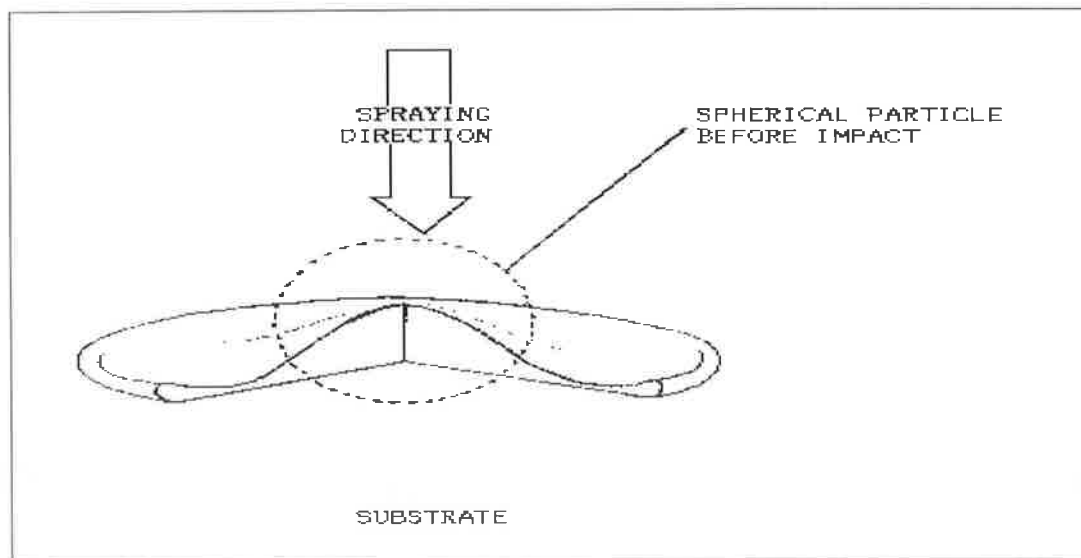


Figure 2.2: Schematic diagram of thermally sprayed spherical particle impinged onto a flat substrate [1]

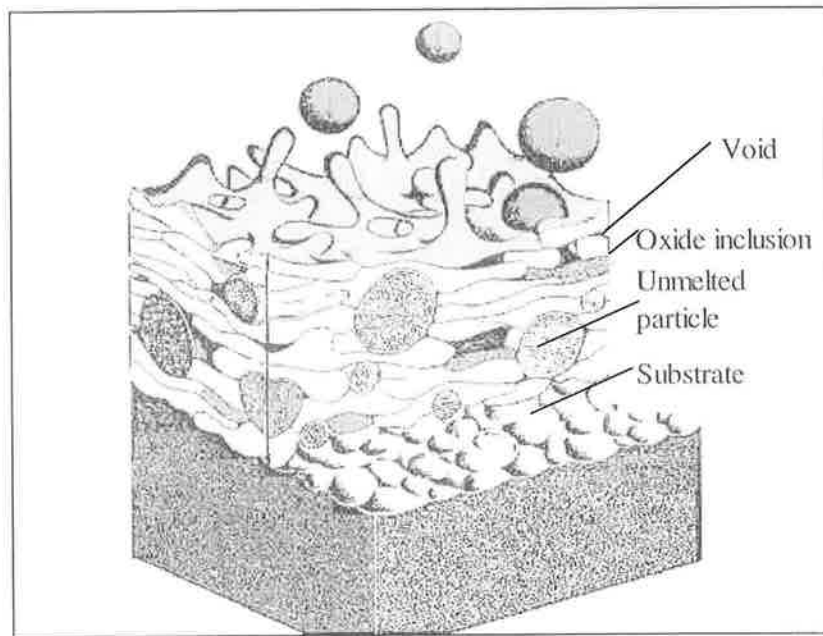


Figure 2.3: Schematic Diagram of a Thermal Spray Metal Coating [1]

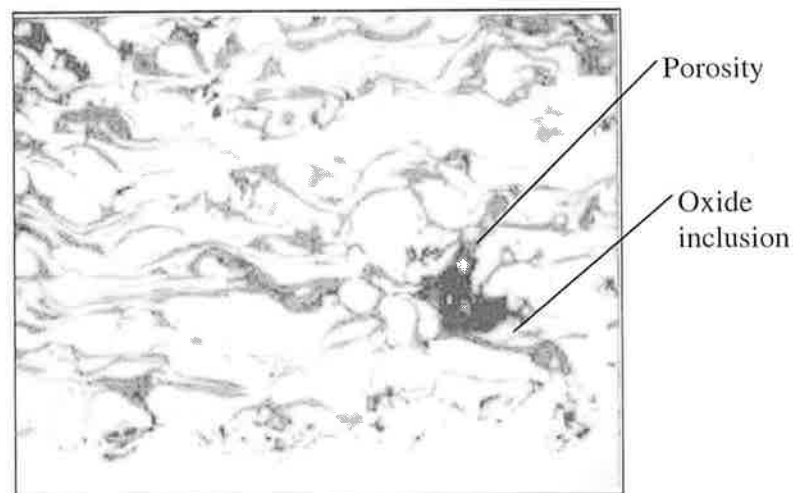


Figure 2.4: A typical microstructure of a metallic thermally sprayed coating. The lamellar structure is interspersed with oxide inclusions and porosity. [1]

The industrial benefit of thermal spray coatings is the attainment of cost-effective solutions in reducing wear and corrosion. The tailoring of components, or specific areas, to counteract damaging effects, prolongs new parts or provides cost-effective renovation of worn parts. For example; substrate materials such as low carbon steel can be thermally sprayed with thin layers of nickel alloys to provide a cost-effective solution for corrosion resistance [27]. HVOF thermal spraying has emerged as one of the most attractive processes for depositing cermet

coatings, 200–400 μm thick, which have low porosity and are well bonded to the substrate [28, 29].

The thermal energy used to melt the coating material, may be separated into two categories; electrical and flame heating (Table 2.1).

Table 2.1: Electrical Heating and Flame Heating Process

Electrical Heating	Flame Heating
Electric arc process	Flame spraying process
Plasma arc process	Spray and fuse process
Low pressure plasma spraying	HVOF thermal spray process

Further information has been reported by Stokes [30] on each of the techniques described; hence this will not be discussed. The HVOF thermal spraying process is relevant to this study, hence this will be and discussed further in the following sections.

2.4. HVOF THERMAL SPRAY PROCESS

Unlike other flame spraying processes, the HVOF thermal spray process utilises only powder as the coating material rather than wire or rod [31]. The high velocity oxy fuel (HVOF) process is reported to be a versatile technology and has been adopted by many industries due to its flexibility, cost effectiveness and the superior quality of coating produced [32]. There exists two types of HVOF processes; (1) the Detonation Gun HVOF system and (2) the Continuous combustion HVOF system. The difference between each of these systems is the use of different fuel gases, cooling systems and the fact that the penultimate combustion is maintained by a timed spark, used to detonate the particle and gas mixture, but otherwise their underlying function is the same [30]. This report concentrates on the latter process only.

A) Continuous Combustion HVOF System

Within the continuous combustion HVOF process there are different types of systems namely; the Diamond Jet (DJ HVOF) and DJ Hybrid gun developed by Sulzer METCO (Figure 2.5), the Jet Kote system developed by Browning Engineering, the HV-2000 through Praxair Surface Technology, the HP/HVOF developed by TAFE to mention a few [33-35]. The continuous combustion Jet Kote HVOF thermal spray system was developed as a substitute to the Detonation Gun system in 1982 [36, 37]. Following the Jet Kote system, the Diamond Jet (DJ) HVOF thermal spraying process was developed in 1988 by Sulzer METCO. Due to its flexibility and cost-effectiveness, it has been broadly adopted in many industries [23]. This system produces dense coatings through low porosity and high bond strength due to the high kinetic energy related with the system to propel the molten material at supersonic speeds [38-41].

There are a number of HVOF guns, which use diverse methods to attain high velocity spraying. One method is essentially a high pressure water cooled HVOF combustion chamber and long nozzle (Figure 2.5). Fuel (kerosene, acetylene, propylene and hydrogen) and oxygen are fed into a chamber. Combustion causes a hot high-pressure flame, which is forced down a nozzle and in turn increases its velocity. Powder can be fed axially into the HVOF combustion chamber under high pressure or fed through the side of a de Laval type nozzle where the pressure is lower. Fuel gas and oxygen, combust outside the nozzle but within an air cap supplied with compressed air. The compressed air acts as a coolant for the HVOF gun

and pinches and accelerates the flame particles. Powder is fed at high pressure axially from the centre of the nozzle towards a receiving substrate [42].

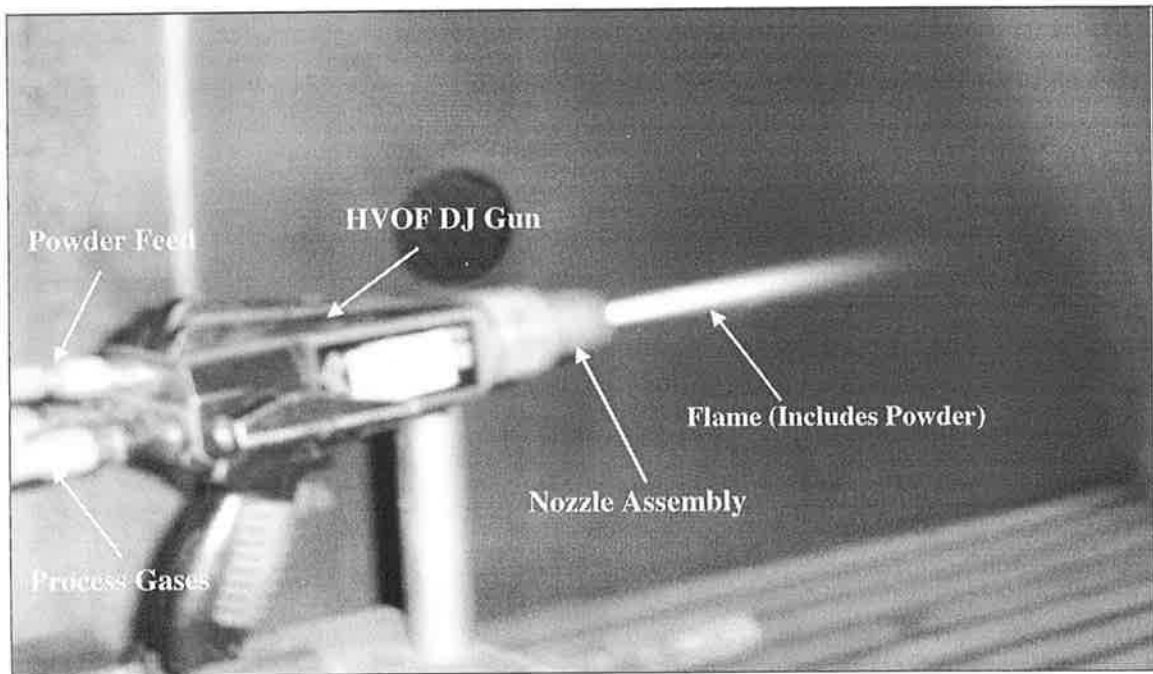


Figure 2.5: Sulzer Metco HVOF Diamond Jet Gun used in DCU.

The coatings produced by the HVOF process are akin to those produce by the detonation process. HVOF coatings are very thick, strong and demonstrate low residual tensile stress or in some cases compressive stress, which facilitate much thicker coatings to be deposited than formerly possible with other Thermal Spray processes [32]. The very high kinetic energy of particles striking the substrate surface does not require the particles to be completely molten to form these HVOF coatings. This is definitely an advantage for carbide cermet type coatings and is where this process excels [42], as the coating retains the bulk properties of that of the powder materials.

HVOF coatings are used in applications requiring the maximum density and strength, not found in most other thermal spray processes. New applications, formerly not suitable for thermal spray coatings are also becoming feasible, such as Bio Engineering [42].

In the Diamond Jet HVOF thermal spraying process, the powder material is melted by the means of combustion of oxygen and a fuel gas (in this case Propylene), and propelled at a high velocity of approximately 1350 m/s [43] by the combination of combustion, compressed

air and nozzle assembly as shown in Figure 2.6. In the combustion zone, the powder material enters the flame, where it becomes molten or semi-molten depending on the melting temperature of the powder material. The flame temperatures of the HVOF process ranges from 2300 to 3000 °C depending on the oxygen to fuel ratio or flow rate used [43]. Due to the high kinetic energy experienced by the impinging particles, the DJ HVOF system exhibits one of the maximum bond strengths and least porosity among all thermal-spraying processes [44]. When compared to other thermal spraying techniques such as plasma spraying, the DJ HVOF system exhibits low thermal residual stress; consequently coatings of higher thickness may be deposited [45]. The reason for this is that the spray gun temperature for the plasma spraying process is approximately 16000 °C [27], whereas the HVOF system is much lower (<3000°C) limiting the development of residual stress [23].

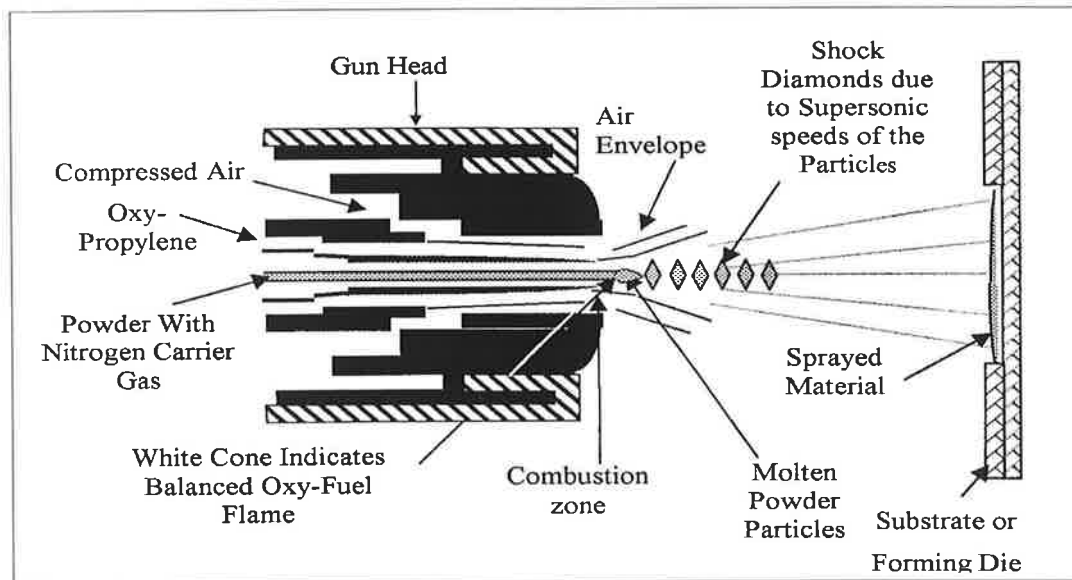


Figure 2.6: Schematic of cross-section of a Diamond Jet spray gun [23].

2.4.1 HVOF Gun Design

HVOF guns can be classified into two groups; Throat and Chamber Combustion. The main difference between these groups is the location of the combustion. The HVOF gun used in the current research has a chamber combustion burner so this is described further.

Chamber Combustion Burner

In a chamber combustion burner, the fuel gas is introduced into a combustion chamber with a larger diameter compare to that of the spray gun barrel. The combustion chamber is either at a right angle or positioned axially with the barrel as revealed in Figure 2.7. Powder injection may be axial, radial or central [46], where this process uses axial. There are also some chamber combustion burners, where powder is injected beyond the flame at the exit of the barrel [47, 48].

Chamber combustion burners present coatings with improved wear and corrosion resistance, relatively with those produced by throat combustion chambers [46]. These advanced coatings are a result of large diameter combustion chambers, which results in a higher throughput and chamber pressure, leading to higher gas and powder velocities [46]. But, due to this increased surface area, heat loss from the chamber combustion burner is greater, which reduces particle heating [49]. Table 2.2 shows some of the significant characteristics associated with the different thermal spraying processes.

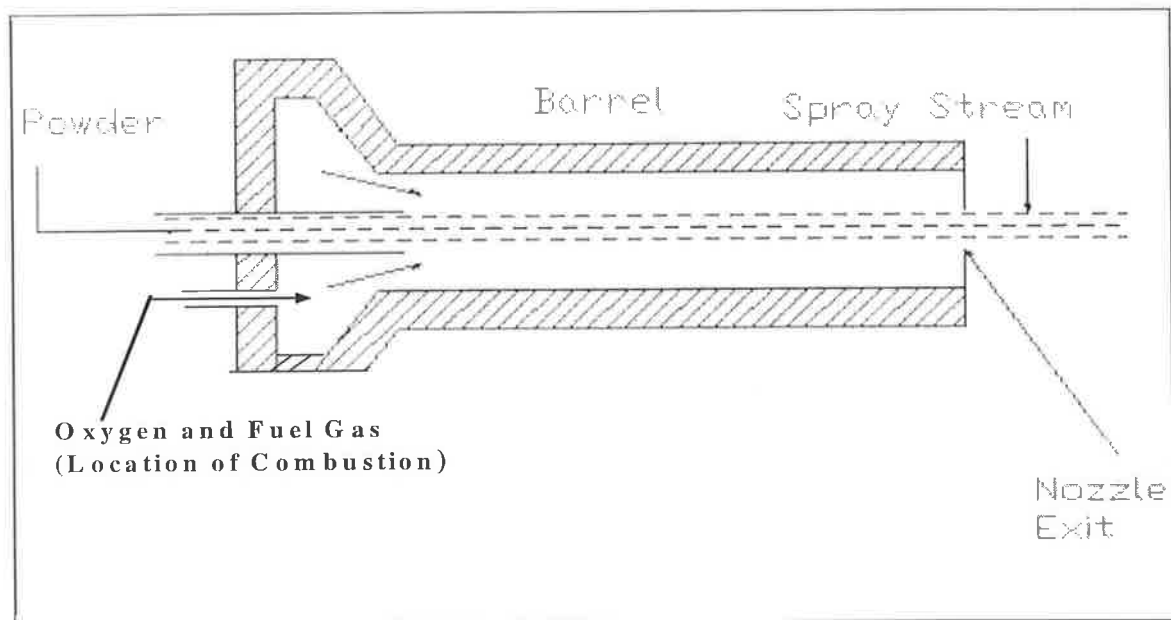


Figure 2.7: Schematic of a chamber combustion burner HVOF gun.

Table 2.2: Characteristics of different thermal spray techniques [31, 50].

Deposition Technique	Spray Gun Temp. ($^{\circ}\text{C}$)	Particle Velocity (m/s)	Coating Materials	Bond Strength (MPa)	Porosity (% Volume)	Hardness*
Electric Arc	6000	240	Ductile Materials	40-60	8-15	40R _h -35R _c
Plasma Spraying	16000	120-600	Metallic, ceramic, compound	30-70	2-5	40R _h -50R _c
Low Pressure Plasma	16000	900	Metallic, ceramic, compound	>70	<5	---
Spray & Fuse	---	---	Fusible metals	>70	<0.5	---
Flame Spraying	3300	240	Metallic, ceramic	20-28	10-20	30R _h -20R _c
HVOF Detonation Gun	4500	800	Metallic, ceramic, compound	>70	0.1-1	---
HVOF Sulzer METCO DJ Gun	2800**	1350	Metallic, ceramic	40-96	0.5-2	100R _h -50R _c

* R_c = Rockwell hardness on C scale

* R_h = Rockwell hardness on H scale

** Same as the one in the present work

2.5 COMBUSTION AND GAS DYNAMICS OF THE HVOF SYSTEM

The HVOF process uses an arrangement of thermal and kinetic energy for the melting and acceleration of powder particles, in order to deposit the required coating. Hydrocarbon gases or pure hydrogen are usually used as the fuel gas. The gun consists of three sections: a mixing zone, a combustion zone and a nozzle. Combustion and gas dynamics are vital characteristics in producing coatings. They affect the coating quality in the following two ways [51]:

- (1) The particles injected into the gas stream must be accelerated in order to strike the target at high velocity
- (2) Heat transfer to the particles from the gas stream is required to melt them prior to impact

Oxygen and fuel gas at certain pressures, are firstly mixed in the mixing zone and then sent on in the direction of the combustion zone. After ignition with an external ignitor, a chemical reaction takes place which releases heat energy. The pressure increases with an increase in temperature, and this result in the high gas velocities [52, 53]. The Stoichiometric (theoretically required for complete combustion) oxygen to fuel ratio approximately 4 to 1 (Figure 2.8 [36]). The energy released by the chemical reaction of the gases is used to heat and accelerate both the emerging gases and the spraying powder.

The selection of fuel gas depends upon economics, coating material and desired coating properties. Hydrogen fuel gas is used when processing oxygen sensitive materials; Propylene should be used when high heat input is necessary [43]. High melting, oxide based ceramics can only be sprayed by the HVOF process when acetylene fuel gas is used [49]. Table 2.3 shows the variation in different properties for 86WC/10Co/4Cr, produced by the HVOF Process using different fuel gases [54].

Table 2.3: Variation of properties of 86WC/10Co/4Cr, produced by different fuel gases [54].

Fuel Gas	Hardness (HV 0.3)	Roughness (μm)	Porosity (%)	Strength (MPa)
Hydrogen	1093	2.20	<1	>70
Propylene	1065	2.45	<1	>70
Natural Gas	1114	2.97	<1	>70
Liquid Propane	1016	2.52	<1	>70

The variation of spray parameters, such as the powder feed rate, oxygen to fuel flow rate ratio, flow rate of the compressed air and spray distance also effects the HVOF sprayed deposition thickness and properties. With a decrease or increase in the oxygen to fuel ratio from it's stoichiometric range (3.2-3.8), the deposition temperature decreases (as shown in Figure 2.8) [36]. This in turn decreases residual build-up in the coatings, (as will be indicated by Equation 2.1 later) however will affect the melting kinetics of the particle. With an increase in the spray distance, the flight time of the particles from the gun to the substrate is increased, which results in lower particle velocities and lower impact temperatures. Lower particle velocities and temperature causes inferior deposition thickness with lower residual stress in the coatings [55] and less bonding rates due to 'cold' particles striking the surface and re-bonding off the substrate. Compressed air is used in the HVOF process to accelerate powder particles onto the substrate [30]. Thus, an increase in the flow rate of the compressed air causes the particle velocities to increase inside the gun, as well as from the gun to the substrate. Higher particle velocities also decrease premature solidification of coating material before impact with the substrate [49].

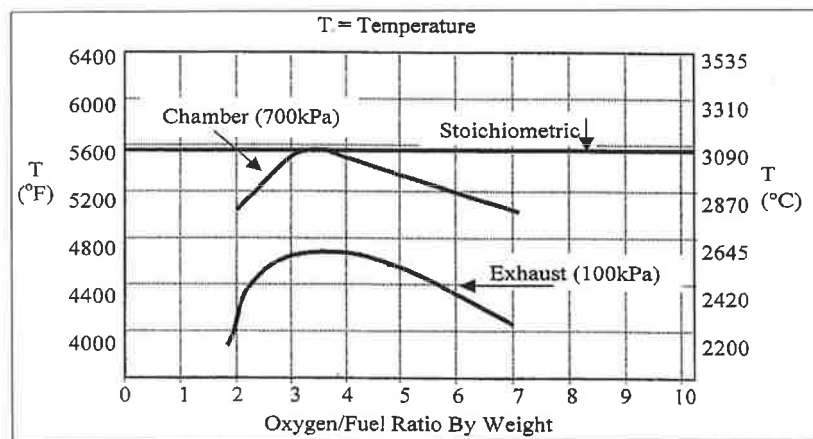


Figure 2.8: Theoretical flame temperature against oxygen/fuel ratio

Adopted from [36].

2.5.1 Features and Benefits of the HVOF Coating

Particle velocity is extremely significant in the thermal spray process, as the higher the velocity, the higher the bond strength, and the lower the porosity [36]. This is because particles have less time to cool down at high velocities. The HVOF process is designed around producing high velocities and this provides many of the advantages that the HVOF technique has (Table 2.4) over other thermal spray techniques [36, 56-58], which include:

1. More uniform and efficient particle heating, due to the high turbulence experienced by the particles
2. Much shorter exposure time in flight due to high particle velocities
3. Short particle exposure time in ambient air, once the jet and particles leave the gun, which results in lower surface oxidation of particles
4. Lower flame temperature compared with plasma spraying
5. Lower ultimate particle temperatures compared to other processes
6. Lower capital cost and ease of use compared to other processes
7. Very high coating thickness than with plasma and arc spraying can be produced
8. Excellent bond coatings
9. Low oxide metallic coatings (containing low content of oxide inclusion)
10. Dense with low porosity
11. Optimized microhardness
12. Predictable coating chemistries
13. Smooth as-sprayed surface finish
14. Excellent machined surface finish
15. Process can be automated
16. Dense, tightly bonded
17. Superior adhesion
18. High bond strength

Table 2.4: Benefits of using the HVOF coatings [23].

Coating benefit	Main reasons for this benefit
Higher density (Lower porosity)	Higher impact energy
Improved corrosion barrier	Less porosity
Higher hardness ratings	Better bonding, less degradation, denser coatings
Improved wear resistance	Harder, tougher coating
Higher bond and cohesive strength	Improved particle bonding
Lower oxide content	Less in flight exposure time to air
Fewer unmelted particle content	Better particle heating
Greater chemistry and phase retention	Reduced time at higher temperature
Thicker coatings	Less residual stress
Smoother as sprayed surface	Higher impact energies

2.5.2 Limitation of the HVOF System

1. The amount of heat content in the HVOF system while not as high as Plasma is still very high, so over heating of the substrate is quite likely. Therefore extra cooling of the substrate is often necessary, and cooling with liquid CO₂ is now a standard with the new HVOF process which applies during spraying [55, 59, 60].
2. Masking of the part is still a great problem as only mechanical masking is effective. It is very difficult and time consuming to design an effective mask for a complex component with areas, which do not require deposition.

2.6 THERMALLY SPRAYED COATINGS

A thermally sprayed coating produced in air is an assorted mixture of sprayed materials, oxide inclusions and porosity [10]. Each particle interacts with the adjacent environment during flight from the gun to the substrate. Sprayed coatings have individual characteristics that differentiate them from materials manufactured by other routes such as casting or sintering. Usually any material that does not decompose, vaporize, sublime or dissociate on heating, can be thermally sprayed.

2.6.1 Powder Description

The composition, particle size and some other properties of the nickel base alloy and stainless steel powders are shown in Table 2.5.

Table 2.5: Detail information of the nickel base alloy and stainless steel powder [61, 62].

SULZER METCO Name	Powder	Bond Strength MPa	Thickness Limit MM	Chemical Composition wt%	Hardness Macro/ Micro	Size Range μm
DIAM- ALLOY 1003	Austenitic Stainless Steel	61	2.5	Cr 17% Ni 12% Mo 2.5% Si 1% C 0.1% Fe Bal.	R _b 89	-53+20
DIAM- ALLOY 1005 Known as Inconel 625	Nickel/Chro mium Molybdenu m Base supper alloy	69	2.5	Cr 21.5% Mo 9.0% Nb 3.6% Ti <0.4% Al<0.4% Fe<0.5% Ni Bal.	R _c 30-34/ or DPH ₃₀₀ 350-450	-53+20
DIAM- ALLOY 2001	Fusible Nickel Base Alloy	64	2.5	Cr 17 Fe 4% Si 4% B 3.5% C 1% Ni Bal.	R _c 53-58/ or DPH ₃₀₀ 600-750	-53+20

Atomization is a eminent process of producing powder materials. It may be defined as the break-up of a liquid into fine droplets [63]. Both elemental and pre-alloyed powders can be formed by atomization. The types of atomization comprise of; gas atomization, water atomization, centrifugal atomization and so on, however gas and water atomization are most popular. Gas atomization uses air, nitrogen, helium or argon as a fluid for breaking up the liquid. It produces powders of more spherical and rounded shape and has lower oxygen content. On the other hand, water atomized powders are elongated in shape and have higher oxygen content. For high volume and low cost production, water atomization is preferred over gas atomization.

Thermal spraying can be used to deposit a wide range of coating materials. They can be divided into three main categories; metal/alloys, ceramics and cermets [64]. Examples of the first category are; copper, tungsten, molybdenum, tin, aluminium, zinc to mention a few. The second category includes; chrome oxide, aluminium oxide, alumina/titania composite, stabilized zirconia and so on. The third category, cermet consists of a ceramic and a metal or alloy. Examples are tungsten carbide in a cobalt matrix, chrome carbide in a nickel/chrome matrix and so on. In the current research the nickel base alloys and stainless-steel powders are used to achieve the surface properties as good corrosion and wear resistance. In the current research Diamalloy 2001 and Diamalloy 1005 was produced using the gas atomisation, while Diamalloy 1003 was produced using water atomization [65].

2.6.2 Coating Deposition, Solidification and Build-Up

During the spraying process, particles become superheated and are projected towards the substrate at a high velocity [66]. The common feature of thermally sprayed coatings is their lenticular or lamellar grain structure. Initially the particle are melted and propelled out from the gun in the form of a sphere, then at its first contact with the substrate the impact creates a shock wave inside the lamella and the substrate [41]. The behaviour of particle on impact has been researched intensively by various authors [67-69]. The shape and structure of the splat reveals a lot of information about the spray parameters, such as whether the correct spraying distance or spray angle have been utilised or not [70-72].

Molten particles deform into lamella and solidify giving a columnar structure [73]. Figure 2.9, shows a cross-section of a single lamella. In most typical conditions, the solidification process starts at the interface between the particle and the substrate, this interface forms a heat sink for the liquid. Formation of solidified grains depends on a number of factors determining particle deformation (spraying technique, method of spraying, powder grain size and sprayed material properties) and on the substrate (roughness, temperature and type of material). Substrate roughness must be adequate during spraying, otherwise adherence loss may occur [74, 75]. Gawne et al. [74] reported a linear increase of coating adhesion with an increase in substrate roughness in the range of 4 -13 μm .

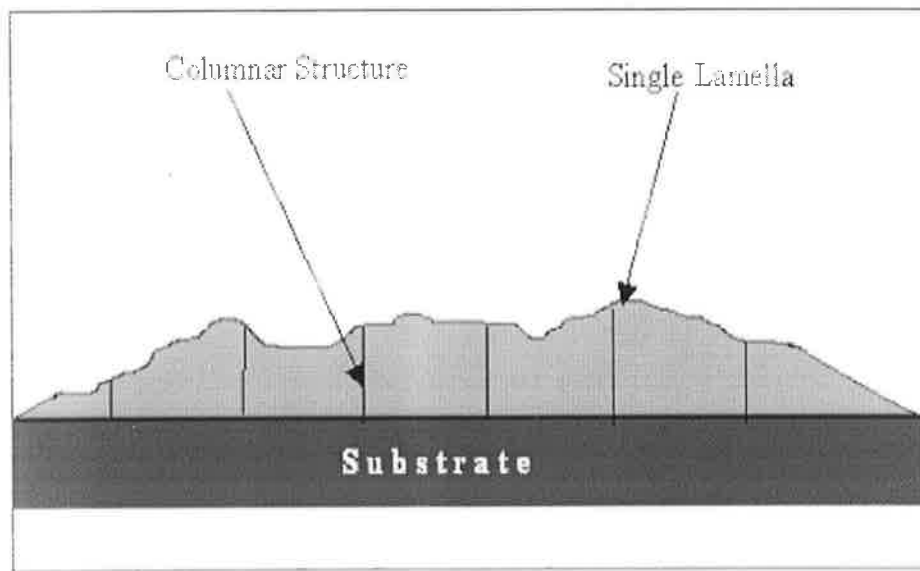


Figure 2.9: Cross-section of a columnar structure (single lamella) formed after solidification [49].

The coating is a build-up of individual particles that strike the substrate. Particles can be fully or partially melted at the moment of impact, depending on the relative difference between their melting temperature and the flame temperature. The rate of heat transfer from the flame to the particles also affects the degree of melting of coating material. Solid particles may rebound or remain weakly associated with the rest of the coating, resulting in lower bond strength. That is why cautious optimisation of the spray parameters is necessary to reduce such problems. Commonly, the spray gun is allowed to make numerous passes across the work piece in order to build-up a coating. The first pass of the gun deposits the first layer. It (first layer) composes usually of 5-15 lamella depending on the processing parameters [41]. This layer may be subjected to oxidation (for oxidizable material) and cooling. On the second

pass, the first layer (which may be partially solidified) cools the second layer due to the temperature difference amongst the two layers. The final coating may comprise of a number of passes of the deposited material. Afterwards, the coating is allowed to cool down to the room temperature.

2.6.3 Residual Stress

One of the most unavoidable problems in the build-up of thermally sprayed coatings is the formation of residual stress, particularly in the development of thick coatings [76-78]. In the HVOF thermal spraying process, individual molten or semi-molten particles impact the substrate or pre-existing molten material at high speed. Thus despite their low mass, they cause certain deformations to the pre-existing material. The impingement of each particle incurs stress fields, which depend upon the solid state of the pre-existing material. In addition to the mechanical effects of impact temperature, this has a huge influence on stress development [49]. In the combustion chamber of the HVOF gun, each particle is heated and then projected towards the substrate. On impacting the substrate, the particles deform into lamella and cool down to their melting temperature and solidify. The temperature decrease experienced by the particles is immense. This leads to the formation of stress in each lamella. Phase transformation stresses can also develop in thermally sprayed coatings if phase transformation occurs during processing [41]. S. Sampath, et al. [79] found that the evaluation of elastic-plastic characteristics showed how superior the HVOF deposit was in terms of mechanical properties compared to the Air Plasma Spray (APS) and Twin Wire-Arc spraying (TWA) techniques. This research also found that in the HVOF deposit, the average stress was compressive; due to additional high velocity impact that causes plastic deformation in the underlying layers and thus compressive stress (peening effect). There are mainly two mechanisms of residual stress development in thermally sprayed coatings, namely quenching and cooling.

Quenching Stress

According to Pawlowski [41], as many as 5 to 15 lamellae exist in a single pass of spray. As the lamellae solidify they contract, but are constrained by each other, and by the substrate, thus generating high tensile stresses in the individual lamellae as shown in Figure 2.10. Tensile quenching stresses are unavoidable and may be estimated by the following:

$$\sigma_q = \alpha_c (T_m - T_s) E_c \quad \text{-----} \quad \text{Equation 2.1}$$

Where

σ_q = quenching stress (Pa)

E_c = elastic modulus of the coating (Pa)

α_c = coefficient of thermal expansion of the coating (/K)

T_m = Temperature of the combustion chamber (K)

T_s = Temperature of flame at the substrate (K)

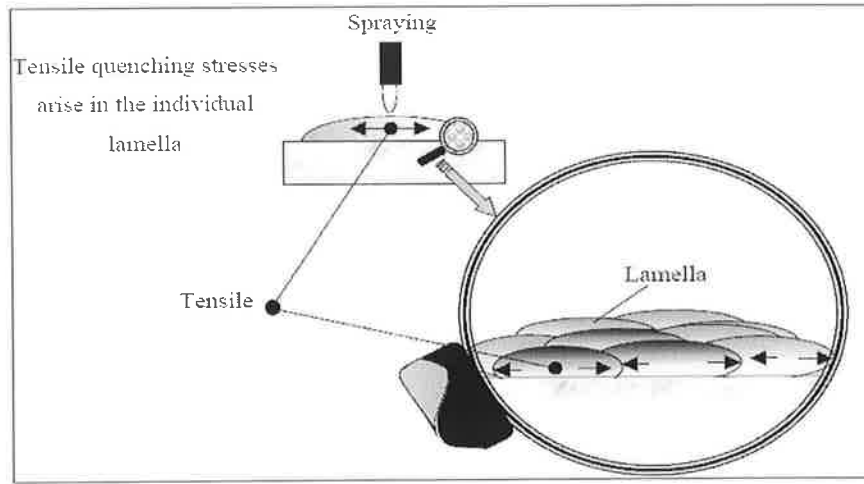


Figure 2.10: Schematic of quenching stresses adopted from [23].

Development of quenching stress through different layers of a five layer Nickel base alloy/Stainless steel graded coating (explained later) is predicted by adopting a mechanistic model of stress development described by Stokes [23]. This quenching stress may be estimated by the following equation [80]:

$$\sigma_q \cong \alpha_c \Delta T E_c \quad \text{-----} \quad \text{Equation 2.2}$$

Where, σ_q is the quenching stress. Temperature difference (ΔT) between the lamella melting/combustion temperature and the substrate is approximately the same throughout the quenching cycle; hence equation 2.2 can be written as:

$$\sigma_q \propto \alpha_c E_c \quad \text{-----} \quad \text{Equation 2.3}$$

Cooling Stress

When deposition is ceased or interrupted, cooling stresses initiate, mainly due to the thermal expansion co-efficient mismatch between the substrate and the coating material. If the coating contracts to a greater extent than the substrate ($\alpha_c > \alpha_s$), a tensile stress is generated in the coating [41]. This may lead to adhesion loss and cracking of the coating [81]. If the co-efficients are equal, then no cooling stress will develop. If the coating contracts by a smaller amount than the substrate ($\alpha_c < \alpha_s$), the resulting cooling stress will be compressive as shown in Figure 2.11 [41]. The cooling stress can be estimated using the following equation [80,82-84]:

$$\sigma_c = \left[\frac{E_c (T_f - T_R) (\alpha_c - \alpha_s)}{1 + 2 \frac{E_c t_c}{E_s t_s}} \right] \quad \text{----- Equation 2.4}$$

Where

σ_c = cooling stress (Pa)

E_c = Young's modulus of the coating (Pa)

E_s = Young's modulus of the substrate (Pa)

α_c = coefficient of thermal expansion of the coating (/K)

α_s = coefficient of thermal expansion of the substrate (/K)

t_c = thickness of the coating (m)

t_s = thickness of the substrate (m)

T_f = deposition temperature (K)

T_R = room temperature (K)

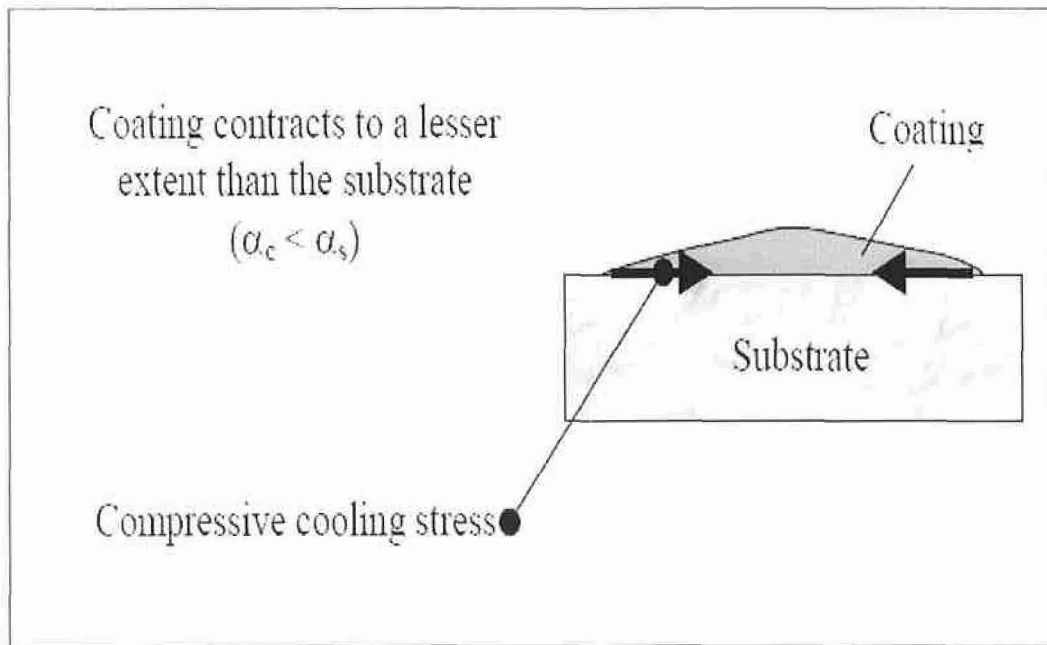


Figure 2.11: Schematic of cooling stresses adopted from [23].

The cooling stress can be predicted using equation 2.4. For a particular coating-substrate system, the coating thickness (t_c), substrate thickness (t_s), deposition temperature (T_f) and room temperature (T_R) can be kept constant. Then equation 2.4 can be written as:

$$\sigma_c \propto \frac{E_c (\alpha_c - \alpha_s)}{1 + 2 \frac{E_c}{E_s}} \quad \text{Equation 2.5}$$

Both the quenching and cooling stresses may be dissimilar to that predicted, as the Young's modulus and co-efficient of thermal expansion values for each layer may be different realistically from the values used here (derived from the Rule of mixture). The combination (summation) of the quenching + cooling stress produces what known as the residual stress. The nature of the overall residual stress may be resolved by the following criteria [41], if:

- a) $\alpha_c < \alpha_s$ stresses in the coating may be either tensile or compressive,
- b) $\alpha_c = \alpha_s$ stresses in the coating are tensile,
- c) $\alpha_c > \alpha_s$ stresses in the coating are tensile.

The possibility of either tensile or compressive residual stress (when $\alpha_c < \alpha_s$) arises if the compressive cooling stress is less or greater than that of the tensile quenching stress [41]. If the cooling stress is greater, then the resultant stress is compressive, and if it is less then the residual stress is tensile. Through suitable selection of the coating and substrate material, the high tensile quenching stress can be cancelled out by the compressive cooling stress. Generation of residual stress increases with an increase in coating thickness, thus resulting in a lower bond strength deposit [85]. Increasing the thickness of the deposit, increase the residual stress promoting fracture or failure of such coatings [32, 86].

2.6.4 Coating Structure and Properties

The deposit surface profile development depends on the coating structure and adhesion of the coating material to the base material [87]. A typical traverse section of a single-pass spray deposit has a conical profile, with the majority of the spray deposit concentrated around the central section [50]. Figure 2.12 shows a schematic section of a deposit in sequence P-Q, Q-R, R-S, where P is the periphery of the deposit, while S is the centre. The particles in the outer periphery tend to be commonly spaced and inadequately adhered to the substrate. The region from R to R is the densest and thickest coating deposited area [49]. The section Q-R is the transition from a dense coating to a porous coating structure. The edge sections (P-Q) can be enormously porous [49].

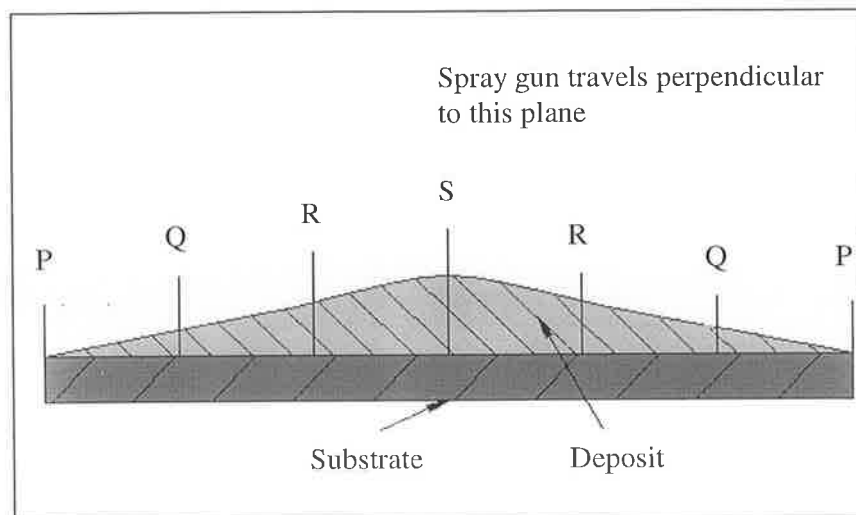


Figure 2.12: Schematic section of a spray deposit.

Thermal spraying has the ability to produce coating properties to suit the application required. Materials may be sprayed to create a hard or soft, dense or porous coating, thus it is difficult to report its typical coating properties. This report concentrates on functionally graded deposits; hence the properties of the coating will be discussed in the next Section 2.8.2.

2.7 FUNCTIONALLY GRADED MATERIALS (FGM)

Functionally graded materials are those materials used to produce components featuring engineered gradual transitions in microstructure and/or composition, the presence of which is motivated by functional performance requirements that vary with location within a component. With functionally graded materials, these requirements are met in a manner that optimises the overall performance of the component. [49]

Functionally graded materials have the potential to improve the thermo mechanical characteristics of a component in several ways [88]:

1. The magnitude of the thermal stresses (residual stresses) can be minimised
2. The onset of plastic yielding and failure can be delayed for a given thermomechanical loading by decreasing the magnitude of thermal stress below the yield stress of the material
3. Severe stress concentrations at intersections between free edges and interfaces can be suppressed
4. The strength of interfacial bond between dissimilar solids, such as a metal and a ceramic, can be increased by introduction of continuous or stepwise graduations in composition as compared to a sharp interface
5. The driving force for crack growth along an interface can be reduced by tailoring the interface with gradients in its mechanical properties
6. Gradients in the composition of the surface layers can be tailored to suppress the singular fields, which arise at the root of sharp indentations on the surface, or to alter the plastic deformation characteristics around the indentation

Functionally graded materials can be manufactured by two main methods [88]. Their names and classifications are shown in Table 2.6. Further information about these two processes are reported by Hasan [49].

Table 2.6: Names and classifications of different types of FGM manufacturing processes.

(a) Constructive Processes	(b) Transport-Based Processes
1. Powder densification processes	1. Mass transport processes
2. Coating processes	2. Thermal processes
3. Lamination processes	3. Setting and centrifugal separation
4. Deformation/martensitic transformation	4. Macrosegregation and segregative darcian flow processes

2.8 FUNCTIONALLY GRADED COATINGS

A functionally graded coatings is one in which the composition, microstructure and properties vary gradually from the bond coat to the top coat [89]. An example of a graded coating of material R and S is shown in Figure 2.13.

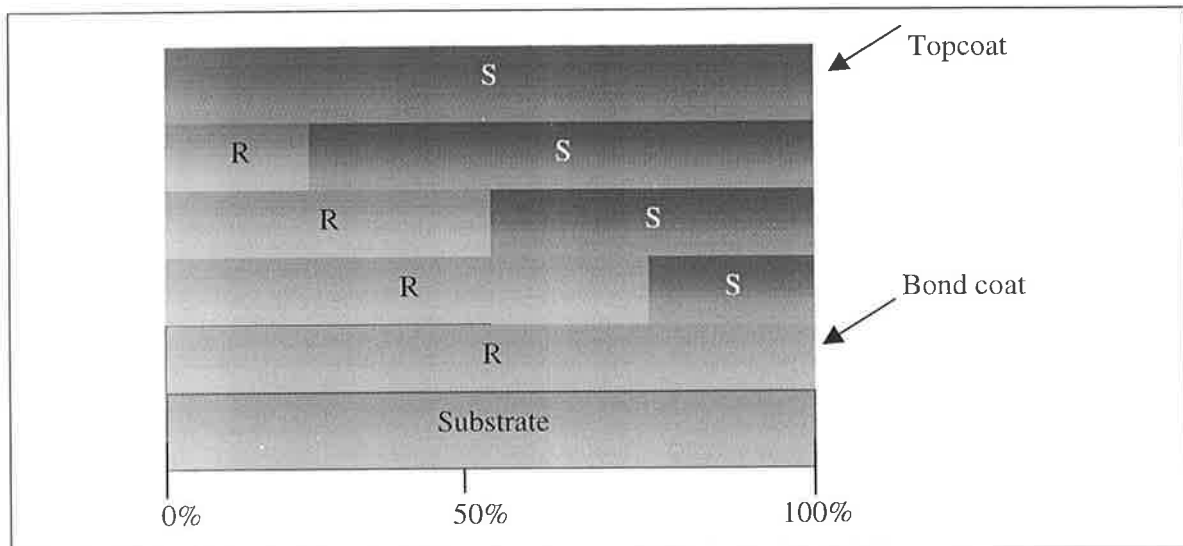


Figure 2.13: Schematic of Functionally graded coating of material R and S.

The bond coat is 100 percent R (coating similar to that of the Substrate material) and the top coat is 100 percent S (Hard Layer). The percentage of material R decreases from the bond coat to the top coat, while the percentage of material S increases from the bond coat from zero percent to 100 percent towards the top coat. Gradual changes in the composition and microstructure results in gradual changes in the elastic modulus and thermal expansion coefficient [90]. This in turn reduces coating residual stresses and stresses induced during heating and cooling (Equations 2.1 and 2.2). Residual stresses also decrease with an increase

in number of graded layers [85, 91]. So a duplex coating (two layers) would have a higher residual stress than a layered coating (more than two layers) of same thickness [49].

2.8.1 Different Techniques Producing Functionally Graded Coatings

The first development of functionally graded coatings was carried out in Japan in 1987 using the CVD (Chemical Vapour Deposition), PVD (Physical Vapour Deposition) and Plasma thermal spraying processes [92]. Since then some other techniques was used to manufacture graded coatings, (further details have been reported by Hasan [49]). The current research is interested in HVOF Thermal Spraying process; hence this is described in the following sections. The method by which Functionally Graded Coatings were deposited will be explained in full later.

HVOF Thermal Spraying Process

Compare to other thermal spraying processes, the HVOF process is relatively new in producing functionally graded coatings. Previous research [93-95] shows that the HVOF process has the potential to produce graded coatings. But the range of materials used in the research to date has been limited to WC-Co, stainless steel (SS) and MCrAlY/Al₂O₃-YSZ. Sampath et al. [93] used the HV 2000 HVOF system to manufacture graded coatings of WC-Co and stainless steel onto a steel substrate. In this research [93] two powder feeders were used for two different powders with a single gun. The feed rates of two powder feeders were changed to vary the proportion of the two powders to form different interlayers. The top coat was 100 percent WC-Co and the bond coat was 100 percent steel. The HVOF sprayed coatings had denser microstructure, uniform phase distribution within the layers and lower wear rates than graded coatings produced by plasma spraying. Peters et al. [94] manufactured MCrAlY/Al₂O₃-YSZ functionally graded coatings using the oxy-acetylene HVOF (OSU type gun) thermal spraying process. The bond coat was 100 percent MCrAlY; interlayers consisted of different proportions of Al₂O₃ and YSZ with increased amount of Al₂O₃ from the second layer to the top layer, while the top coat consisted of 75 percent YSZ and 25 percent Al₂O₃. HVOF sprayed graded coatings had a dense net-like structure. On the other hand, as a coating method modified Plasma Transferred Arc (PTA) welding process and TIG welding have been used to obtain these thick graded coatings on aluminium based materials with an increased hardness and improved wear resistance. PTA welding using an electrode with a permanent

positive polarity is suitable for producing wear resistant coatings based on aluminium alloys (base materials: AlMg4.5Mn and AlSi7Mg; filler materials Al–Cu–Ni) with high hardness. As materials, the ternary system Al–Cu–Ni proved to be suitable for providing high hardness as well as sufficient toughness. The content of copper was up to about 50 wt.% while a nickel content of about 20 wt.% was achieved. The hardness of the alloyed matrix depended on different factors, for example content of copper—mainly forming Al_2Cu phases—as well as nickel, where additional intermetallic phases like AlNi_4Cu_7 were identified. Therefore, the graded layers possess a large gradient in hardness with a maximum level of about 700 HV mostly in the top layer. As a result the HVOF sprayed graded coatings yielded better wear and erosion resistance than the graded coatings produced by air plasma spraying (APS). Kim et al. [95] manufactured NiCrAlY/YSZ functionally graded coatings using the Detonation Gun HVOF thermal spraying process. An alternative spraying method of ceramic YSZ and metallic NiCrAlY was used in their research. Two powder feeders were utilised to carry two different powders. The bond coat was 100 percent NiCrAlY, while the top coat was 100 percent YSZ. The interlayers consisted of varying proportions of NiCrAlY and YSZ. Using different shot ratios of those powders the research varied the percentage of ceramic and metallic powders in the interlayers. As an example, spraying with a shot ratio of 1:3 meant that spraying sequence consisted of three shots of metal powders followed by one shot of ceramic powder, resulted in a mixture of ceramics and metals with ceramic to metal volume ratio of 1:3. In the area overlapped by consecutive shots, an excellent mixture of ceramic and metal was produced. The Functionally graded NiCrAlY/YSZ coatings resulted in having better thermal shock resistance than duplex NiCrAlY/YSZ coatings.

There are large ranges of materials, which have potential to benefit from graded structures yet to be researched. The current study aims to contribute new knowledge in these areas by depositing nickel base alloy/stainless steel functionally graded coatings on steel substrates using the HVOF process. Nickel base alloy/Stainless steel graded coatings are used in the automotive and marine industry not only to increase strength of the coated system but also for corrosion applications. Previous researchers have used the same system to deposit two different coating materials to producing graded coatings, which was time consuming. The current study aims to deposit graded coatings in a more cost effective way. Thermal spraying can be used to produce inter layers of FGM coating in two methods; Using premixed powder to produce each different layer and secondly Co-injecting two different powders and varying their relative proportions during deposition. Most researchers [2-6] have used the former

method while producing functionally graded coatings; however the latter method was used in this project. This idea for this project evolves from the initial idea/concept within the following patent: Stokes, J., Hasan, M., et al. Irish Patent number 2006/0821, Nov, 2006.

2.8.2 Characteristics and Properties of Functionally Graded Coatings

The most important characteristics of functionally graded coatings are the gradual change in coating structure, which results in gradual change in coating properties. Some of those properties, such as; microstructure, hardness, corrosion resistance, porosity and residual stress which are described below.

(a) Microstructure

Several researchers [5,96-103] have reported the gradual change in microstructure within graded coatings. Khor et al. [4-6] manufactured ZrO_2 -NiCrAlY graded coatings by plasma spraying using premixed powders. From the NiCrAlY base layer to the ZrO_2 top layer, NiCrAlY changed its morphology from lamellar to a dispersed structure, while the morphology of ZrO_2 was changed from a dispersed to a porous structure. No clear interface between the two adjacent different layers was found. For the NiCrAlY/ ZrO_2 - Y_2O_3 [93] or NiCrAl-Mg ZrO_3 [101] coated specimens the researchers reported a gradual change of coating structure was found.

(b) Hardness

Thermal spray coatings generally include voids and oxides within the coating, thus macro-hardness levels are less than those of the equivalent material in wrought or cast form [49]. There are two ways to measure hardness; macro hardness test and micro hardness test. To determine the resistance of the total coating deposit to point penetration, macro hardness tests are carried out using either the Brinell or Rockwell hardness test. While micro-hardness tests are carried out at low loads on individual particles using, what is identified as the Knoop or Vickers hardness test [104]. Functionally graded coatings produce gradual deviation of hardness throughout the coating thickness. Numerous researchers [5, 91, 93, 96, 97] have measured the hardness value of graded coating using different types of hardness tests. In each

case hardness changed gradually (increasing) from the base layer to the top layer of the coatings. Khor et al. [91, 97] measured hardness values of a five layer graded coating and a duplex coating of same materials and reported almost same surface hardness values for the two types of coatings. But deposition thickness was different for the two cases. However, Hasan [49], found the hardness to decrease with an increase in number of layers.

(c) Corrosion Resistance

Corrosion means the electrochemical degradation of metals/alloys or chemical degradation of materials (glass, plastic and so on) due to a reaction with their environment; usually accelerated by the presence of acids or bases [105]. Iron and steel are the most common materials of interest where their corrosion characteristic in neutral waters is important. When steel corrodes, the corrosion rate is usually governed by the cathodic reaction of the corrosion process, and oxygen is an important factor. In neutral waters free from dissolved oxygen, corrosion is usually negligible. The presence of dissolved oxygen in the water accelerates the cathodic reaction; and consequently the corrosion rate increases in proportion to the amount of oxygen available for diffusion to the cathode. Where oxygen diffusion is the controlling factor, the corrosion rate tends to increase also with rise in temperature. In acid waters ($\text{pH} < 4$), corrosion can occur even without the presence of oxygen [106].

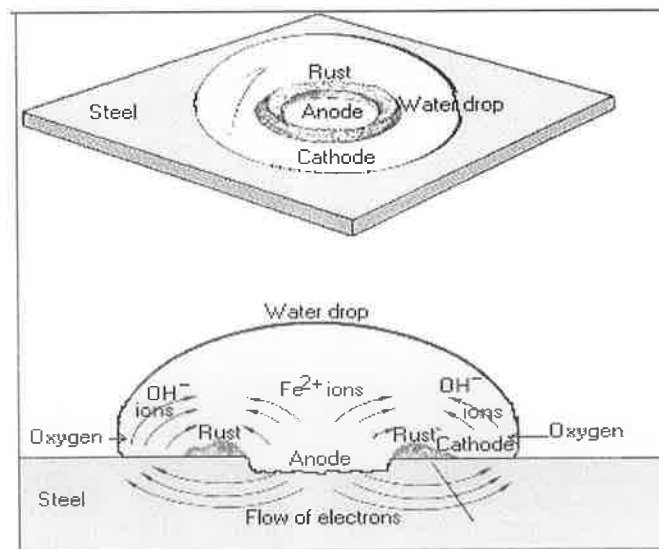


Figure 2.14: Schematic of Corrosion of steel under a droplet of water [106].

Ideally, a material, which is inherently resistant to its service environment, meets with the mechanical, formability and economic requirements would be the first choice for selection.

Unfortunately, this is not often the case. Many materials will need a method of corrosion control and there are three main approaches [106]:

- Modification of the environment to which the material is exposed
- Electrical methods of control
- Use of protective coatings

Thermal spray coatings are widely used in preventing corrosion of many materials, with very often; additional benefits of properties such as wear resistance, due to the very wide selection of coatings that can be sprayed. Broadly, thermal spray coatings fall into three main groups [106]:

- Anodic Coatings
- Cathodic Coatings
- Neutral Coatings

Cathodic coatings are those, which comprise a coating metal, which is cathodic with respect to the substrate. A stainless steel or nickel alloy coating would be cathodic due to its steel base. Cathodic coatings can provide excellent corrosion protection. There is a very wide choice particularly for steel base materials ranging from stainless steel to more exotic materials like tantalum to cater for the more extreme corrosive environments. However, an outstanding limitation of such coatings is that they must provide a complete barrier to the substrate from the environment. If the substrate is exposed to the corrosive environment, the substrate will become the anode and corrosion will be dramatically accelerated resulting in spalling of the coating. Generally, sealing of these coatings is always recommended. Processes, which provide the densest coatings, are preferred (HVOF, plasma and fused coatings). Thick coatings will provide better protection than thin coatings [106]. Boiler steels are unable to meet simultaneously the requirements for both the high temperature strength and the requirements for both the high temperature corrosion resistance, so protective coatings are used to prevent from corrosion [107]. Metallic coatings sprayed on the superheater tubes have reduced the erosion and corrosion in the selected cases [108]. The NiCr coating provided the best protection to the substrate steel, which may be due to the formation of NiO, NiCr₂O₄ and Cr₂O₃ as confirmed by XRD, EPMA and EDAX analysis. These phases are reported to be protective oxides [109, 110]

Welding or electroplating has been traditionally used to deposit corrosion resistant coatings, but these applications have been restricted by metallurgical incompatibility between the overlay and the substrate [111]. Thermal spraying can also deposit functional coatings onto substrates, but the porous nature of thermally sprayed coatings limits its application in corrosive environments. The HVOF and HVAF techniques are comparatively new thermal spraying methods which can produce high quality and low porosity coatings well bonded to the substrate [111–113]. Browning invented the high-velocity impact forging (HVIF) thermal spray technique which improves the density of sprayed coatings over those deposited by HVOF thermal spraying and HVAF thermal spraying [114]. With the technical improvement of thermal spraying, various coatings can be used as corrosion resistant surfaces in the future. It is hence necessary to study the mechanistic corrosion process of films produced by thermal spraying. Nickel-base super alloy INCONEL alloy 740 has been shown to improve structure stability and corrosion resistance [115]. The effect of heat treatment on the microstructure and properties of HVOF-sprayed Ni–Cr–W–Mo–B alloy coatings [116] and the effects of thickness of the coating on the electrochemical behaviour of Cr₃C₂–NiCr coatings [117] has also been reported. The corrosion resistance of nickel-based alloys in 5% NaCl and 0.5 M H₂SO₄ [118,119] has been studied. Harvey et al. [120] studied the relationship between spraying parameters and microstructure and corrosion resistance of coatings of nickel alloy, cobalt alloy, duplex stainless steel and iron based materials. Other reports in the literature also attempted to relate the corrosion resistance to metal contents such as Zn and Al deposited by arc spraying [121–127]. Most researchers have so far focused on comparing the performance of the corrosion behavior of different materials in one or more corrosive medium(s), but very few researchers have studied the mechanistic process of corrosion [128], especially the NiCrBSi alloy that is a commonly used corrosion resistant material.

The adverse effect of fluids on a solid surface is the result of the complex interaction of chemical and physical forces. Direct exposure to liquids, gases and particle solids can quickly produce chemical corrosion or erosion of a solid surface. The high-speed movement of these corrosive fluids prevents the protective oxides and permits this hostile interaction of corrosion or erosion to take place. Cavitation occurs when pressure changes in the liquid lead to the formation and collapse of vapour bubbles. This produces high-pressure shock waves that can destroy metallic surfaces. Particles within the fluid can impact the surface, damaging it even further [129]. HVOF with its different powder characteristics would suit most applications to minimise the erosion or corrosion of the internal parts of the industrial equipments [130].

Repair shops could customise their requirements by utilising HVOF coatings. For instance; a carbon steel pump shaft could be coated with Inconel-625 to increase its corrosion resistance [130]. The same shaft could be enhanced in terms of wear resistance if coated using Tungsten Carbides (WC) [131]. NiCrBSi alloy powders were coated on a low carbon steel substrate using HVOF thermal spraying, and corrosion tests were carried out. It was found that the corrosion of the NiCrBSi coating first occurred around the particles that had not melted during spraying and the defects such as pores, inclusions and micro cracks, then followed by the development along the paths formed by pores, micro cracks and lamellar structure, resulting in exfoliation or laminar peeling off. Adjusting the thermal spraying parameters to reduce the electrochemical unevenness or sealing the pores can improve the corrosion resistance of the coating [132].

One of the applications of thermal spraying is to increase corrosion resistance to such materials as iron and steel are often subjected to these effects [62]. Steel valves used in the marine industry are subjected to corrosion from salt water; hence failure of such component is inevitable over time.

FGM deposition is one way of increasing corrosion resistance of a substrate material. Suman [133] studied the morphology, composition and erosion-corrosion behaviour of Ni-Cr-Si-B cremet coating overlaid on a carbon steel substrate by HVOF thermal spraying. Erosion-Corrosion tests were carried out in a solid free seawater impinging jet of velocities 17, 25, 50 and 72 m/s at temperatures of 180°C and 500°C. The behaviour of the coatings was followed by undertaking electromhchemical (E/C) monitoring during the impingment erosion process. This involved anodic polarization scans which demonstrated the effect of the impinging jet and increased temperature in reducing the resistance of the coating under erosion-corrosion conditions in comparison with corrosion in static seawater and corrosion at ambient temperature. Evans et al. [134] reported increased corrosion resistance of overlay MCrAlY/Al graded coatings. The bond coat was NiCrAlY or CoCrAlY and the top coat was an Al enriched β -NiAl. At high temperature, the top coat gave the component its corrosion resistance, while at low temperature the interlayer and bond coat provided corrosion resistance for the substrate.

(d) Porosity

Porosity or voids in the coating structure is a vital concern in thermal spraying as it affects many other mechanical properties, such as bond strength [43]. Depending on the thermal spraying process utilised, porosity may vary from 0.1 to 15 of the volume percent. The HVOF process exhibits the lowest porosity among all of the thermal spraying processes due to its high particle impact velocity that compresses most air pockets out of the microstructure [31]. Table 2.7 shows porosity results for various Diamond Jet HVOF coatings.

Table 2.7: Coating porosity in various Diamond Jet HVOF coatings [62,135].

Coating material	Porosity (%)
Nickel/Chromium Molybdenum Base Superalloy	1
Tungsten Carbide-Cobalt	<0.5
Cobalt Base Alloy	1.5
Chromium Carbide/ Nickel Chromium	1
Tool Steel	<1
$\text{Al}_2\text{O}_3\text{-13TiO}_2$	1.2

Because of the gradual structural changes from the bond top layer to the top layer in FGMs, porosity in functionally graded coatings changes gradually through coating thickness as reported by Khor et al. [99,102]. Khor et al. [99] reported a gradual increase of porosity from the NiCoCrAlY base layer to the YSZ top layer, the author [136] again reported gradual change of porosity from the Ti-6Al-4V base layer to the HA (Hydroxyapatite) top layer. In each case, the plasma spraying was used to deposit graded coatings.

(e) Residual Stress

Cooling residual stress, mentioned earlier occurs due to mismatch of properties between the substrate and coating and also between different layers of the coating. Co-efficient of thermal expansion (CTE) and elastic modulus are the two main properties causing cooling stress build-up in the coating. Graded coating is one way of reducing cooling stress as it reduces the difference of the CTE and elastic modulus between the substrate and coating and also between different layers of the coating. Several researchers reported gradual change in the CTE and elastic modulus including [3, 90, 93, 137-139], which resulted in a reduced residual stress in coatings. Residual stress increases with an increase in coating thickness, while an increase in number of graded layers maintaining, the same thickness decreases in residual

stress [85, 91]. Hasan [49] found that the residual stress decreased with an increase in number of deposited layers.

2.8.3 Applications of Functionally Graded Coatings

Thermally sprayed nickel-based alloy coatings are used in a variety of applications, for example as bond coats for thermal barrier coatings (TBCs) on turbine components, as restorative layers for machine parts, as bond coats in internal combustion engine cylinders, for corrosion protection of boiler tubes and in numerous other applications requiring wear-, high temperature- and corrosion-resistant surfaces [140–145]. Since its invention in 1987, functionally graded coatings have been applied to various fields and sectors to enhance the performance of components. The most frequent application of functionally graded coatings is as TBC. Duplex thermal barrier coatings, consisting of a metallic bond coat and a ceramic top-coat, are applied in diesel engines, gas turbines and aircraft engines to increase the service life of their components [146-149]. The metallic bond coat increases adhesion with the substrate, while the ceramic top-coat reduces the temperature of the bond coat and substrate. However mismatch of properties between the bond coat and top-coat induces cooling residual stress, which in turn causes delamination and spalling of the duplex coatings [150,151]. Functionally graded coatings, consisting of a metallic bond coat, ceramic top coat and intermediate layers consisting of different compositions of ceramic and metallic materials, is one way of reducing delamination and spalling of thermal barrier coatings [3, 5, 91, 97,152, 153]. The bond coat increases adhesion with the substrate; the top coat reduces temperature of the interlayers and substrate, while the intermediate layers decrease residual stress.

Another important application of graded coatings is in the biomedical field. Several researchers report the use of functionally graded coatings in engineering [154-162]. Kon et al. [154] and Wang et al. [156] manufactured functionally graded coatings of calcium phosphate/titanium. The calcium phosphate top coat gave excellent biocompatibility; the titanium bond coat gave mechanical adhesion strength with the substrate, while the gradient interlayers decreased residual stress build-up and increased coating adhesion. Verne et al. [159] deposited bioactive glasses and particle reinforced composites on alumina substrate in order to combine mechanical properties of high strength alumina with the bioactivity of the coating. A graded structure in the coating was used to minimise the stress build-up. Khor et

al. [136] manufactured hydroxyapatite/Ti-6Al-4V functionally graded coatings using the plasma spraying process. Hydroxyapatite (HA), which is widely preferred as the bioactive material in both dentistry and orthopaedics gave favourable osteoconductive and bioactive properties, titanium bond coat gave excellent strength to the coatings, while the interlayers decreased stress. Remer et al. [157] reported improved bond strength of titanium/hydroxyapatite (HA) coatings, while Liu et al. [158] reported improved bond strength of Ni-P-PTFE coating by obtaining composition gradation in their coatings. Multilayered non-graded HA coatings have already been manufactured using the HV 2000 HVOF process [163], so this process may be the next technique in producing functionally graded hydroxyapatite coatings, not only to reduce residual stress, but also to produce coatings suitable for biomedical applications.

The Automotive industry may be a potential field for the application of graded coatings. Weight reduction in automobiles is particularly important. The average vehicle weight is expected to increase, as the automobile industry continues to market new models with luxury, convenience, performance and safe cars as demanded by their customers [164]. According to the “European Transport Policy for 2010: time to decide”, by 2010, the demand for mobility will increase in the EU by 24 percent in the passenger domain [165]. Replacing steel or iron parts by lightweight materials is a useful way of reducing vehicle weight. Several researchers [166-172] mentioned the importance of lightweight materials like aluminium, magnesium and titanium in the automotive industry. Reduction in vehicle weight, in turn increases fuel efficiency. As an example, 10 percent of vehicle weight reduction results in a 8 to 10 percent fuel economy improvement [164].

HVOF sprayed Inconel-625 [173] coating has demonstrated that spraying process variables are important factors where corrosion and erosion are concerned. Low porosity and oxide content generated from low powder feeding rate and short spray distance within the specified range from the equipment manufacturer produce hard coating surfaces with good corrosion and erosion resistance. These coatings are also applicable for the severe corrosion and erosion environments of different industrial applications [173]. A wide range of alloys is being evaluated for use in a new generation of seawater valves for the U.S. Navy [174]. This new generation of valves is being developed to reduce valve life cycle costs and to ensure materials compatibility with advanced seawater piping materials such as commercially pure titanium. Part of the evaluation includes assessing the corrosion performance of candidate

valve materials. Crevice corrosion performance is of particular interest since valves are connected to shipboard piping systems with flanges and since valves contain numerous internal crevices. The Crevice corrosion tests were performed at constant temperature, in natural seawater under both quiescent and flowing conditions. Bronze, copper-nickel, and nickel-copper alloys, which are currently used in Navy valves, were used as standards by which the performance of stainless steel, nickel-base, titanium, and cobalt alloys could be measured. No crevice corrosion was observed on any of the titanium or cobalt alloys tested while the stainless steel and nickel-base alloys ranged from fully resistant to highly susceptible to corrosion [174]. The Wrought alloys were typically more resistant to crevice corrosion than their cast equivalents [174].

A series of NiCr spray forming runs were completed in order to investigate the mechanisms for exceptional high strength and ductility in previous spray formed (using whole process) 50Ni-50Cr (all compositions in wt %) tubes. Although test results showed good strength, the best mechanical properties of these spray formed alloys were not achieved. The mechanical properties of this eutectic region alloy were found to be sensitive to small changes in processing parameters and chemical composition. More specifically, it was found that slight increases in chromium and nitrogen content could increase strength but decrease ductility and fracture toughness. Crevice corrosion testing was also performed on a spray formed 50Ni-50Cr disk. After a six-month exposure in coastal seawater, the alloy showed no evidence of crevice corrosion. This result may be a result of one or all of three different known corrosion resistance enhancements: small-scale spray formed microstructure, increased chromium, and increased nitrogen. Slow strain rate (SSR) tests were also performed on 50Ni- 50Cr samples, which showed good performance under freely corroding conditions, but experienced a reduction in maximum load under polarized conditions. Based on the results of this series of NiCr spray forming experiments, it is proposed that their future work included NiCr alloys with slightly higher nickel and lower chromium contents (52Ni-48Cr). These changes are likely to increase fracture toughness values without compromising strength and corrosion resistance. It is also suggested that future corrosion tests compare spray formed and cast NiCr alloys, as well as varying the chromium and nitrogen components in order to pinpoint and capitalise on the reason for the excellent crevice corrosion resistance of the 50Ni-50Cr materials [175]. Recently, a host of carbide based alloys including WC-Co-Cr, NiCr-Cr₃C₂, WC-WB-Co and so on have been developed in an attempt to bridge the gap between providing both wear and corrosion protection [176,177]

Functionally graded coatings have other potential application areas including improved machine tools with high fracture toughness, lightweight armour materials with high ballistic efficiency [137], optical components [178] to mention a few. Thin film optical coatings play an important role for the design of optical components used in the laser field. Optical components with graded coatings allow the improvement of the quality of the laser beam without introducing additional optical elements inside the cavity.

According to the Thermal Spray Materials Guide [65], typical properties and applications of Diamalloy 1003, Diamalloy 1005 and Diamalloy 2001 powders are shown in Table 2.8 with chemical composition.

Table 2.8: Typical applications of stainless steel/nickel base alloy powder [61, 65, 179]

Iron Base Alloys						
Code Name of Coating powder	Powder Type	Composition	FST p/n	Size Range (µm)	Typical Properties and Application	Typical Applications
Diamalloy 1003	316 Stainless Steel	Cr 17% Ni 12% Mo 2.5% Si 1% C 0.1% Fe Bal. Atomised	M-684.33	-53+20	<ul style="list-style-type: none"> • Good corrosion properties • Smooth and easy to machine coatings • Good against fretting, cavitation and erosion • Good for dimensional restoration and build-up • Equivalent to: 1236 °F 	Gas Turbine Fan Seals, Low Temp. Practice Erosion

Nickel Base Alloys						
Diamalloy 1005	Inconel 625	Cr 21.5% Mo 9% Nb 3.6% Ti <0.4% Al <0.4% Fe <0.5% Ni Bal	M-326A.33	-53+20	<ul style="list-style-type: none"> ●HVOF and Air Plasma ●Excellent high temperature oxidation and corrosion properties ●Good for repair and build-up similar chemistry super alloy components ●Useful up to 980 °C (1800 °F) ●Equivalent to: Diamalloy 1005, 1265 °F 	Chemical Processing & Pollution Control Equipment, Repair & Restoration of Inconel 625 Gas Turbine Components
Nickel Base Alloys						
Diamalloy 2001	NiCrSiB	Cr 17% Fe 4% Si 4% B 3.5% C 1% Ni Bal. Gas Atomised	M-771.33	-53+20	<ul style="list-style-type: none"> ●HVOF ●Self Fluxing type alloy ●Good corrosion and wear resistance ●Serviceable up to 820 °C (1500 °F) Coatings are dense and essentially oxide free ●Equivalent to: 1275H, Diamalloy 2001 	Piston rings, Cylinder liners, Utility exhaust fans, Thread guides, Hot forming dies, Forging tools

In current research all of the three powders mention above (and these are all used in this research) contain Nickel and Chromium. Chromium improves corrosion resistance and mechanical properties at elevated temperatures [115], and Nickel and Chromium combined (Diamalloy 1005) increases strength and weld ability [115].

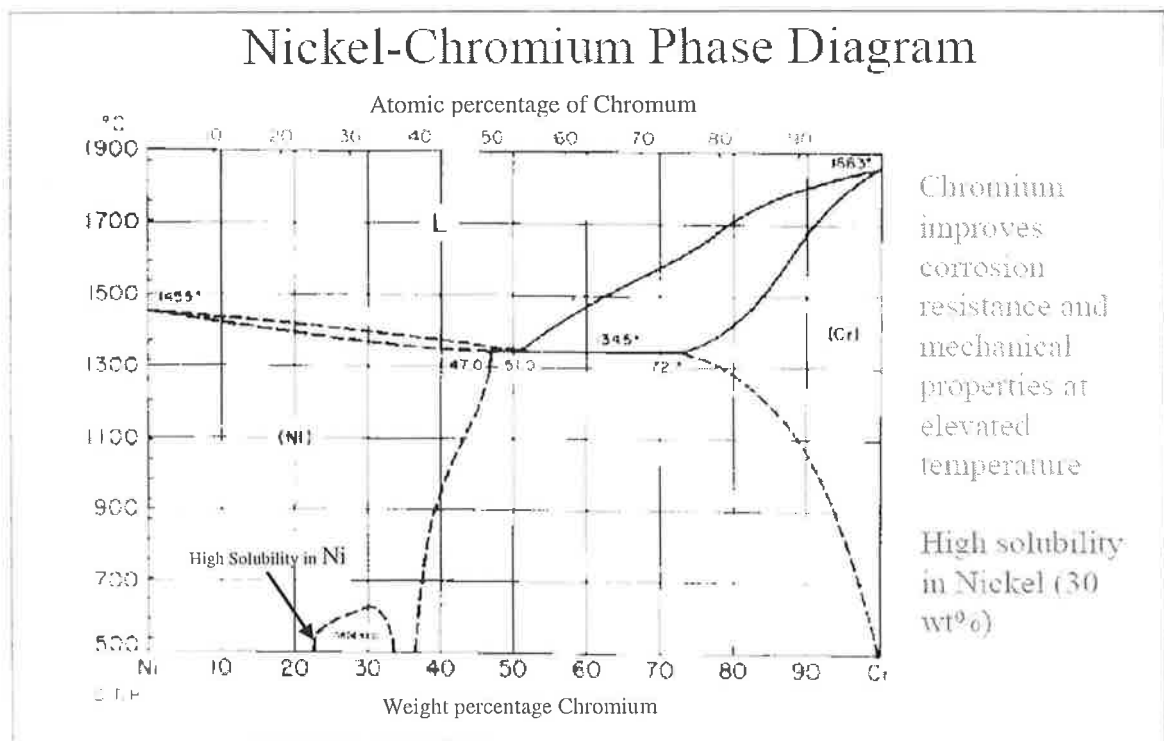


Figure 2.15: Nickel-Chromium Phase Diagram [115].

The thermal spray coatings deposited by the HVOF process, exhibit lower cavitations wear rates than the thermal spray coatings deposited by the plasma spray process, as determined by laboratory testing using the cavitations jet test apparatus [180].

Corrosive environments, on the other hand, call for different materials, and hardness is not normally a factor. 316 stainless steel is the most universally selected material for use in corrosives environments. It has a wide resistance to corrosion, and because of this many manufacturers have made this a standard material, due to its reasonable cost [181].

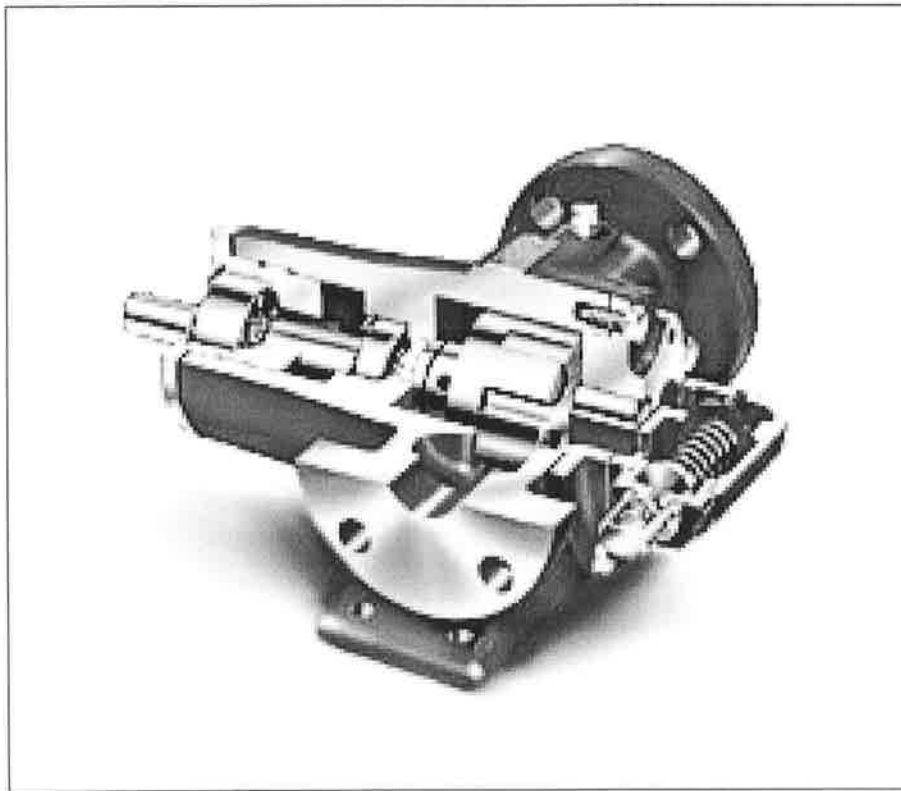


Figure 2.16. A corrosion-resistant 316 stainless steel pump [181].

HVOF thermal sprayed coatings offer higher density, better wear and corrosion resistance, higher bond strength, lower oxide content, less unmelted particle content, better chemistry and smoother as-sprayed surfaces compared to other thermal spraying processes. This is due to the high particle velocities associated with the system to propel molten material at supersonic speed towards the substrate [44]. However the deposition of thick coatings is still a problem due to the build-up of residual stress [77-78]. Functionally graded coatings in which the CTE and elastic modulus vary gradually from the substrate to the coating [3, 21, 90, 93,137] are clearly one method of reducing residual stress. The current research investigates an innovative modification of a commercial HVOF thermal spraying process to produce nickel base alloy/stainless steel functionally graded coatings to prevent the surface of substrate from erosion or corrosion. A two-powder co-injection method is chosen here to deposit graded coatings. The current HVOF thermal sprayed facility, along with the design of a dual powder feed which was manual operated system required to deposit graded coatings is described in the following chapter. While the functionality of the Nickel based alloy/Stainless Steel coatings under corrosion environments will not be tested in this research, the aim will be the design of an automation system to mix powders and to produce FGMs.

CHAPTER 3

HVOF EXPERIMENTAL EQUIPMENT AND PROCEDURES

3.1 INTRODUCTION

The aim of present study is to produce Functionally Graded Thermal Spray Stainless Steel and Nickel base alloy coatings. In this chapter, the HVOF thermal spray facility used in the research is described. In addition to the process equipment, the newly installed Vaporising unit used during this technique is also presented.

In this current research the HVOF thermal sprayed facility used is a manually controlled continuous combustion Sulzer Metco Diamond Jet thermal spray system. It consists of two units: the spraying system and its support system. A newly installed vaporizer unit has been used to get better flow rate of fuel gas, which was installed in 2006 by the B.O.C gases company (U.K) and it is a part of the support system. Both systems are integrated together, to produce coatings. Figure 3.1 shows the complete thermal system used in this present research.

3.2 HVOF THERMAL SPRAYING SYSTEM

The HVOF thermal spraying system consists of the following:

1. Diamond Jet (DJ) gun
2. Powder feed unit
3. Gas supply and flow meter unit

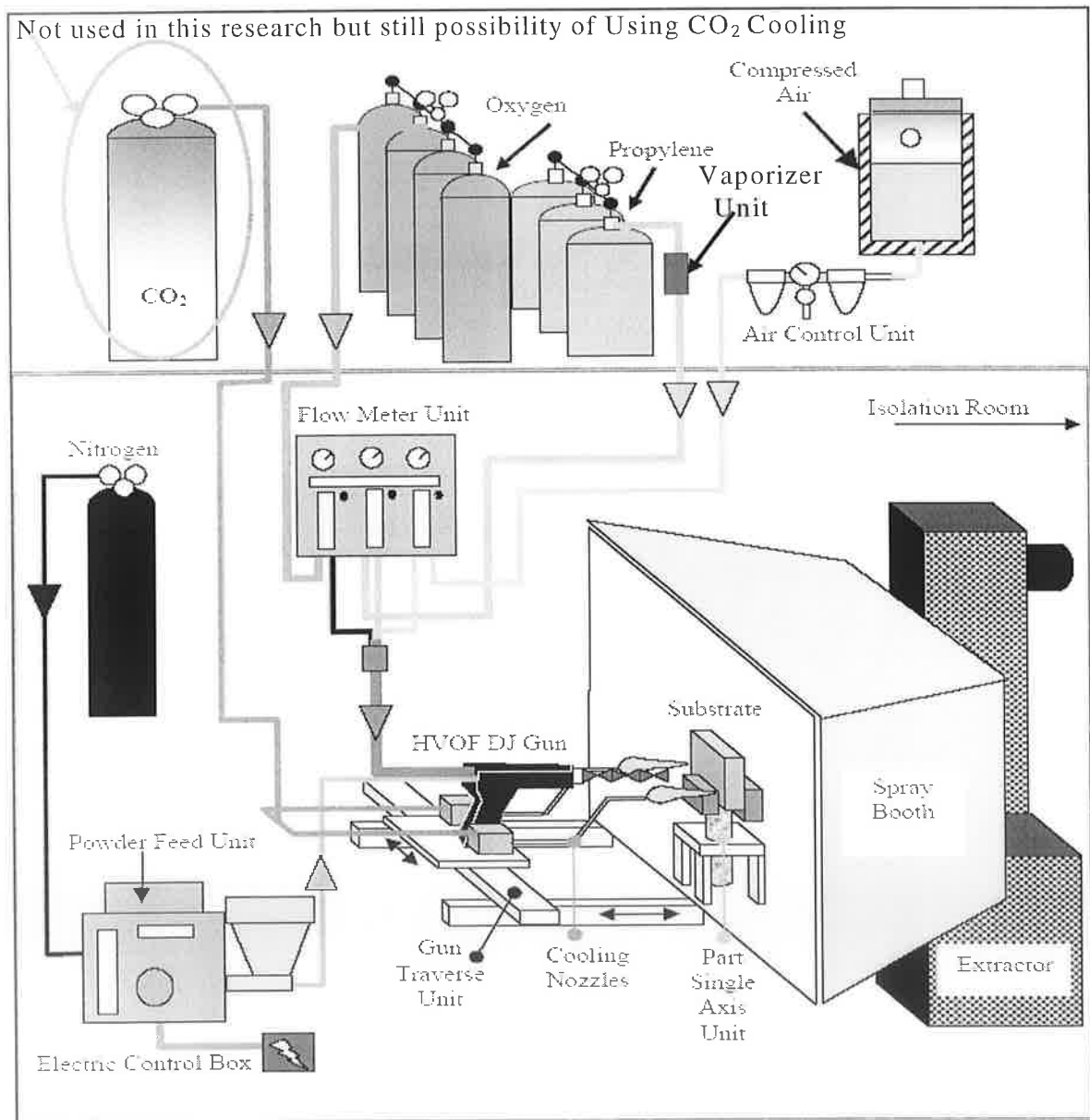


Figure 3.1: Schematic of the HVOF Thermal spray system [30].

3.2.1 Diamond Jet (DJ) Gun

A schematic and photo of the Diamond Jet (DJ) gun used in the research are shown in Figure 3.2. The gun weighs approximately 2.27 kg and may be hand held. The Sulzer Metco thermal spraying system uses oxygen and fuel gas to melt the particles and compressed air to cool and produce a high velocity gas stream in the gun nozzle. This gas stream, when ignited to the front end of the gun, as a luminous white, produces a supersonic flame containing diamond-shape shock waves hence the name 'Diamond Jet'. In this current research, propylene (C_3H_6) was used as a fuel gas. Due to combination of high fuel gas, oxygen flow rates and high pressure generate this supersonic flame. The system gases and powder material enters the back-end of the gun and pass axially through towards the front end, where mixing of the gases and combustion occurs by igniting the front of the gun using a flint lighter. The high kinetic energy of the powder produces well-bonded coatings with high bond strength and low porosity [182]. It must be noted that HVOF systems from different manufacturers, can produce different coatings and vary in their properties. Different HVOF system differences have been reported by Harvey et al. [183].

The front end of the gun consists of various nozzles and inserts designed to control the flow rates of the individual gases. These nozzles and inserts increase the pressure of the gases and this, together with the combustion of the gases, increases particle velocities up to 1350ms^{-1} [43]. The nozzle and insert sizes may be changed depending on the type of powder material in use. The materials will have different melting temperatures and grain sizes, therefore varying the gas flow rates, increases or decrease the combustion temperature (used to melt the powder particles) of the chamber, and velocities of the powder material. The front end of the spray gun consists of four concentric assemblies, a powder injector, a siphon plug, a nozzle assembly and an air cap assembly, as shown in Figure 3.3. Further in depth information about this HVOF DJ gun description has been reported by Stokes [30].

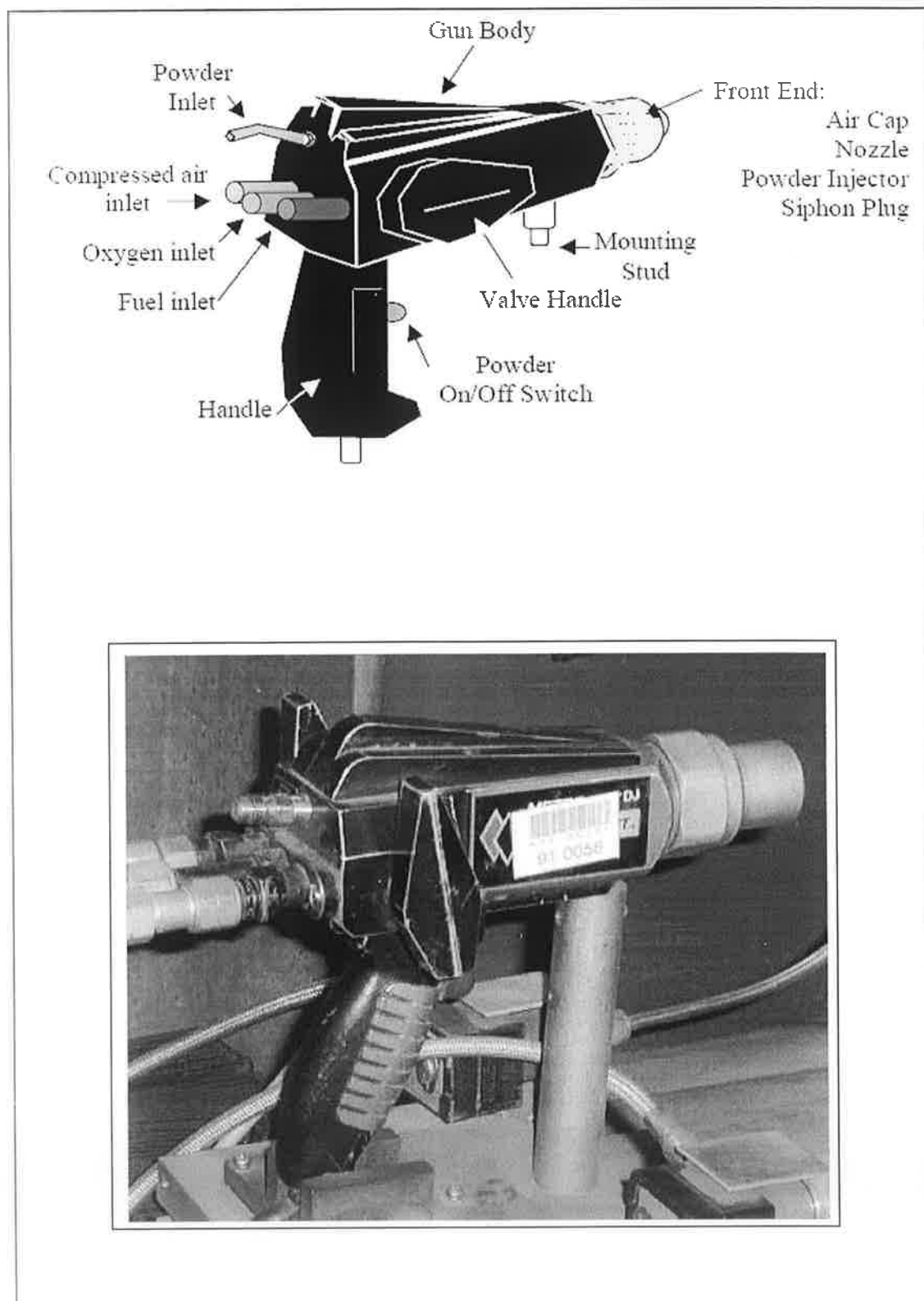


Figure 3.2: The Sulzer METCO Air-Cooled HVOF type Diamond Jet (DJ) gun [30].

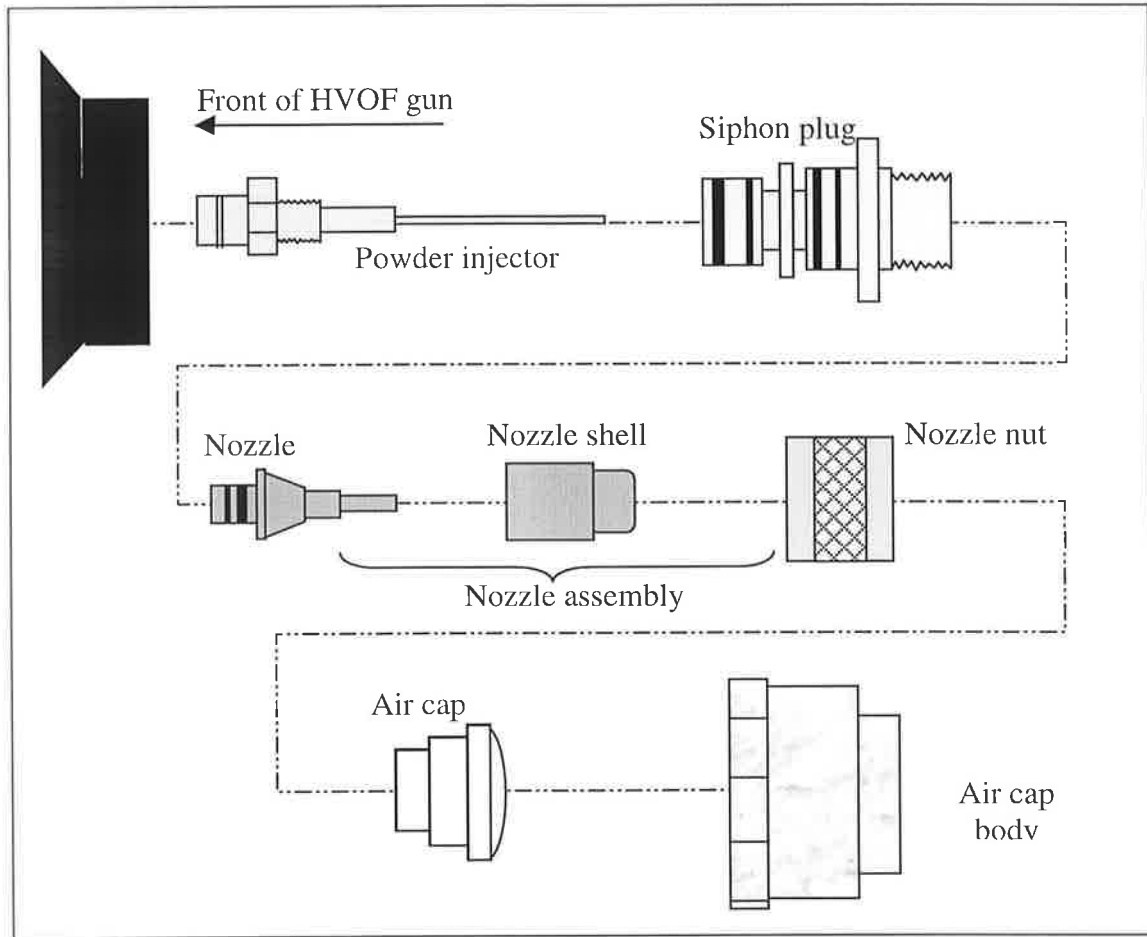


Figure 3.3: Schematic of the HVOF DJ gun front-end hardware [30].

3.2.2 Powder Feed Unit

Sulzer Metco provides a powder feed unit to go with their DJ HVOF Thermal Spray system. The desired powder is fed from the powder feed unit through a carrier gas, to the DJ gun where combustion occurs. Typically nitrogen is used to carry the powder particles. The powder feed unit comprises a hopper assembly, air vibrator, load cell, feed rate meter and control cabinet as shown in Figure 3.4. The unit is completely self-contained and is designed to deliver the powder to the gun at a precise flow rate [184]. The powder material is placed inside the hopper assembly. Due to action of gravitational force, vibration of air vibrator and nitrogen gas pressure within the chamber powder

drops into the powder port shaft (Figure 3.5). The nitrogen carrier gas flows through this port shaft and, whilst doing so, carries the powder on its way to the combustion zone of the gun. By adjusting the carrier gas flow meter control, the flow rate of the nitrogen gas is regulated and this is set according to the data outlined in the application charts [62]. A switch on the gun activates the powder allowing it to flow from the hopper to the combustion chamber within the DJ gun, and the amount flowing is displayed on the feed rate meter (in gmin^{-1} or lbs (hour)^{-1}), measured by the load cell provided. The feed rate meter has an accuracy of $\pm 0.1 \text{ gmin}^{-1}$ and a range of 0 to 100 gmin^{-1} . There are two different coloured lights present on the control panel of the feed unit system, which act as Pressure and Powder Feed ON/OFF indicators. Further details have been reported by Stokes [30], hence these details will not be expanded upon here.

The current research is mainly concerned about the development and re-design of the Hopper unit, which will be detailed in the following chapter.

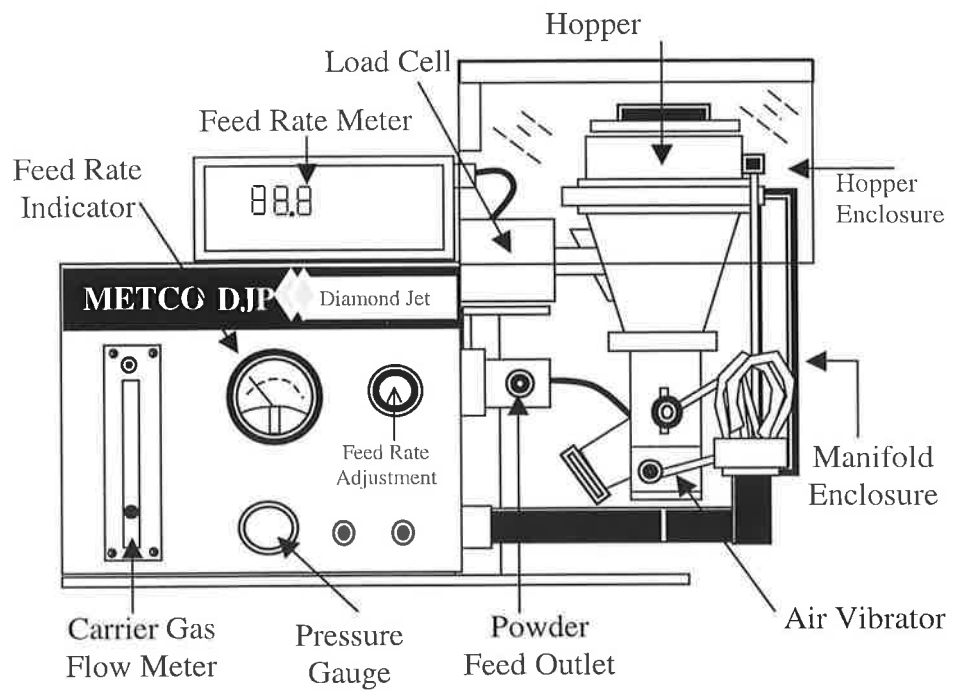


Figure 3.4: The DJP powder feed unit used in the HVOF process [30].

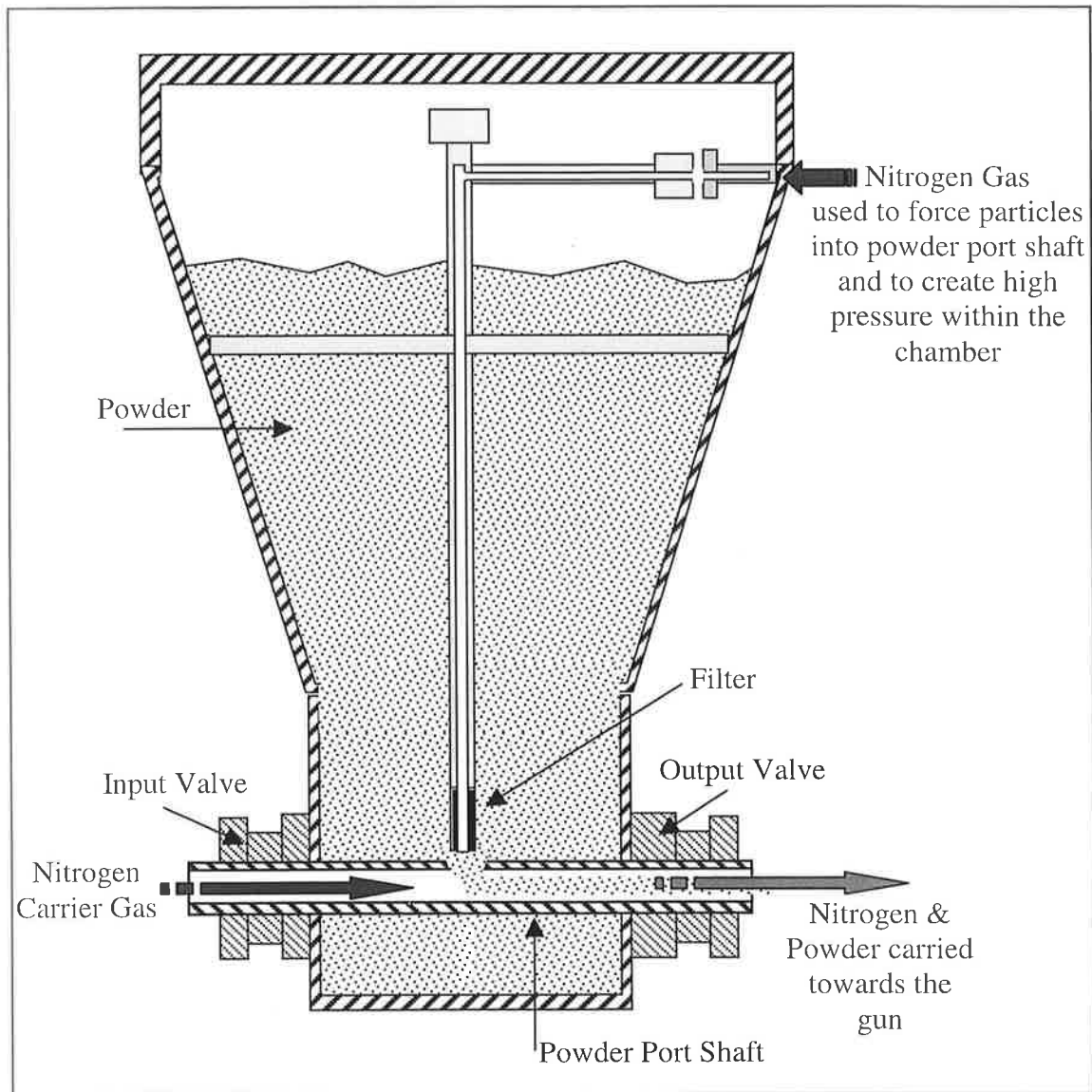


Figure 3.5: Schematic cross section of the hopper assembly on the DJP powder feed unit [30].

3.2.3 Gas Supply and Flow Meter Unit

The current HVOF thermal spraying system uses oxygen, and propylene as the combustion gas. Oxygen is used as an oxidant during combustion, and is required at high flow rates. Propylene is used as fuel during combustion. The pressures may be adjusted at the manifolds of each set of fuel tanks. Compressed air is also used by the system for four reasons. A small proportion of the compressed air is used to cool the combustion chamber of the gun (as the gun is air-cooled), while the majority of the air is fed through

the nozzle assembly to accelerate the particles onto the substrate. The compressed air requires an air control unit, to filter and control the air pressure to the gun. The compressor providing the compressed air operates at pressures in the range 6.8 to 10.2 Bar, and flow rates from 300 to 1500 SLPM (Standard Liters Per Minute). Another small amount of compressed air used to control the linear motion of the DJ gun. Finally some air is also used to accelerate the Air Vibrator in the hopper unit. Nitrogen gas used as the powder carrier gas in the system. The cylinder of nitrogen gas has located outside the HVOF lab, and another nitrogen gas cylinder was also placed outside of the HVOF lab with the other gases and used to pressurise the propylene cylinder.

The optimum pressures of these gases depend on the powder material used for deposition and suggested pressure values may be found in the Sulzer METCO data charts [62]. For safety reasons, each gas facility mentioned was repositioned during this study outside to the HVOF lab in the thermal spraying housing area, all except the compressed air. A vaporizer was installed which was connected with the fuel (propylene) gas (as shown in Figure 3.1 and 3.8) to attain better flow rates during the winter or in cold weather. A detail about this has been described later on support system section. The gases (oxygen, air and propylene) leave their supply units and flow to the gas flow meter, where their flow rates are regulated (Figure 3.6). A type DJF gas flow meter unit as shown in Figure 3.6 was used to control and regulate the supplied gases. There are mainly three parts; gas tube flow meters, pressure gauges and accurate flow adjustment valves. The rate of different gases required depends on the spraying condition and the coating material. Twisting the respective adjustment valve can control the flow rate of a particular gas. Flashback arrestors and check valves are installed in both the oxygen and propylene lines to guard against the danger of backfire and to make the system safer. The pressure and flow rates may be adjusted within ± 0.1 Bar and ± 1 Flow Meter Reading (FMR); within a range from 0 to 11 Bar and 0 to 100 FMR respectively.

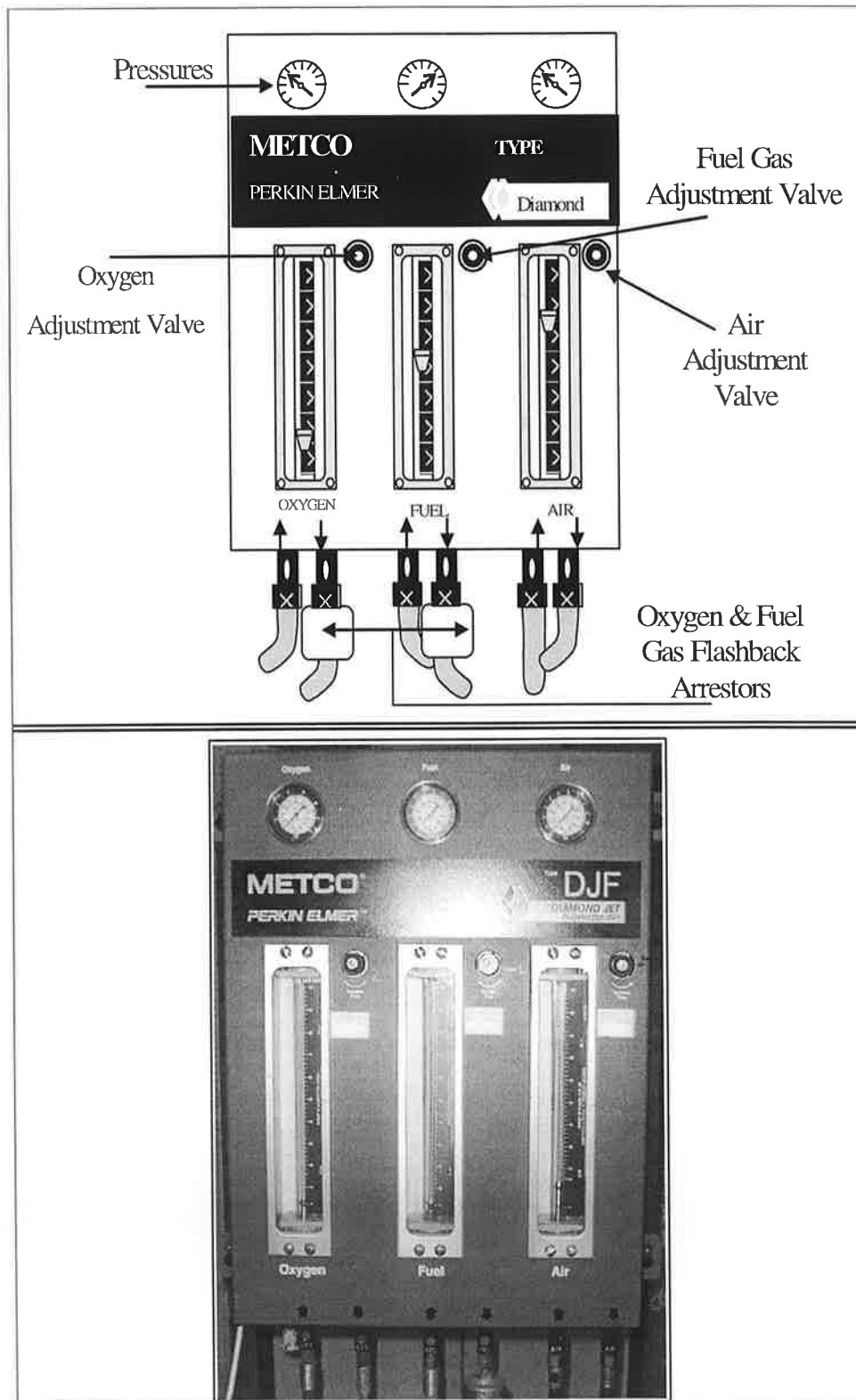


Figure 3.6: Type DJF Diamond Jet gas flow meter unit used in the HVOF process [30]

3.3 SUPPORT SYSTEM

Thermal spraying equipment should be operated in a safe and workable environment. Due to safety reason; proper functioning facilities must be installed prior to the spraying. In addition powder materials that are used during thermal spraying are very often hazardous. These powder materials are very fine and these are seriously harmful to lungs and eyes; therefore personal safety equipment must be worn before spraying. Under the heading of supporting systems, the following are discussed: the vaporiser unit, grit blasting unit, traverse unit, spray booth and exhaust system, facility isolation, cooling system furnace and safety equipment.

3.3.1 Vaporiser Unit

The main objective of this newly installed vaporiser unit is to evaporate liquid propylene and pressurise it; hence the designed flow rates of this fuel gas are achieved during cold weather. Up to the previous research, propylene gas cylinders were placed inside a room (in the R+D building) and this gas was heated up by increasing the room temperature using electrical heaters, which was not a safe system. Last year a propylene vaporiser unit was installed and integrated with the DCU HVOF thermal spray system.

A schematic diagram of this vaporiser has been shown in Figure 3.7. This Vaporiser requires water (D-Ionised Water) plus 33% Glycol Mixture (Ordinary Anti-Freeze) and is heated up by electrical power supply (heating element). First, one switches on the power supply, the Flame Proof Lid should be open as shown in Figure 3.7 (b) To set the Vaporiser Operating Temperature as shown in Figure 3.7 (c) to 70 °C and the Cut-Off to 80 °C. This means that if the Vaporiser for some reason goes above 80 °C, rather than the element burning out, the green trip switch would go to an 'OFF' position as shown in Figure 3.7 (c). At this position the heater turns off. To turn it on again operator must press the green trip switch to its 'ON' position as shown in Figure 3.7 (c).

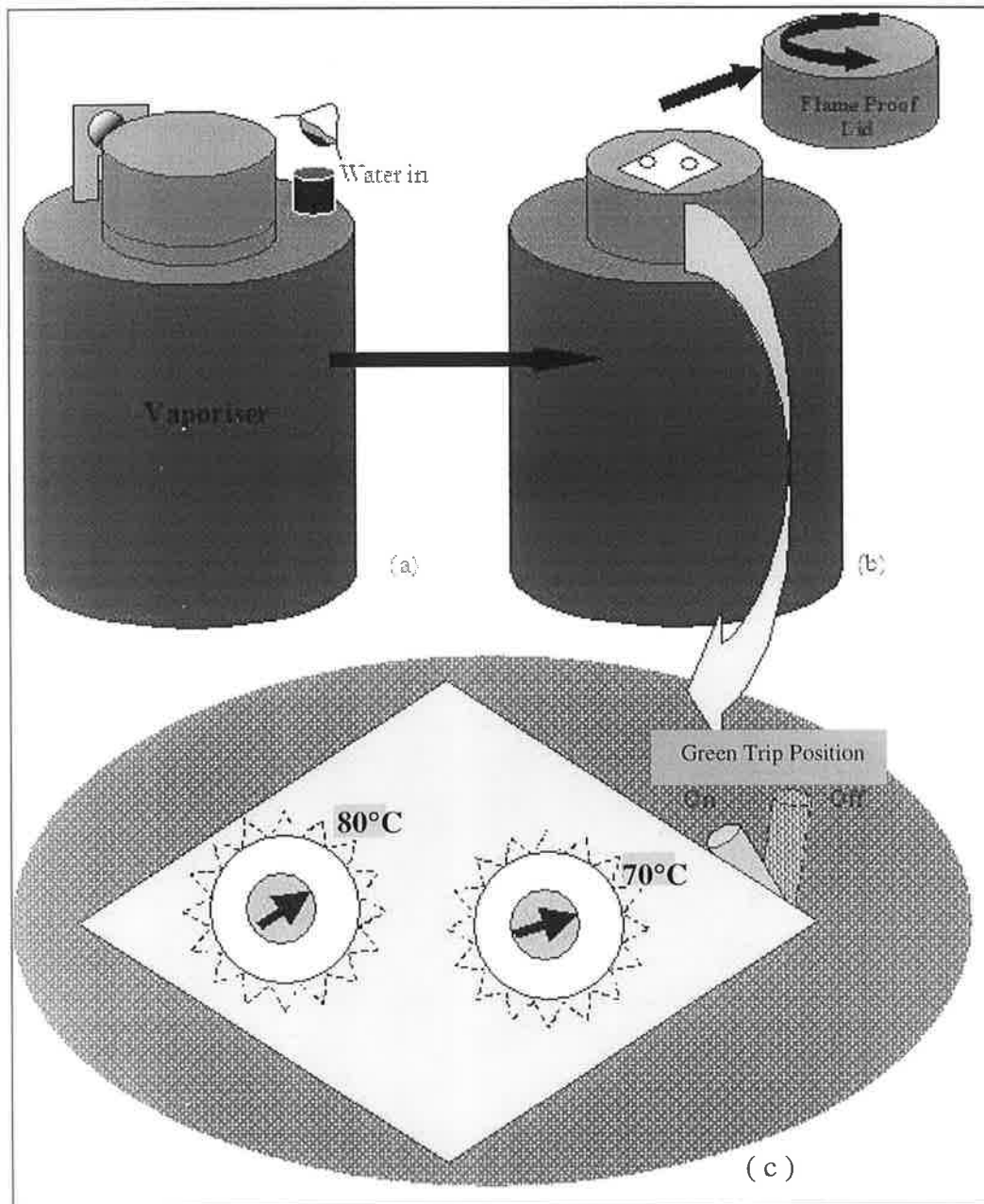


Figure 3.7: A schematic diagram of vaporiser and its initial set up [185].

A schematic diagram of the connection of vaporiser system is shown in Figure 3.8. After switching on the electrical power supply one must wait for 30 minutes (approximately, depends on atmospheric temperature) for the Vaporiser to heat up to the 70 °C, according to the Vaporiser Temperature Gauge (Figure 3.8-(a)). To allow the propylene to flow to the HVOF process; one must open the nitrogen line and then set the nitrogen pressure

(which pushes the propylene) regulator to 7 Bar. Then the propylene lines are opened, first the Blue tap and then the red tap as shown in Figure 3.8 (b). Propylene will only flow into the vaporiser if the vaporiser is at 50 °C or higher (as set on the Blue bimetallic strip arrangement Control behind the Flame Proof Lid (Figure3.8-(a)). So the summary of this system is; when nitrogen goes into the propylene cylinder it forces liquid propylene towards the pre-heated vaporiser and is vaporised and then finally flows to the HVOF facility (via into the gas flow meter onto the DJ gun).

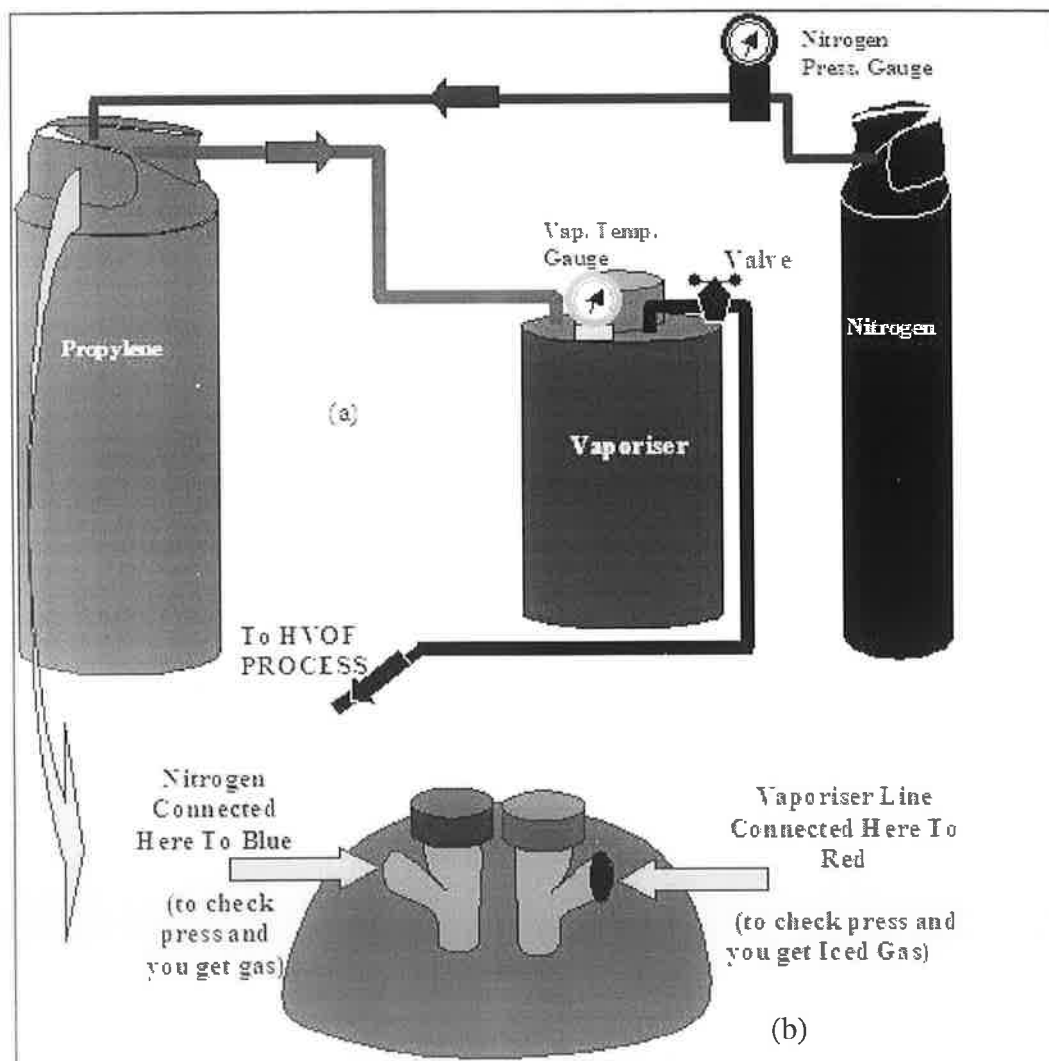


Figure 3.8: A schematic diagram of the connection of vaporiser unit [185].

3.3.2 Grit blasting unit

A clean substrate surface is key to achieving good quality coatings, and there are several methods of preparing substrates surfaces, grit blasting being one of them. Grit blasting can often be used as a dry particle erosion device and as a shot peening operation. The adhesion of a coating is directly related with the cleanliness and roughness of the substrates surface. Increasing the roughness of a substrate is a familiar method of cleaning a surface [186], and this has the added advantage of increasing the bond strength between a coating and its adjoining substrate. A grit-blasting unit supplied by Sulzer METCO, known as the Ventublast Mammouth (shown in Figure 3.9), was used to prepare substrate surfaces for the research carried out at DCU. It has a large internal area of 0.87 m² and the system also includes a hand held blasting gun and a grit collector facility. The grit is collected into a compressed air stream by vacuum effect, and propelled onto the substrate. The impinging grit falls down through a grid into the collector for recycling purposes. This blasting unit also consists of an eye visor by which the entire process can be observed by the user. Varying the air pressure and the blasting distance; controls the substrate surface roughness within the range of 6 to 15µm (for SiC which was used in this study). A mount designed previously for the erosion of coated samples, allows various blasting distances and impact angles to be selected accurately.

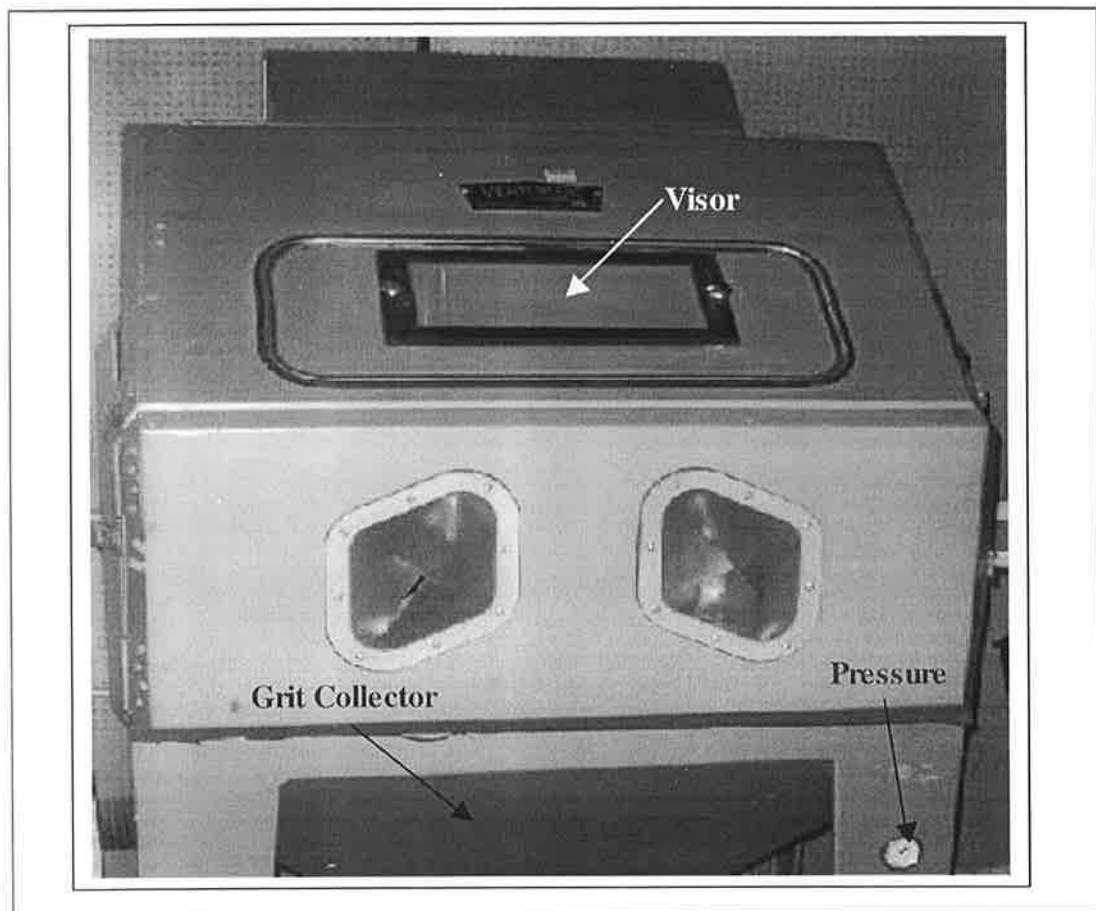


Figure 3.9: Photo of the grit-blasting unit used to prepare samples for coating deposition.

3.3.3 Gun Traverse unit

Previous research indicates that, due to manual operation of a thermal spraying process, residual stress was found to increase in the deposited material [30]. Hence to overcome such a problem, a semi-automated process for traversing the spray gun was developed in the DCU Materials Processing Research Centre [30]. A LX-L20 Series Linear Stepper Motor (LX stands for Linear X-direction) was used to traverse the spray gun back and forth across the face of the substrate. This traverse unit developed by the Parker-Hannifin Compumotor Division operates using electrical magnetic principles. It has two main components; the stationary component called a platen, and the moving part on which the gun is mounted, called the forcer, (Figure 3.10). To control this unit a driver (provided by Parker-Hannifin Compumotor Division) is used and the traverse procedure is

communicate to the driver by the user through a computer connected via its serial port. A specially written computational program was used to control speed and accelerations to accomplish an ideal path of motion of the gun during spraying. The distance was set by moving the assembly inwards/ outwards from the substrate, (Figure 3.10).

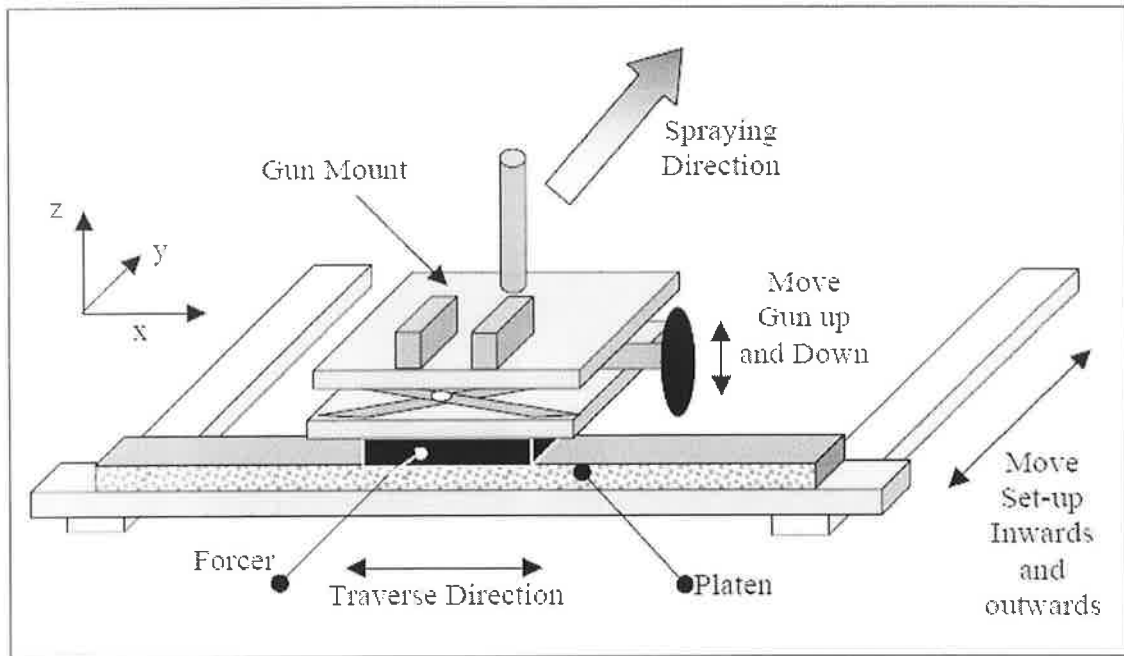


Figure 3.10: Various planes and directions relevant to the linear traverse unit [23].

3.3.4 Spray Booth and Exhaust System

For the health and safety reasons it is important to limit the hazardous effect of fumes and airborne materials on the operator. Due to this reason a spray booth (Figure 3.1) collects all airborne dust, fumes and over-spray within its enclosure. This wet collector extracts these hazardous materials. This works on the principle of sucking air (by a centrifugal fan) from the operation area (picking up all air-borne particles and fumes) carrying them through a water reservoir, where the waste products submerge. It is essential to confirm that the water level is topped up before deposition, and that contents within the reservoir are properly discarded, to get the best performance out of the system.

3.3.5 Facility Isolation

During the thermal spraying operation, airborne metallic dust particles and fumes and high sound levels (126 dB [30] as measured in the DCU HVOF lab) are generated in the surrounding area. Most of these are removed by the extraction system, however the thermal spray gun (HVOF DJ gun) during thermal spraying operation generates high noise levels in the region of 126dB [30] (similar to that generated by a jet airplane). Additionally the extraction system generates 85dB [30]. When both systems (gun and extraction) are run together; they generate up to 130dB [30]. Hence it is essential not only to isolate the spraying equipment into a confined room, but also to insulate the room with a sound proof material. In the HVOF lab facility a cavity wall of peg-board sheets is built in, where the central portion is filled with fiberglass. To support the structure and protect the surrounding room in case of fire, the exterior of the room is covered with Steel sheet material.

3.3.6 Cooling System

In order to run continuous spraying, while limiting the rise in spraying temperature, a carbon dioxide cooling system facility is also available in DCU HVOF facility. Stokes [23] reports details about this cooling system; however as this was not used in the current study no more discussion on this will be made here.

3.3.7 Furnace

After spraying, post-heat treatment reduces internal stresses in the coatings for this reason a furnace is used. In DCU's Materials Processing Research Centre; Post-heat treated samples are heated in a furnace developed by Lenton Thermal Designs (Type EF 10/8) up near the coatings recrystallisation temperature and allowed then to cool slowly in the furnace according to stress relieving techniques. The furnace is equipped with an

analogue temperature controller, which controls the temperature to within ± 3 °C. This furnace operates at a temperature range between 0 to 1000°C.

3.3.8 Safety Equipment

For safety issues, caution and care must be exercised during the thermal spray operation and full and appropriate attention must be given to the instruction and cautionary statements detailed in the operational and installation manuals. Users must be properly trained on how to safely use the equipment, and in addition become familiar with the safety practices of the process according to the specified regulations. There are few basic safety measures for thermal spraying, which should always be observed. These include, good housekeeping, proper material/gas storage and handling practices, appropriate use and maintenance of equipment, appropriate training for operators, proper exhausting of gases and fumes and appropriate safety protection attire (clothing, ear, eyes and respirator protection).

During thermal spraying operation, personal safety is always up to the operator. The operator must always be aware of all of the hazards that may be present (that is eye, skin, hearing, respiratory). Eye protection is required when one uses the HVOF spray equipment due to the presence of ultraviolet and infrared radiation. Eye protective glasses or shields of shade #5 (welding glasses) or greater is essential for the operator during thermal spray. Operators need earmuffs and earplugs due to high level of noise (130dB) generated during HVOF thermal operation [187]. Fire resistant clothing and heat resistant gloves are necessary during the operation. Two-filter type (one for particles and another for gas protection) respiratory mask must be worn not only during thermal spray but also during powder pouring or powder changing with the powder hopper. Clear eye protection and rubber gloves are also necessary to protect the eyes and skin from the powder material as some of them cause irritation. Once the HVOF operation has finished, hands must be properly washed with soap and water to avoid ingestion or irritation of the powder material.

In industrial sector, normally the operator remains outside of the spraying area and control the whole process from a monitor station. But in research operators need to stay within the housing area in order to assess the quality of their results. In current research, one proposal has been made; to make the process semi controlled from outside the spraying room. The DCU HVOF lab will be monitored by a computer and web cams instead of installing expensive CCTV system during thermal spray. For this purpose four web cams and a controlling software would be needed, while the computer is already available in DCU HVOF lab. For this installation, the cost would be approximately €250. The adaptation of this proposal may be the focus of future work.

3.4 HVOF SPRAYING PROCESS

The total HVOF thermal spraying process used to produce stainless steel and nickel base alloy coatings is described in the following sections; surface preparation, pre-heat treatment, spraying process and the post-heat treatment.

3.4.1 Surface Preparation

In most coating processes the integrity of the deposit is vitally dependent on the condition of substrate surface. However surface cleanliness in the true scientific sense is never achieved. Generally eroding the surface by a harder material carries out this cleaning process of the substrate surface; grit blasting is well-known process for this. For heavy-duty applications large metallic grits which, because of their momentum, can remove surface scales as well as providing a coarse texture to support thick coatings. On the other hand for thin coatings this process is carried out with finer ceramic (Al_2O_3 , SiC) grit materials. A freshly prepared surface is very effective and thermal spraying operation must be carried out as soon as possible after grit blasting.

3.4.2 Pre-Heat Treatment

Exposing the surface to a high temperature, a process known as pre-heat treating, eliminates moisture build up on the substrate surface. This is done by igniting the gun and heating the substrate with the gun's flame up to the desired pre-heat temperature before spraying; prior to deposition. This process has also been shown to reduce residual stress during quenching [23].

3.4.3 Spraying Process

Spraying of a material depends on the thermal spraying process used and the type of material being sprayed. Sulzer METCO has outlined recommended spraying parameters

for the deposition of stainless steel and nickel base alloy powder as shown in Table 3.1. In terms of coating quality, optimisation of these parameters is essential. All safety issues that were described earlier must be confirmed before spraying commences. The vaporiser unit must be turned on first. After this the extractor is switched on and the stainless steel-nickel base (SS-Ni) alloy powder is poured into the hopper of the powder feed assembly. The compressor should be turned on before igniting the gun (keeping the gun cool) and the pressures and flow rates shown in Table 3.1, for lighting must be set. The oxygen bottles are opened and set to the pressure as shown in Table 3.1, and then its gas flow rate is adjusted at the gas flow meter. Propylene is then lastly run through and its parameters are set. The gun is then ignited and set up for spraying of the SS-Ni base alloy. Nitrogen is allowed to flow through the powder feed unit by adjusting its parameters. The powder is fed to the gun by switching on the feed button on the gun. The flow rate of the gas and powder is then adjusted to 50 FMR and 38gmin^{-1} respectively. The powder ratio mix of SS and Ni powders entering the gun is controlled by newly developed automated system with two linear actuators via a computer. The development of this facility is the main concern of this current research, which will be detailed in the next chapter. The spraying distance is controlled by the use of the linear motor and it also controls the traverse speed of the deposit (120 mm/s). After deposition, the samples of coated substrates are ready for post-heat treatment.

Table 3.1: Gun settings and spray parameters for Stainless steel and Nickel base alloy coating material [188]

Gun settings and spraying parameters	Powder Material		
	Austenitic Stainless Steel Diamalloy 1003	Nickel base Super alloy Diamalloy 1005	Fusible Nickel base alloy Diamalloy 2001
Siphon plug	2	2	2
Air cap	2	2	2
Shell	A	A	A
Insert	3	3	3
Injector	3	3	3
Oxygen Pressure (Bar)	10.3	10.3	10.3
Oxygen Flow (SLPM)	265.4	309.7	278.1
Air Pressure (Bar)	5.2	5.2	5.2
Air Flow (SLPM)	317.0	345.5	338.6
Propylene Pressure (Bar)	6.9	6.9	6.9
Propylene Flow (SLPM)	71.4	74.9	74.9
Spraying Rate (gm/min)	45	60.5	38
Spraying Distance (mm)	200	150-300	150

A Stainless Steel (EN-standard Steel Name: X2CrNiMo18-14-3 or ASTM/ASTI Steel Type: 316L) Substrate was selected according to the following dimensions and after grit blasting it was placed onto the holder (as shown in Figure 3.11) and this holder was then placed onto a holding vice for spraying. Two types of spraying combination was selected; one for Diamalloy 1003 with Diamalloy 1005 and another for Diamalloy 1003 with Diamalloy 2001. A spray distance of 200 mm was selected for the first combination and 150 mm for the second one according to [188].

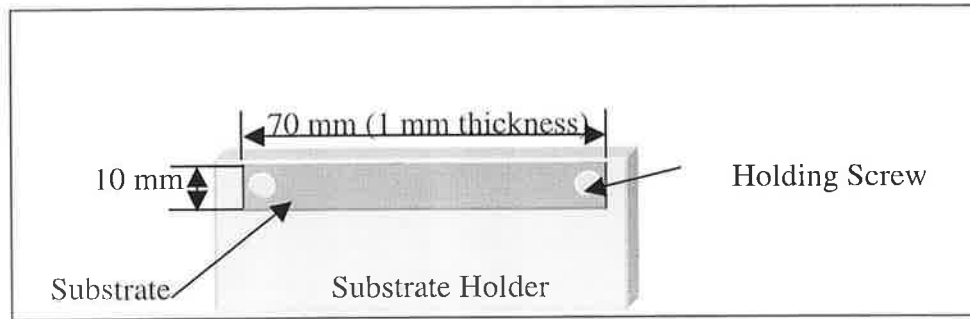


Figure 3.11: Sample substrate (Stainless Steel) onto a substrate holder.

3.4.4 Post-Heat Surface Treatment

Basically these sprayed coatings are ready to use. But in most specific applications they need to be ground and polished to reduce them to the required surface roughness. To change the coating phase composition, to reduce porosity or to improve other coating characteristics heat treatment via the use of a furnace is essential. There are several ways of heat treatment process but furnace treatment is common for this application in research laboratories such as DCU.

3.5 COATING CHARACTERISATION TECHNIQUES

Observation of a specimen was conducted visually either macro or microscopically, to enable the detection of the coating quality. These are the primary characterisation techniques used to gain coating microstructure information (chemical composition, grain morphology and orientation, defects and so on). There are numerous microscopic analysis techniques available, including Optical Microscopy (OM), Scanning Electron Microscopy (SEM) and X-ray Diffraction (XRD). However the XRD technique is not used in this research but further information on the operation of these techniques may be found in additional report by Stokes [189]. In most cases the coating surface (cross section) is grounded and polished properly before optical examination. Blemishes resulting from poor preparation include scratches, deformation, smearing, pull-out, cracks, contamination and so on are detailed by Glancy [190].

3.5.1 Microscopy

(a) Metallographic Preparation

To characterise of thermally sprayed coatings; Metallographic specimen preparation is a valuable tool. This process can be categorise into the following four different areas; sectioning, mounting, grinding and polishing.

(1) Sectioning

Sectioning is essential when the component under investigation is too large to handle effectively. Sectioning control is necessary as inaccurate operation of sectioning equipment causes debonding and over – heating of the section surface [191]. The Buehler Abrasimet 2 Abrasive Cutter was used in the MPRC of the Dublin City University. To section the specimen; force need to apply manually, hence the rate at which sectioning proceeds, was determined by the operator.

(2) Mounting

There are two techniques available; hot-compression mounting and cold-castable mounting. Hot-compression mounting involves setting the sample in the thermoplastic or thermosetting resin subjected to elevated temperature (140-200) °C and high pressure (20-40 MPa) for 7-10 minutes. In cold- castable mounting, the sample is cured in epoxy at 80°C for 60 minutes and mounted in a vacuum. For the present research the Buehler Simplimet 2000 Mounting Press was used to mount different types of graded coatings using the first technique. A Phenolic resin (Phenocure[®]; high Carbon contains) was used as a mounting material.

(3) Grinding

The next step of this metallographic preparation is grinding. The Buehler Motopol 2000 Semi-Automatic Specimen Preparation unit was used in the MPRC. The Grinding technique was divided into two stages; plane grinding and fine grinding.

(a) Plane Grinding

This is the removal of the damage experienced during sectioning and brings all the specimens in the holder to the same plane; plane grinding process was carried in this research. P60 (very coarse) Silicon Carbide paper with water as lubricant was used for 60 seconds to machine away the excess damage of the surface; after which the abrading particles were washed away.

(b) Fine Grinding

This is the removal of the deformation experienced during the plane grinding stage and is referred to as fine grinding. During this process again silicon carbide paper is used to fine grind the samples, but the procedures moves from a coarse (P200) up to a fine abrasible paper (P1200) plus water as lubricant. Each abrasive size is used for five minutes in turn, starting from P200 towards P1200. Finally a Diamond solution can be used to reveal the final microstructure of the sample. In the present research, only the P240, P400, P600 and P800 abrasible papers plus water were used for a duration of four minutes to fine grind the graded coating samples.

(4) Polishing

Optical microscopy requires that a specimen must be both flat and highly reflective. Hence the polishing is a necessary step in metallographic preparation. Figure 3.12 shows a sample specimen after sectioning, mounting and polishing. Extensive details on the grinding and polishing procedure may be found in additional report by Stokes [189].

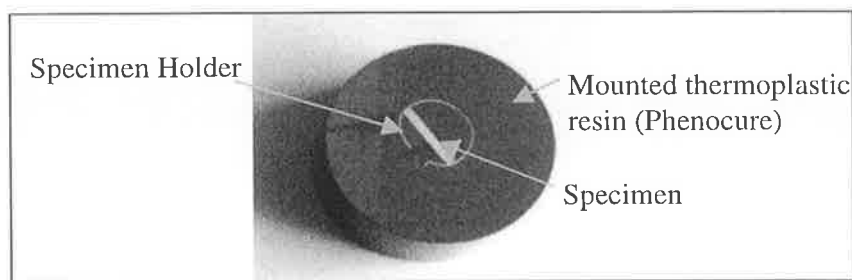


Figure 3.12: Sample specimen of a functionally graded coated (Diamalloy 1003 and Diamalloy 1005) Stainless Steel substrate.

CHAPTER 4

PRODUCT DESIGN, VERIFICATION AND OPERATING PROCEDURES

4.1 INTRODUCTION

As mentioned earlier, thermal spraying can be used to produce interlayers of functionally graded coatings in two ways:

1. Using pre-mixed powders to produce different layers or
2. Co-injecting two different powders and varying their composition during spraying

In this current research the latter method will be demonstrated as a method of producing functionally graded coatings. However as this research will use the existing HVOF facility, only one or a single powder mixture can be sprayed at any one time. Therefore some initial developments of the existing system were carried out by a previous researcher Hasan [49] and the resulting patent in the MPRC to deposit two dissimilar powders simultaneously. So at present there is a manual design in HVOF facility to spray two powders at the same time in order to produce FGM coatings as designed by Hasan [49]. However as this system is manually operated, the operator must control the proportion of powder flow of the feed unit system by hand, which leads to very little control of the resulting microstructure. The aim of this current research is to automate this device and enhance the design as recommended by Hasan [49]. This chapter includes details about the proposed new design and the control system by which the device becomes fully automated.

4.2 DESIGN SPECIFICATION FOR AUTOMATED HVOF SPRAYING EQUIPMENT (Dual Powder Feed Unit System)

The overall aim is to design and manufacture a mechanism, which will provide an automated facility to control the proportion of the powder materials from an existing feed unit device (known as the “Hopper”), in order to produce FGM coatings. The mechanism designed should be capable of being integrated into the existing DJ powder feed system. The proposed designs should try where possible to interface with as much of the existing hardware or software within the HVOF facility.

4.2.1 Design Brief and Investigation of Possible Solutions

To develop a design solution for the current problem the following design specification has to be considered. Considering performance; the design should be able to provide steady, controllable motion either in the vertical or horizontal direction. These mechanisms will have to operate in a dusty environment (powder materials). Lifetime without maintenance should be at least 5 years. Installation cost should be reasonable excluding PC resources. Any future maintenance cost should be low. This mechanism must fit into the existing Hopper Feed unit system currently positioned within the HVOF lab and must not restrict any other previous set up. The manufacturing of the device must be limited to those provided by the DCU mechanical Workshop; such as; Milling, Drilling, Turning etc. The design should comply with all necessary safety regulations. All electrical equipment must be insulated and grounded. The overall operating system should be easy to use and the design process should be well documented to allow for future reference by an operator and future developers of the system. Considering the above description, the following investigation has been carried out to arrive at the above solutions.

4.2.2 Existing Products or Methods

Figure 4.1 shows the schematic diagram of the existing feed unit device proposed by a previous researcher in DCU [49]. The proportion of the powder flow rate was controlled by turning needle shaped bolts and this was carried out using manually. These needle shaped bolts act as gate-valves. Basically these needles increased or

decreased the opening diameter of the powder flow tube according to a desirable amount related to rotation angle of the needle. This is controlled from the top (as shown in Figure 4.1, marked by '1'). To make this an automated system any rotary or linear motion must be controlled to vary the opening diameter of the flow tube.

4.2.3 Design Concepts and Possible Solutions

In the current research all of the design concepts are based on the existing powder feed unit mechanism. Figure 4.1 shows a schematic diagram of the existing device post this current research. Sections 1, 2 and 3 as shown in Figure 4.1 will be described as concepts in the following section.

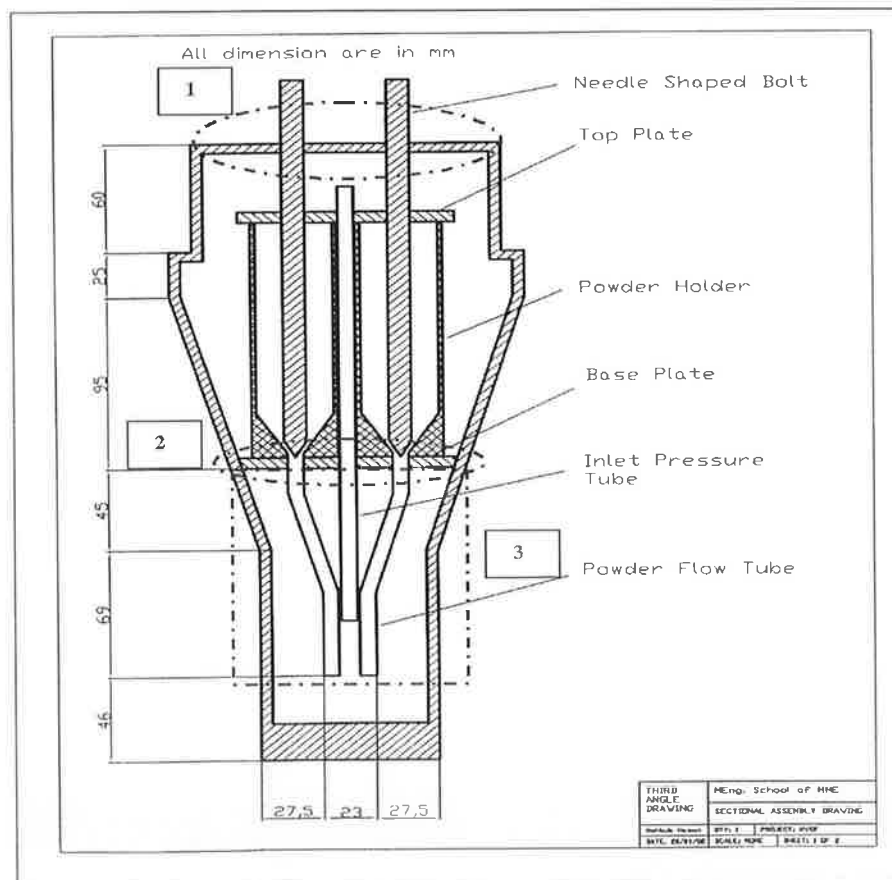


Figure 4.1: Sectional assembly drawing of the needle shaped bolt, the top plate, the individual powder holders, the base plate, the inlet pressure tube, the powder flow tubes and the powder feed hopper [49].

Concept 1:

Figure 4.2 shows a sketch of Concept 1. (Section marker 1 of Figure 4.1) This concept proposes two linear actuators (Linear actuator is based on a four phase permanent magnet stepper motor technology and utilises a rotor with an internal thread to provide linear motion via a lead screw) are supported by the hopper cover plate. These linear actuators are provided with a lead screw and would have to be coupled with the needle shaped bolts. When the lead screw is fixed (unable to rotate), the operation of the motor imparts linear motion to the screw (this is transfer directly to the needle shaped bolts). After energising the linear actuators, the needle shaped bolts move upwards or downwards. Two linear bearings must be placed on the hopper cover plate to align the needle shape bolts and these linear bearings also provide a smooth vertical motion of the needles, thus the ultimate objective (Controlling the diameter of the powder flow orifice) will be achieved.

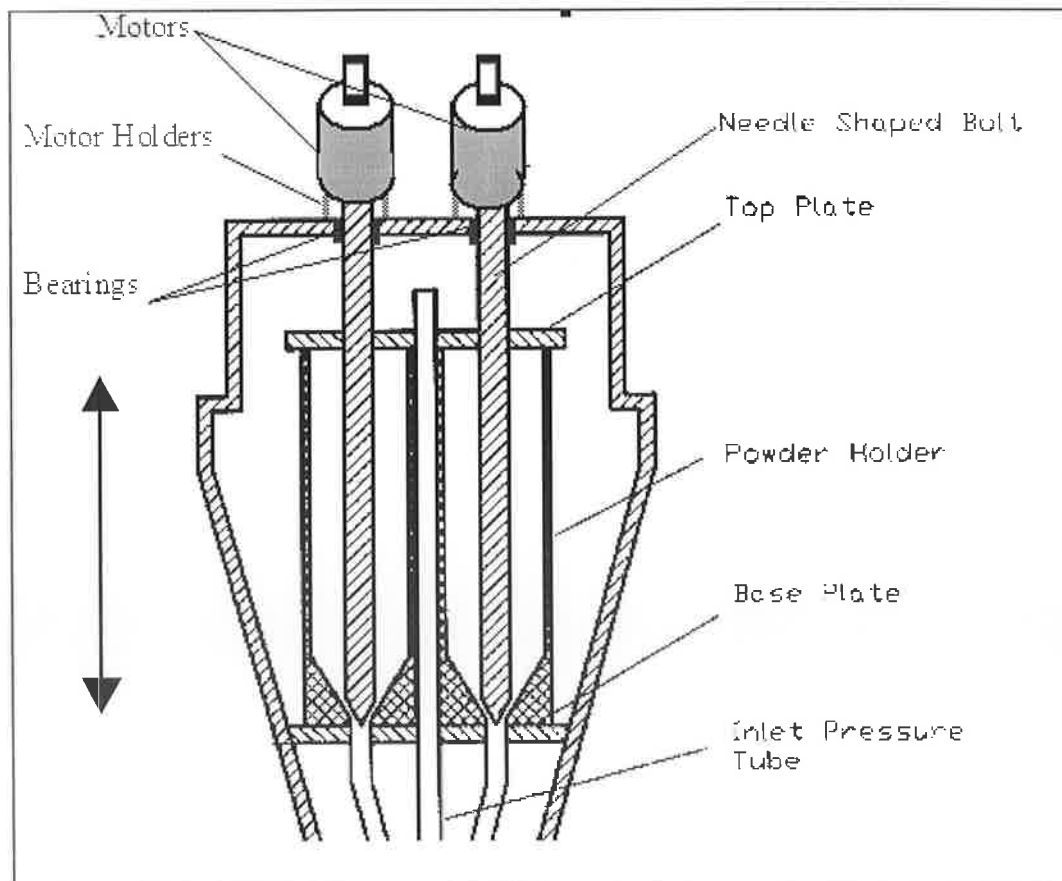


Figure 4.2: Schematic diagram of Concept 1.

Advantages:

- The lead screw of the linear actuator provides a linear relationship between motor rotation and vertical motion enabling open loop control to be used; that is no sensors are required to define the position of the assembly if the previous amount of motor rotation is known.
- Installation of this design will not require much alternation to the existing hopper design.
- Percentage of dust particle contamination to the lead screw of the linear actuator is less, through the use of bearings.
- No lubrication is necessary.

Disadvantages:

- Initial powder pouring into the device could be quite difficult as there may be misalignment of the pointed end of the needle due to bearings placed at the top of the device.
- Requires the re-design of few parts, so as to incorporate this concept into the original design by Hasan [49].

Concept 2:

Figure 4.3 shows a schematic diagram of Concept 2 (Marker 2 shows the implement area of this concept in Figure 4.1). A two-stepper motor is placed in from the side of the Hopper casing and attached to two shafts. These shafts have two through holes, which would allow powder to pass from the dual powder holder to the powder flow tube. These shafts would be set on the base plate of the powder holder. In order to couple the shafts and the motor, the hopper casing would require milling. Basically this mechanism will work as a “water tap type configuration” where the rotation is provided by the stepper motor. Due to motor rotation, the through hole of the shaft also rotates. Which means the flow area will increase or decrease according to the desired rate.

Advantages:

- Powder pouring will be easier compared to the Concept 1.
- Controllability should be easier.

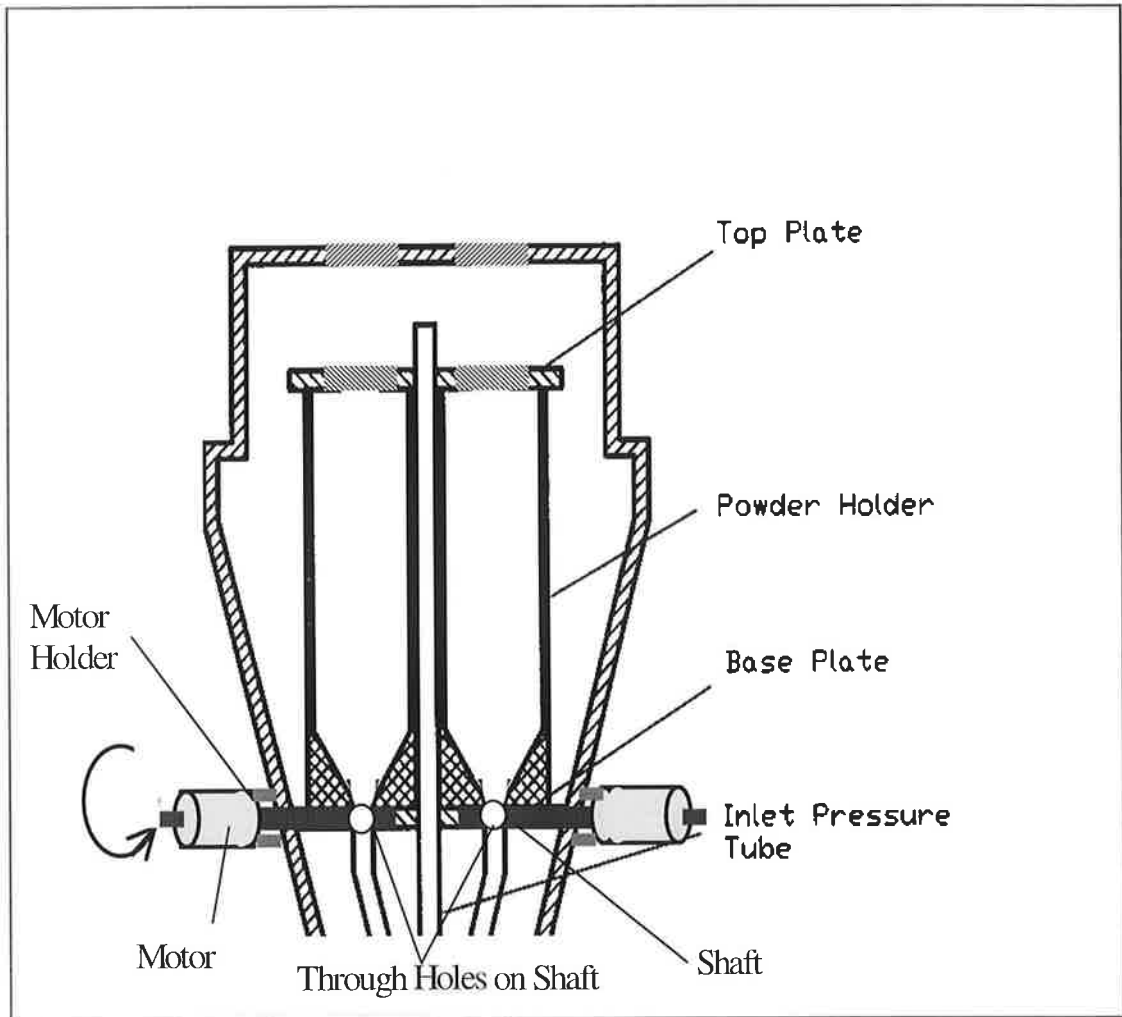


Figure 4.3: Schematic diagram of Concept 2.

Disadvantages:

- Machining of the original hopper casing is necessary, which is the main limitation of this current research, as the hopper will never be able to return to a single powder feed system if required.
- To buy another hopper to have as a replacement is too expensive.
- No room for motors within hopper chamber; hence external operation is the only solution here.

Concept 3:

Basically the mechanism described in Concept 3 is very similar to Concept 1. However, Concept 3 replaces and re-designs the whole dual powder unit, as designed by previous researcher Hasan [49] (instead of redesign of few parts) to produce a more accurate powder-producing device.

Advantages:

- Re-design will be easier, providing the exact required dimensions and controllability of powder flow.
- Will satisfy the aim of this project

Disadvantages:

- Re-design of whole device will be costly rather than replace and re-design of few necessary parts, which are important for the current project.
- Designing and Manufacturing time will be increased compared to Concept 1.

4.2.4 Concepts Evaluation and Description of the Final Solution

After analysing the basic outline of the above of concepts to fulfil the requirements of the project; the next step was the evaluation stage of each concept. The evaluation process must fulfil two objectives: justify the chosen design and show why one concept is better than the other ideas presented. A weight analysis approach was used to evaluate each concept, based on a number of important factors. Each factor was given a weight that was determined by how important that factor related to the final design. The higher the weight value the more important that factor was to the final design. This weight analysis provides a disciplined approach with rules and procedures for the assessment of different concepts, and is a standard technique to use when designing a product.

Four factors were chosen as the most important attributes in determining the quality of each concept, namely:

1. *Cost of Manufacture and Upkeep*: The cost of making and operating a device like this must be taken into account. This was given the highest weighting of 5.

2. *Manufacture ability*: This is the amount of manufacturing time required to produce the design and the complexity of the process involved. This was given a medium weighting of 3.

3. *Installation*: This category represents the complexity in assembling and also the amount of modifications required to integrate the design into the existing equipment in the facility. This was given a medium weighting of 3.

4. *Controllability*: The ease or difficulty of implementing electronic control into the system. This was given a high weighting of 4.

Table 4.1 shows the weight analysis approach where the concepts are listed along the horizontal axis of a matrix (plus each level weighting); and on the vertical axis are the categories under which the design approaches are to be evaluated. Each category is given weighting between 1 and 5 (5 = Priority), defining how essential it is to the final design. This is done using product design specification (PDS) as a guideline. Concept 2 and 3 were rated against Concept 1. In Concept 1 column, a level value of 2 times each weighting is placed, and this was set as the point of reference. The other designs were then compared to Concept 1 using levels as follows:

Better-3 x weighting

Same-2 x weighting

Poor- 1 x weighting

Table 4.1: Weight analysis table for the proposed three concepts

Category	Weighting (W)	Concept 1		Concept 2		Concept 3	
		Level (L)	W x L	Level (L)	W x L	Level (L)	W x L
Cost	5	2	10	1	5	1	5
Manufacture	3	2	6	1	3	2	6
Installation	3	2	6	1	3	3	9
Controllability	4	2	8	3	12	2	8
Total (Sum of Weighting x Level)		30		22		28	

After observing the weight analyse table, it is clear that Concept 2 was evaluated as the worst although it scored more in terms of controllability compared to Concept 1 and 3. The main reasons Concept 2 fails are as follows:

- Installation of the motor from side of the hopper casing is quite impossible due to the hopper casing space. Machining of the main hopper (Powder feed unit, provided by SULZER METCO) would be necessary to implement this design, thus this was the main limitation of this current research as previously explained.
- Damage of the outer casing of the feed unit is also a vital issue in terms of cost.

Concept 3 and 1 scored almost the same but Concept 1 is acceptable as the best design concept due for the following reasons:

- Replacing the whole unit (Concept 3) will demand extra manufacturing time and cost.
- Re-design (Concept 1) of few components is more logical.

4.2.5 Detailed Drawings of the Chosen Solution

This stage of the design involved taking the sketch (Figure 4.2) of the chosen concept and expanding it into a detailed design of each component involved in the assembly. The objective of this process is to create a set of documents that will define the exact mechanical configuration of the design. Measuring the dimensions of the hopper unit was quite difficult due to its complex shape. Once all of dimensions and shape were defined for all components; the next step was to create the drawing of the component. The detail drawings were created using Mechanical Desktop and layout drawings of all components created to the required dimensions may be seen in Appendix A.

To implement Concept 1, five components were re-designed and one component (Motor/Actuator holder and bearing cover) was newly designed. The designed parts (different to those involved in Hasan's [49]) are listed as follows:

1. *Actuator holder and bearing cover*: Figure A1 (Appendix A) shows the details of this design. Two linear actuators will be used. These will also work as bearing covers simultaneously. These holders (block type) were designed to attached to the top of the top cover of the hopper unit.

2. *Needle shaped bolt*: Two bolts were designed to be attached to linear actuators. For coupling purpose the top of the needles were drilled and tapped and the lead screw of the actuators were screwed into them. After that two M2 grub screws were used to fix/lock each of them. Figure A2 (Appendix A) shows all the dimensions and the shape of the Needle shaped bolts.

3. *Top plate of the powder holder*: This plate required re-design because; there were two M10 threaded holes where the needle shaped bolt were placed in the previous design [49]. However in the current project no threaded hole was necessary. The surface of these holes was to be finely finished to allow smooth rotation of the needle shaped bolts. Figure A3 (Appendix A) shows all the dimensions and shape of the re-designed component.

4. *Top cover plate of the hopper unit*: Figure A4 (Appendix A) shows the schematic diagram of this plate with all of its dimensions. Basically this plate will be a base plate for the linear actuators mountings. The two linear bearings will be placed on to this plate, which will allow smooth linear motion to the needle shaped bolts and also helps to hold them at the top of the hopper unit. Its shape could be square or disc shaped depending on available material size in the workshop. This plate was designed to fix to the main hopper unit with four 8mm diameter counter bore 13 mm diameter bolts.

5. *Funnel shaped powder flow tube*: This is the top part of the section 3 design in Figure 4.1. Figure A8 (Appendix A) shows a schematic diagram of this component with all of its dimensions. This part will be attached to the base plate of the powder holder (Figure A6 of Appendix A). This part allows the flow of coating materials to the mixing zone at constant rate.

6. *Conical shaped powder mixing zone*: This is a very important component in the current research. Figure A9 (Appendix A) shows the details of this designed shape and dimensions of this component. This component was designed to be placed inside the hopper, on top of the built in (Hopper unit) powder pick up shaft.

To fully complete Concept 1, two components were purchased from supply manufacturers, such as;

1. Two linear actuators
2. Two linear bearing, which act also as bushings

The detailed drawings could not be completed until the exact information about these components were known. These details of this component selection process are described in the next few sections. It was necessary during this process to consult with the technicians in the DCU mechanical engineering workshop about their ability to produce the discussed components in the design. Manufacturing time, process and machine restrictions were vital at this stage. When all of the drawings of each design component was completed; a hardcopy of each drawing was printed out and given to the mechanical engineering workshop for manufacture.

Some considerations were required during this drawing stage, which are as follows:

- Developing a simple non-complex component in order to keep manufacturing time low.

Ensuring that the dimensioning style was consistent with workshop practices to minimise manufacturing delay.

4.2.6 Design of the Motor Holder

Concept 1 was selected as the best mechanical solution, however as pointed some modifications were necessary to improve the design, that is, to change the linear actuators holders initial design concept. Instead of two separate holders (for each motor), a single block type holder was designed, which contains both actuators, and works as a bearing cover. This is why there was no necessity for separate bearing covers. Figure 4.4 shows a drawing of the block type actuator holders, which was designed to be fixed to the top of the top cover of the Powder hopper unit. Further detail design drawings (including dimensions) are shown in Appendix-A.

The modified design has a few benefits, which may be described as follows:

- Possibility of contamination of dust is very low.
- Manufacturability is improved, as there is a reduction in the number and complexity of the components.
- Linear actuators (Motor) will remain safe and steady inside the block.
- Installation will be easier.

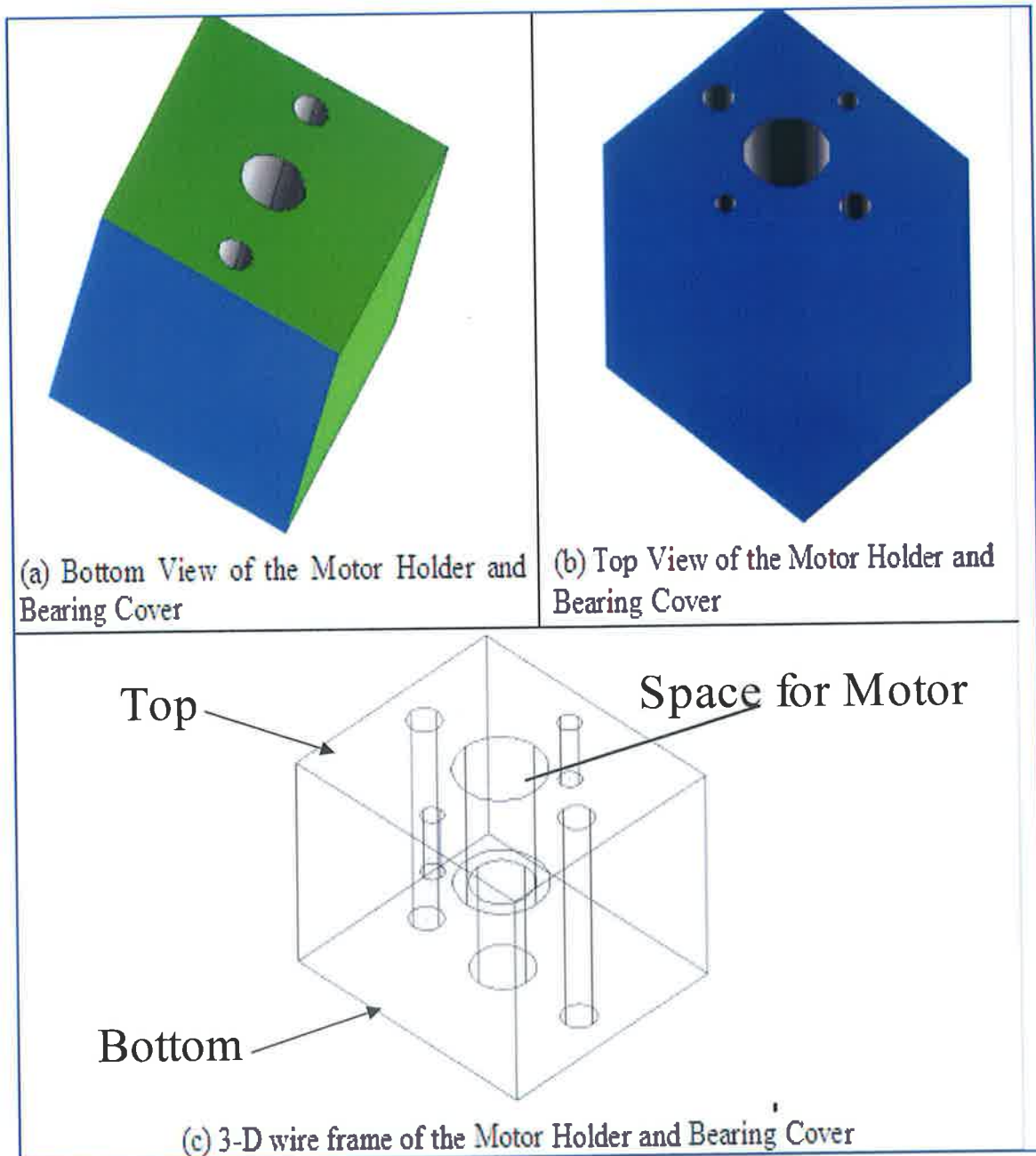


Figure 4.4: Schematic diagram of the Motor Holder and bearing cover.

4.2.7 Needle Material Selection

A designer can choose from a range of materials such as metals, polymers, ceramics, composite and so on. One of the first tasks in a detailed design is the selection of a suitable material for the design. The material's attributes must be looked at in detail; factors such as load carrying ability, working environment, machining ability and so on must be considered [192].

For the entire mechanism, the needle shaped bolts are the most sensitive, as they will be attached to the linear actuators to achieve linear motion. So the needle shaped bolts have to be made of a light material such as nylon or aluminium. However nylon and aluminium could be worn out and contaminate the coating materials.

Calculation for needle shape bolt density was necessary; to determine whether a stainless steel or aluminium based material would be selected for these components. In order to reduce the 'effort' generated by the motors, a light material was desired. These needle shape bolts were designed to be attached to the linear actuators; however the mounting area of these two linear actuators was limited. Hence it is not possible to use bigger size actuators on top of the powder holder unit. For this reason the weight or density of the needle shaped bolts were considered a critical factor. The calculation was as follows:

The needle shaped bolts (Figure 4.5) was divided into two shapes. Top part was cylindrical and the bottom part was triangular shaped. So, the volume of a bolt was calculated using the following equations:

$$\text{For a cylindrical shape volume (V)} = \Omega r^2 h \text{ [r=Radius and h=Height]} \quad \text{Equation 4.1}$$

$$\text{For a conical shape volume (V)} = 1/3 \Omega r^2 h \text{ [r=Radius and h=Height]} \quad \text{Equation 4.2}$$

$$\begin{aligned} \text{So, volume of the cylindrical shape was } V &= \Omega \times (5/1000)^2 \times (106.34/1000) \text{ m}^3 \\ &= 8.35 \times 10^{-5} \text{ m}^3 \end{aligned}$$

$$\begin{aligned} \text{And volume of the conical shape was } V &= 1/3 \times \Omega \times (5/1000)^2 \times (8.66/1000) \text{ m}^3 \\ &= 2.27 \times 10^{-7} \text{ m}^3 \end{aligned}$$

Adding these two, the total volume of the designed needle shaped bolt was found to be:

$$V = 8.58 \times 10^{-5} \text{ m}^3$$

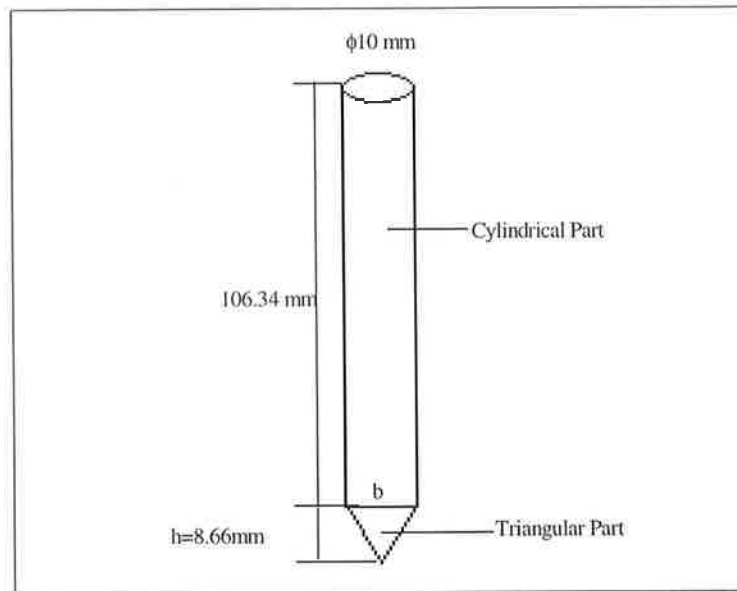


Figure 4.5: Schematic of a needle shape bolt for design calculation.

For Mass calculation the following equation was used:

$$\rho = M/V \quad \text{Equation 4.3}$$

Where, ρ =Density, M =Mass and V =Volume.

For Aluminium $\rho = 2.7$ [193] mg/m^3

And for Stainless steel $\rho = (7.5 \text{ to } 8.1)$ [193] mg/m^3

Hence by Equation 4.3, the mass of Aluminium was:

$$M = \rho \times V = 2.7 \times 10^6 \times 8.58 \times 10^{-5} = 231.623 \text{ gm}$$

So, the Force calculation using the following equation

$$F = mg \quad \text{Equation 4.4}$$

$$\text{Gives } F = (231.62/1000) \times 9.81 = 2.27 \text{ N}$$

Similar for stainless Steel, (Considering $\rho = 8.0 \text{ mg/m}^3$)

$$M = 8 \times 10^6 \times 8.58 \times 10^{-5} = 686.291 \text{ gm}$$

And the Stainless Steel Force required:

$$F = (686.291/1000) \times 9.81 = 6.73 \text{ N}$$

Although to drive stainless steel type needles requires more force compare to aluminium made needles, stainless steel was chosen as the desired material for the needle shaped bolts due to its better wear resistance property and the fact that the force value for stainless steel was lower than the value given (Max. linear force 7.23 N and min. holding force 11.13 N) as per the linear actuator specification (Appendix B1). The stainless steel was selected for this purpose and verified by a bench test where the linear actuators were tested to see if the actuators were able to rotate the stainless steel type needles.

4.2.8 Re-design of the Bottom Part of the Dual Powder Feed unit System

As the working environment of this mechanism is free from temperature, pressure and force; thus the rest of the components (Cover of the hopper, Top plate of the powder holder and Two Motor holder & Bearing cover) could be made by either stainless steel or aluminium depending on its availability within the DCU workshop and machinability. Stainless steel has good corrosion resistant properties (both chemical and oxidation) and stiffness's at higher temperature. On other hand ductile aluminium is readily machine able and also has good corrosion resistance but it is not as strong or a cheap alternative material to stainless steel. Due to the cost restrictions on the design stainless steel was utilised where possible.

Figure 4.6 illustrates the geometry of the model designed by the previous researcher, Hasan [49] (Free standing outside the hopper unit). To produce FGM coatings in the DCU HVOF facility a Dual powder feed unit system was essential. In current research, that design has been modified in order to gain better flow rate/control during FGM coating and to enhance the system flexibility based on the recommendations by Hasan [49]. A Finite Element analysis (FEA) model was carried out using FLOTRAN CFD software to predict the powder flow within the device and details about the FEA will be reported in Chapter 5. After FEA the modified designs were created using Mechanical Desktop. Figure 4.6 depicts A-B as the top section (Powder flow tube & Inlet Pressure tube) and B-C as the bottom section (Mixing Zone). The bottom section (B-C) was the main focus of the current research (shown in Figure 4.7) however it

was found that section A-B had also to be design within this research. In Figure 4.1, section 2 to 3 is the redesign area for these two components.

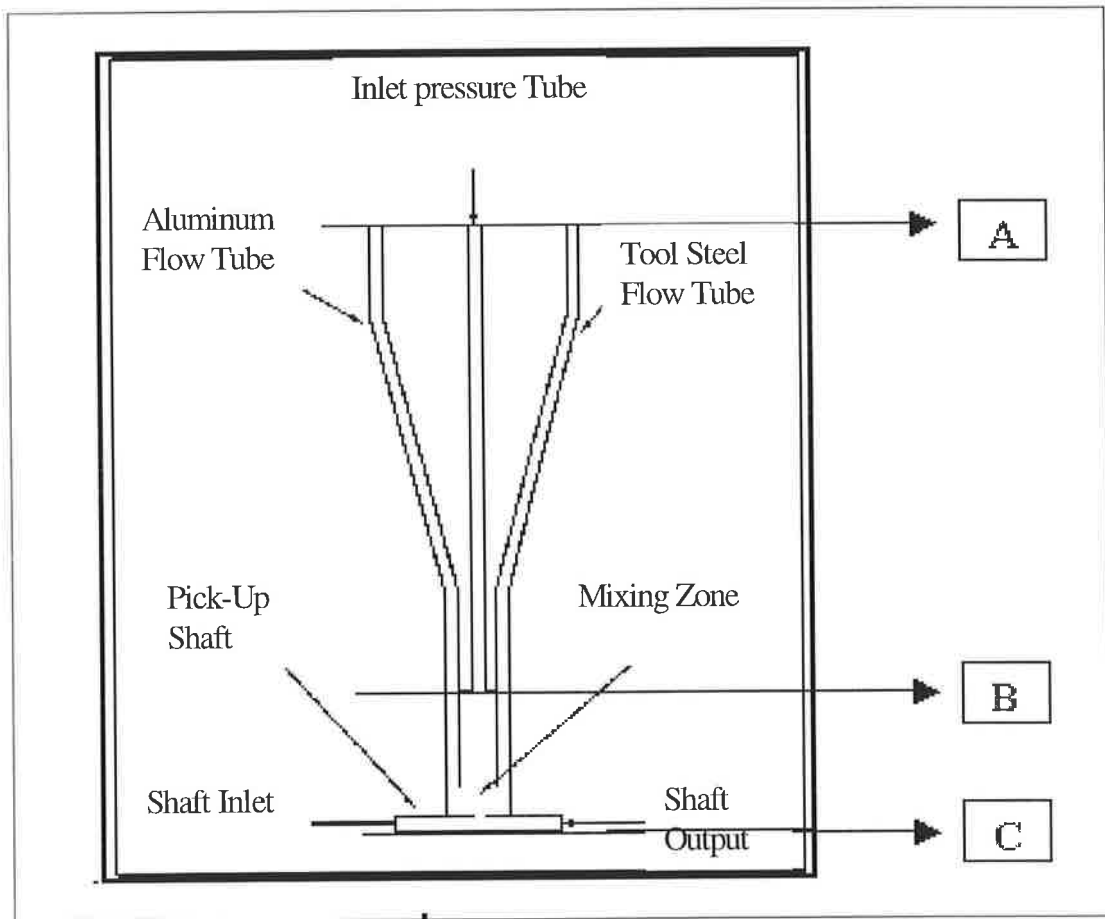


Figure 4.6: Geometry of the model Designed by Previous researcher [49].

The CFD results predicted the geometry (given in Figure A10 of Appendix A) and shape, (shown in Figure 4.7) which would provide efficient flow characteristics for any powders used in the DJ hopper unit.

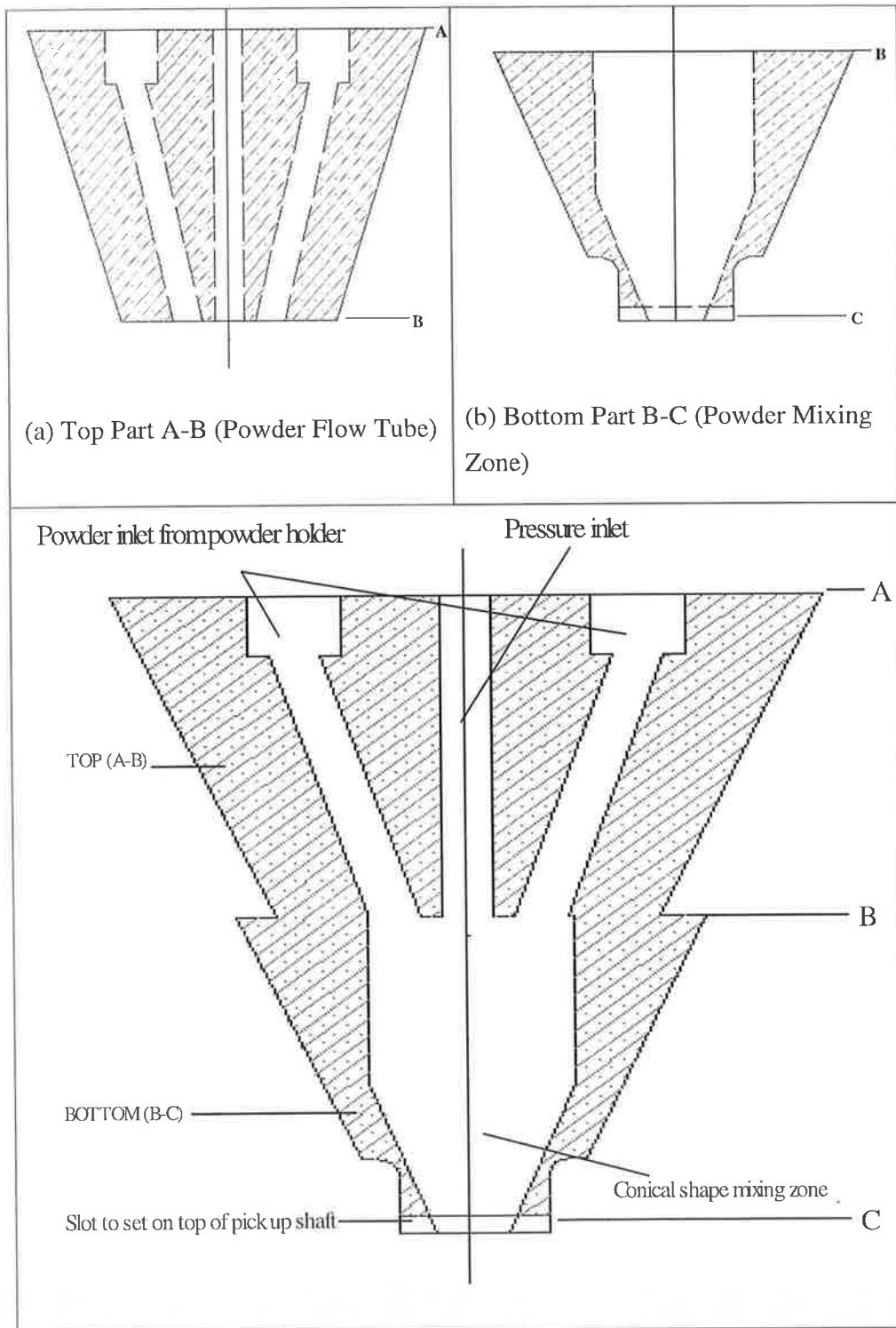


Figure 4.7: Cross sectional Diagram of Flow Tube (a) and powder Mixing Zone (b) and Cross-sectional (assembly) view of the Geometry of the model.

4.2.9 The Control System and Two Axis integration problem

The aim of this research is to re-design the HVOF Feed unit as shown the two needles will be computer controlled rather than manually controlled [49]. To develop software code to control the designed twin feed unit and monitor it in service, experimentation was carried out to analyse the effect of the Nickel base alloy FGM coatings applied on to Stainless steel substrates.

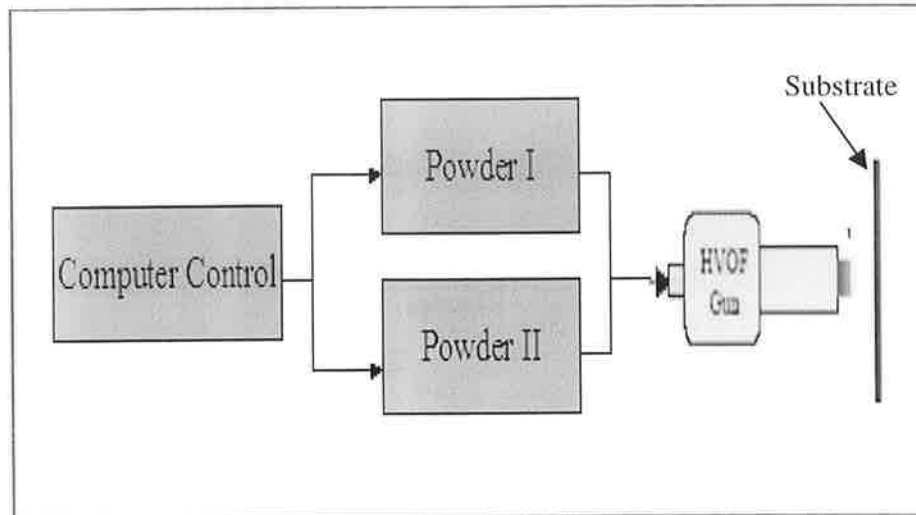


Figure 4.8: Schematic diagram of computer controlled Powder feed system.

Figure 4.8 represents a flow diagram of the proposed system used to control the powder flow rate from the dual powder holder to the HVOF gun. Implementation of the control system using a computer was decided due to the following reasons:

- An existing linear motor within the facility was already computer controlled.
- The vertical position controller for the substrate developed by Lyons [194] was also controlled by a PC.
- A computer could also be used for other applications such as measurement of heat flow inside the spray booth and around the substrate.

An automation control system could be developed in two ways; one as open loop and another as closed loop. Open loop control system can be described as a control system that does not have a feedback loop and thus is not self-correcting. In contrast to an open loop control system, closed loop is a control system contains an active feedback loop. An open-loop control process requires human intervention, whereas a closed-

loop system is entirely automated. Figure 4.9 represents basic flow diagram of an open loop control system and Figure 4.10 for a close loop control system.

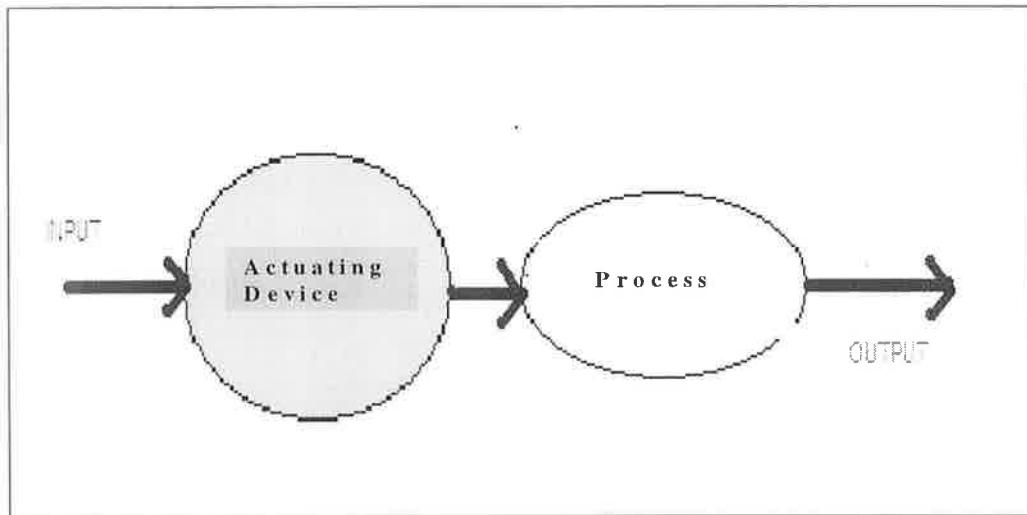


Figure 4.9: Open loop control system, adapted from [195].

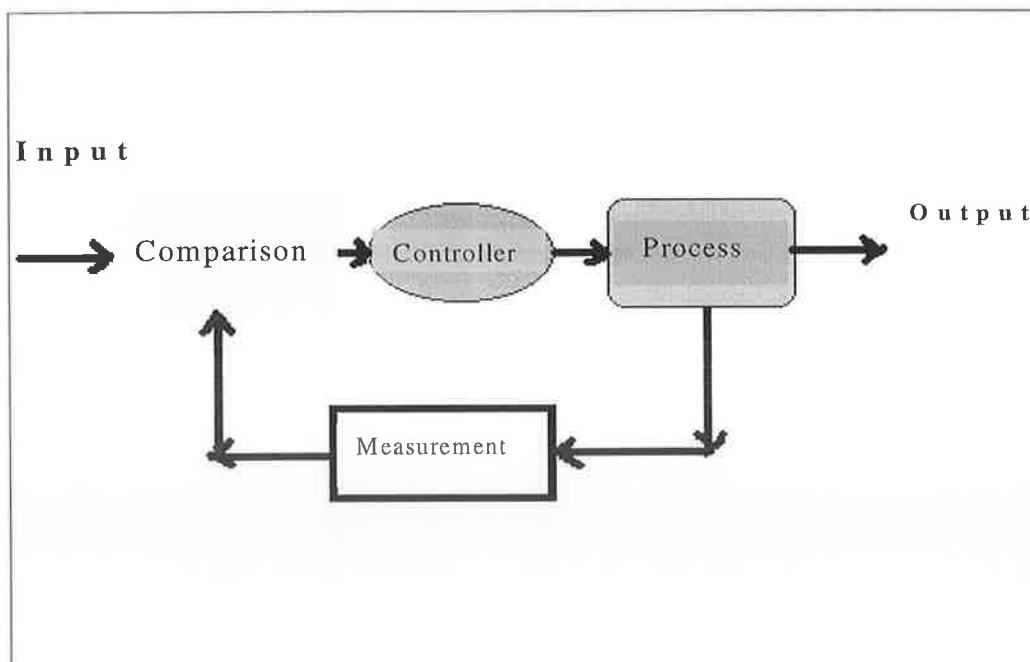


Figure 4.10: Close loop control system, adapted from [195].

The selection of what type of control system will be discussed in this section however a few points were considered initially. A closed loop control system gives high accuracy and controllability. However, the implementation of feed back system can increase the complexity of the system and hence cost. Additionally the selected linear motor driver did not support a closed loop control system. On the other hand, an open loop control system will be cost effective due to its simple design and due to the fact that the linear motor driver supports this system. Therefore an open loop system was selected for the proposed design.

In the present research the HVOF spray gun moves by the use of a linear motor controlled by a LX driver and this driver communicates with a PC via the RS232 serial port where the commands are sent in binary format by means of this connection. The LX driver interprets those binary signals and causes linear movement through an use of electromagnets.

On the other hand, electronic pulses can be used to move linear actuators, the number of which determines the movement distance in order to control the powder flow rate mechanism.

These two driving systems are different from each other. To overcome this problem the solution was to obtain an integrated program, which would be capable of sending signals to each of the actuators. Communication with the LX drive via the computer serial port was chosen as the solution. However the stepper drive board required three programmable outputs (Clock, Direction and Full or Half step) to control the linear actuators, thus it was difficult to interface these two different type drivers together. The control program also required an input parameter to determine the position of the spray gun or how many passes does it complete in relation to control of the flow rate of powder material used in thermal spraying. To solve this; a limit switch was placed at a certain position (approximately 2/3 of a single pass of the gun) on the track of spray gun linear motion. This was used to feed back to the actuator program, to signal if a command was required to change the composition of powder. To control the system a suitable programming language was also required to interface with the PC and the driver.

The decision regarding the choice of language used for software development was a vital factor to the success of this innovative development [196]. At this stage, there were four important features considered in the choice of a programming language which were as follows:

1. Interface capability with other programming languages (LX drive's command structure).
2. Interface ability with the outside world, which is called I/O capability, (the stepper motor drive and axes limits).
3. Ability of the chosen language to handle the Control flow structure such as; while loop, for loop, case structure and so on.
4. Ease of use for development.

4.2.10 Software and I/O Solution

Depending on the above discussion a number of programming languages were examined such as C, Visual Basic. Searching the Internet the author found that there were a few two axis motor controllers available in the market that operate by their own programming language. One of these was chosen as the best software as its I/O solution was based on LabVIEW (Laboratory Virtual Instrument Engineering Workbench) from National Instruments. This software fills the gap between powerful and flexible programming languages and the ease-of-use of configuration-based equipment. LabVIEW facilitates an intuitive graphical development environment that effectively defeats the idea that a tool cannot be both powerful and easy-to-use. It includes features that make it the ideal tool for creating test, automation, measurement, and control applications regardless of industry, area of expertise, or programming knowledge [197]. For measurement and automation purpose data acquisition cards could be used which support this software and are provided by the manufacturer themselves (National Instruments). There are different types of DAQ cards available, and the selection of the correct DAQ card depended on the following factors:

1. *Number of Inputs and outputs:* Digital and Analogue; these two types of inputs and outputs are available in a DAQ card. To drive the linear actuators; digital input and output facility was required for a DAQ card.

2. *Sample rate*: means the speed at which the DAQ card read the inputs and sends to the computer for upgrade and it is measured in samples per second.
3. *Resolution*: is the interval at which the ADC (Analogue to Digital Converter) samples the analogue signal.

After examining the DAQ option available and consultation with our electronic technician it was decided to use the existing AT-MIO-16XE-10 DAQ card (already in use in the HVOF facility to control the substrate position in the DCU HVOF) in the current project, (the specification of the DAQ card is available on data sheet in Appendix B2 [198]).

4.2.11 Electronic Design

The DAQ card works with a digital logic of 0 volts equal to Boolean false or 0 and 5 volts for Boolean true or 1. However the stepper drive board requires 12 volts as a Boolean true or 1. To solve this problem an amplifier circuit was design (as the majority of the electronic devices of this research were “off the shelf components”). The amplifiers were used to amplify the 5 volts output supply from the DAQ card to 12 volts so as to operate the actuator drive board.

The behaviour of most configurations of op-amps can be determined by applying the "golden rules" [199]. For a non-inverting amplifier, the current rule tries to drive the current to zero at point A (Figure 4.11) and the voltage rule makes the voltage at an equal to the input voltage [199].

This leads to

$$\frac{V_{in}}{R_1} = \frac{V_{out} - V_{in}}{R_f} \quad \text{Equation 4.5}$$

and amplification

$$\frac{V_{out}}{V_{in}} = 1 + \frac{R_f}{R_1} \quad \text{Equation 4.6}$$

$$V_{out}/V_{in} = 12/5 = 2.4$$

Therefore

$$R_f = 1.4 \times (R_1)$$

In this case the output will be connected with the logic inputs of the motor drive board. So the value for R_1 is not critical; its value depends on the amount of current that the output of the amplifier circuit will draw. Due to this reason an arbitrary value of R_1 equal to $10\text{ K}\Omega$ was selected and R_f equal to $14\text{ K}\Omega$. Unfortunately a $14\text{ K}\Omega$ resistor was not commercially available hence a $15\text{ K}\Omega$ was chosen which gives a V_{out} of 12.5 volts and this was seen as acceptable.

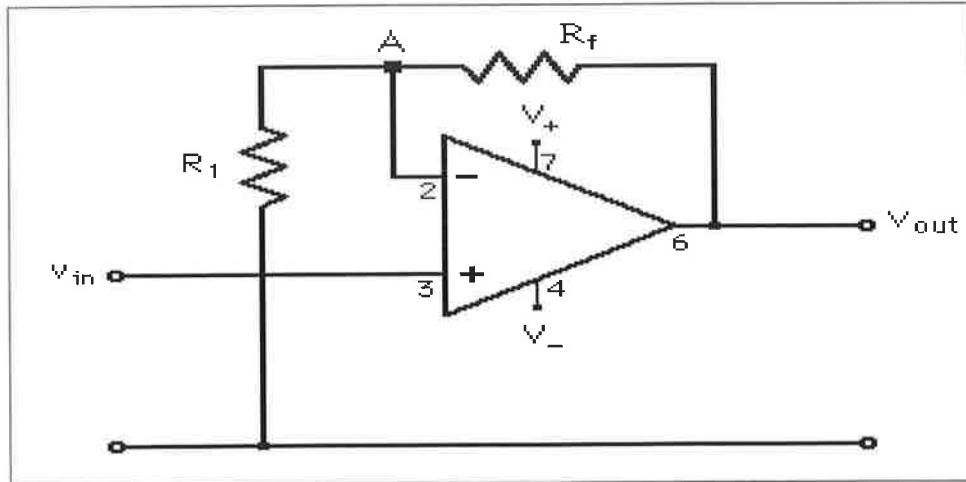


Figure 4.11: Non Inverting amplifier, adapted from [199].

To develop this amplifier circuit design, two type 741 operational amplifiers (op amp) were used and Figure 4.12 shows its circuit diagram. The Data sheet of this 741-type op amp is reported in Appendix B3. Although there were three inputs into the motor drive board, one of these inputs, Half or Full step would be connected to the amplifying circuit. Half step gives better resolution compared to Full step, so the Half step should be kept as the default mode and not wired into the amplifier circuit. The clock and direction were connected to the amplifying circuit (Figure 4.12).

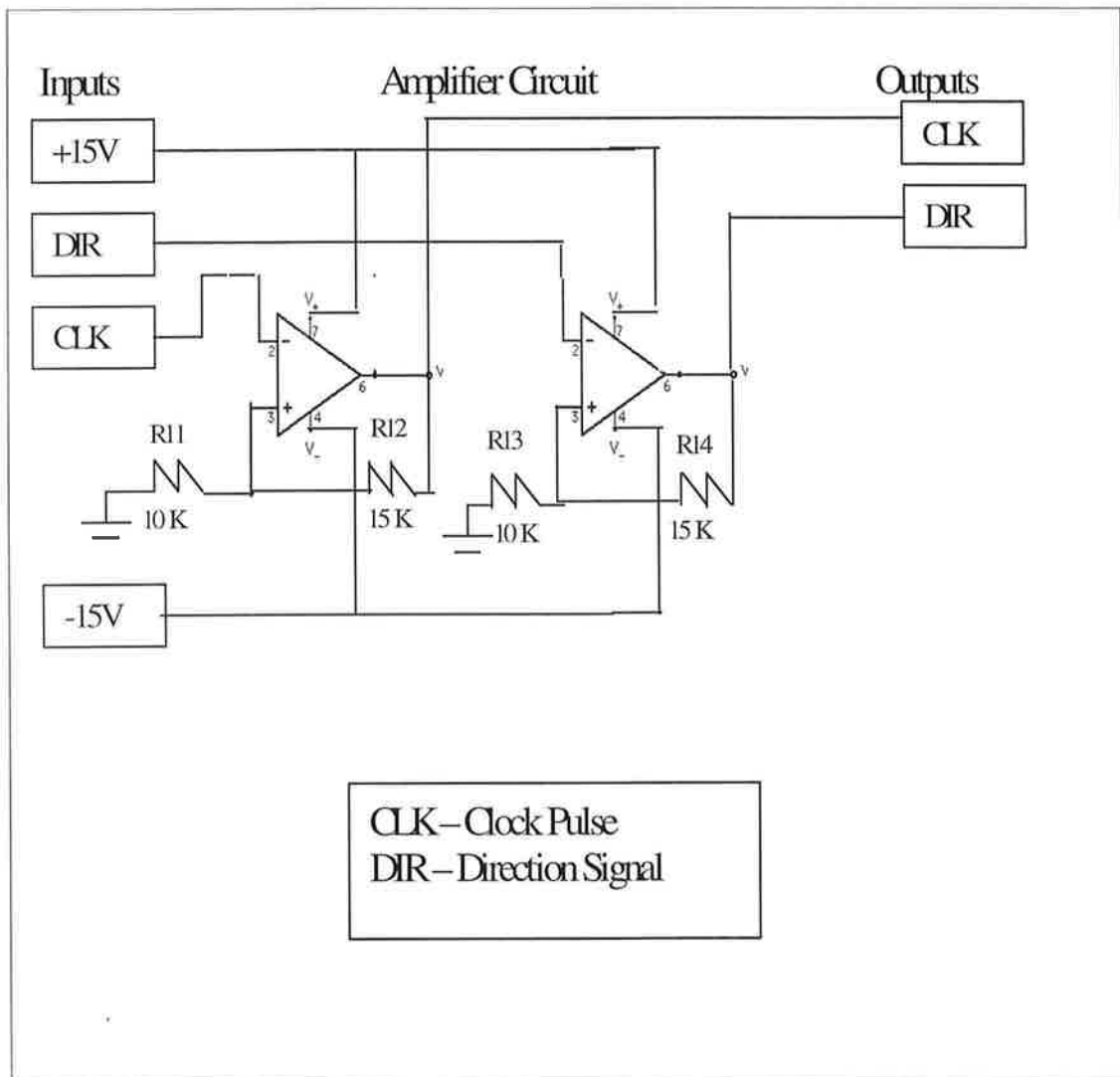


Figure 4.12: Full two input amplification circuit.

4.3 REALISATION

Realisation of the design and specifications of the project was the next evaluation stage of this process, which includes the evolution from detailed drawing, circuit diagram and specifications to a working prototype. The following sections of this chapter include the activities undertaken such as; purchasing components, production and assembly of the computer controlled powder feed unit and finally the development of the controlled software.

4.3.1 Component Selection and Purchasing

After analysing the final drawings of each component, design calculations and the overall proposed process, it was determined that some components had to be purchased. These were as follows:

1. Two linear bearings to support the needle shaped bolts.
2. Two linear actuators to provide linear motion to the needle shaped bolts
3. Two drive boards to control the linear actuators.

During the selection of these components; the main concern was that those components performance and low in cost. An investigation into the selection of components provided by different suppliers was conducted to, determined one supplier to be chosen for the electrical components and another for the mechanical components providers.

The electrical components (linear actuators and drive boards) were purchased from Radionics Ltd. As Radionics do not provide mechanical parts (linear bearings), these were ordered from Dixon bearings suppliers, according to the following specifications; Outer Diameter: 17 mm, Inner Diameter: 10 mm and Length: 26 mm

The design of the Top cover plate of the Hopper unit and its inner diameter was critical as the diameter of the needle shaped bolts required were 10 mm diameter. The depth for the bearings positioning hole on the top plate did not affect the overall design of the project.

The most vital part of this current project was the linear actuators and the drivers for them. Appendix 1 shows the data sheet of the linear actuators, actuators wiring instruction and drivers. The reason these linear actuators were selected instead of ordinary stepper motors was that the actuators were designed with internally gears and coupled with lead screws hence no additional lead screw assembly was necessary. These actuators provided 0.0508 mm vertical movement per step. The driver selected was directly compatible with the linear actuators. Finally use of the Op Amp Amplifier generated the required 12 volt output.

4.3.2 Manufacture of Unique Parts

Production of each component was carried out in the DCU mechanical workshop following the detail design drawings. Minor alternations were made to the detailed drawings in order to accommodate materials, which were readily available, and dimensions. The shape of the top cover of the hopper unit or the base plate for the actuators mounting could be either square or round, as a round plate design was chosen due to availability of the material. To count the number of passes of the spray gun, positioning of a limit switch was necessary. So few tapped holes were drilled on to the bottom surface of the platen (Figure 3.10).

Production of the design's components were carried out almost without any major difficulties due to extensive consultation with the workshop technicians during the design phase to ensure that the drawings were comprehensible and easy to construct.

4.3.3 Mechanical and Electronic Assembled Components Integration with Existing Equipment

When all the required components were manufactured and purchased parts (Linear bearings, linear actuators and drivers) arrived from the suppliers, it was then necessary to assemble them to satisfy the objective of this current project.

Figure 4.13 shows the entire newly designed dual powder feed device. Linear bearings were placed on the top cover or base plate of motor mounting. The bearings are covered by the actuators holders. This design is then placed inside the existing

powder hopper, which will act as an outer casing and top hopper cover is attached using four screws. Figure 4.14 shows the digital picture of the assembled set up after the dual feed device is placed inside the existing hopper.

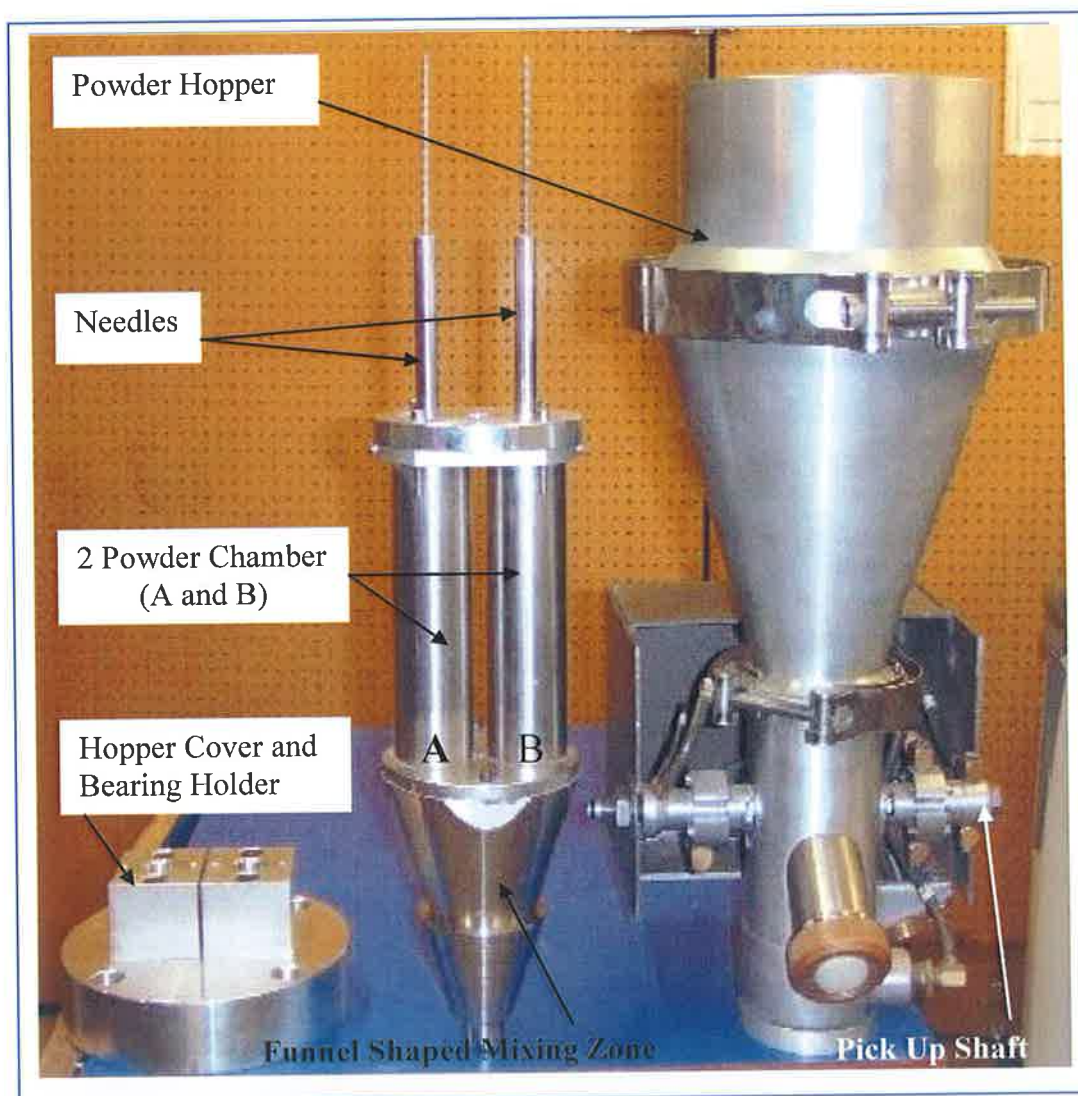


Figure 4.13: Digital picture of the newly designed dual powder feed device.

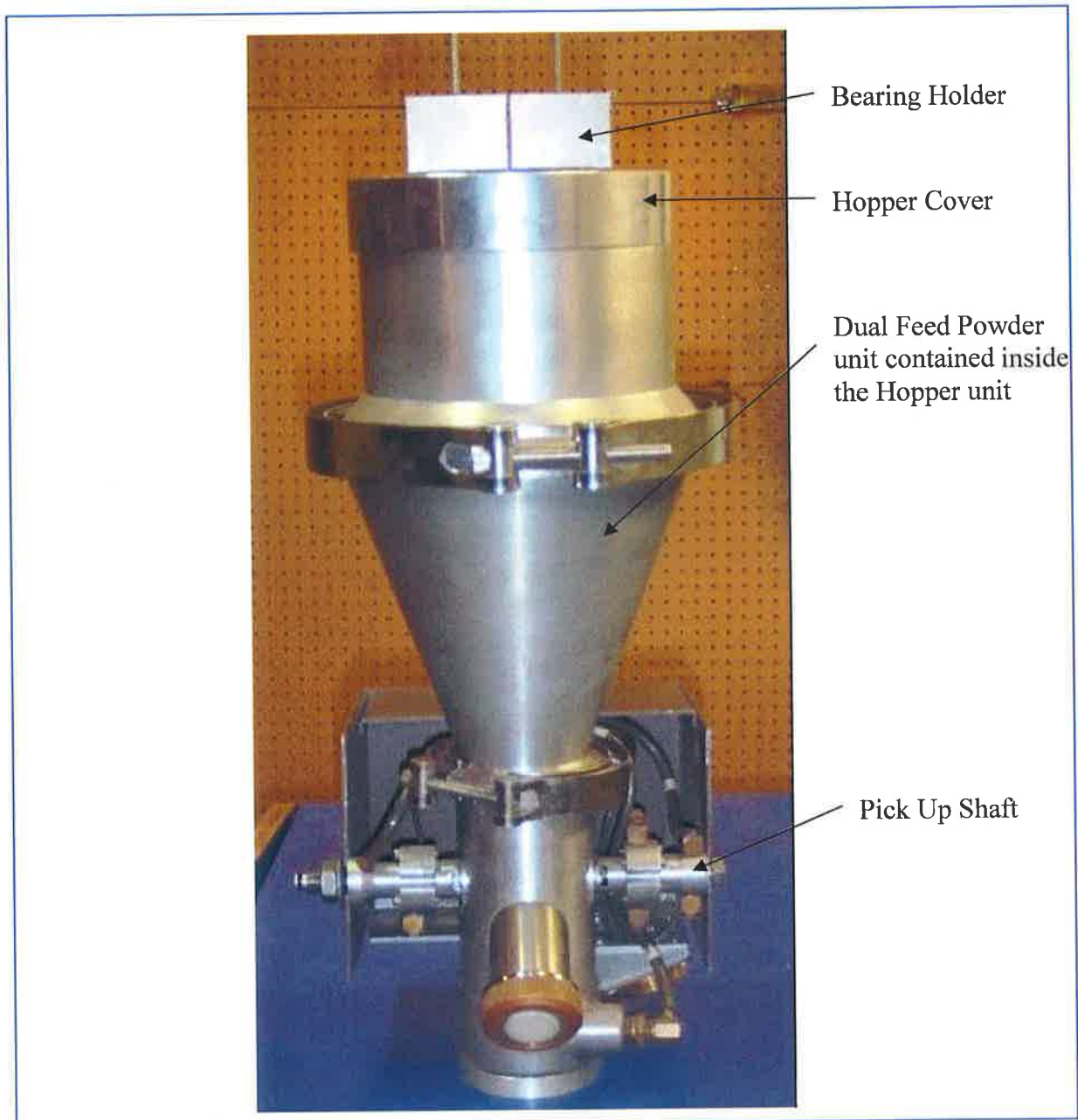


Figure 4.14: Digital picture of the entire set up after assemble with the existing powder hopper in HVOF Lab.

The linear actuators were placed on top of the motor holder and fixed by screws. Figure 4.14 shows the actuators set up with their holder. These linear actuators were connected to the drivers' separately. Wiring of these actuators was carried out during the electronic design phase. The data sheet for the wiring instruction is reported in Appendix B1.

During the spray process chamber A and B (Figure 4.13) contains dissimilar powder. The linear actuators open fully one chamber and keep the other closed. Then after a certain desired number of passes of the HVOF gun (after the bond coat was sprayed

on) each actuator moves; needle 'A' down (close) and needle 'B' up (open) to change the amount (composition) of powder flow.

Apart from the physical wiring of the motor, limit switches, another electrical assembly required was the signal amplifiers for the linear actuators control. To satisfy this a circuit was designed (as reported in section 4.2.11), and the circuit was assembled onto a breadboard. After verifying the operation, (producing the required signal) the circuit was soldered onto a Vero board for each stepper motor driver and assembled into two separate plastic enclosures to protect them from the HVOF operating environment as shown in Figure 4.15.

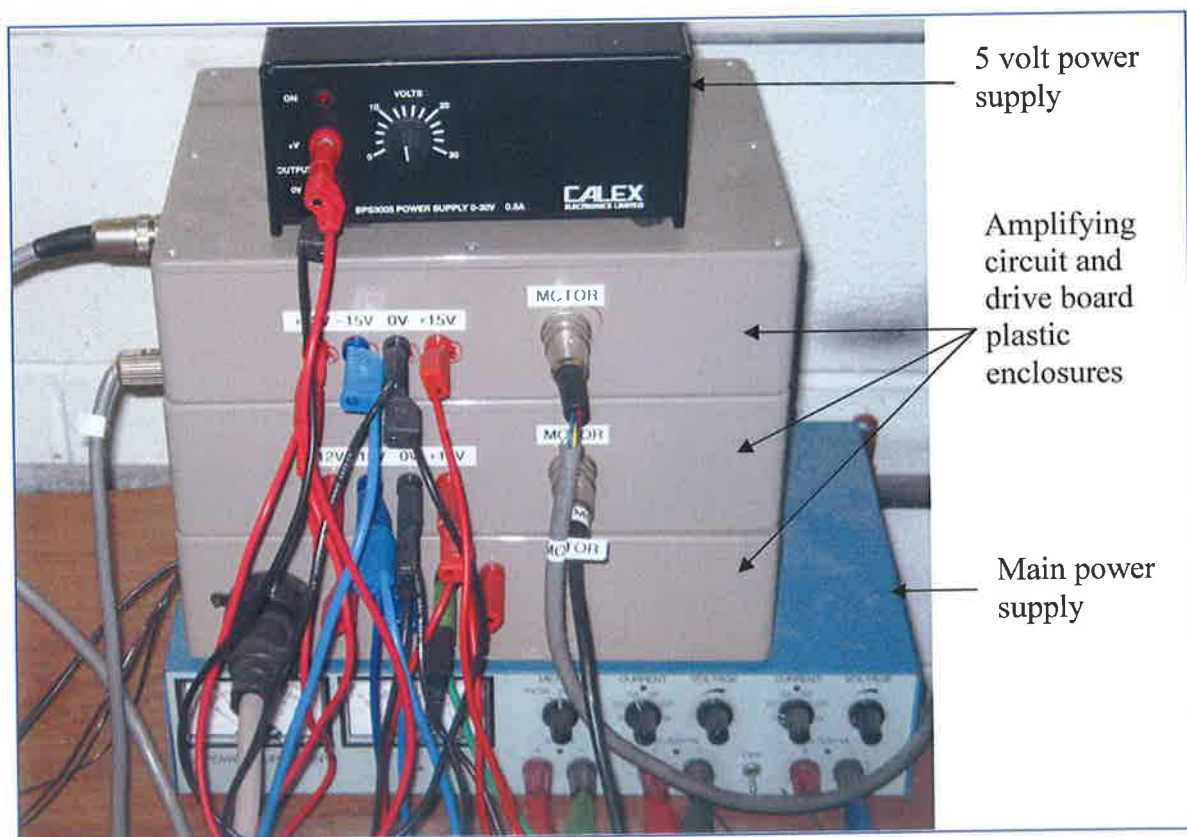


Figure 4.15: Assembled enclosure for stepper driver and amplifiers with power supply unit.

Each of the enclosures consisted of a closed plastic box with an output cable to the linear actuator and a control cable from the DAQ card. Figure 4.16 shows a digital picture of the existing DAQ card connections, which connects with the computer, and with a power supply unit (Figure 4.15).

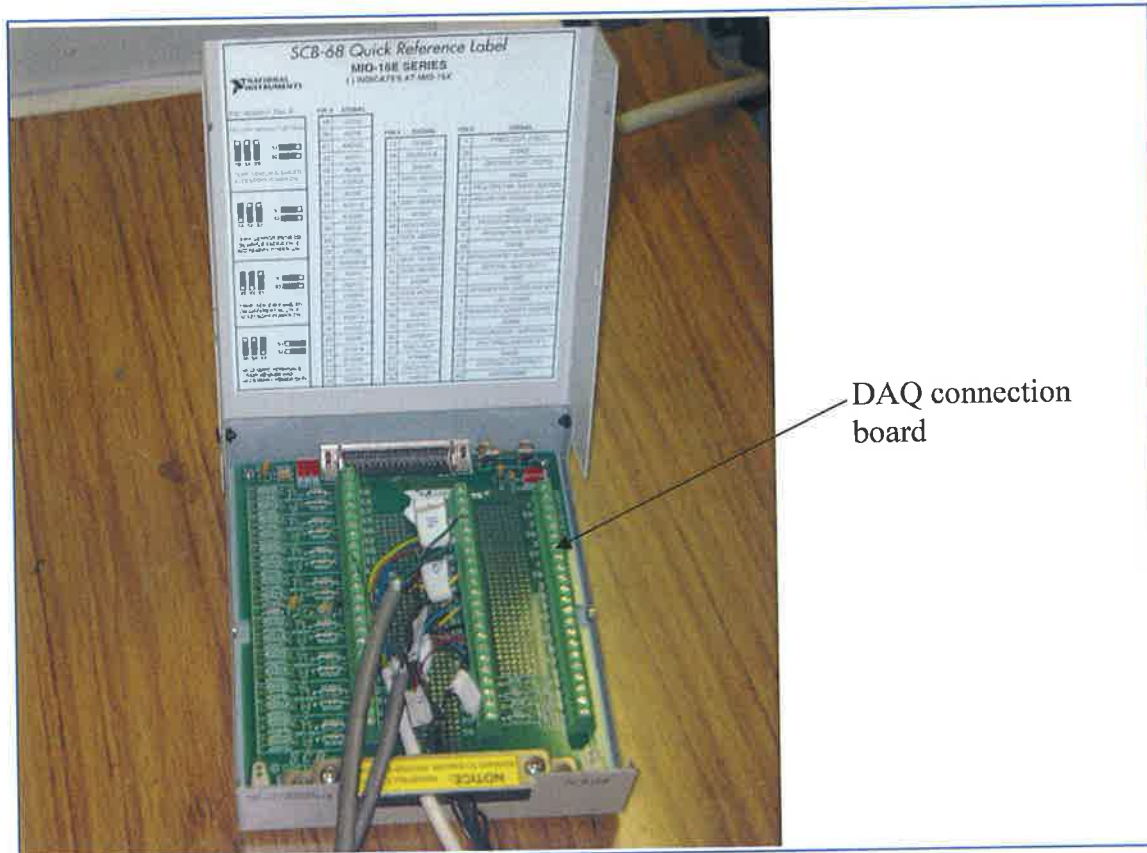


Figure 4.16: DAQ connection board wired with limit switch and stepper drivers.

4.3.4 Software Design

The achievement of entire project depends on the controlling software development. Hence this was an important part of the current project. So that it was vital to take a structured approach to the software development. The primary step was to determine the program's procedure, (which steps are necessary for the program while it executes).

The procedure of the needle shaped bolt movement along vertical axis control application was as follows:

- Move the spray gun a prescribed number of times across the substrate which will be counted in passes and each pass will be considered as a complete stroke, (the gun will move across the substrate and then back again).
- Pause the spray gun for a very short time.
- Move the needle shaped bolt along the vertical axis a defined distance that is required to get the desired flow of the powder materials before the spray gun starts its next pass.

- Repeat this cycle as long as operator has pre-programmed to do so.
- Contain an option for both actuators to be operated simultaneously according to specific requirements to allow any variation (composition) of powder proportion in the resulting coating microstructure to be achieved.

At this stage it was necessary to gain a good working knowledge of the use of the two programming languages (Lab VIEW and LX Drive command languages) to develop a control program with the above criteria, for software control.

The following sections detail the operation of the actuators control program (Lab VIEW) and the LX programme used to control the linear gun motion. The operation of the application's code is first explained then a user reference guide is detailed which explains all about the controls used in this program and operating procedures. The entire block diagram of the Lab VIEW program is shown in Figure 4.17 and the following sections describes each component separately for one linear actuator control. For a more detailed overview of programming in Lab VIEW information can be found from the National Instruments web site [197] and from Wells [200].

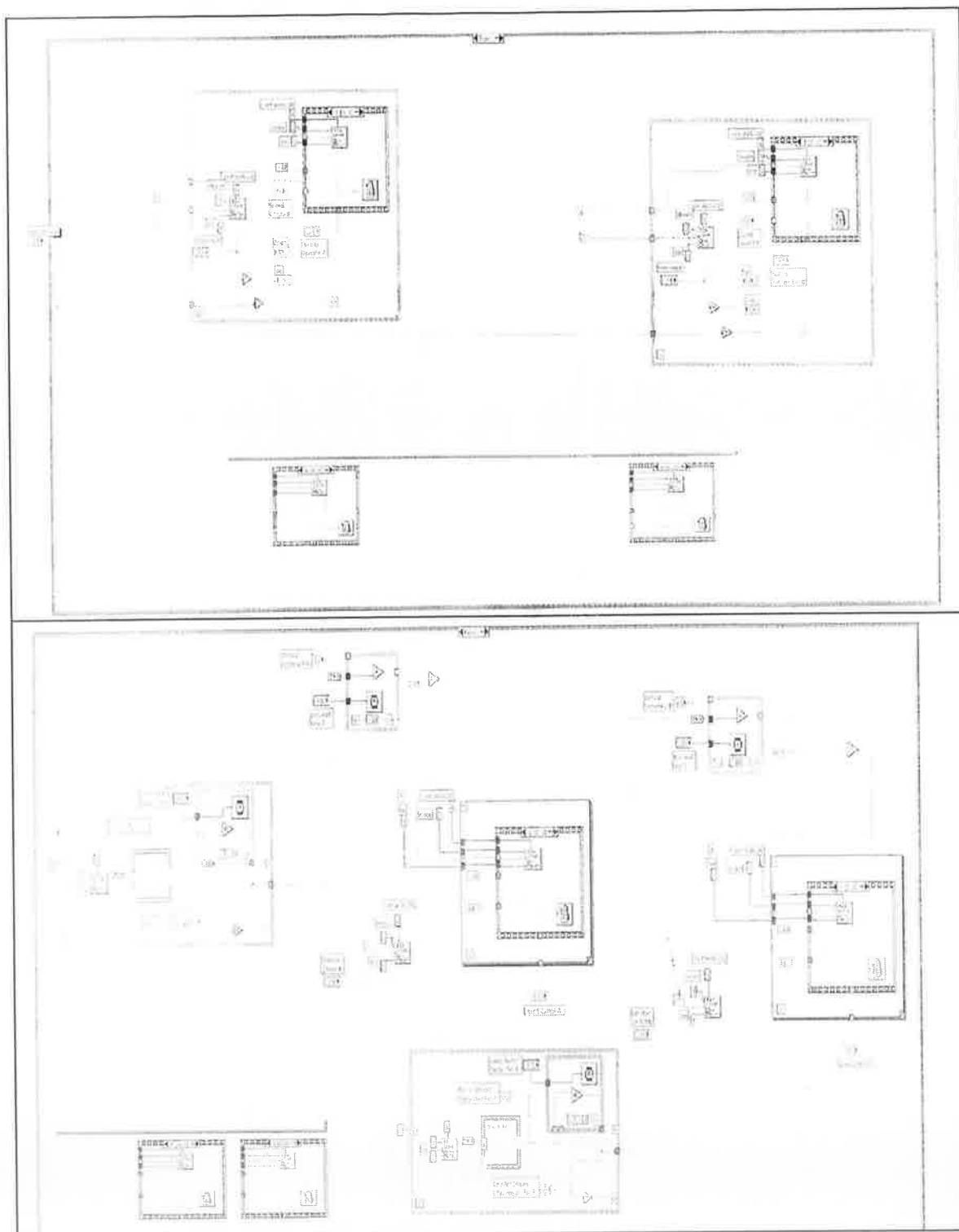


Figure 4.17: Lab VIEW Block Diagram for linear actuators control used in current research.

(i) Controlling the Stepper Motor

A clock pulse signal is necessary in the stepper driver circuit to move the linear actuator. The code used to generate this clock pulse is shown in Figure 4.18. For this purpose an OUT-PUT function named 'Write to Digital Line' was used within a sequence structure, which in turn results in a For Loop. The Sequence structure, shown in Figure 4.18, looks like a frame of film. It executes the code in frame one, followed by the code in next frame and so on the frame number shown on top of the structure, i.e. 0,1. The output function (Write to Digital Line) sends the value of generated clock pulse signal to a predefined digital output line of the DAQ card through the interface board. For this purpose in this programme, line 1 is used to receive a signal for actuator 'A' and line 2 for actuator 'B'. One frame of this Sequence structure is set with a Boolean constant value of false or zero volts connected to the output function. Another one is exactly the same except the value of Boolean constant is true or 5 volts. To generate a square wave pulse, these two frames execute frequently within the 'For loop'.

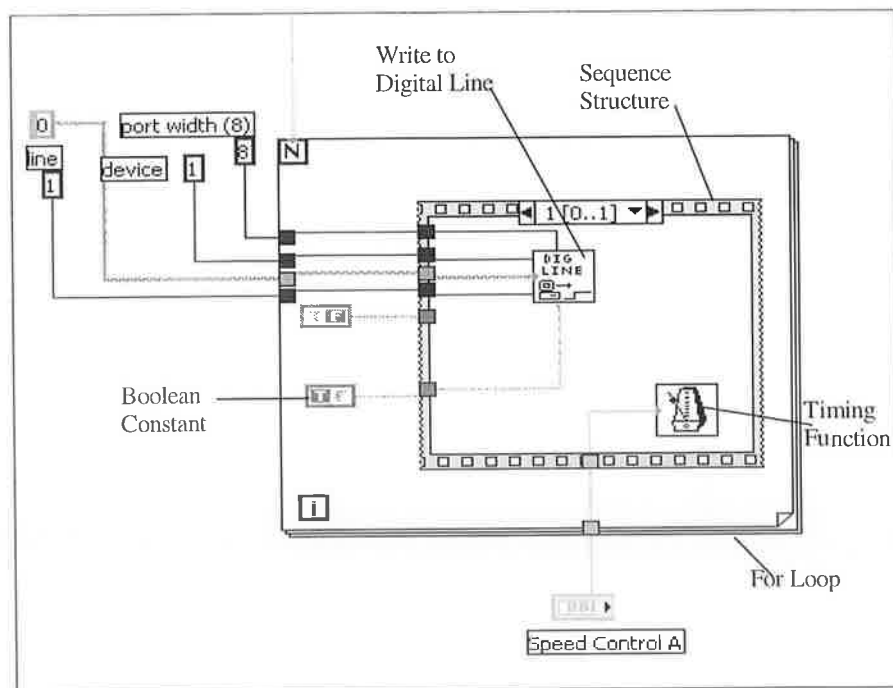


Figure 4.18: Section of the Lab VIEW Block Diagram, which generate clock pulse.

The speed of the linear actuators is dependent on the frequency of the clock pulse generation; therefore a Timing function was added within the loop, which causes a time delay between the executions of two frames hence defining the wavelength or frequency of each pulse. This function was connected with a vertical slide control in the control panel. The linear actuator will move according to the amount of clock pulse supplied and the amount of the positive cycles in the clock pulse must be controlled (completed using a for loop). This For Loop executes a specified number of times from $i = 0$ to N and the count terminal N is connected to another function which controls the vertical movement of the actuator as shown in Figure 4.19.

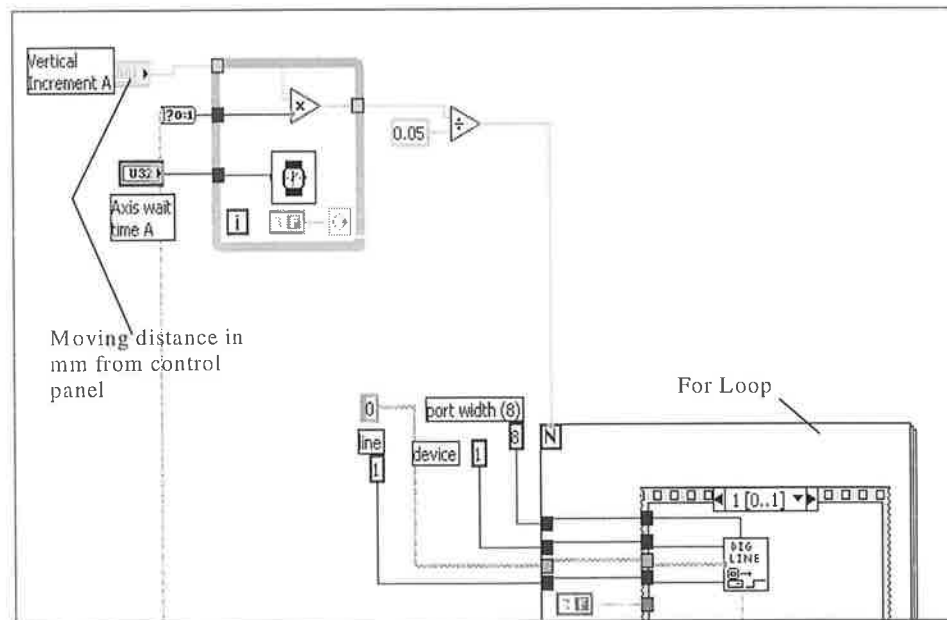


Figure 4.19: Lab View Code used which will act as a distance converter to move per step.

To obtain the value of N (distance to be move per step) the following calculation must be made. From Data sheet (Appendix B1) it is found that the linear movement of the actuator is 0.0508 mm ($= 0.05 \text{ mm}$) per step. Hence the following formula was used to get the value of N and implementation of this code is shown in Figure 4.19:

$$N = D / 0.05$$

Where, N = Number of steps to move and D = Distance in millimetres to move.

To summarise the distance to be moved by the actuators is converted to a value of N . Within the For Loop, a sequence structure generates one cycle of clock pulse with a required frequency for each iteration of the For Loop. Finally the output function

(Write to Digital Line) sends the overall processed signal to the DAQ interface board through a specified digital line.

(ii) Linear Motor Control

As previously mentioned, the linear motion of the spray gun is control by a LX driver using a program named 'XWare'. This program consists of a text editor panel where the command sequences have to be written and after execution of this program those sequences of commands are sent to the LX driver and converted into electrical signal, which creates the linear motion of the spray gun.

There is a user manual provided for the LX driver and the XWare programming which details the command required to control the linear motion of the spray gun and this is available in the DCU HVOF facility. The pseudo code controls the movement of the spray gun during the automated spraying process as follows:

- Complete a specified number of passes in front of the substrate in order to preheat the substrate.
- Pause to run the Lab VIEW program to control the linear actuators, which will vary the ratio of the powder flow.
- Pass again to deposit a coating and loop the Lab VIEW procedure until the final layer of coating has been applied.

During the programming of the XWare code, it has to be remembered that all units of distance, velocity and acceleration are measure in inches (imperial). Figure 4.20 shows the command-editing window of the XWare program where the font should be in capital letters and spaces between command sequences are important factors.

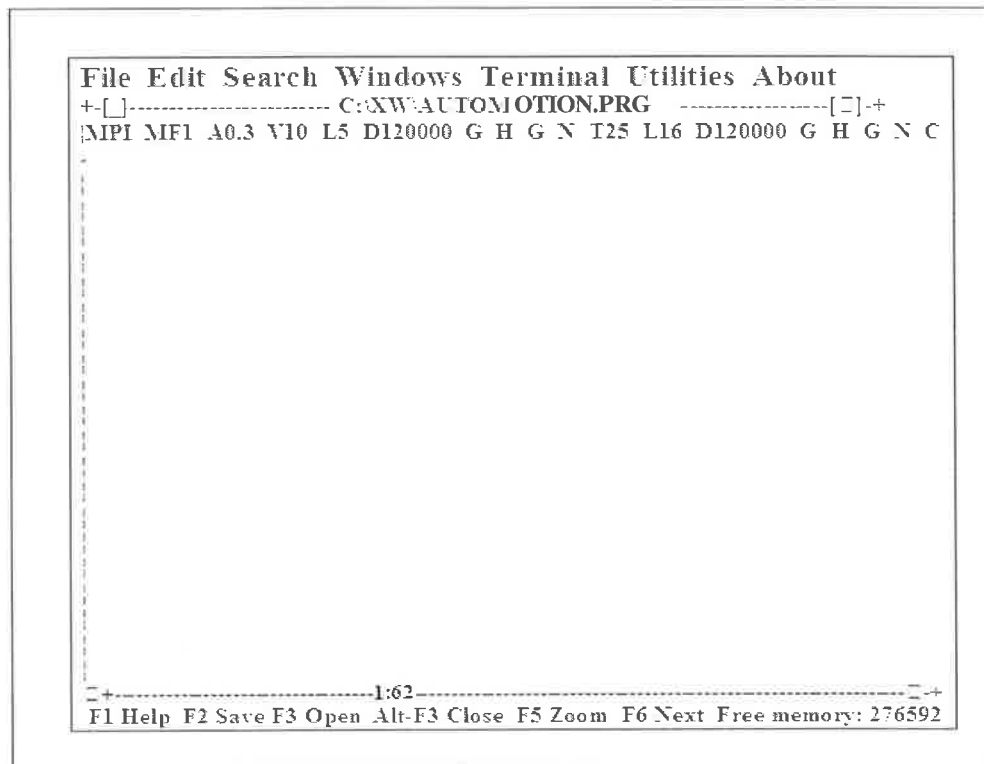


Figure 4.20: AUTOMATION.PRG, the command sequence used to control the linear motion of the spray gun.

The meanings of the command used during programming for the current research are as follows according to the user reference guide [201].

MPI – Sets unit to incremental position mode, i.e. the moves that follow will be carried out in incremental moves.

MF1 – Define move from one.

A0.3 – This command sets the acceleration of the linear motor to 0.3 g (2.943 ms^{-2})

V10 – Sets velocity to 10 ips (ips = inches per second) (0.254 ms^{-1})

L5 – Loops following code five times for pre-spray treatment.

D120000 – Sets distance to 12,0000 steps (1000 steps = 1 inch or 0.0254 m).

G – Execute the move (GO).

H – Reverse the direction.

G – Go.

N – Ends loop

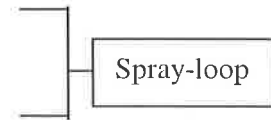
Pre-Heat
treatment
loop

T25 – Wait 25 seconds before carrying out next operation (Allow 25 seconds time delay before starts the next procedure during this 25 seconds Lab VIEW program will turn on to control the powder flow rate and the powder feed will be turn on after this).

L16 - Loop sixteen times.

D120000, G, H, G, and N – Same as described earlier.

C – Initiates command execution to resume.



iii. Relative Motion Between Axes

There was no existing software link between the linear gun motion control and the actuators vertical motion control. However for the current project it was necessary to establish a relationship between these two types of motion axes. For this purpose a limit switch was placed at one end of the linear motion path and connected to the DAQ interface card as an input signal. Using this limit switch, the Lab VIEW program counts the number of passes performed by the spray gun and according to this count, the Lab VIEW program executes the desired powder flow ratio. Figure 4.21 shows the code used in Lab VIEW program to count the number of gun passes across front of the substrate using the limit switch. This diagram is simpler to describe if it is divided into three sections.

The first step includes two important functions; one is the Read from Digital Line and another one is the Formula node. Read from Digital Line function reads the value from a predefined digital line (Line three of the DAQ interface card is connected with the limit switch) and takes the value as an input signal to the program. These two functions are placed into a While Loop that iterates until the condition terminal gets a value of false. When the Formula node receives the latest count value, it compares to the maximum count input provided from the control panel by the operator to check if the While Loop should terminate or not. In Figure 4.21, a time delay function is placed (labelled as pause function) into another While Loop (labelled as Pause Loop), which is necessary for the counting function. The condition terminal of the While Loop was unwired so it will only iterate once and causes a pause in the program execution equal to the value entered from the control panel. It allows a pause to the

limit switch so the gun can move off the switch and return to its starting point (end of the pass). Hence the event will not be counted twice.

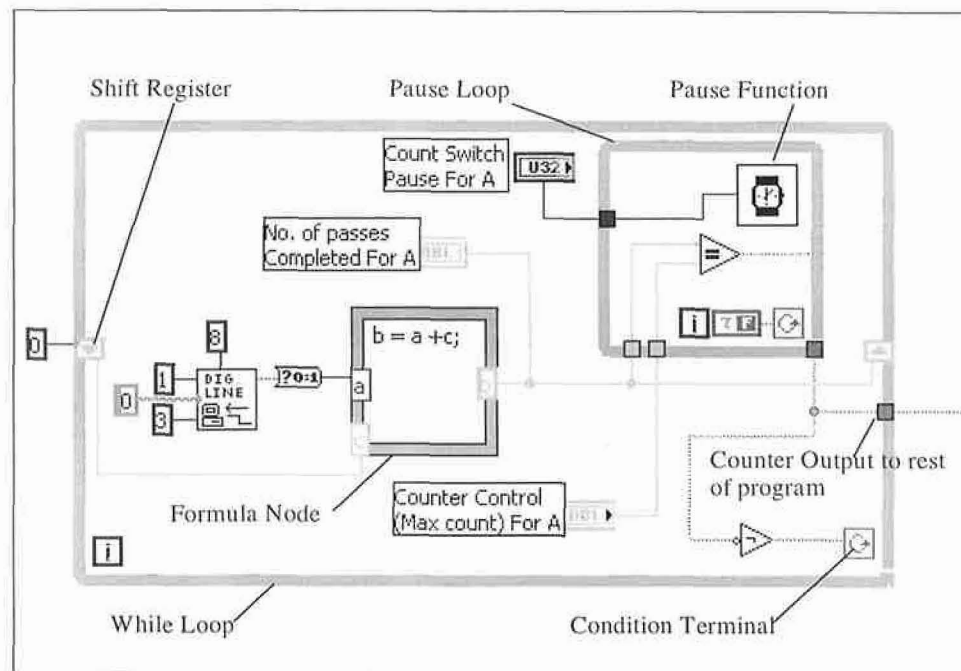


Figure 4.21: Counting Loop of the Lab VIEW program.

The OUT-PUT count value from the formula node is compared to the value of maximum count provided from the control panel inside the pause loop. If the two of these values are equal to each other, a true value is passed out side the loop and the entire counting function terminates. Using a NOT gate inverts this signal and sends it to the condition terminal to stop the While Loop. Hence a true value is sent to the rest of the program to signal that the spray gun has completed the required number of passes and the vertical movement of the linear actuators will commence.

Figure 4.22 shows the final part of this program that how it is connected between the output of the counter and the linear actuator control. The output signal from the counting function passes through another While Loop (Labelled as Axis Wait Loop in Figure 4.22). Inside this loop the vertical increment input is provided from the control panel and multiplied by the count value (either zero or one). The counter output is one when the count value is equal to the maximum count value hence the vertical increment value will be buffered through the loop, if not then the counter output is zero and so on, hence the vertical increment will be remain as zero. A wait function is

also placed inside the Axis Wait Function loop to control the axis wait timing during the operation. In the present research, the axis wait time was set as zero which gave the next ratio of powder flow time to be available in the system before the next pass starts.

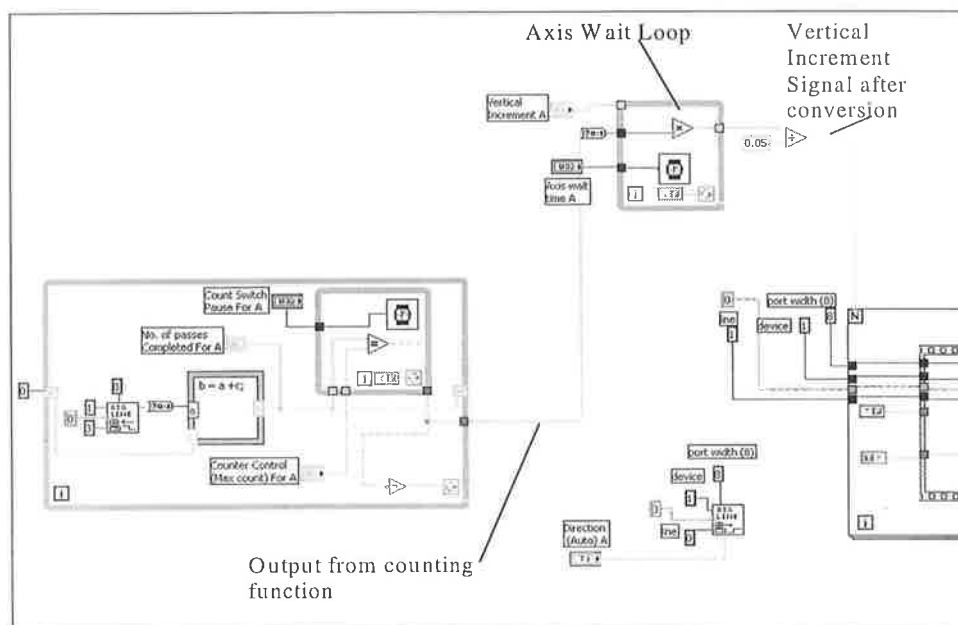


Figure 4.22: Connection between Counting Loop and Linear Actuator Control.

Another Write to Digital Line function is placed in the program which allowed control of the moving direction of the actuator (to open/close a powder carrying chamber) and was controlled from the control panel according to the following requirements. The actuators direction signal was wired to the DAQ interface card. Line zero of the DAQ interface card was used for actuator 'A' and Line four was used for actuator 'B' (that is each chamber).

The overall program was developed to control the two actuators in order to allow the flow of two different powder materials.

(iv) **Manual And Automatic Modes**

These two types of operating modes (Manual and Automatic) are available in the Lab VIEW programme to control the powder flow rate of the thermal spray. If an operator wants just to open and leaves a chamber open or after the coating (Bond coat) wants

to re-set the needle position to its initial condition, the Manual option is used (or for pre spray set up). During the deposition the Automatic mode is selected. To create this option a Boolean Case Structure was used during the program development as shown in Figure 4.23. This case structure has two sub diagrams, case zero or one change to FALSE and TRUE (here, TRUE for Manual mode and FALSE for Automatic mode) and it was connected to a vertical switch labelled as 'Auto/Manual' on the control panel.

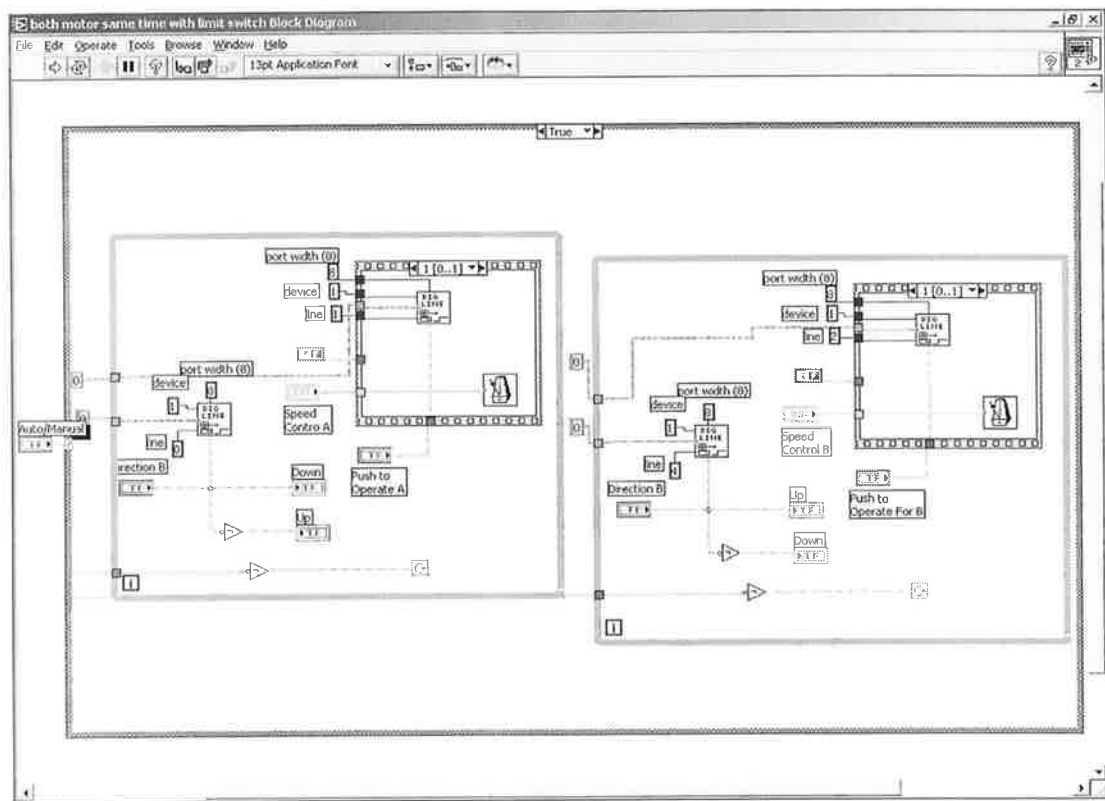


Figure 4.23: Block Diagram for Manual Control.

4.3.5 Control Software Reference Guide

The control software reference guide is essential for those new to these procedures (new operators) hence this section is aimed at providing an initial point of start for new operators. There are two types of controlling software used in this current research; one is vertical movement control of the linear actuators using Lab VIEW programming and another is linear gun motion control using the XWare programming. The reference guide to each of these are detailed below:

(i) Vertical Axis Control of the Linear Actuators

The procedure used to open the Lab VIEW program from the DCU HVOF facility computer is as follows:

- From the Task bar click the **Start button** → **Programs** → **National Instruments Lab VIEW**
- Once the Lab VIEW program has opened, from Menu bar select **Open VI**
- Select the file named '**Automated powder feeding.vi**' from the selection window which can be found on the desktop of the HVOF facility computer

When the file is opened the control panel interface will appear on the computer monitor as shown in Figure 4.24. It is divided into four areas; two of them are used to control Actuator 'A' (chamber A) with auto or manual option, another two is used to control the Actuator 'B' (chamber B) with the same options as mentioned for actuator 'A'.

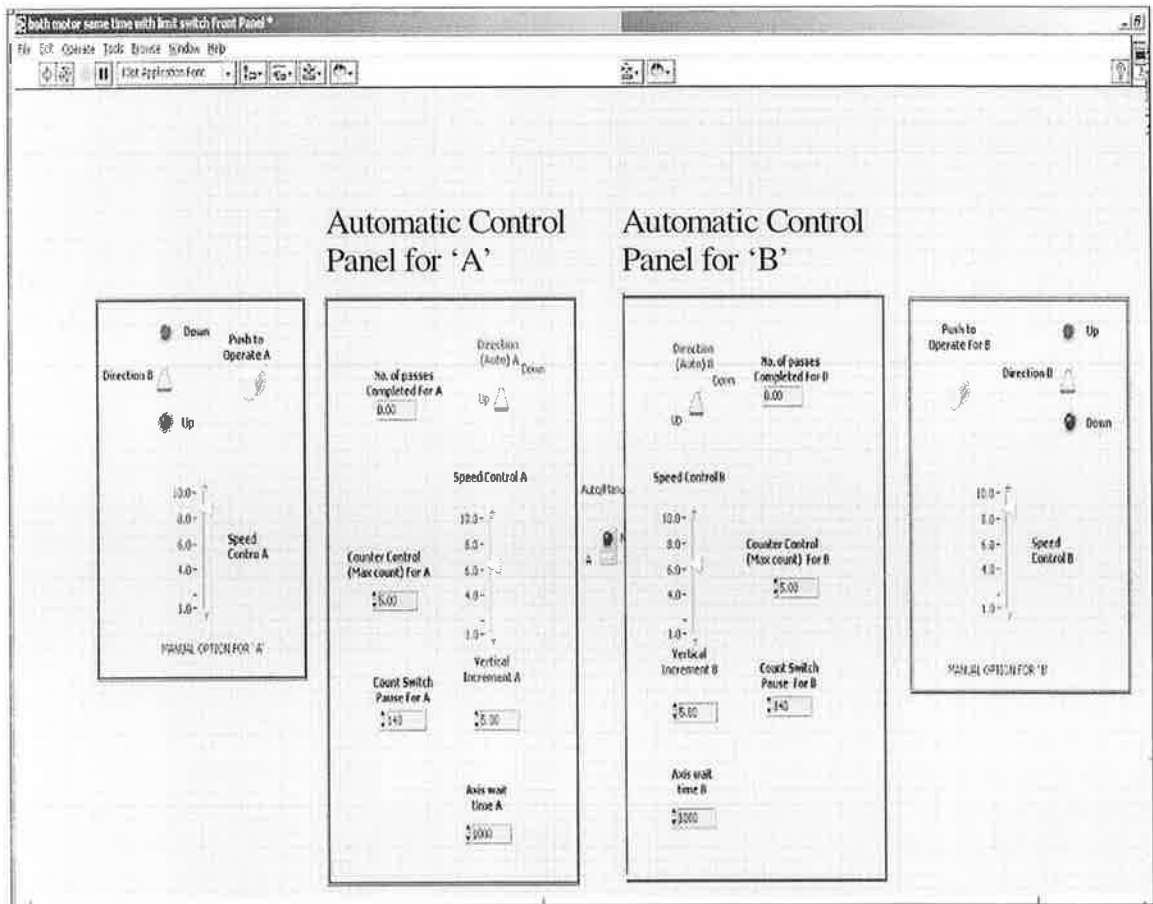
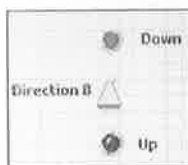


Figure 4.24: Control Panel for linear actuators 'A' and 'B'.

This Auto/Manual button is used to switch between automatic and manual option.

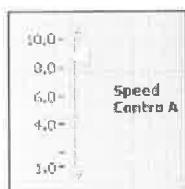


When the red led is on then the manual options for both actuators 'A' and 'B' are activated. If this red led is off then the automatic control panels for both actuators are ready for linear motion operation.



This vertical toggle switch is used to control the direction of the actuator. There are four of them on the control panel as shown in Figure 4.24. Each of them could be

controlled separately. Two of these switches are used in manual mode to control the direction of the actuators 'A' and 'B' and the remaining two used in automatic mode.



This vertical slider is used to control the speed of the actuator where 1.0 is top speed and 10.0 is the slowest. There are four of these icons used to control the speed and the controlling option of each of them is independent to the direction control switches.



This button works when the Manual/Automatic toggle switch was set to its manual option. When one presses this button the actuator moves according to the directional button position. This button is used to reset the position of the needle shaped bolt inside the powder holder. So it is advisable to be attentive during this operation so that the tip or ends of the needles do not cross their positioning limit as marked on them.

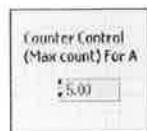
The following five control buttons are used twice; one set for actuator 'A' and another is for actuator 'B' in automatic panel:



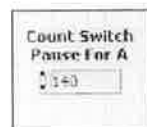
This channel is used to INPUT the vertical movement measured in millimetres and has a default value of 5 (5 mm). This input value determines the amount of needle movement after a prescribed number of passes by the spray gun (this can set by using the Counter Control input box and the calculation from number of turns was calibrated by the actuator).



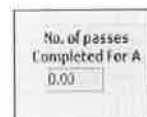
This Axis Wait Time is used to set the time delay of the linear motion of the actuators before incrementing the following signal from the counting function due to a required number of passes completed by the spray gun. This value is measured in milliseconds and has a default value of 1000 milliseconds (or 1 second). It is advisable to set the value to zero or lower than the time required for one pass by the spray gun in order to get an exact number of layers of coating in the final passes of spray gun.



The counter control is number of passes before next increment of actuator occurs. The value of this counter control is used to control the timing of the linear movement of the actuator compare to the spray gun movement (number of passes). The linear motion of the actuator occurs; once the pass counter reaches the number of passes entered. The default value of this counter is 5.



This display allows a pause before the limit switch initiates increment of the next program, so as to give the gun time to move off the limit switch back to its initial starting pass position. The default value is 140 milliseconds.



This output indicator shows the number of passes that have been completed by the spray gun. This increases from zero to the value entered in the counter control (Max. count). Once complete the actuator becomes zero again and runs through the next loop until the coating has been deposited.

(ii) Linear Motor Control-XWare

The procedure used to open the XWare program from the DCU HVOF facility computer is as follows:

- From the Task bar click the **Start button** → **Programs** → **XWare**
- Once the XWare program has opened, from Menu bar select **File** → **Open**
- Select the file named '**Automation.prg**' from the selection window.

When the file is opened the text editor panel will be appear on the computer monitor as shown in Figure 4.20. It is important to place the courser at the very end of the command sequence, after that press the F4 button on the keyboard to execute the program.

4.4 DESIGN CALIBRATIONS AND TEST

The following section describes the qualification procedure used to assess the functionality of the Dual Powder Feed device. The hypothesis of this research was to control the flow of two different powders at a various ratios, to produce a desired coating composition as showed in Table 4.2. To achieve this objective a number of experimental tests were carried out on the current project design. This section describes the calibration test conducted on the final design to verify if this concept fulfilled the project objectives.

The powder flow bench tests were carried out to calibrate the powder flow for various vertical movements of the needle shape bolts (Figure 4.5) which were coupled with two linear actuators and controlled with Lab VIEW software via a PC.

Table 4.2: Hypothesis of the two different powder flows controlled by the vertical movement of the linear actuators 'A' & 'B'.

Vertical movement of linear actuators (mm)	Positions of needles are closed (0) or open (4).		Desired composition of FGM coating of different powder (%)	
	Needle 'A'	Needle 'B'	Chamber 'A' (Stainless Steel SS)	Chamber 'B' (Nickel base alloy)
	4	0	100	0
	3	1	75	25
	2	2	50	50
	1	3	25	75
	0	4	0	100
Assumption: travelling distance is 4 mm and time delay for each step is equivalent to eight passes of the spray gun across the front of the substrate.				

➤ Bench Tests of Powder Flow:

The bench tests were carried out to calibrate the movements of the bolts inside the powder holders, labelled as chambers 'A' and 'B'. These needle shaped bolts move upwards and downwards according to the users requirement inside the chamber (controlled by the Lab VIEW software). When the bolts are in a fully closed position or zero position, no powder flows. With the increase of the vertical movement, powder starts to flow from the chamber into the mixing zone (Figure 4.7).

Initially the dual feed powder holder was placed inside the powder hopper and then the needle shaped bolts were placed inside the both chambers. The stainless steel powder (Diamalloy 1003) was poured into the chamber 'A' and the hopper cover was attached. After that the linear actuators were coupled with the needle shaped bolts. Variation of vertical movement was carried out controlled by Lab VIEW to calibrate the flow of powder flowing through the hole at the bottom of the chamber. During this process, powder particles were collected into a pre-weighted container at each stage of vertical increment starting at the bottom of the powder flow tube. The mass of powder flow was measured over a 10 second time period (which means the needle shaped bolt was opened for 10 seconds at every stage of vertical increment) and the weight of the powder collected was calculated subtracting the weight of the container from the total weight of both container and powder. For each step vertical increment three readings were taken.

Next the nickel base alloy Diamalloy 1005 and Diamalloy 2001 were poured separately into the chamber 'B' and the above procedure was repeated. To verify the results, chamber 'B' was filled also with stainless steel (Diamalloy 1003) and chamber 'A' was filled with nickel base alloy Diamalloy 1005 and Diamalloy 2001, to justify if there was any difference between the two chambers results. Results of the above calibration testes are discussed in Chapter six.

Another test was carried out to check the mixing ability of the re-designed mixing zone. In order to characterise this, two powders, Stainless steel (Diamalloy 1003 is light in colour compared to nickel base alloy Diamalloy 2001) and nickel base alloy Diamalloy 2001 powders were poured into chamber 'A' and 'B' respectively. During this test the feed unit system and the nitrogen gas flow were operated under running

condition. A container was placed to collect the resulting powder mixture from the tube connected to the pick up shaft. Visual inspection was carried out to confirm that the light coloured and dark coloured powder particles were mixed properly or not.

To measure the density/flowability of the three different powders one pre-measured container was used. Two volumes were used (50 ml and 100 ml) and filled with Diamalloy 1003, Diamalloy 1005 and Diamalloy 2001 separately and measured with scales to determine the weight of the powder separately. Using Equation 4.3 the densities of each powder was measured. Result of this test is detailed in Chapter 6. The summary of this test method is a weighted mass (50.0 gm) of metal powder is timed as it flows through the calibrated orifice of a funnel. Details of the procedure are presented in Appendix E.

CHAPTER 5

MODELLING

5.1 INTRODUCTION

In order to check the effectiveness of the design of section A-B and B-C in Figure 4.7; a finite element analysis was carried out before manufacturing these components using the FLOTRAN CFD ANSYS software. This chapter includes description of the different stages that were involved during the modelling procedure.

The current research includes the modelling for the following reasons:

- The design developed by the previous researcher Hasan [49] was found to produce inadequate flow of powders within this proposed design. So, to continue from the previous research it was necessary to create an enhanced design, which would allow the powder materials to flow, and mix to provide a functionally graded coating.
- At this stage it was decided to modify the previous design using CFD FLOTRAN to predict better flow rates and better mixing ability.
- The model dimensions were constrained to those of the internal dimensions of the hopper chamber.

A detailed information about the powder flow modelling is described in the following sections.

5.2 THE F.E.A PROCESS

A brief introduction into ANSYS FEA will be described; however as this research is more focused on the design of a dual powder feeder, less emphasis will be made on the FEA research. The procedure of finite element modelling is generally separated into the following three stages:

- Pre-processing
- Solution phase
- Post-processing

Each of these is discussed with specific reference to CFD FLOTRAN modelling in the ANSYS FLOTRAN program.

5.2.1 Pre-processing

Pre-processing involves the total preparation (CAD drawing, boundary conditions) of the model for the next step of solving which includes the sub stages of:

➤ Discretisation

This is the primary step in any FEA analysis to produce the geometry of model, constructed in the ANSYS program. Figure 5.1 shows the geometry of the powder flow and mixing component (Simplified version of Figure 4.6). Meshing is vital placing emphasis on the regions where it is thought that a huge change in velocity or pressure; resulting in high solution gradients. The most important area is the mixing zone due to its high gradients of change, thus it requires a greater mesh density in order to achieve a better solution.

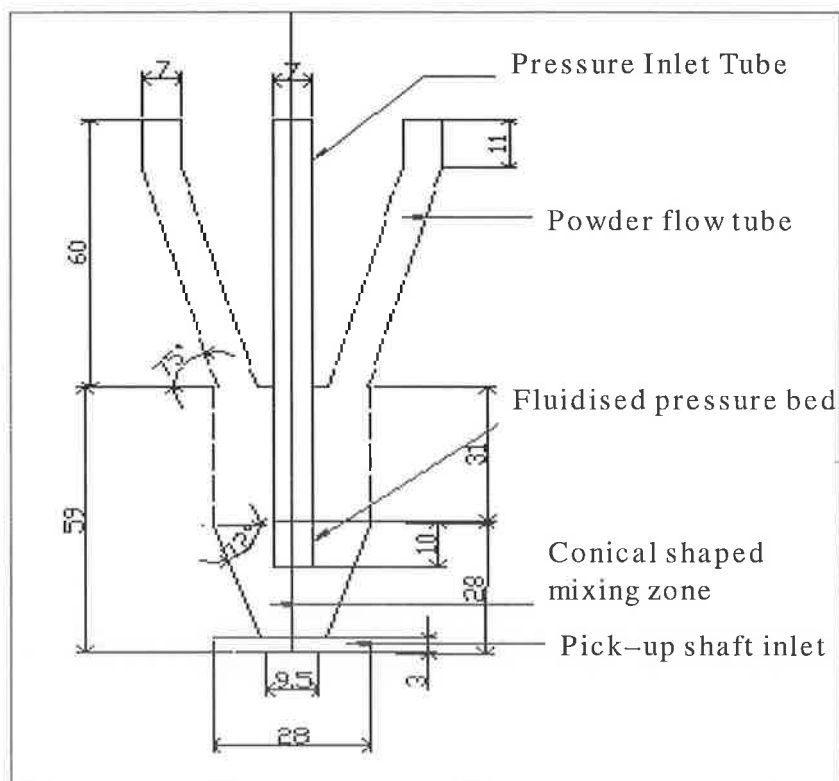


Figure 5.1: Schematic of the geometry of the powder flow and mixing component.

➤ **Element Formulation**

Element formulation is concerned with assigning a shape function to the various elements to represent the physical behaviour of the element/application. There are two Flotran types element available in ANSYS; FLUID 141 for two-dimensional flow and another one is FLUID 142 for three-dimensional flow. FLUID 141 can be used to model transient or steady state fluid/thermal systems which entail fluid and/or non-fluid regions, allowing solutions for flow and temperature distributions within a region, making it the best selection for this condition. Hence the current model assumed a single-phase fluid during the simulation (air and particle represented by a mixed gas, as the program could not cater for multi-phase systems), therefore the FLUID 141 element was selected.

The conservation equations for viscous fluid flow and energy are solved in the fluid region and the energy equation solved in the non-fluid region. The velocities were obtained from the conservation of momentum principle and the pressure obtained from the conservation of the mass principle. Details of these governing equations have been reported by Ansys help [202], hence will not be discussed in this report.

➤ **Application of loads and boundary conditions**

In the current research, two types of boundary conditions were employed. These were velocity and pressure. Figure 5.2 shows all the applied boundary conditions applied to the model, where the velocities of the stainless steel and nickel base alloy powder velocities were applied as an inlet velocity to the top of the model. Nitrogen gas velocity was applied to the top of the pressure tube inlet and pick-up shaft inlet as per the Hopper equipment details. Zero velocity was applied to the walls of the model (based on boundary layer analysis) {1-18} boundaries and zero pressure applied on outlet of the pick-up shaft (to allow the mixed flow to flow “out” of the model).

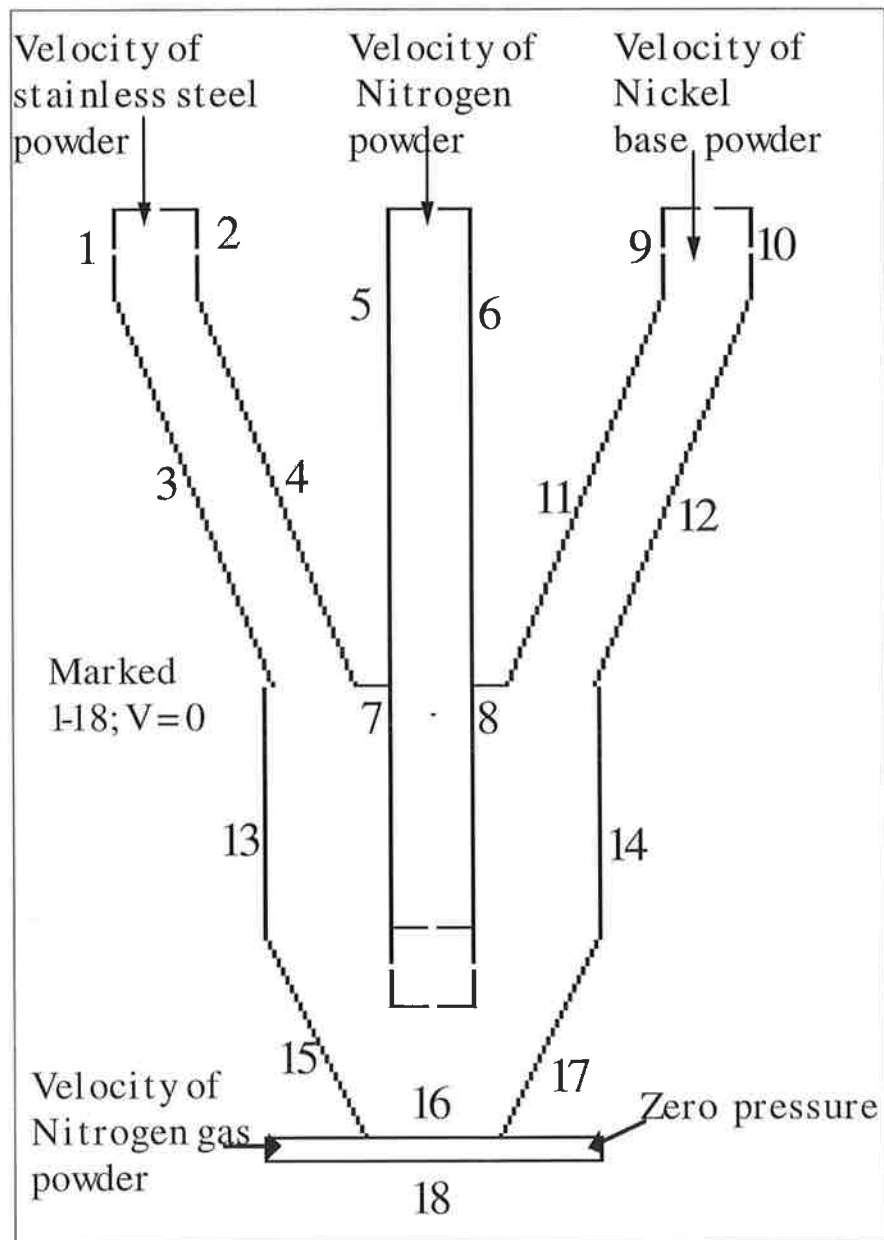


Figure 5.2: Schematic diagram of the applied boundary condition.

5.2.2 Solution Phase

The solution phase converges and solves the model. In order to get an accurate solution the following factors must be properly adjusted and controlled:

➤ **Fluid properties:**

The Fluid properties were entered in order to classify whether the fluid being used was a gas or liquid and then the user must enter a pre-determine density and viscosity. These material properties were necessary to create the velocity profiles along with the resultant flow patterns.

The Density and viscosity of nitrogen gas, stainless steel and nickel base alloy were taken as follows:

Density:

Nitrogen gas-0.00125 g/cm³ [203]

Stainless steel powder-8.03 g/cm³ [193]

Nickel base alloy powder-8.602g/cm³ [193]

Viscosity

Nitrogen gas-0.000173 g/cm.s [203]

Stainless steel powder- 0.000173 g/cm.s [203] (Assumed to be the same as that of Nitrogen/Air)

Nickel base alloy powder-0.000173 g/cm.s [203] (Assumed to be the same as that of Nitrogen/Air)

➤ **Selection of solver**

There are three types of solver available for Fluid 141. These are as follows:

1. Tri-Diagonal Matrix Algorithm (TDMA) is a Fast Approximate Solver used in ANSYS. This is not recommended for pressure Degree of Freedom (DOF) models.
2. Conjugate Residual Exact solver is best in solving both the velocity and pressure DOF models.
3. Sparse Direct solver, which is not suitable for velocity DOF models.

However as both velocity and pressure DOF was necessary for the current research modelling, the Conjugate Residual Exact solver was selected to simulate the powder flow mode.

➤ Analysis Selection Type

To simulate the current research mode, the multiple species transport analysis was chosen which enables the tracking of several different fluids simultaneously. There are three types of multiple species transport analysis available in the ANSYS program; namely the dilute mixture analysis, composite gas analysis and composite mixture analysis. The composite mixture analysis calculates the properties used in the solution from a linear combination of the species, weighted by mass fractions as a function of space. The solution of the momentum equation depends on the species distribution, so the momentum and transport equation are strongly coupled [202]. Hence this type of analysis was chosen to simulate the current modelling of nitrogen gas-powder flow.

5.2.3 Post –Processing

Once a solution to the model has been found, post-processing means reviewing the results of an analysis. This step is most important during a simulation, because it involves trying to understand the effect of the applied load on the model and quality of the mesh generated. This step produces a predicted (theoretical) result of the entire simulation process. Using the post processor menu, velocity and pressure results and graphs of these modelling results can be obtained, which will be analysed in the next chapter.

5.3 Summary

The model was conducted prior to the manufacturer of the proposed device to predict adequate flow and mixing in order to produce functionally graded coatings by varying the dimension of the proposed design. Therefore the next chapter will discuss these results first.

CHAPTER 6

RESULTS AND DISCUSSION

6.1 INTRODUCTION

The present study investigates an innovative modification of a HVOF thermal spray process to produce functionally graded thick coatings. In order to deposit thick coatings, certain problems have to be overcome. More specifically these problems include minimizing residual stresses, which cause shape distortion in as-sprayed components. Graded coatings enable gradual variation of the coating composition and/or microstructure, which offers the possibility of reducing residual stress build-up in coatings [90].

In order to spray such a coating, modification to a commercial powder feed hopper (DJF) was required to enable it to deposit two powders simultaneously which allows the deposition of different layers of coating with varying chemical compositions, without interrupting the spraying process. Various concepts for this modification were identified and one design was selected as described in Chapter four. This design was validated through the use of Finite Element Analysis, in order to arrive at the final dimensional design.

This chapter is divided into a series of sections and will discuss the results found for both the Modelling and Experimental Validation, described under the following headings:

- Description of ANSYS simulation
- Results of the Bench Test for the newly designed and developed Automated Graded Powder Feed Unit System
- Experimental sprayed functionally graded coatings results

6.2 SIMULATION RESULTS

This ANSYS simulation was carried out mainly to verify the following two questions:

- Whether the design parts would be able to transfer the powders into the mixing zone (inside the component) where they are supposed to mix.
- Whether the mixed powder particles would then be carried out by the nitrogen gas flow inside the pick up shaft towards the spray gun.

During the FEA simulation approach different nitrogen gas pressure ratios (ratio between the top of the pressure inlet tube and the pick up shaft) were applied and an approximate nitrogen gas pressure ratio was determined to cause powder mixing and to force the mixed powder into the carrier gas flow (nitrogen gas) inside the pick up shaft. Table 6.1 shows the different pressure ratios used for three different input velocities of nitrogen gas.

Table 6.1: Pressure ratio for different velocity input of nitrogen gas

Velocity of nitrogen gas		Nitrogen gas pressure		Nitrogen gas pressure ratio applied to the inlet pressure tube and pick up shaft (obtain from pressure plot from the ANSYS results)
Inlet pressure tube (m/s)	Pick up shaft (m/s)	Inlet pressure tube (MPa)	Pick up shaft (MPa)	
3470	2965	5.54	5.54	1.00 : 1.00
4470	2965	7.25	3.22	2.25 : 1.00
4722	2965	7.50	4.17	1.80 : 1.00

The velocities of the stainless steel (Diamalloy 1003) and nickel base powders (Diamalloy 1005 and Diamalloy 2005) were calculated by carrying out some experimental flow tests in each designed chamber and using equation 6.1.

$$\text{Average Velocity} = \frac{\Delta \text{ position}}{\text{time}} = \frac{\text{displacement}}{\text{time}} \quad \text{Equation 6.1}$$

From this test it was observed that (for each type of powder particle) it took each powder 2 seconds to fall a distance of is 130 cm. Hence the average velocity of each type of powder particle flow is 65 cm/s. This value was inputted as model velocities for the stainless steel and nickel base alloys (see Figure 5.2). Figure 6.1 shows the two types of meshing techniques were used in each model (homogeneous mesh and fine mesh).

Three different models were applied at three different nitrogen pressure ratios (1:1, 2.25:1 and 1.8:1 respectively) and the best result was found at a 2.25:1 pressure ratio. This pressure ratio was calculated from the pressure plot of ANSYS results and is shown above in Table 6.1.

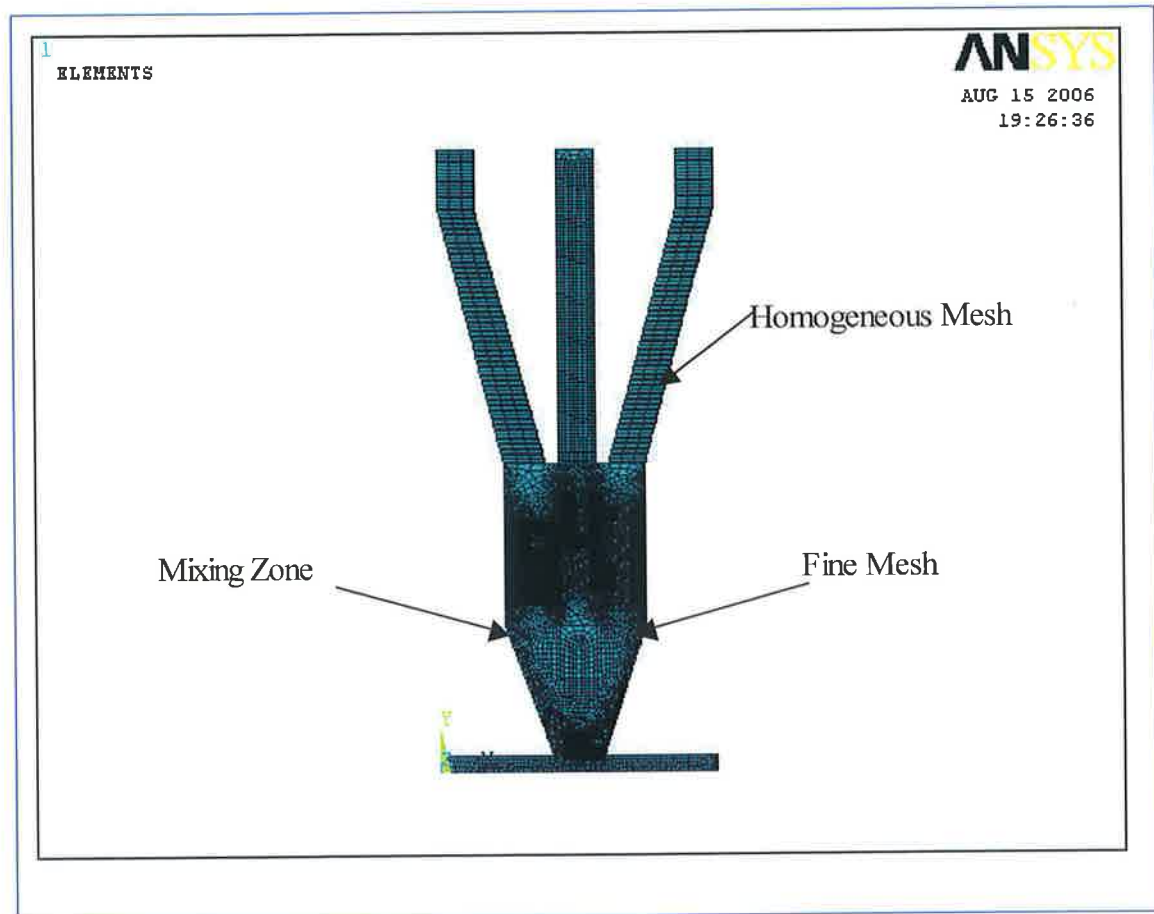


Figure 6.1: Dual powder feed unit with fine mesh in the mixing zone and homogeneous mesh in rest of the modelling.

6.2.1 Results

To meet the requirements of the current project objective it was necessary to compare the velocity, pressure plot and particle flow trace found in each of the ANSYS models. Table 6.2 shows the difference of velocity plot and pressure plot between three different models (obtained from ANSYS results). Table 6.3 shows the difference of particle flow plot between three different models (obtained from ANSYS results).

Table 6.2: Difference of velocity plot and pressure plot between three different models.

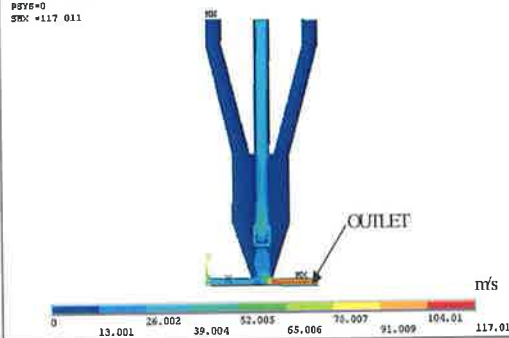
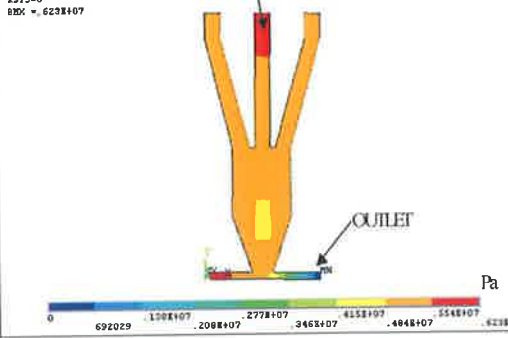
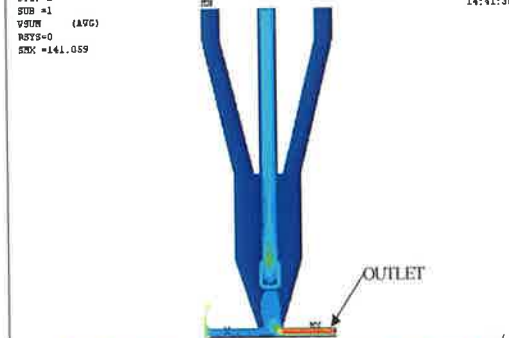
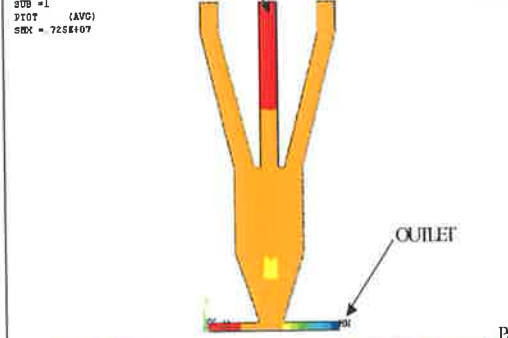
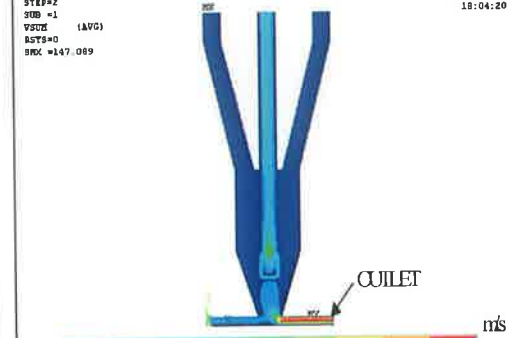
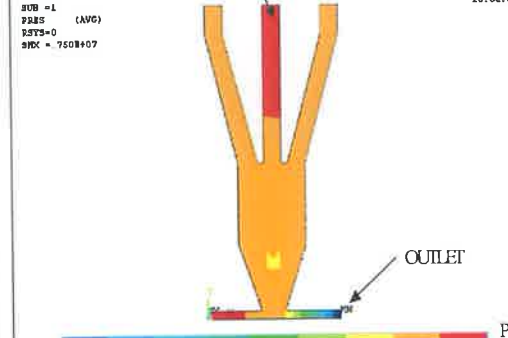
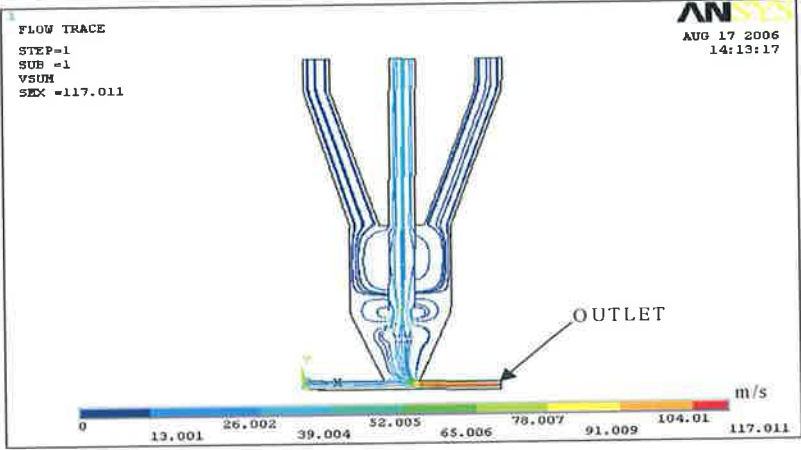
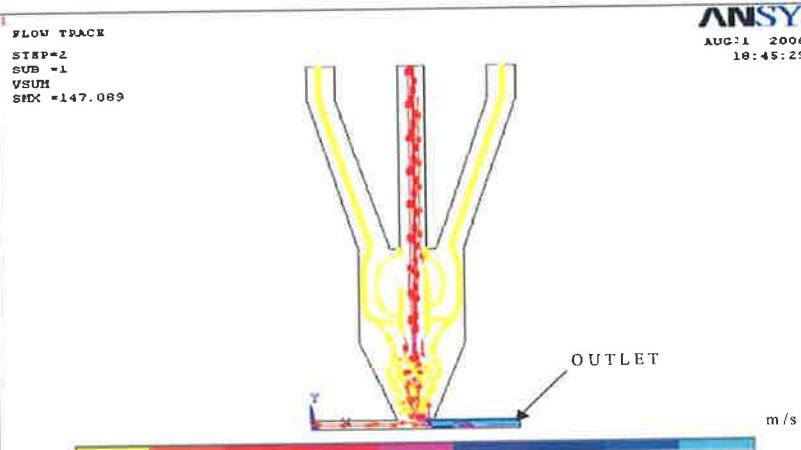
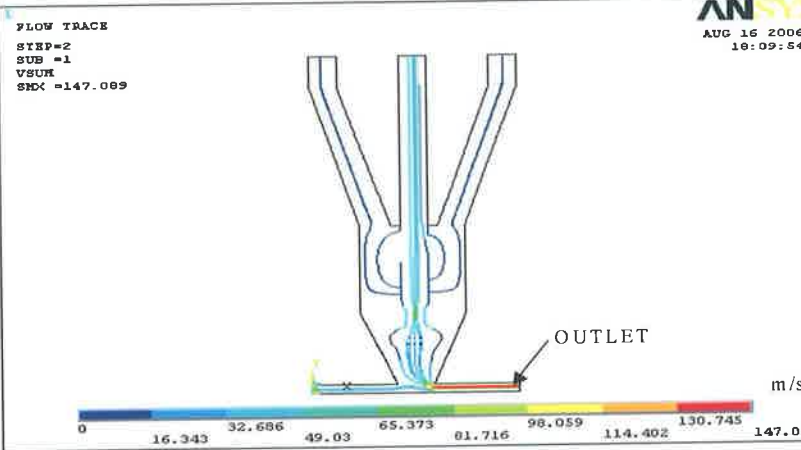
Nitrogen gas pressure ratio	Velocity Plot	Pressure Plot
1.00 : 1.00	<p>ANSYS</p> <p>MODAL SOLUTION STEP=1 SUB =1 VSUM (AVG) RSTY=0 SMX =117.011</p> <p>AUG 17 2006 13:44:39</p>  <p>0 13.001 26.002 39.004 52.005 65.006 78.007 91.009 104.01 117.011 m/s</p>	<p>ANSYS</p> <p>MODAL SOLUTION STEP=1 SUB =1 PRES (AVG) RSTY=0 SMX = 623E+07</p> <p>AUG 17 2006 13:44:05</p> <p>Inlet pressure Tube</p>  <p>0 692029 150E+07 277E+07 346E+07 415E+07 554E+07 623E+07 Pa</p>
2.25 : 1.00	<p>ANSYS</p> <p>MODAL SOLUTION STEP=1 SUB =1 VSUM (AVG) RSTY=0 SMX =141.059</p> <p>AUG 21 2006 14:41:39</p>  <p>0 15.673 31.346 47.02 62.693 78.366 94.039 109.712 125.385 141.059 m/s</p>	<p>ANSYS</p> <p>MODAL SOLUTION STEP=1 SUB =1 PRES (AVG) RSTY=0 SMX = 725E+07</p> <p>AUG 21 2006 14:42:09</p> <p>Inlet Pressure Tube</p>  <p>0 803E15 161E+07 242E+07 322E+07 403E+07 483E+07 564E+07 725E+07 Pa</p>
1.80 : 1.00	<p>ANSYS</p> <p>MODAL SOLUTION STEP=2 SUB =1 VSUM (AVG) RSTY=0 SMX =147.089</p> <p>AUG 16 2006 18:04:20</p>  <p>0 16.345 32.689 49.03 65.373 81.716 98.059 114.402 147.089 m/s</p>	<p>ANSYS</p> <p>MODAL SOLUTION STEP=2 SUB =1 PRES (AVG) RSTY=0 SMX = 750E+07</p> <p>AUG 16 2006 18:04:51</p> <p>Inlet Pressure Tube</p>  <p>0 833606 167E+07 230E+07 333E+07 417E+07 500E+07 584E+07 750E+07 Pa</p>

Table 6.3: Difference of particle flow plot between three different models.

Nitrogen gas pressure ratio	Particle flow plot
1.00 : 1.00	 <p>Flow Trace STEP=1 SUB =1 VSUM SDX =117.011</p> <p>ANSYS AUG 17 2006 14:13:17</p> <p>OUTLET</p> <p>0 13.001 26.002 39.004 52.005 65.006 78.007 91.009 104.01 117.011 m/s</p>
2.25 : 1.00	 <p>Flow Trace STEP=2 SUB =1 VSUM SDX =147.089</p> <p>ANSYS AUG 11 2006 18:45:29</p> <p>OUTLET</p> <p>0 16.343 32.686 49.03 65.373 81.716 98.059 114.402 130.745 147.089 m/s</p>
1.80 : 1.00	 <p>Flow Trace STEP=2 SUB =1 VSUM SDX =147.089</p> <p>ANSYS AUG 16 2006 18:09:54</p> <p>OUTLET</p> <p>0 16.343 32.686 49.03 65.373 81.716 98.059 114.402 130.745 147.089 m/s</p>

From Table 6.2 and Table 6.3 it is clear that when the nitrogen gas pressure ratio on the inlet pressure tube to pick up shaft was 2.25:1 (as mentioned in Table 6.1) the best simulation result was obtained compared to other two different combinations (detailed in Appendix C) due to the attainment of the highest particle velocity at the outlet (although the velocity and pressure plots were almost the same at 2.25:1 and 1.8:1 pressure ratios, flow trace plot reveals better mixing results at the 2.25:1 pressure ratio). Figure 6.2 shows the vector plot results for 2.25:1 ratio and it shows the path of the powder particles where a maximum velocity ranges from 109 to 141 m/s was attained at the outlet. The velocity range of the powder flow at mixing zone is given to be between 0 and 15 m/s.

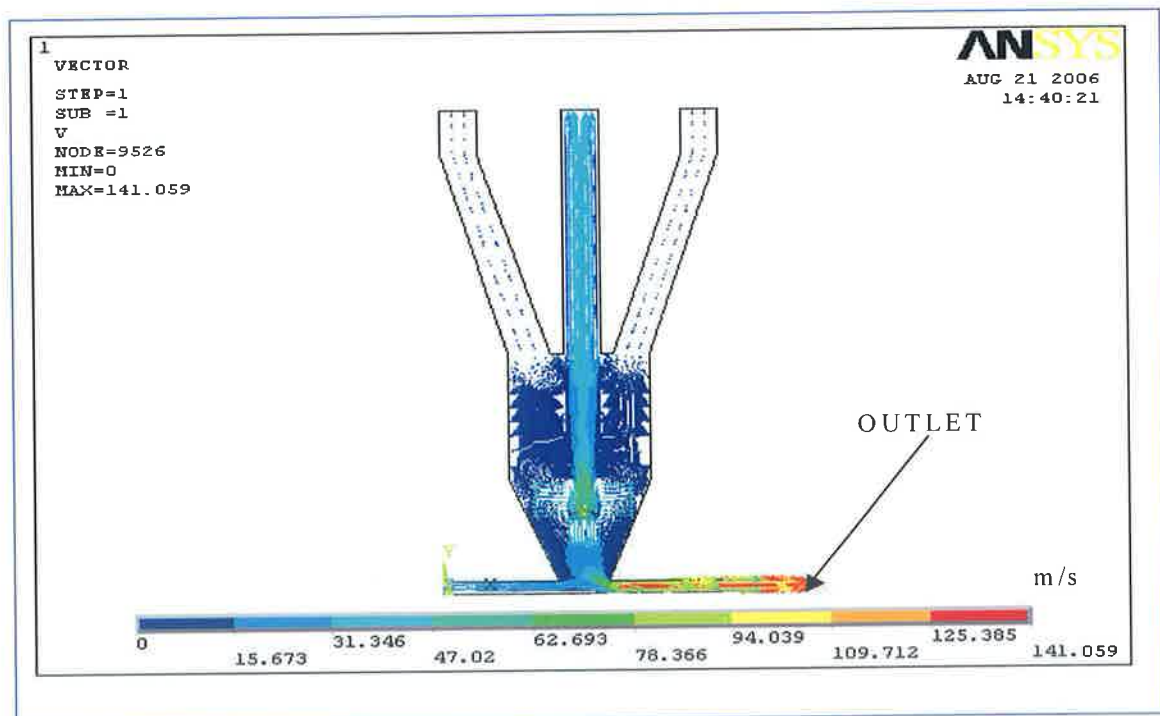


Figure 6.2: Vector plot showing the path of the velocity particles.

Figure 6.3 represents the pressure plot for 2.25:1 pressure ratio of the nitrogen gas in Pascals. Maximum pressure occurs at the inlet of nitrogen gas on pick up shaft and the inlet pressure tube (6.44 to 7.25 Mega Pascal), thus the low pressure around the mixing zone and the inlet to the pick up shaft aids mixing and transfer to the HVOF gun

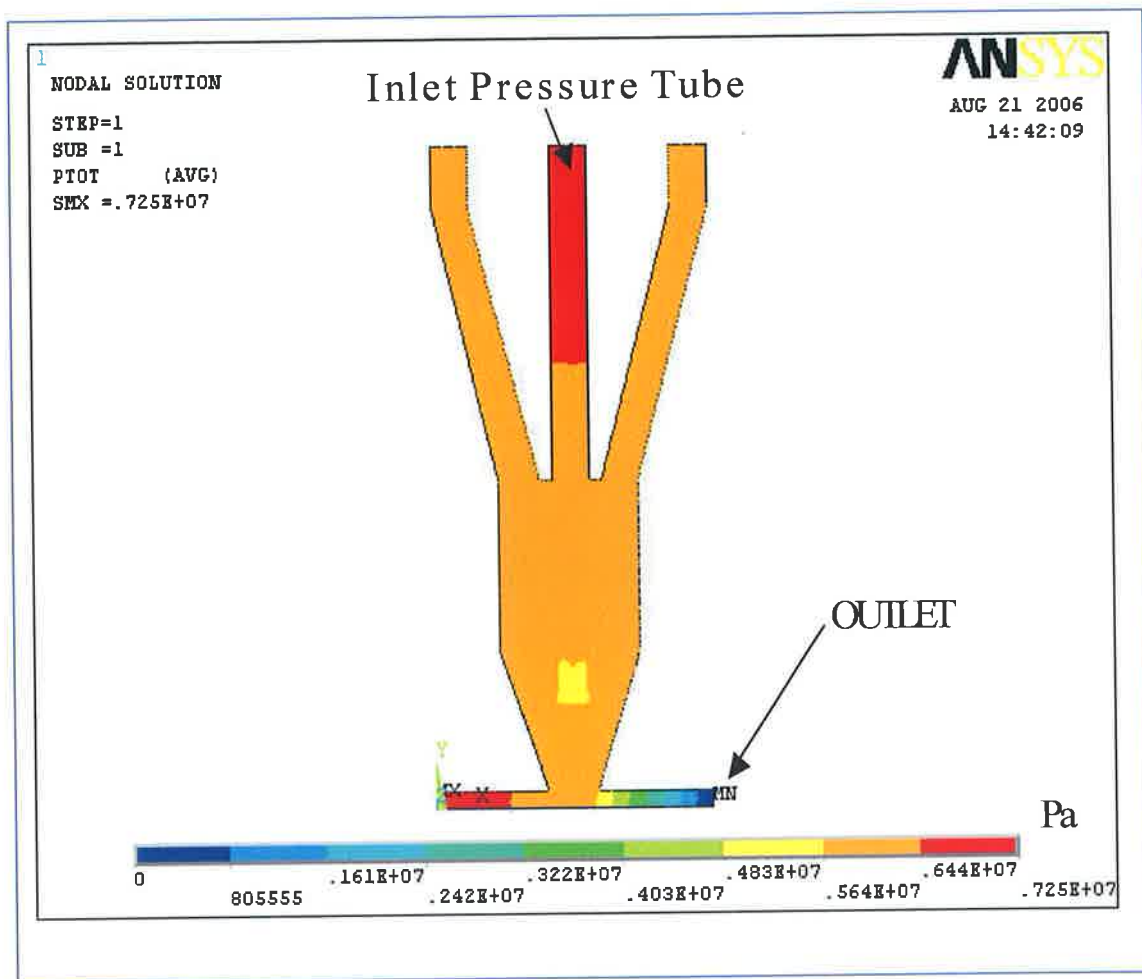


Figure 6.3: Pressure plot from nodal solution.

Figure 6.4 shows the velocity plot of the modelling from the nodal solution where the maximum velocity was found at the outlet and ranged from 109 to 141 m/s, and a minimum velocity range found at the inlet of the powder particle 0 to 15 m/s. Figure 6.5 shows the graphical presentation of the velocity at outlet in both the x (velocity V_x) and y (V_y) directions. It can be seen that the central nitrogen line (with its filter attached to its end) purges the powders into the pick up shaft, forcing all of the powder in the x direction (V_x plot Figure 6.5) skewed slightly towards the top of this outlet pipe.

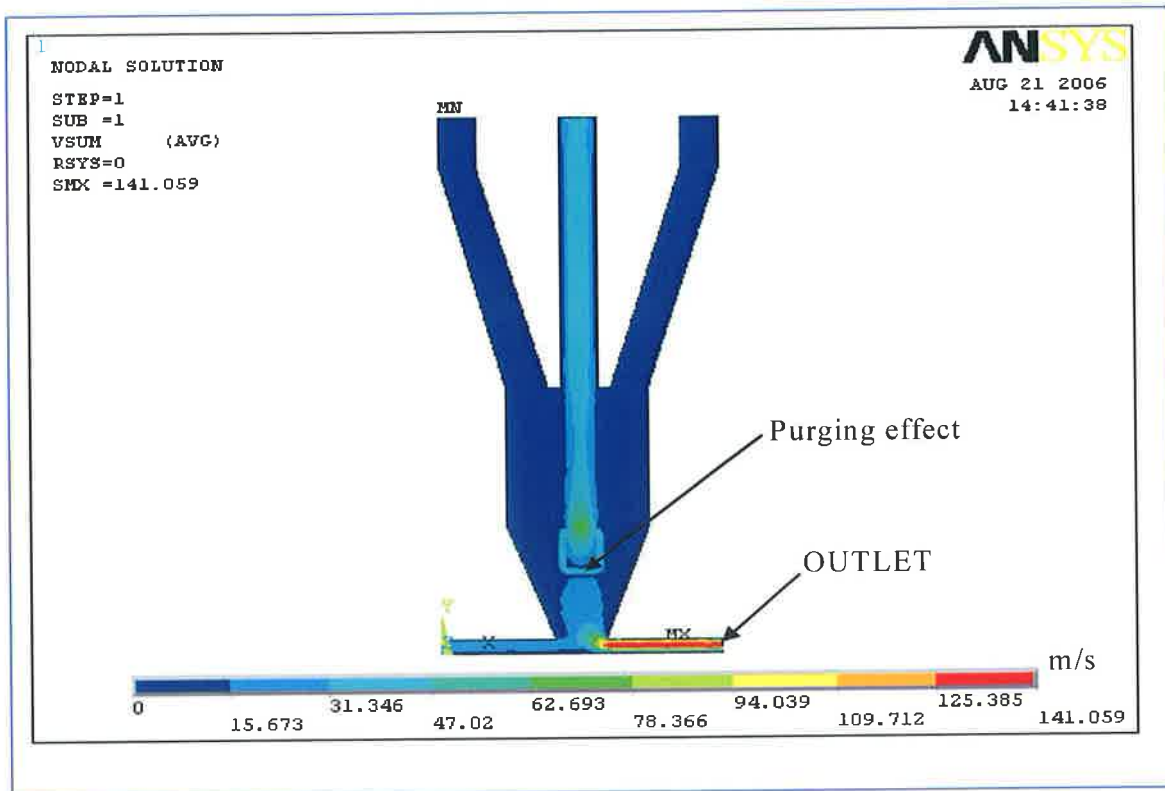


Figure 6.4: Velocity plot of the model from the nodal solution at a 2.25:1 pressure ratio.

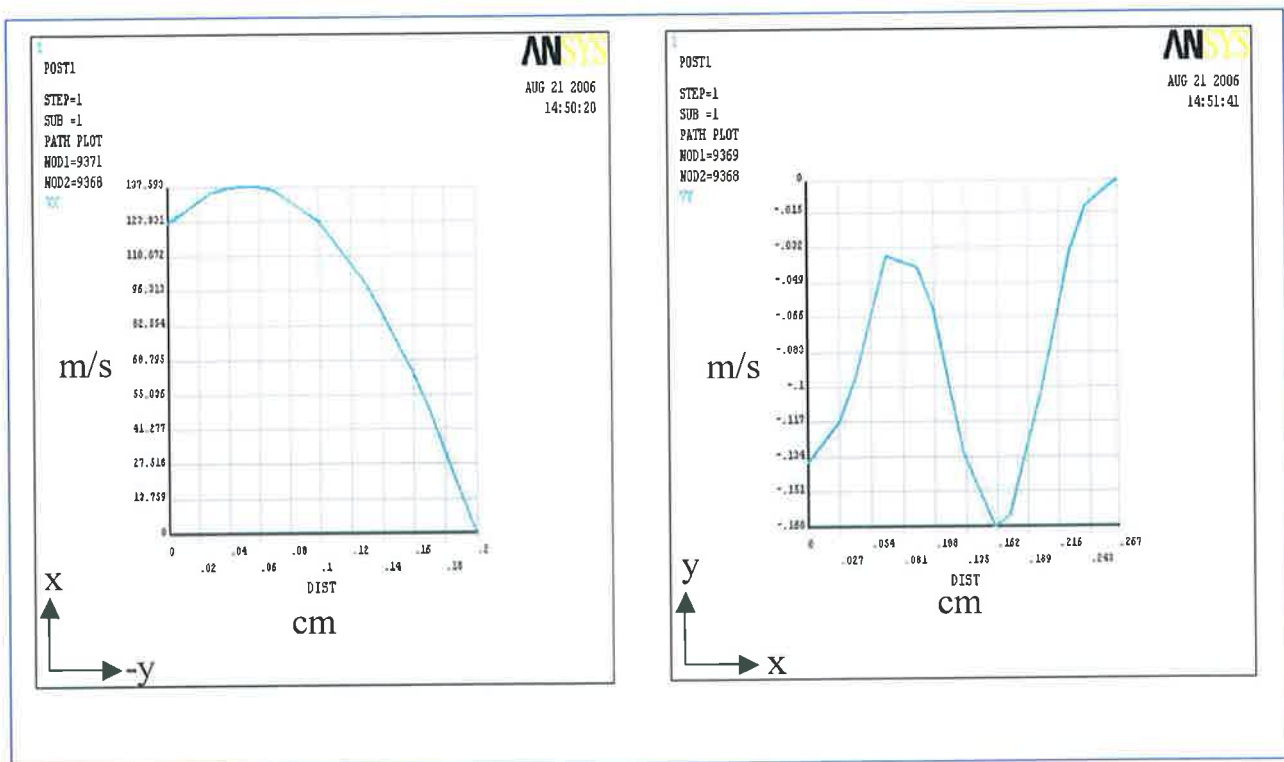


Figure 6.5: Velocity profile at outlet at 2.25:1 pressure ratio (left VX and right VY).

Figure 6.6 is the combine graphical representation of the velocities in both the x and y directions (VSUM) at the outlet position when the pressure ratio is 2.25:1, which depicts an almost uniform flow region.

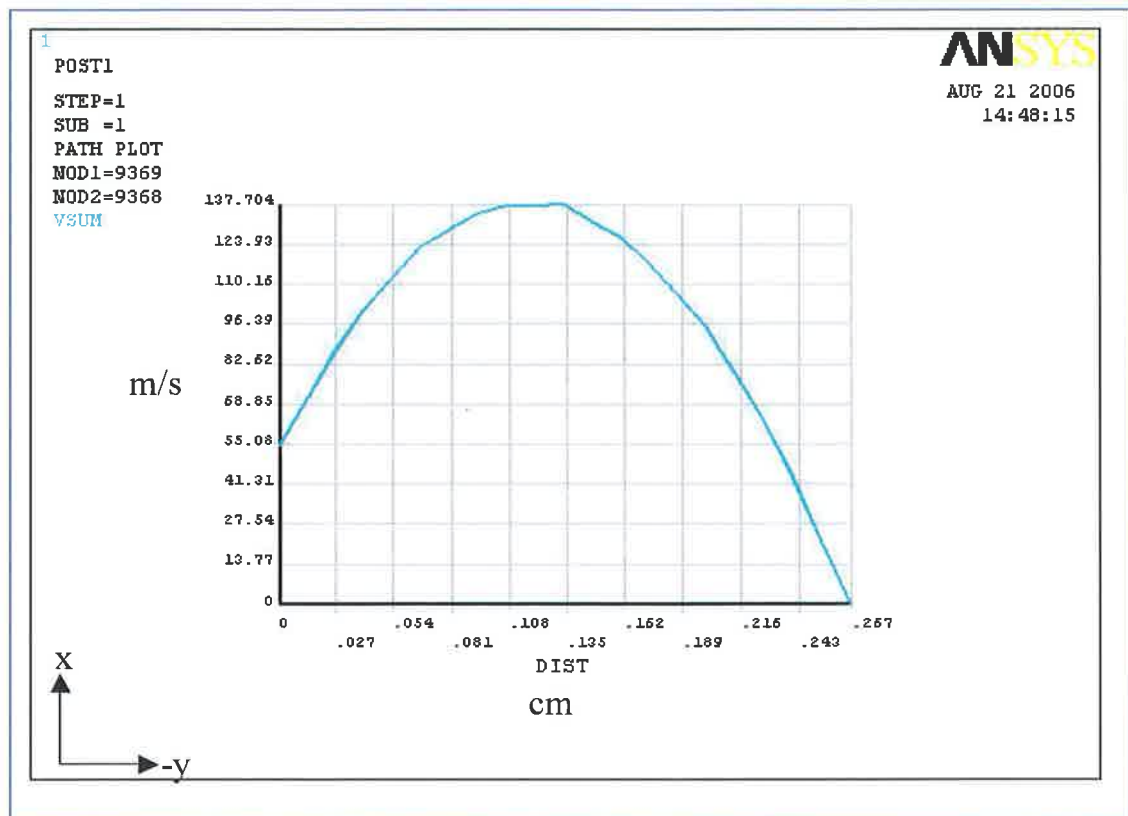


Figure 6.6: VSUM at the outlet when the pressure ratio is 2.25:1.

Figure 6.7 shows the Flow trace of nitrogen gas and powders for a pressure ratio of 2.25:1 where the maximum velocity found at the outlet ranged from 130 to 147 m/s and this analysis shows that the powder particles are able to mix with each other in side the mixing zone at a velocity range of 0 to 16 m/s.

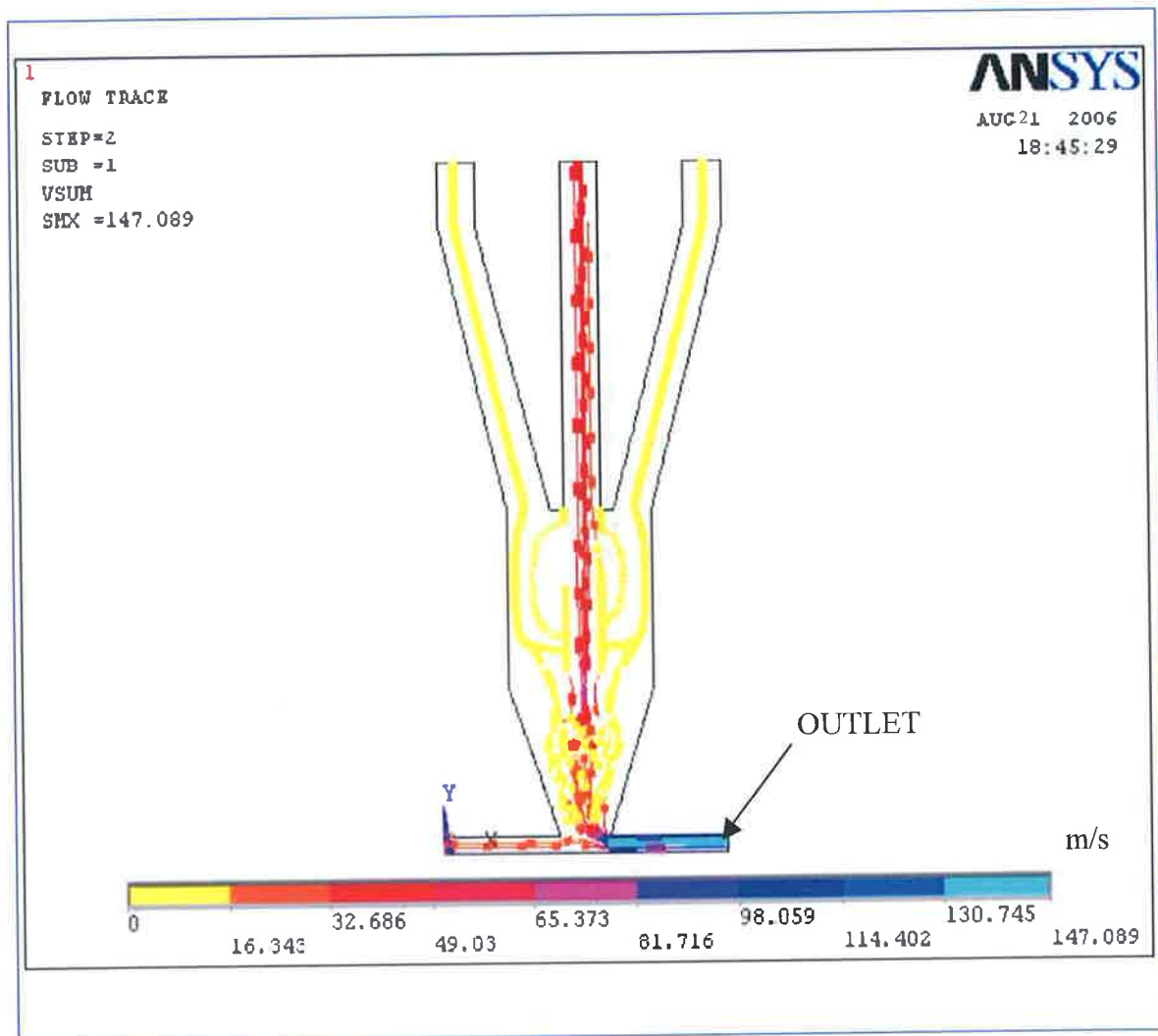


Figure 6.7: Particle flow lines for the nitrogen gas and powders for a pressure ratio of 2.25:1.

Figure 6.8 shows the particle flow lines for the nitrogen gas and powders for a pressure ratio of 10:1 and powder ratio of 1:3, which was obtained as the best simulation result by the previous researcher Hasan [49]. This ANSYS results show that the velocity range of this researchers [49] outlet from 0 to 10.49 m/s where this current study simulation best result, shows the outlet velocity range from 130.745 to 147.089 m/s with lower pressure ratio required. This means the current design is much more efficient than the previous concept described by Hasan [49], hence was expected to produce more accurate mixing of the functionally graded powders.

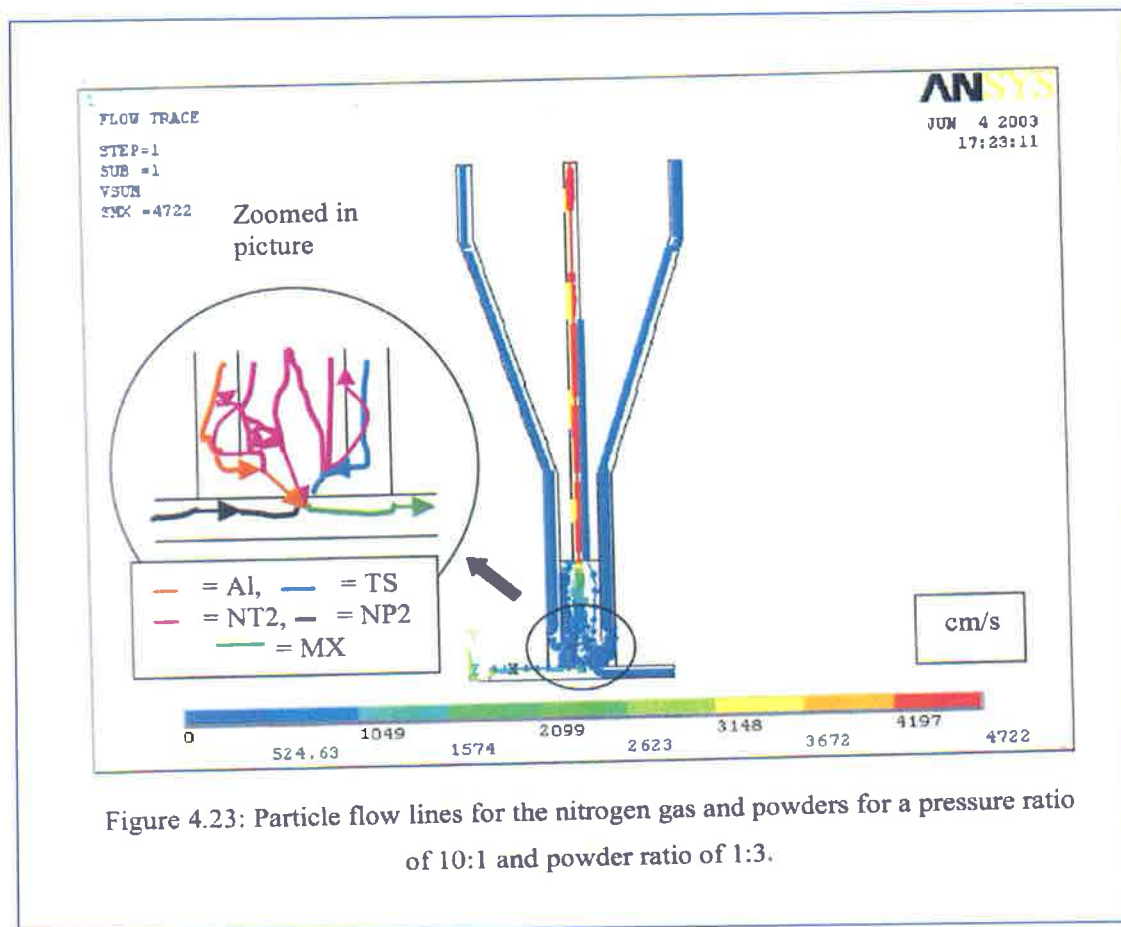


Figure 6.8: Particle flow lines for the nitrogen gas and powders for a pressure ratio of 10:1 [49].

6.2.2 Conclusion of the ANSYS Simulation Results

The simulation results show that the design is able to satisfy the main objectives required by the design part in the current research. This design was able to mix the two different powders in the mixing zone and force this mixture into the pick up shaft where the powder mixture is carried to the thermal spray HVOF gun. Thus the dimensions and gas pressures were used in the experimental work that followed.

6.3 BENCH TEST RESULTS ON THE NEWLY DESIGNED AND DEVELOPED AUTOMATED POWDER FEED UNIT SYSTEM

Based on the FEA results a Dual Feed device was manufactured and tested. At this stage of the present research it was necessary to determine, at what turning increment of each of the needle shape bolts causes 100% of powder flow for each powder type (Diamalloy 1003, Diamalloy 1005 and Diamalloy 2001). To determine this a bench test was carried out on the new Dual Feed design. The three different powder types were poured into chamber 'A' separately and gradually the needle shaped bolts were vertically incremented (via rotation of the stepper motor) to 5 mm using the Lab VIEW software programming. The details of the bench test are shown in Table 6.4, 6.5 and 6.6 for Diamalloy; 1003, 1005 and 2001 respectively. This procedure was repeated using Chamber 'B' to determine if any difference between Chamber 'A' and chamber 'B' was found. These results are shown in Appendix D.

Table 6.4 shows the weight measured at different stage of gradual vertical increment of the needle shaped bolt when Chamber 'A' was filled with stainless steel (Diamalloy 1003) and Chamber 'B' was empty.

Table 6.4: Weight of stainless steel (Diamalloy 1003) from chamber 'A' for various increments of its associated Needle.

Experiment Number	Vertical Increment of the Needle (mm)	Weight of the container (gm)	Total weight (Container + Powder) (gm)	Powder weight (gm)	Average weight (gm)
A1	1.00	8.41	10.47	2.06	2.08
A2			11.01	2.60	
A3			9.98	1.57	
A4	2.00	8.41	20.62	12.21	10.70
A5			17.98	9.57	
A6			18.73	10.32	
A7	2.50	8.41	26.98	18.57	18.98
A8			25.57	17.16	
A9			29.61	21.20	
A10	3.00	8.41	35.37	26.96	25.49
A11			32.92	24.51	
A12			33.41	25.00	
A13	4.00	8.41	90.05	81.64	80.78
A14			88.52	80.11	
A15			89.01	80.60	
A16	4.50	8.41	90.37	81.96	82.22
A17			91.52	83.11	
A18			90.01	81.60	
A19	5.00	8.41	91.81	83.34	83.03
A20			90.51	82.10	
A21			92.01	83.60	

Figure 6.9 shows a graphical representation of the data obtained from the Table 6.4 for Diamalloy 1003. The marked points from 4 mm to 5 mm vertical increment of the needle shaped bolt, shows a constant powder particle flow. Hence, a 4 mm vertical increment of needle shaped bolt was required to give 100% powder flow rate of Diamalloy 1003.

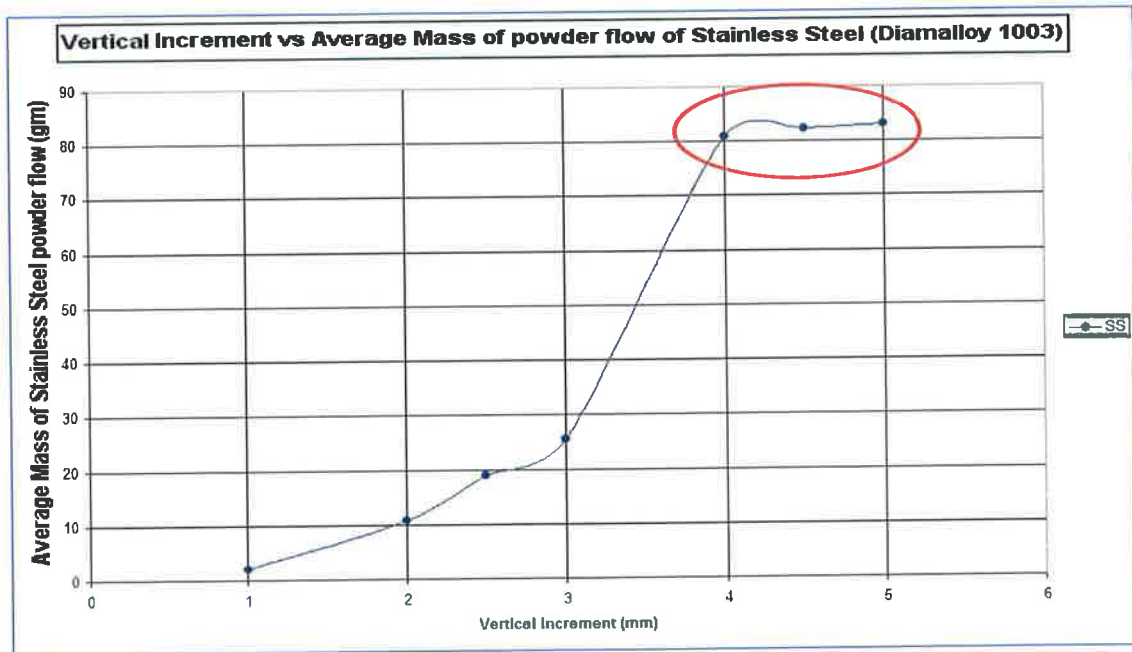


Figure 6.9: Average mass of stainless steel (Diamalloy 1003) powder flow with vertical increment of the needle shaped bolt controlled via LabVIEW programming.

Table 6.5 shows the weight measured at different stage of gradual vertical increment of the needle shaped bolt when Chamber 'A' was filled with nickel base alloy¹ (Diamalloy 1005) and Chamber 'B' was empty.

Table 6.5: Weight of Nickel alloy¹ (Diamalloy 1005) from chamber 'A' for various increments of its associated Needle.

Number of Experiment	Vertical Increment of the Needle (mm)	Weight of the container (gm)	Total weight (Container + Powder) (gm)	Powder weight (gm)	Average weight (gm)
B1	1.00	8.41	10.39	1.98	1.59
B2			9.65	1.24	
B3			9.95	1.54	
B4	2.00	8.41	20.39	11.98	11.39
B5			19.98	11.57	
B6			19.02	10.61	
B7	2.50	8.41	26.95	18.54	18.83
B8			25.67	17.26	
B9			29.11	20.70	
B10	3.00	8.41	38.23	29.82	34.35
B11			44.01	35.60	
B12			46.05	37.64	
B13	4.00	8.41	92.49	84.08	80.61
B14			86.56	78.15	
B15			88.01	79.60	
B16	4.50	8.41	92.06	83.65	83.28
B17			92.18	83.77	
B18			90.83	82.42	
B19	5.00	8.41	91.48	83.07	83.24
B20			90.65	82.24	
B21			92.83	84.42	

* Nickel Alloy – Diamalloy 1005

Figure 6.10 shows the graphical representation of the data obtained from Table 6.5 for Diamalloy 1005. Similarly a 4 mm vertical increment of needle shaped bolt was required to provide 100% powder flow rate of Diamalloy 1005.

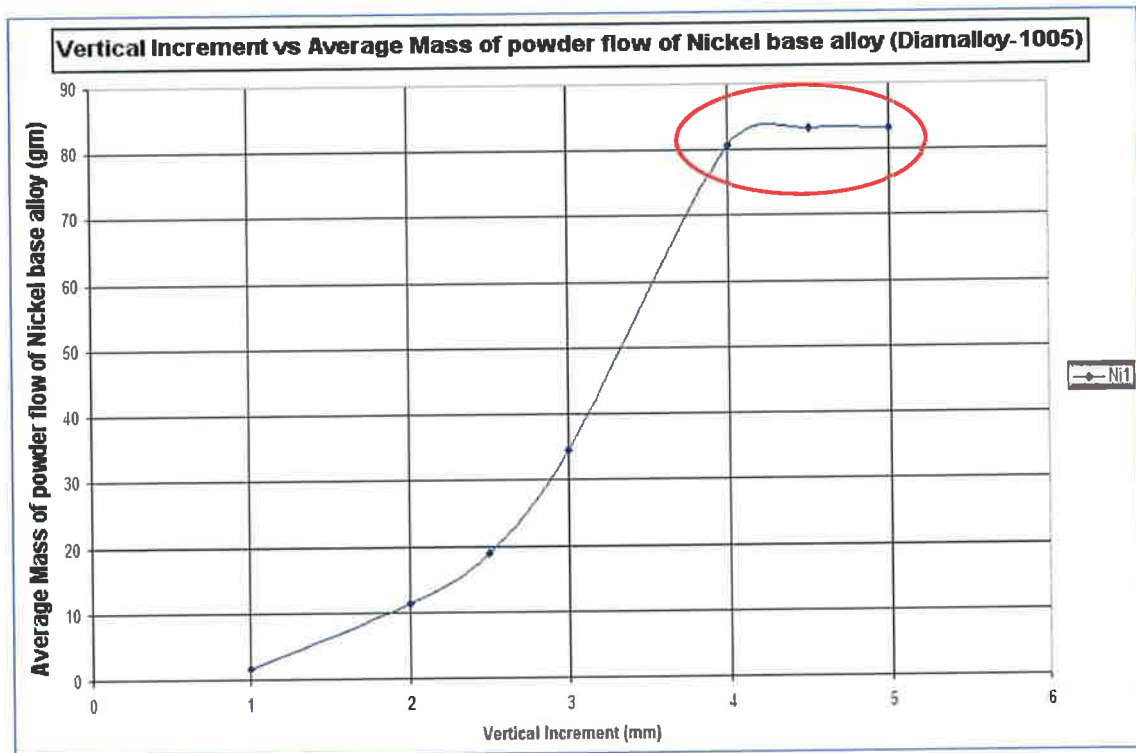


Figure 6.10: Average mass of nickel base alloy¹ (Diamalloy 1005) powder flow with vertical increment of the needle shaped bolt controlled via Lab VIEW programming.

Table 6.6 shows the weight measured at different stage of gradual vertical increment of the needle shaped bolt when Chamber 'A' was filled with nickel base alloy² (Diamalloy 2001) and Chamber 'B' was empty.

Table 6.6: Weight of Nickel alloy² (Diamalloy 2001) from chamber 'A' for various increments of its associated Needle.

Experiment Number	Vertical Increment of the Needle (mm)	Weight of the container (gm)	Total weight (Container + Powder) (gm)	Powder weight (gm)	Average weight (gm)
C1	1.00	8.41	15.35	6.94	9.66
C2			21.64	13.23	
C3			17.21	8.88	
C4	2.00	8.41	47.11	38.70	39.97
C5			50.03	41.62	
C6			48.01	39.60	
C7	2.50	8.41	59.78	51.37	51.74
C8			61.79	53.38	
C9			58.87	50.46	
C10	3.00	8.41	71.84	63.43	62.58
C11			71.23	62.82	
C12			69.89	61.48	
C13	4.00	8.41	102.90	94.49	93.75
C14			101.45	93.04	
C15			102.13	93.72	
C16	4.50	8.41	102.85	94.44	94.54
C17			103.03	94.62	
C18			102.96	94.55	
C19	5.00	8.41	105.03	96.62	95.85
C20			103.66	95.25	
C21			103.73	95.32	

* Nickel Alloy² – Diamalloy 2001

Figure 6.11 shows the graphical representation of the data obtained from the Table 6.6 for Diamalloy 2001 where again a 4 mm vertical increment of needle shaped bolt provides 100% powder flow rate of Diamalloy 2005.

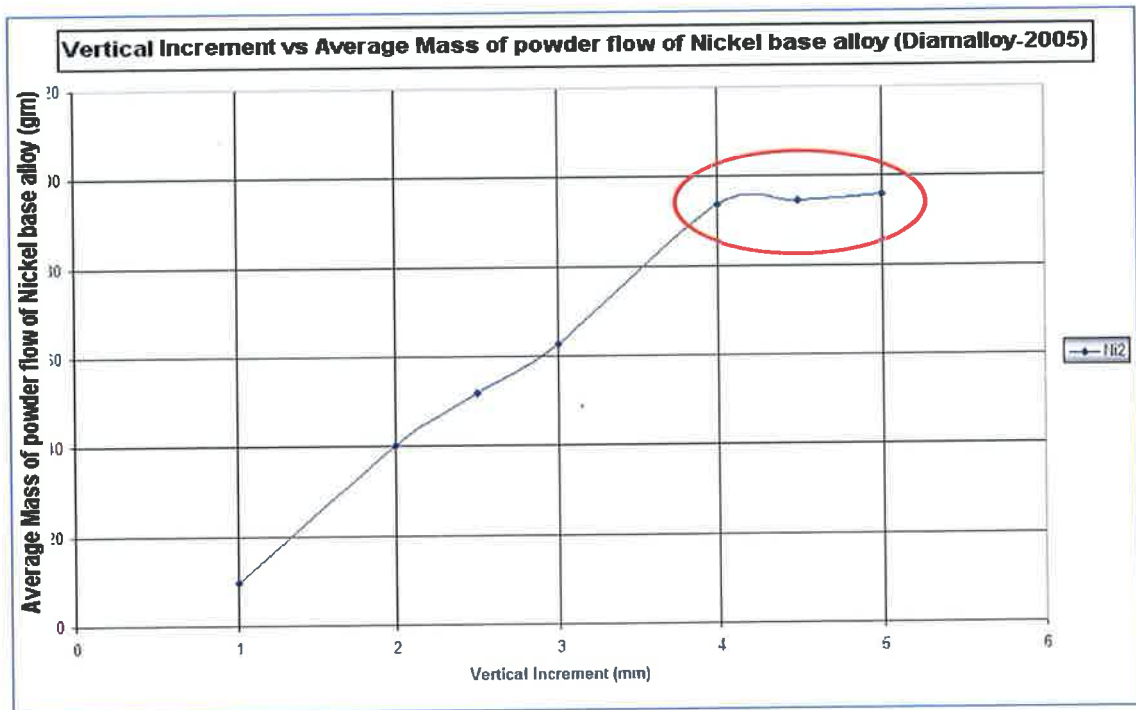


Figure 6.11: Average mass of nickel base alloy2 (Diamalloy 2001) powder flow with vertical increment of the needle shaped bolt controlled via LabVIEW programming.

Figure 6.12 shows the combine graphical representation of Figures 6.9, 6.10 and 6.11 for Chamber A and Figure D1, D2 and D3 for Chamber B. This result of 4 mm increment was also valid for Chamber 'B' for all powders, details is shown in appendix D.

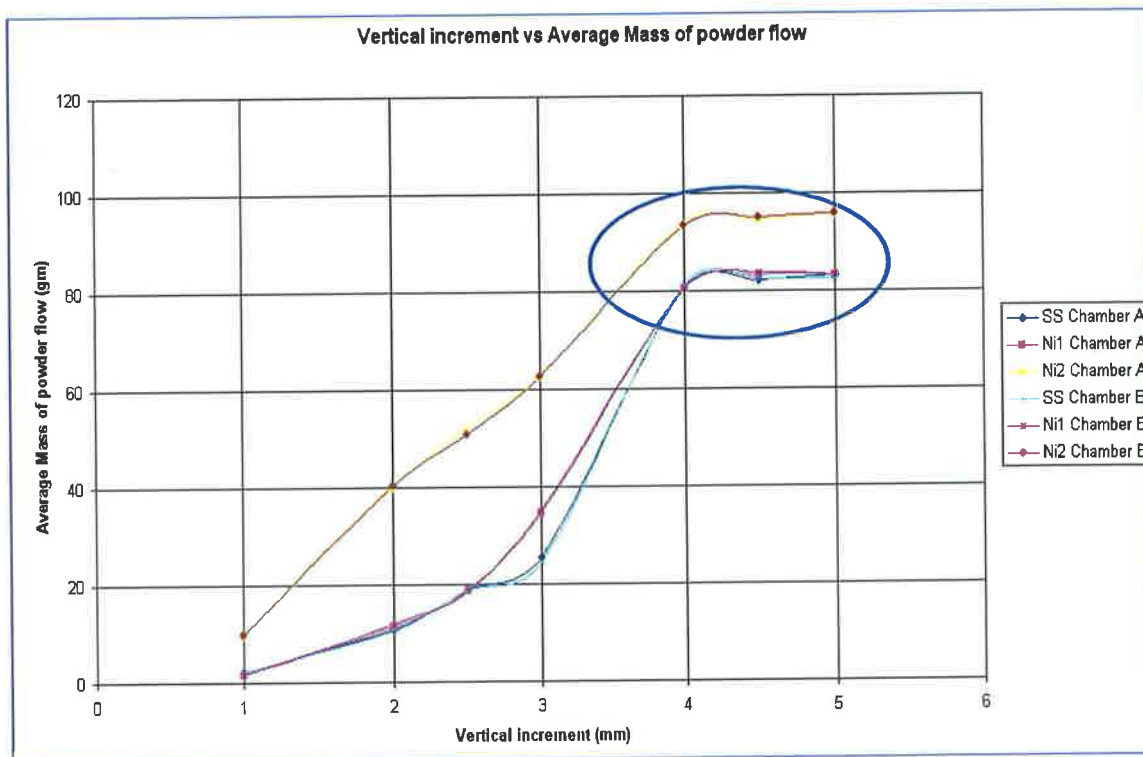


Figure 6.12: Comparison of average mass of stainless steel (Diamalloy 1003), nickel base alloy¹ (Diamalloy 1005) and nickel base alloy² (Diamalloy 2001) powder flow against vertical increment of the needle shaped bolt controlled via LabVIEW programming for both Chambers (A and B).

Although Figure 6.12 shows that a 4mm vertical increment of needle shaped bolt is the optimum level for 100 % particle flow for all three different powders, however it also shows that a difference exists in the mass of powder flow found between each other. The possible reason behind this is, the different densities/mass between the powders (as the volume may be the same), and the difference size and shape of the each powder particles material type between. Verification of this is discussed in Section 6.3.1.

Considering a 4 mm vertical decrement as the base point (100% powder particle flow), Figure 6.13 shows the average mass of powder flow when the needle shaped bolt is closed from 4mm to 0 mm for each powder comparing with the average mass of powder flow when the needle shaped bolt is opening (0 - 4 mm) . Individual data is

available in Appendix D. These results are not linear due to the critical flowability of each individual powder, which is described later in Section 6.3.1.

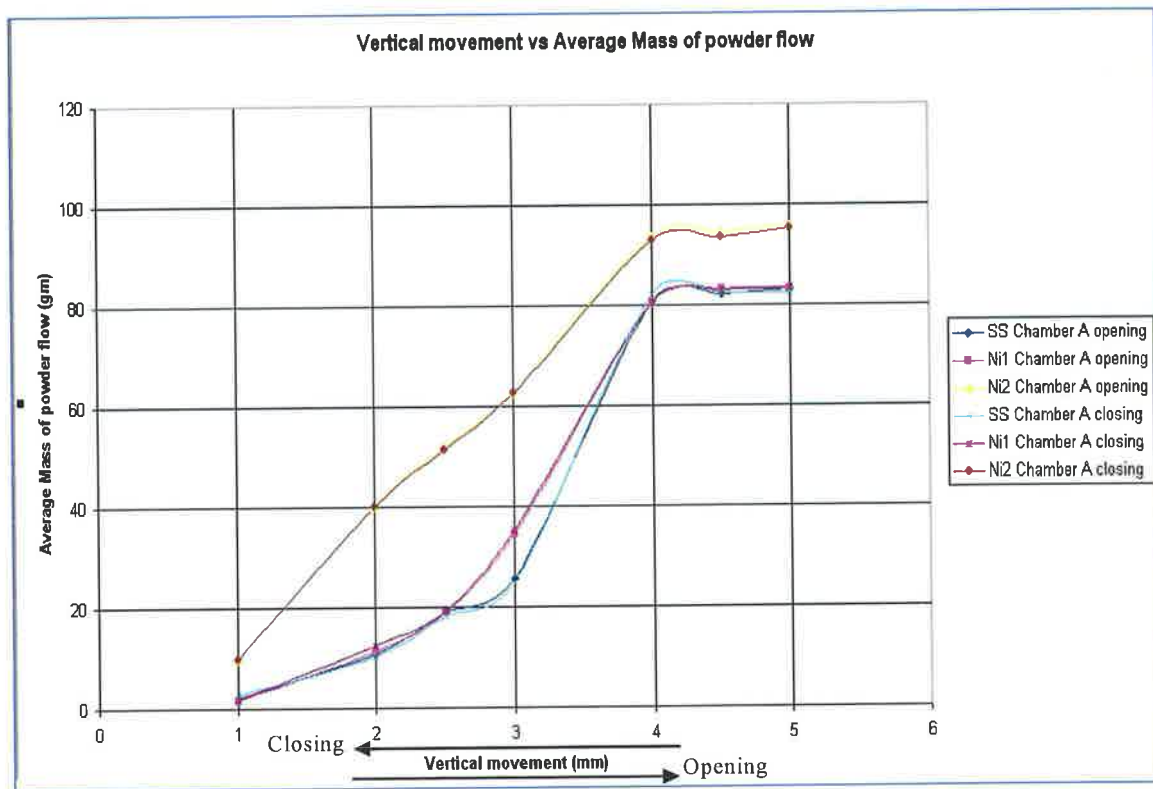


Figure 6.13: Comparison of Average mass of powder flow for vertical movement (Opening and Closing) of needle shaped bolt from 100% powder flow at 4 mm vertical increment to 0% at 0 mm position. Data obtained from Table 6.4, 6.5, 6.6, D4, D5 and D6 respectively (Appendix D).

From the above discussion one can see that there was no traceable difference between Chamber A and B. However Diamalloy 2001 was found to flows at the highest rate compared to Diamalloy 1003 and Diamalloy 1005.

6.3.1 Difference between Material Particles

The possible reason behind the difference of mass of powder flow between each powder flow test (Figure 6.12) is due to the different size and shape of the powder particles between each other and their relative densities. To confirm these 2 experiments were carried out as follows:

- Density/Flowability measurement
- Optical microscope test

Density/Flowability measurement

To measure the density/flowability of the three different powders one pre-measured container was used. The average value of density of each powder which is shown in Table 6.7.

Table 6.7: Different densities of three different powders (Diamalloy 1003, Diamalloy 1005 and Diamalloy 2001).

Experiment Number	Volume of container filled with powder =V (ml or cm ³)	Weight of the container (gm)	Total weight (Container + Powder) (gm)	Powder weight =M (gm)	Measured density (gm/cm ³)	Average density for each powder (gm/cm ³)
D1 for Diamalloy 1003	100	101.87	587.01	485.14	4.8514	5.0513 (For Diamalloy 1003)
D2 for Diamalloy 1003	50		364.43	38.70	4.8514	
D3 for Diamalloy 1005	100	101.87	585.31	483.44	4.8344	4.901 (For Diamalloy 1005)
D4 for Diamalloy 1005	50		350.25	41.62	4.9676	
D5 for Diamalloy 2001	100	101.87	568.13	466.26	4.6626	4.6248 (For Diamalloy 2001)
D6 for Diamalloy 2001	50		331.22	39.60	4.587	

From the above Table 6.7 it was observed that the density of the Diamalloy 2001 was lower than other two powders (Diamalloy 1003 and Diamalloy 1005).

Since the density was not a consistent solution, another standard test method (for flow rate of metal powders) was followed. This test method covers the determination of the flow rate of metal powders (Diamalloy 1003, Diamalloy 1005 and Diamalloy 2001). Table 6.8 shows the results of the test for flow rate of metal powders (Diamalloy 1003, Diamalloy 1005 and Diamalloy 2001).

Table 6.8: Results of standard test method for flow rate of metal powders.

Powder Type	Experiment Number	Weight of Powder (gm)	Time of Flow through the calibrated Orifice (sec)	Average Time (Sec)	Average Flow Rate (gm/sec)
Diamalloy 1003	1	50	45	43.60	1.15
	2		46		
	3		42		
	4		42		
	5		43		
Diamalloy 1005	6	50	29	28.8	1.74
	7		30		
	8		29		
	9		28		
	10		28		
Diamalloy 2001	11	50	22	21.6	2.31
	12		22		
	13		21		
	14		21		
	15		22		

From this test it is found that the Diamalloy 2001 flows faster than Diamalloy 1003 and Diamalloy 1005. Hence this is clear that the flowability of Diamalloy 2001 is higher than Diamalloy 1003 and Diamalloy 1005.

Optical microscope observation

From visible observation it has been found that the powder particle of Diamalloy 1003 and Diamalloy 1005 are more or less of the same size and shape. Certain amounts of three different powder particles were observed using the optical microscope and the images are shown in Figure 6.14, 6.15 and 6.16. The powder particles of Diamalloy 1003 and Diamalloy 1005 are denser and smaller in size compare to Diamalloy 2001, which is clear from Figure 6.14, 6.15 and 6.16.

Diamalloy 1003 and Diamalloy 1005 powders have a tendency to agglomerate due to their fine size where as Diamalloy 2001 was more granular but flows easier compare to the other two types.

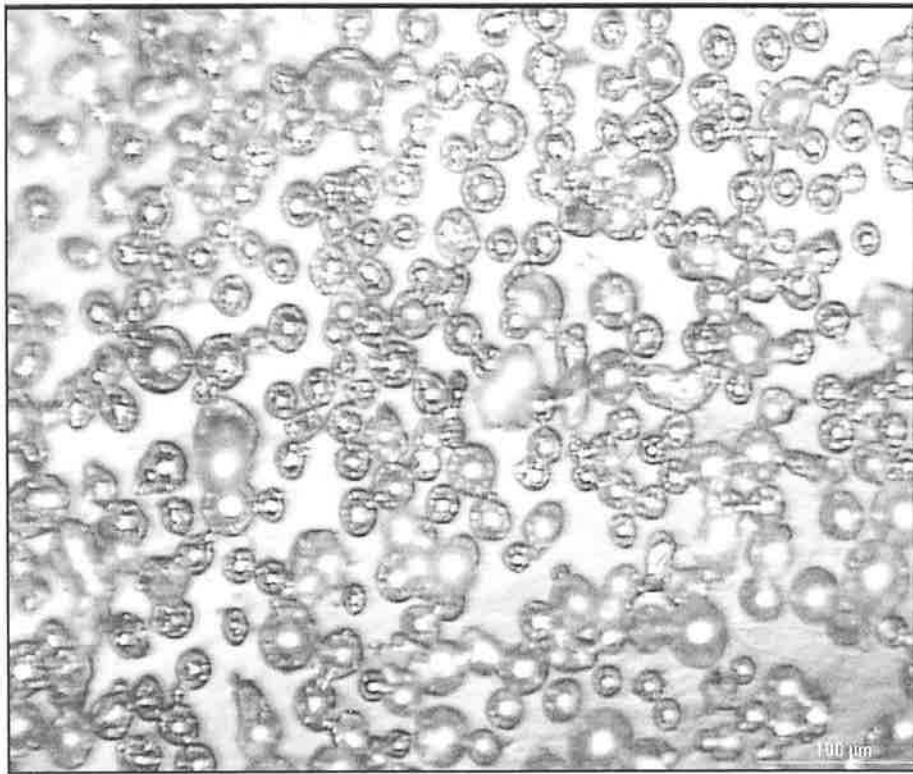


Figure 6.14: Optical microscope image of Diamalloy 1003.

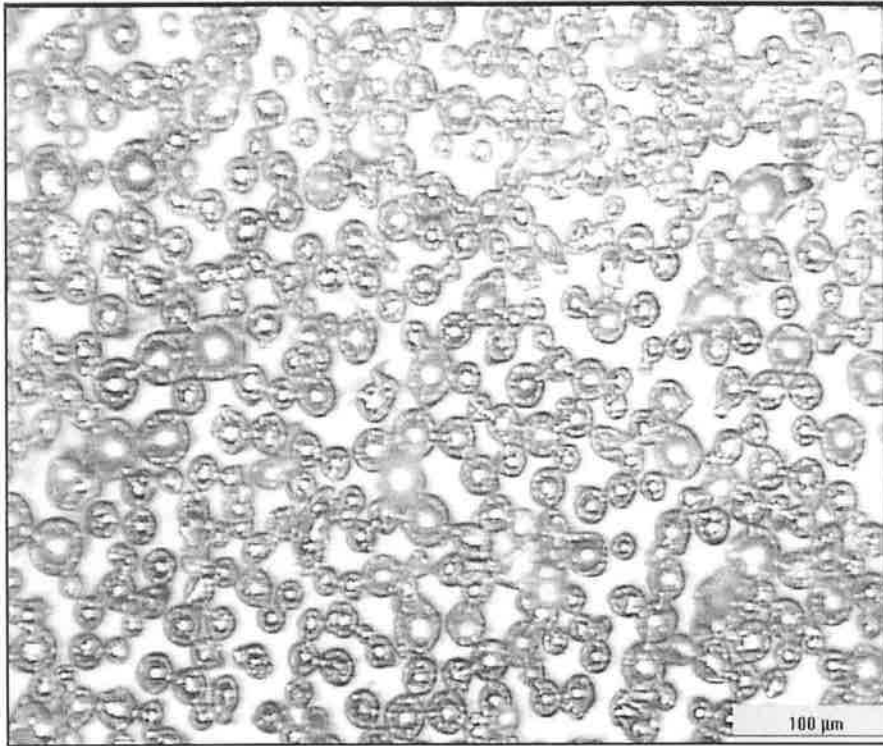


Figure 6.15: Optical microscope image of Diamalloy 1005.

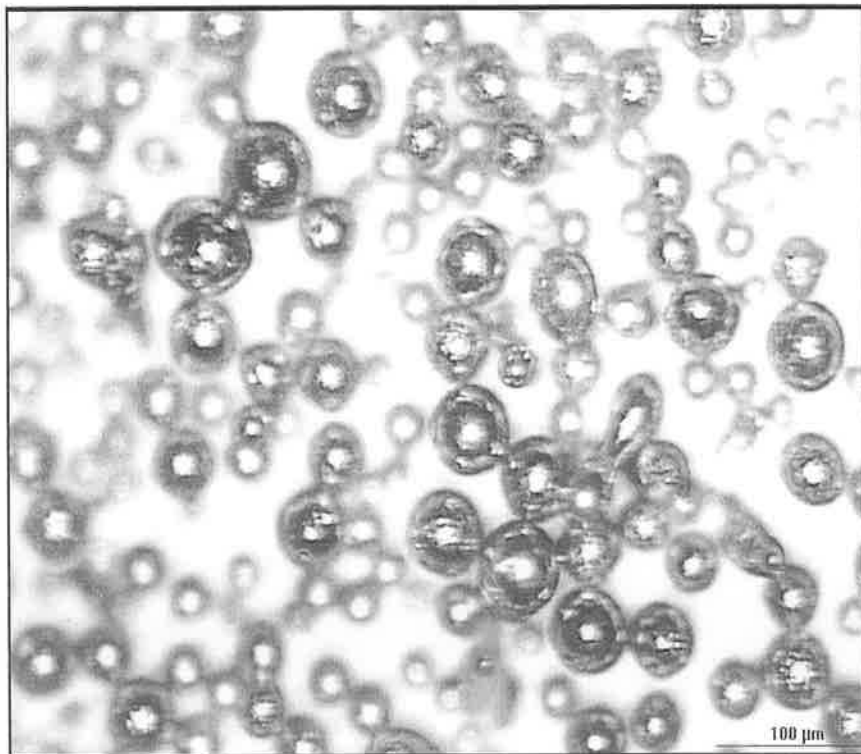


Figure 6.16: Optical microscope image of Diamalloy 2001.

6.3.2 Conclusion of the Powder flow Bench Test Results

From the powder flow bench test results it has been determined that during the coating process to get the 100% flow of powder particle vertical increment of the needle shaped bolts will be 4 mm from zero position using any Chamber either 'A' or 'B'. Each stage of vertical increment or decrement will be 1 mm to achieve 25% powder composition, as 25% is $\frac{1}{4}$ of 100%. Hence to obtain a 1000 μm (approximately 1 mm) thick coating, the spray gun needs to produce 32 layers on the substrate, which is 16 passes (as each layer is 30 μm thick) where a pass refers to the gun moving over and back across the substrate. So in the LabVIEW programme the limit switch will send a signal to create the vertical increment or decrement of the needle shaped bolts every 8 layers ($\frac{1}{4}$ of overall coating thickness) which mean the value of counter control (max. Count) will be set at 4 for both linear actuators. The above procedure is applicable when the flow ability of the two powders is more or less same, for example here, base powder material Diamalloy 1003 and coating powder material Diamalloy 1005. But when the flowability of two powders (for example base powder material Diamalloy 1003 and coating powder material Diamalloy 2001) is different then it is necessary to determine the powder composition ratio with the vertical increment or decrement of the needle shaped bolts. So before doing any functional graded coating with this device it is important to do a powder flow bench test (as described earlier) to find out the composition ratio of the coating material powder where the base material powder flows 100% at 4 mm vertical increment of the any needle ether filling Chamber 'A' or Chamber 'B'. For current research Diamalloy 1003 was used as a base material powder. If the coating powder material is Diamalloy 2001 instead of Diamalloy 1005 then vertical increment of needle shaped bolt which control the flow of this powder varies according to data found in the following Table 6.9. Table 6.9 shows the vertical increment or decrement

of each needle shaped bolt according to the amount (mass) of powder found in the mixture as determined by the powder bench test.

Table 6.9: Vertical increment or decrement composition of needle shaped bolt with different powders.

Percentage of powder composition	Diamalloy 1003 (Base powder material)		Diamalloy 1005		Diamalloy 2001	
Needle shape bolt either 'A' or 'B' (%) [Initial position is zero]	Increment or Decrement (mm)	Approximated mass of powder (gm), Time delay, T=10 sec (Data from Figure 6.12)	Decrement (mm)	Approximated mass of powder (gm), Time delay, T=10 sec (Data from Figure 6.12)	Decrement (mm)	Approximated mass of powder (gm), Time delay, T=10 sec (Data from Figure 6.12)
100	4.00	80	4.00	80	4.00	90
75	3.50	60	3.50	60	3.10	68
50	3.00	40	3.00	40	2.20	46
25	2.50	20	2.50	20	1.30	24
0	0	0	0	0	0	0

So, these increment (or decrement) values for each powder-controlling needle, was expected to give the desired functionally graded coatings. The FGM coating will be as follows where the first coat is 100 % base material powder then the second layer is 75% base material and 25% coating material powder, third one is 50% of each type finally the top coat is 100% coating material powder varying the needle shape bolt according to the above data from Table 6.9.

6.3.2 Experimental sprayed functionally graded coatings results

A 1 mm thick Stainless steel substrate was functionally graded coated with Diamalloy 1003 and Diamalloy 2001 and another one was coated with Diamalloy 1003 and Diamalloy 1005 using the designed semi automated system. Chemical composition of the different layers was determined using the energy dispersive X-ray (EDS) spectroscopy. Three analyses at each point (i.e. Bottom layer, Middle layer and Top layer) were carried out during the chemical composition analysis using SEM technique for each sample. The following section describes the lowest Carbon and oxygen content results for the each sample. Explanation of selecting this lowest Carbon and Oxygen content sample analysis is given in the end of this section. The chemical composition of Diamalloy 1003, Diamalloy 1005 and Diamalloy 2001 are shown in Table 2.5.

(a) Sample 1

For Sample one; the substrate was Stainless Steel, Bond Coat was Diamalloy 1003 and Top Coat was Diamalloy 2001. Figure 6.17 shows a cross sectional SEM image of the functionally graded coating sample 1. Figures 6.18, 6.19 and 6.20 show the chemical composition of this Bond Coat, Middle of the Coating and the Top Coat respectively.

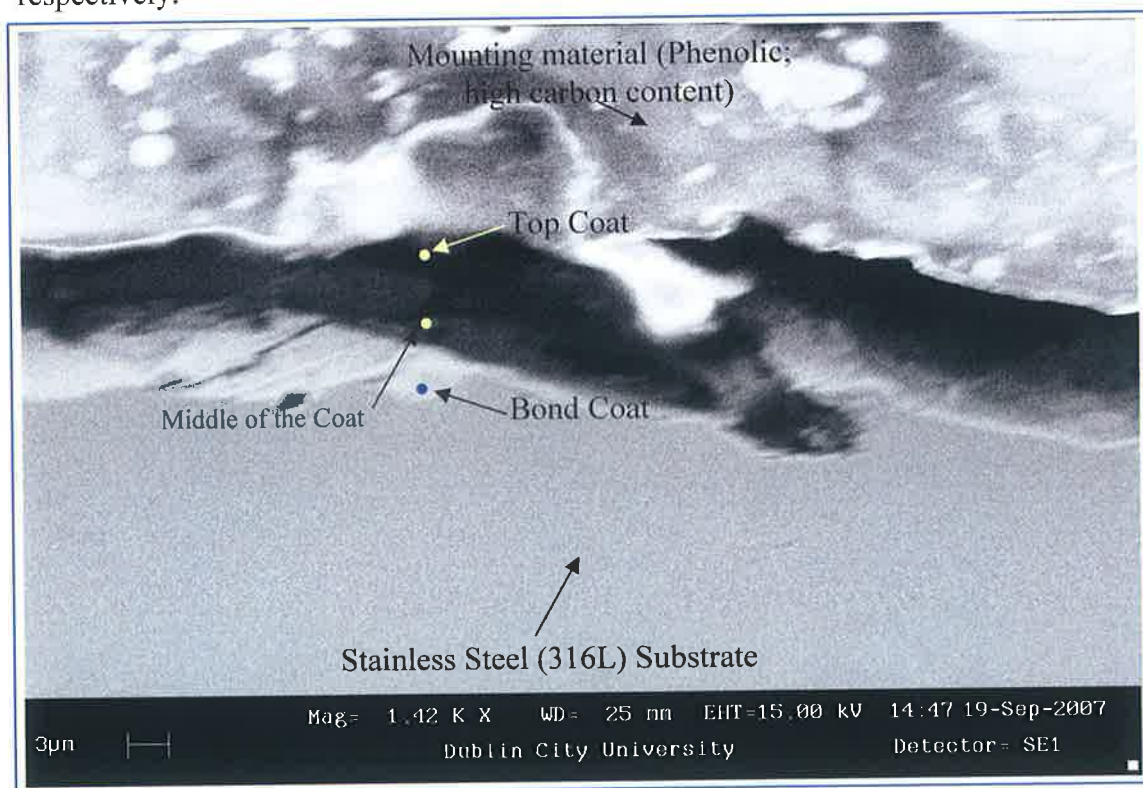


Figure 6.17: A SEM image of the functionally graded coating sample 1 (Diamalloy 1003 and Diamalloy 2001); scale shows the maximum coating thickness 15 µm of the coating.

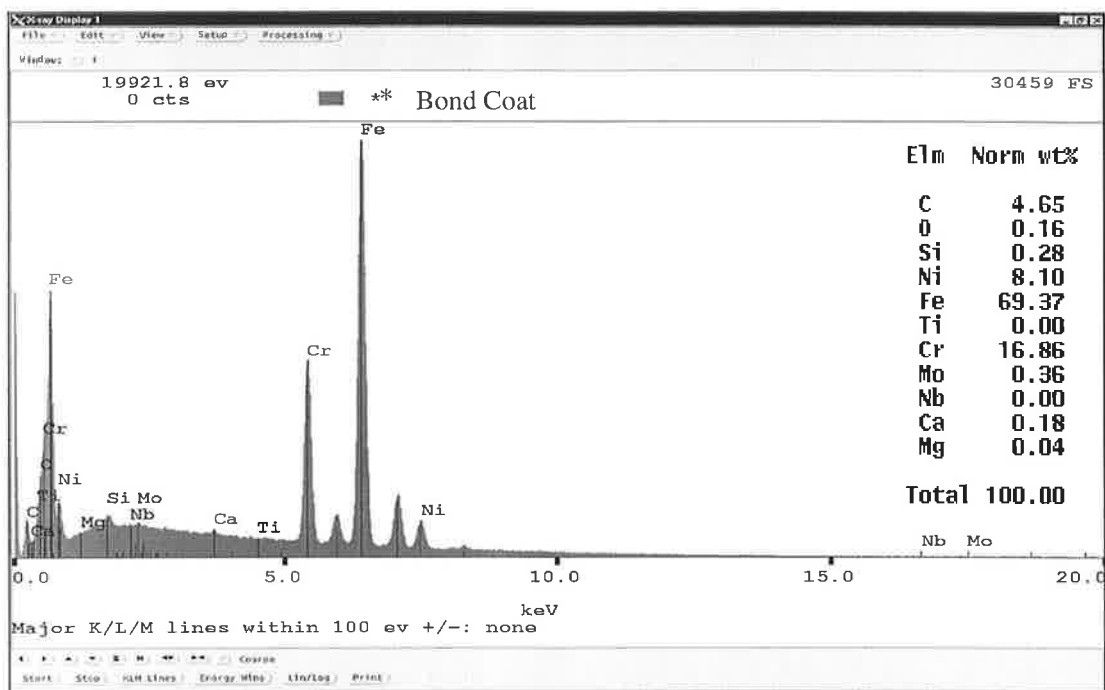


Figure 6.18: Chemical composition of first layer or Bond Coating of Sample 1.

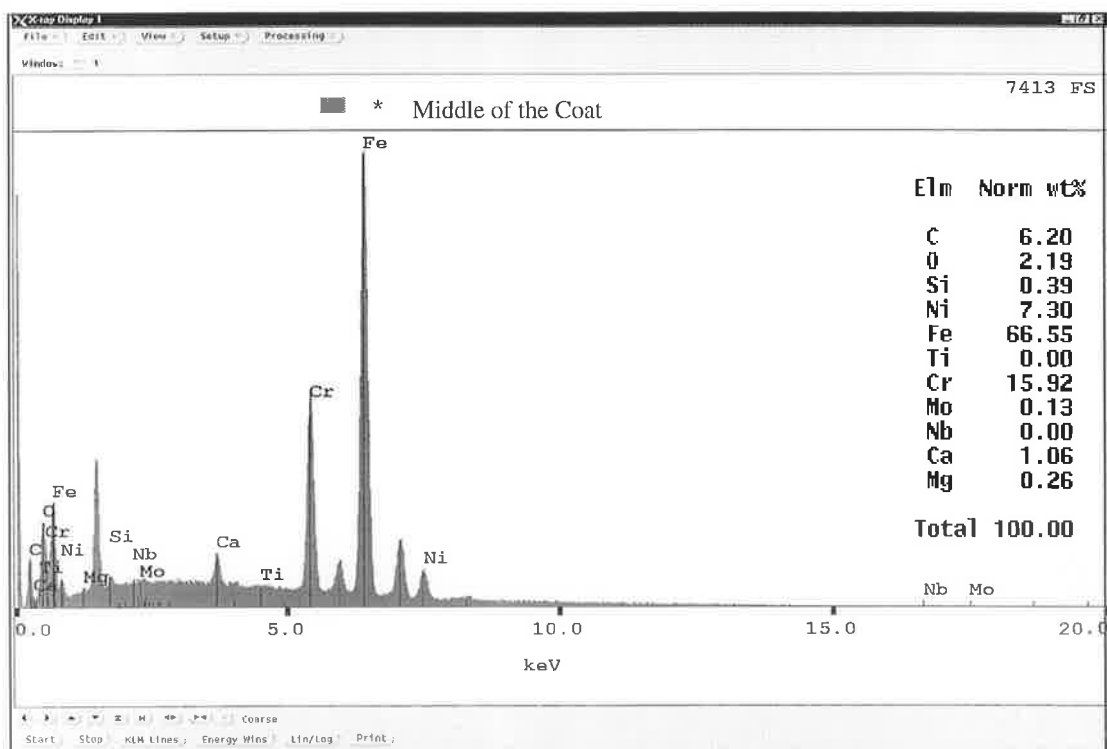


Figure 6.19: Chemical composition of the middle layer or the Middle of the Coating of Sample 1.

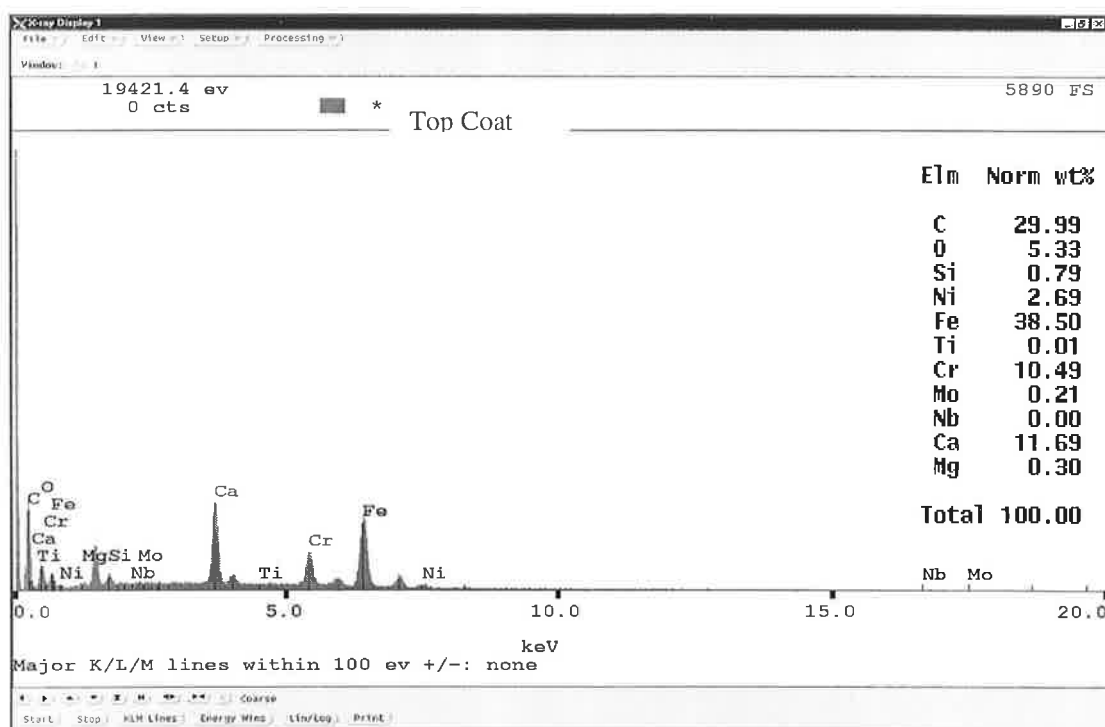


Figure 6.20: Chemical composition of the final layer or the Top Coat/Service Coating of Sample 1.

It can be seen in Table 6.10 that Chromium (Cr) 17% is common for both FGM powders; Boron (B) was not detected by the EDS technique during analysis. Hence Iron (Fe), Molybdenum (Mo) and Silicon (Si) were used to validate the design from Bond coating to Top Coating. The Iron (Fe) desired amount should tend towards 67.4% (Bal.) in the Bond Coating and 4% in the Top Coating according to Table 2.5. The FGM coating obtained values of Iron 69.37% in the Bond Coat, 66.55 % in the middle of the coating and 38.50% in the Top Coat. For Molybdenum (Mo) the desired amount was 2.50% in the Bond Coat and 0% in the Top Coat and again 0.36% was obtained in the Bond Coat, 0.13 % in the middle of the coating and 0.21% in the Top of the Coating. Although there is difference between the desired values and measured values for these two elements (Fe and Mo), but this analysis shows that their chemical composition (wt %) varied (decreased) from the Bond Coat to the Top Coat which was desired. The Silicon (Si) desired amount should tend towards 1.00% (Bal.) in the Bond Coating and 4% in the Top Coating according to Table 2.5. The FGM coating obtained values of Silicon 0.28% in the Bond Coat, 0.39 % in the middle of the coating and 0.79% in the Top Coat. However it's of chemical composition (wt %)

varied (increased) from the Bond Coat to the Top Coat which was also desired. For Nickel (Ni) the desired values and obtained values was not match significantly in this current research. Few possible reasons are detailed in the end of this results discussion.

(b) Sample 2

For Sample two; the Substrate was Stainless Steel, Bond Coat was Diamalloy 1003 and Top Coat was Diamalloy 1005. Figure 6.21 shows the cross section SEM image of this functionally graded coating sample 2. Figures 6.22, 6.23 and 6.24 show the chemical composition of the Bond Coating, Middle of the Coating and Top of the Coating respectively.

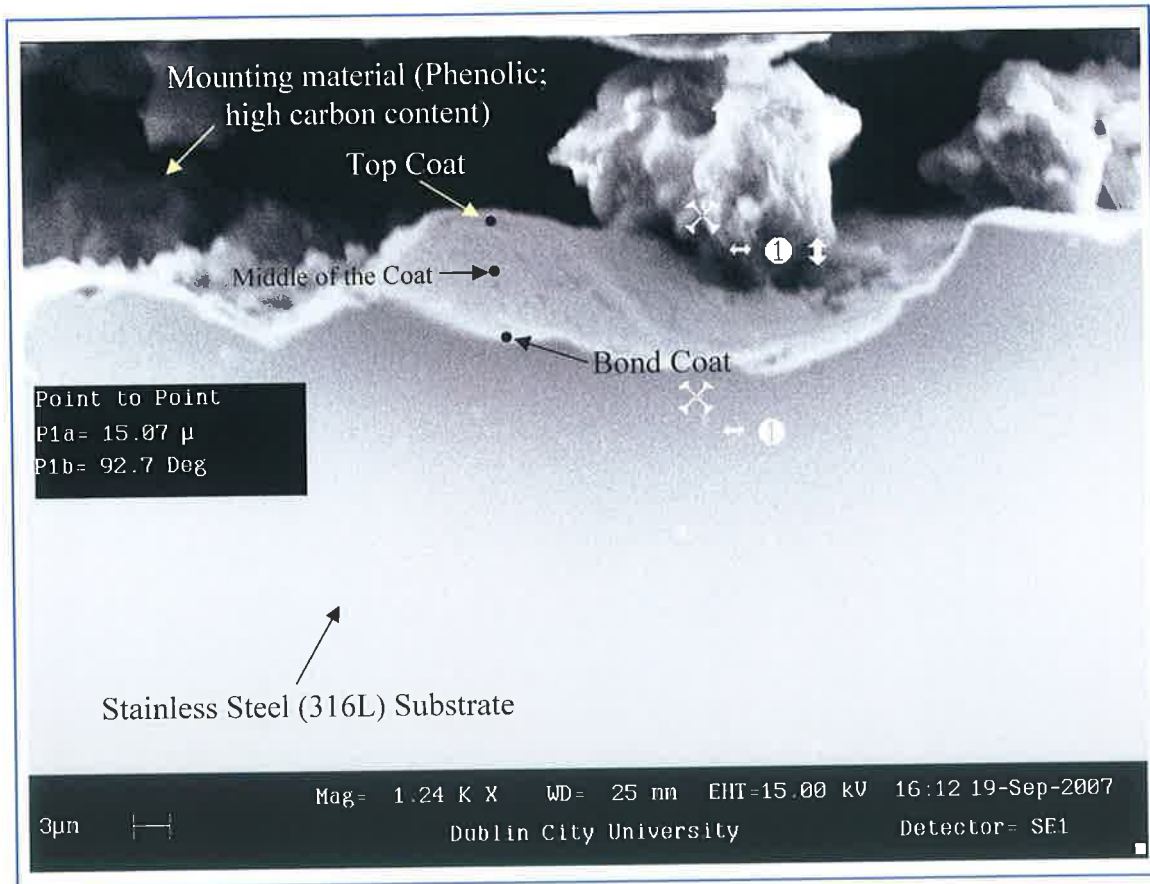


Figure 6.21: A SEM image of the functionally graded coating sample 2 (Diamalloy 1003 and Diamalloy 1005); scale shows the maximum coating thickness 15 μm of the coating.

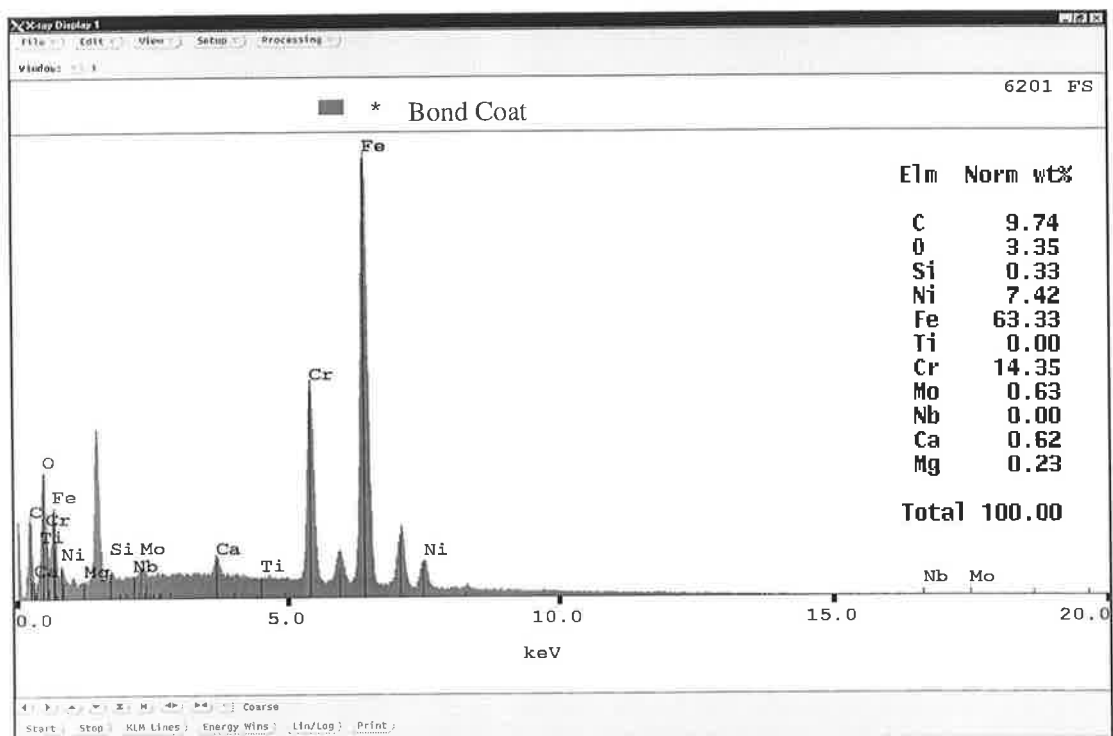


Figure 6.22: Chemical composition of the first coat or the Bond Coat of Sample 2.

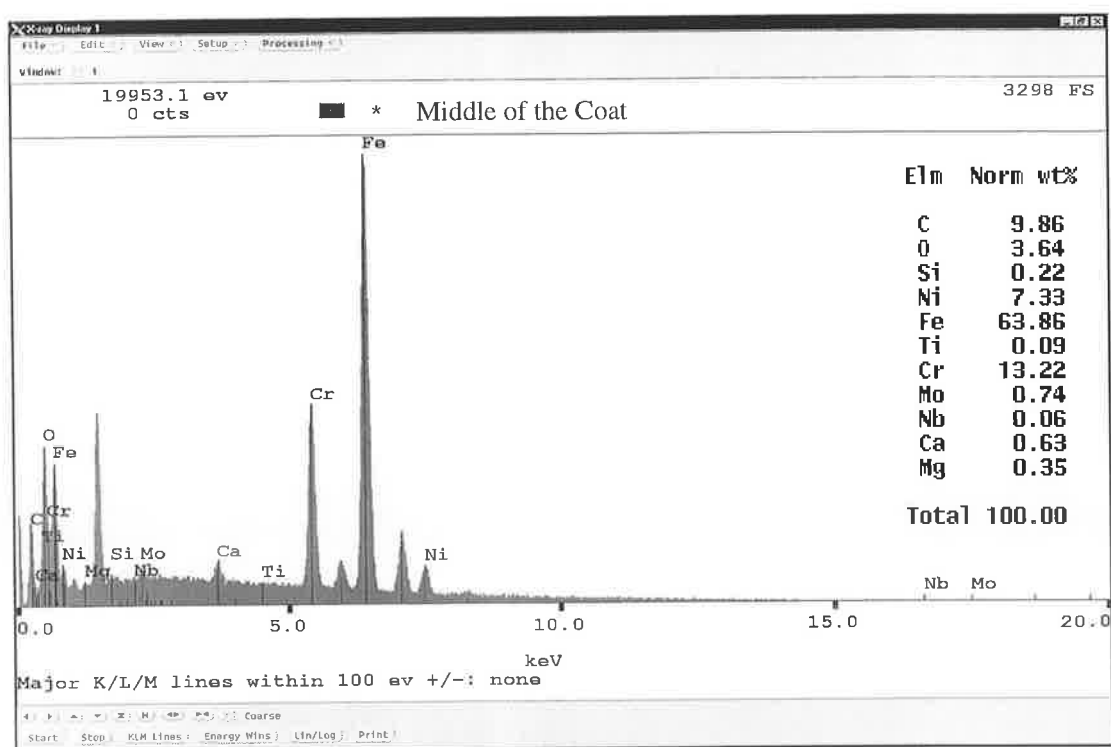


Figure 6.23: Chemical composition of the middle layer or Middle of the Coat of Sample 2.

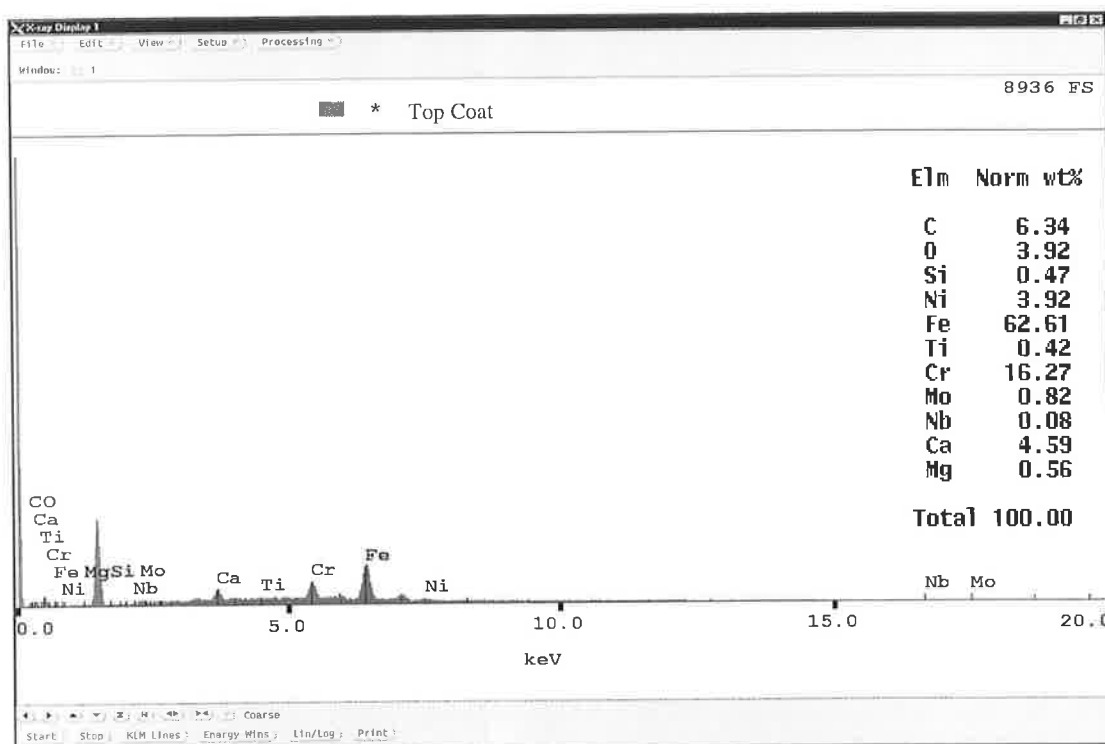


Figure 6.24: Chemical composition of the final coat or the Top Coat/Service Coat of Sample 2.

Again one can see (Table 6.10) that although Chromium (Cr), Nickel (Ni) and Molybdenum (Mo) are common; for both FGM powders, combining these materials will increase by their wt% from the Bond Coat to the Top Coat. Experimental results show (Figures 6.22, 6.23 and 6.24) that the wt% of the chromium, nickel and molybdenum values increased from the Bond Coat (Cr-14.35, Ni-7.42 and Mo-0.63) to Top Coat (Cr-16.27, Ni-3.92 and Mo-0.82) and the values obtained in the middle of the coating were; Cr-13.22, Ni-7.33 and Mo-0.74. Except the Nickel the other two elements (Cr and Mo) composition varied (increased) according to the desired values from the Bond Coat to the Top Coat. However there was little difference between desired and obtained values considering at each point which is negligible as the wt % of each element is depending on the other elements which are present in the same point. Another two element Nb and Ti was used to validate the design from Bond coat to Top Coat. The desired amount of Nb should range from 0% in the Bond Coat to 3.6% in the Top Coat; hence an increase of this element by wt% from the Bond Coat to the Top Coat. The FGM coating obtained values of 0% in the Bond Coat, 0.60% in the middle of the coating and 0.08% in the Top Coat for the element of Nb wt %. The desired amount of Ti should range from 0% in the Bond Coat to <0.40% in

the Top Coat; hence an increase of this element by wt% from the Bond Coat to the Top Coat. The FGM coating obtained values of 0% in the Bond Coat, 0.09% in the middle of the coating and 0.42% in the Top Coat for the element of Ti wt %. The Iron (Fe) desired amount should tend towards 67.40% (Bal.) in the Bond Coating and <0.50% in the Top Coating according to Table 2.5. The FGM coating obtained values of Iron 63.33% in the Bond Coat, 63.86 % in the middle of the coating and 62.61% in the Top Coat. For Silicon (Si) the desired amount was 1.00% in the Bond Coat and 0% in the Top Coat and again 0.33% was obtained in the Bond Coat, 0.22 % in the middle of the coating and 0.47% (0.26% observed in another set of point analysis shown in Appendix F; Figure: A2) in the Top of the Coating. Although there is difference between the desired values and measured values for these two elements (Fe and Si), but this analysis shows that their chemical composition (wt %) varied (decreased) from the Bond Coat to the Top Coat which was desired. Aluminium (Al) was not detected during the analysis using EDS technique in this current research.

Carbon (C), Oxygen (O), Calcium (Ca) and Magnesium (Mg); these four elements were found during this EDS analysis. Comparatively presence of high carbon and Oxygen could be contamination from the mounting powder (Phenolic resin). It was also observed using a point analysis on the mounting element surface during EDS analysis that contains higher percentage of Carbon compared to the sample (both case). However the trend of varying composition of C (from the Bond Coat to Top Coat measured value) is according to the desired value (for the sample 1; increased and for Sample 2; decreased). Calcium (Ca) and Magnesium (Mg) could be contaminated from the hand or oxidation on the surface of the Samples.

When two X-Rays from the same element hits the detector at the same time, these produced an artefact peak called sum peak. This energy values are added together. Such as K 1 line for Ni = 7477 ev X 2 = 14954 ev and For Al = 14870 ev (Which are almost same value and this values were found during EDS analysis). Therefore some Ni X-Ray can be misinterpreted as Al. This could be the possible reason for not detecting Al and B.

For qualitative analysis EDS system is reliable. For quantitative analysis EDS is preferable to analysis with a standard, where by that sample is compared to a standard

of known composition. Otherwise many correction factors are used by the system during the analysis. EDS system is focused on very small volume [189].

Table 6.10: Range of Chemical composition compared for FGM coatings.

Sample No. 1	Desired [62] and Measured values and Trend (↑ - ↓)	Bond Layer wt%	Middle Layer wt%	Top Layer wt%
Fe- Iron	Desired ↓	67.40 (Bal.)	----	4.00
	Measured ↓	69.37	66.55	38.50
B- Boron	Desired -	0	----	3.50
	Measured -	Could not detect	Could not detect	Could not detect
Si- Silicon	Desired ↑	1	----	4
	Measured ↑	0.28	0.39	0.79
Ni- Nickel	Desired ↑	12.00	----	70.50 (Bal.)
	Measured ↓	8.10	7.30	2.69
Cr- Chromium	Desired -	17.00	----	17.00
	Measured ↓	16.86	15.92	10.49
Mo- Molybdenum	Desired ↓	2.50	----	0
	Measured ↓	0.36	0.13	0.21
C- Carbon	Desired ↑	0.10	----	1.00
	Measured ↑	4.65	6.20	29.99
Sample No. 2				
Ni- Nickel	Desired ↑	12.00	----	64.60 (Bal.)
	Measured ↓	7.42	7.33	3.92
Cr- Chromium	Desired ↑	17.00	----	21.50
	Measured ↑	14.35	13.22	16.27
Mo- Molybdenum	Desired ↑	2.50	----	9.00
	Measured ↑	0.63	0.74	0.82
Nb	Desired ↑	0	----	3.60
	Measured ↑	0	0.06	0.08
Fe- Iron	Desired ↓	67.40 (Bal.)	----	<0.50
	Measured ↓	63.33	63.86	62.61
Si- Silicon	Desired ↓	1.00	----	0
	Measured ↓↑	0.33	0.22	0.47
C- Carbon	Desired ↓	0.10	----	0
	Measured ↓	9.74	9.86	6.34
Ti- Titanium	Desired ↑	0	----	<0.40
	Measured ↑	0	0.09	0.42
Al- Aluminium	Desired -	0	----	<0.40
	Measured -	Could not detect	Could not detect	Could not detect

(↑) Increased, (↓) decreased and (-) Not detected

*13 out of 16 Elements showed the same trend in composition FGM coating change as that of bulk powder materials

This confirms while the exact compositions were not attained never the less the proposed design has the potential of producing FGM which is a new venture for HVOF spraying. The reason the proportions are not the same as the starting powder compositions (that is less) is that the cumulative wt % of these elements are dependent on each other, for example if one element is increased/decreased then other elements will be change proportionally (in the range of 100 %), hence the expected composition is in fact lower than would be expected. This is the reason to select the low Carbon and Oxygen content composition for this analysis. However the trend from high to low or low to high composition for each element is maintained throughout the functionally graded deposit.

CHAPTER 7

CONCLUSIONS AND RECOMENDATIONS

7.1 CONCLUSIONS

In this current research, an innovative modification of the HVOF thermal spray process was designed to produce functionally graded coatings. This included design, FEA analysis, calibration and validation of a co-injection semi automated system used to deposit stainless steel/nickel base alloy FGM coatings simultaneously on stainless steel substrate. Following this research:

- It is possible to produce functionally graded deposits according to any desired proportion of two different powder materials using a relatively inexpensive modification of a commercial system. This was validated using chemical composition analysis.
- This current system was developed to improve its range of capabilities and repeatability of the process. This was achieved through flow control of the powder through dual feeder automation.
- The ANSYS FLOTTRAN CFD Finite Element Analysis simulated the flow of the powder/gas mixture through this design system for various input process and yielded the ideal pressure required to predict flow and mixing.
- The designed was manufactured for testing; the Lab VIEW software was designed to control (through programming) the semi-automated powder feed unit device.
- Bench and experimental deposition testes were carried out to test the new device for functionality.
- Post spraying; samples were cross sectioned and prepared for SEM/EDS observation. The results of which showed that the chemical composition of the various layers changed according to the composition type of material been laid down by the HVOF process.
- The chemical composition validation test was based on elements which were expected to increase/ decrease as the powder type changed across the

functionally graded deposit. The values of weight composition (wt %) was found to be lower in the deposit when compared to the initial powder used.

- The device is capable of spraying any grade type/composition make up which will benefit research in HVOF thermal spraying.

7.2 RECOMMENDATIONS FOR FUTURE WORK

The results documented in the present research are significant, however recommendations for further investigation are described below to enhance the research area even further:

Design and Manufacturing:

- Modification of the Design of the Linear Actuator Holder is desirable; to provide a flexible powder pouring system.
- Strength and power of the Linear Actuators could be increased; to help to control the flow of the powders more accurately.

FEA Simulation:

- Simulation of the Finite Element Analysis could be conducted using Fluent CFD Software.

Control and Automation:

- Instead of using the limit switches (act as a counter of the spray gun); the LX indexer could be designed to communicate with the Lab VIEW software itself.

Characterisation of the Material Properties:

- Characterisation and Mechanical testing of the functionally graded coated substrate (the produced coating properties) for corrosion resistance, hardness, bond strength, residual stress and so on could be carried out to define the potential of these FGM HVOF coatings.

PUBLICATIONS ARISING FROM THIS WORK

International Conference Papers:

- M.K. Al Mamun, M. S. J. Hashmi, J. Stokes, “Designing and Integrating a semi automated Powder Feed Device to Produce Functionally Graded Materials (FGM) using the HVOF Thermal Spray Process”, Proceedings of the 24th International Manufacturing Conference, Waterford, Ireland, 2007, vol. 2, pp-1009-1016.

International Conference Papers in Preparation:

- M.K. Al Mamun, J. Stokes, et al. “How to spray Functionally Graded deposits using HVOF Thermal Spray”, International Thermal Spray Conference (ITSC) in Maastricht, Netherlands, June 2008.

Poster Presentation:

- M.K. Al Mamun, M. Hasan, J. Stokes, L. Looney, M.S.J. Hashmi , “Benefit of Using Functionally Graded Materials in the Application of the Thermal Spray Coatings”, Proceedings of the International Conference on Materials-Energy-Design (MED06), Dublin, Ireland, 2006, pp.361-362.
- M.K. Al Mamun, J. Stokes, “Designing and Integrating a semi automated Powder Feed Device for both HVOF and Plasma to Spray to Produce Functionally Graded Materials (FGM) of Ti alloy and HA powders for Biomedical Applications”, Plasma Process for Biomedical Application (One day workshop, 24th May, 2007), Book of Abstracts, pp. P16.

REFERENCES

- [1] Gordon England, 2005 HVOF Process (Online), <http://www.gordonengland.co.uk/tsc.htm>, access date 05/03/2007.
- [2] Khor, K. A., et al., "Non-Destructive Evaluation of Plasma Sprayed Functionally Graded Thermal Barrier Coatings", Surface and Coatings Technology, Vol. 130, Issue. 2-3, 2000, pp. 233-239.
- [3] Khor, K. A., et al., "Influence of Oxide Mixtures on Mechanical Properties of Plasma Sprayed Functionally Graded Coatings", Thin Solid Films, Vol. 368, Issue. 1, 2000, pp. 86-92.
- [4] Khor, K. A., et al., "Microstructure Formation in Plasma-Sprayed Functionally Graded NiCoCrAlY/Yttria - Stabilized Zirconia Coatings", Surface and Coatings Technology, Vol. 114, Issue 2-3, 1999, pp. 181-186.
- [5] Hu, W., et al., "Graded Coatings Prepared by Plasma Spraying With Ni-Coated ZrO₂ Powders", Surface and Coatings Technology, Vol. 105, Issue 1-2, 1998, pp. 102-108.
- [6] Lima, C. R. C., & Trevisan, R. E., "Graded Plasma Spraying of Premixed Metal-Ceramic Powders on Metallic Substrates", Journal of Thermal Spray Technology, Vol. 6, Issue 2, 1997, pp. 199-204.
- [7] Halling, J., "Recent Developments in Surface Coating and Modification Processes", Waveney Print Services Ltd, Suffolk, UK, ISBN No 0852985827, 1985.
- [8] Chapman, B. N., & Anderson, T. C., "Science and Technology of Surface Coating", Academic Press, UK, ISBN No 0121683508, 1974.
- [9] K, Kempton, "Where thermal spray coatings are most cost effective", Weld. J., Vol.70, 1991, pp. 41.
- [10] A. Kuhl and H. Riegger, "Ceramic coatings for pump components", Werkst. Korras., Vol. 45, Issue 11, 1994, pp. 615- 619,

- [11] P.A. Lavin, "The leap from conventional to high-energy plasma spraying", *Rob'act, J.*, Vol. 2, 1983, pp. 32.
- [12] R.W. Smith, D. Wei and D. Apelian, "Thermal plasma materials processing: applications and opportunities", *Plasma Chem. and Plasma Proces.*, Vol. 9, 1989, pp. 135S – 165S.
- [13] G.Y., Lai, "Evaluation of sprayed chromium carbide coatings for gas cooled reactor applications", Technical Report, Conference on metallurgical coatings; 3 Apr 1978; San Francisco, CA, USA.
- [14] V. Ramnath and N. Jayaraman, "Characterisation and wear performance of plasma sprayed WC-Co coatings", *Materials, Science & Technology*, Vol. 5, Issue 4 1989, pp. 382-388.
- [15] J.R. Lindtreen and W.R. Johnson, "Friction and wear behavior of chromium carbide coatings", Technical Report, 14th international conference on metallurgical coatings; 23 Mar 1987; San Diego, CA, USA.
- [16] Ding Chuanxian and Tang Zhaohe, "Sliding friction and wear behavior mechanisms in plasma sprayed ceramic coatings", *Proceedings of Thermal Spray: International Advances in Coatings Technology*, ASM international, Materials Park, OH, 1992, p. 673.
- [17] M. Scroll and P. Clayton., "Abrasive and erosive wear of some hypervelocity air plasma sprayed coatings", *Thermal Spray Coatings: Properties, Processes and Application*, ASM international, Materials Park, OH, 1992, p. 39.
- [18] D.W. Parker, G.L. Kutner, "HVOF-Spray Technology-Poised for Growth", *Journal of Advance Materials and Process*, Vol.139 (No.4), 1991, p.68-74.
- [19] G. Davies, M. Breitsameter, *Weld. Res. Abroad*, Vol. 43, Issue 1, 1997, pp. 5.

[20] Thorpe, R., et al., "HVOF Thermal Spray Technology", Journal of Advanced Materials and Processes, Vol. 157, Issue 4, 2000, pp. 27-29.

[21] Hillery, R.V., "Coatings for High-Temperature Structural Materials, Trends and opportunities", national Academy Press, Washington, ISBN No 0309053811, 1996.

[22] Holmberg, K., & Matthews, A., "Coatings Tribology: Properties, Techniques and Applications in Surface Engineering". Elsevier Science, The Netherlands, ISBN No 0444888705, 1994.

[23] Stokes, J., "Production of Free Standing Engineering Components using the HVOF (High Velocity Oxy-Fuel) Process", Ph.D. Thesis, Dublin City University, Ireland, 2003.

[24] Bhushan, B., & Gupta, B.k., "Handbook of Tribology: Material coating and Surface Treatments", McGraw-Hill, New York, ISBN No 007052492, 1991

[25] Sulzer METCO, "Product Information", 2001, (Online) www.sulzermetco.com. Date of access 08/08/04.

[26] Heimann, R. B., "Plasma-Spray Coating, Principles and Applications", VCH Publishers, New York, USA, ISBN No 3527294309, 1996.

[27] EWI Weldnet Company Document, (Online) <http://www.ewi.org/technologies/arcwelding/thermalspray.asp>, Date of access 09/09/06.

[28] Knight, R., & Smith, R. W., "HVOF Sprayed 80/20 NiCr Coatings: Process Influence Trends", Proceedings of the 13th International Thermal Spray Conference, Florida, USA, 1992, pp. 159-164

[29] H. Herman, S. Sampath, R. McCune, MRS Bull., Vol.25, Issue7, 2000, p.17.

- [30] Stokes, J., "The Theory and Application of the HVOF Thermal Spray Process", School of Mechanical and Manufacturing Engineering, Dublin City University, Ireland, 2003.
- [31] Bhushan, B., & Gupta, B. K., "Handbook of Tribology: Material Coating and Surface Treatments", McGraw-Hill, New York, ISBN No 007052492, 1991.
- [32] Stokes, J. and Looney, L. "Residual stress in HVOF thermally sprayed thick deposit", Surface Coating technology, Vol 177-178, 2004, p. 18-23.
- [33] TAFA, "Model TJ-4000: The Most Affordable HVOF in the World-Product Brochure", TAFA Incorporated, 1998.
- [34] PRAXAIR Surface Technologies and TAFA, "Thermal Spray Solutions-Product Brochure", PRAXAIR Surface Technologies and TAFA Incorporated, 2000.
- [35] AEROSTAR Coatings, "HFPD: The New Alternative for the Thermal Spray Industry", AEROSTAR Coatings, 2000.
- [36] Thorpe, M. L., & Richter, H. J., "A Pragmatic Analysis and Comparison of HVOF Processes", Proceedings of the 13th International Thermal Spray Conference, Florida, USA, 1992, pp. 137-147.
- [37] Gartner, "Professional Thermal Spray Equipment", Gartner Thermal Spraying Company, 1999.
- [38] Helali, M., & Hashmi, M. S. J., "A Comparative Study of Plasma Spraying and HVOF Thermal Spraying", Proceedings of the 10th Irish Manufacturing Committee (IMC-10) Conference, Galway, 1993, pp. 376-387.
- [39] Vuoristo, P., et al., "Abrasion and Erosion Wear Resistance of Cr₃C₂-NiCr Coatings Prepared by Plasma, Detonation and High Velocity Oxyfuel Spraying", Proceedings of the 7th National Thermal Spray Conference, Boston, USA, 1994, pp. 121-126.

- [40] Makela. A., et al., "Rolling Contact Fatigue Testing of Thermally Sprayed Coatings", Proceedings of the 7th National Thermal Spray Conference, Boston, USA, 1994, pp. 759-764.
- [41] Pawlowski, L., "The Science and Engineering of Thermal Spray Coatings", Wiley and Sons, UK, ISBN No 0471952532, 1995.
- [42] Gordon England, Thermal Spraying Process , (Online)
<http://www.gordonengland.co.uk/xhvof.htm>, access date 05/05/2007
- [43] METCO/ Perkin Elmer, "Diamond Jet System and Gun Manual", USA, 1989.
- [44] Thorpe, R., et al., "HVOF Thermal Spray Technology", Journal of Advanced Materials and Processes, Vol. 157, Issue 4, 2000, pp. 27-29.
- [45] Bolles, C. D., "HVOF Thermal Spraying: An Alternative to Hard Chromes Plating", Welding Journal, Vol. 74, Issue 10, 1995, pp. 31-34.
- [46] Concurrent Technologies Corporation Document, (Online)
<http://www.dppr.ctc.com/plating/rhvofspr.htm>, Date of access 06/01/06.
- [47] Hackett, C. M., et al., "Independent Control of HVOF Particle Velocity and Temperature" Proceedings of the 9th National Thermal Spray Conference, Ohio, USA, 1996, pp. 665-673.
- [48] Hackett, C. M., et al., "The Influence of Nozzle Design on HVOF spray Particle Velocity and Temperature", Proceedings of the 8th National Thermal Spray Conference, Texas, USA, 1995, pp. 135-140.
- [49] Hasan. M., "HVOF Thermal Spray Deposition of Functionally Graded Coatings", Ph.D. Thesis, Dublin City University, Ireland, 2004.

[50] Sulzer METCO Company Document, (Online) www.sulzermetco.com/tech/pr-comp.html, Date of access 20/12/2005.

[51] Hackett, C. M., et al., "On the Gas Dynamics of HVOF Thermal Sprays", Proceedings of the 5th National Thermal Spray Conference, California, USA, 1993, pp. 167-172.

[52] Thorpe, R. J., & Thorpe, M. L., "High Pressure HVOF: An Update", Proceedings of the 5th National Thermal Spray Conference, California, USA, 1993, pp. 199-204.

[53] Key, J. F., et al., "Use of De Laval Nozzles in Spray Forming", Proceedings of the 5th National Thermal Spray Conference, California, USA, 1993, pp. 75-80.

[54] Sulzer METCO Company Document, (Online) <http://www.sulzermetco.com/news/nd13.html>, Date of access 21/12/05.

[55] Stokes, J., & Looney, L., "Properties of WC-Co Components Produced using the HVOF Thermal Spray Process", Proceedings of the 1st International Thermal Spray Conference, Montreal, Canada, 2000, pp. 263-270.

[56] Young, P. M., et al., "Parameter Study of HP/HVOF Deposited WC-Co Coatings", Journal of Thermal Spray Technology, Vol. 7, Issue 1, 1998, pp. 97-107.

[57] Jacobs, L., et al., "Comparative Study of WC-Cermet Coatings Sprayed Via the HVOF and HVOF Coatings", Journal of Thermal Spray Technology, Vol. 7, Issue 2, 1998, pp. 213-218.

[58] Li, C. J., et al., "Effect of Types of Ceramic Materials in Aggregated Powder on the Adhesive Strength of High Velocity Oxy-Fuel Sprayed Cermet Coatings", Surface and Coatings Technology, Vol. 145, 2001, pp. 113-120.

[59] Cole, M. A., et al., "Process Gases for High Velocity Oxy-Fuel Thermal Spraying", Proceedings of the 7th National Thermal Spray Conference, Boston, USA, 1994, pp. 233-238.

[60] Cole, M. A., et al., "High Temperature Erosion Properties Thermal Barrier Coatings Produced by Acetylene Sprayed High Velocity Oxygen Fuel Process", Proceedings of the 1st International Thermal Spray Conference, Canada, 2000, pp. 1191-1200.

[61] Goodfellow Company Document, (Online) www.goodfellow.com, Date of access 09/09/06.

[62] METCO/ Perkin Elmer, "Diamond Jet Application Data Charts", USA, 1989.

[63] Metals Handbook, "Powder Metallurgy", Vol. 7, American Society for Metals, Metals Park, Ohio, ISBN No 0871700131, 1984.

[64] Bhol, R., et al., "Splat Solidification of Tin Droplets", Proceedings of the 9th National Thermal Spray Conference, Ohio, USA, 1996, pp. 657-663.

[65] National Thermospray, Inc., (Online) <http://www.hvof.com/material.htm> Date of access 12/08/06

[66] Kadyrov, E., et al., "Interaction of Particles with Carrier Gas in HVOF Spraying Systems", Journal of Thermal Spray Technology, Vol. 3, Issue 4, 1994, pp. 389-397.

[67] Rangel, R. H., et al., "Numerical Investigation of Micro-Pore Formation During Substrate Impact of Molten Droplets in Spraying Processes", Proceedings of the 7th National Thermal Spray Conference, Boston, USA, 1994, pp. 375-380.

[68] Mostaghimi, J., et al., "Deformation and Solidification of Molten Particles on a Substrate in Thermal Plasma Spraying", Proceedings of the 7th National Thermal Spray Conference, Boston, USA, 1994, pp. 405-414.

- [69] Ohmori, A., et al., "Behaviour of Molten Droplets Impinging on Flat Surfaces", Proceedings of the 7th National Thermal Spray Conference, Boston, USA, 1994, pp. 563-568.
- [70] Smith, M. F., et al., "An Investigation of the Effects of Droplet Impact Angle in Thermal Spray Deposition", Proceedings of the 7th National Thermal Spray Conference, Boston, USA, 1994, pp. 603-608.
- [71] Mostaghimi, J., et al., "Droplet Impact and Solidification in a Thermal Spray Process: Droplet-Substrate Interactions", Proceedings of the 9th National Thermal Spray Conference, Ohio, USA, 1996, pp. 637-646.
- [72] Bhol, R., et al., "Splat Solidification of Tin Droplets", Proceedings of the 9th National Thermal Spray Conference, Ohio, USA, 1996, pp. 657-663.
- [73] Jiang, X. L., et al., "Induction Plasma Spraying of Refractory Materials", Proceedings of 13th International Thermal Spray Conference, Florida, USA, 1992, pp. 39-44.
- [74] Gawne, D. T., et al., "Splat Morphology and Adhesion of Thermally Sprayed Coatings", Proceedings of the 8th International Thermal Spray Conference, Japan, 1995, pp. 779-784.
- [75] Roemer, T. J., et al., "Surface Roughness of Thermal Spray Coatings Made with Off-Normal Spray Angles", Journal of Thermal Spray Technology, Vol. 7, Issue 2, 1998, pp. 219-228.
- [76] Greving, J. D., et al., "The Effect of Residual Stress in HVOF Tungsten Carbide Coatings on the Fatigue Life in Bending of Thermal Coatings", Journal of Thermal Spray Technology, Vol. 7, Issue 4, 1998, pp. 546-552.
- [77] Kroupa, F., et al., "Residual Stresses in Graded Thick Coatings", Report from Institute of Electrical Engineering of Academy of Science, Czech Republic, Vol. 39, 1993, pp. 29-74.

- [78] Kroupa, F., "Stresses in Coatings on Cylindrical Surfaces", Report from Institute of Electrical Engineering of Academy of Science, Czech Republic, Vol. 39, 1994, pp. 243-274.
- [79] Sampath, S., et al., "Role of thermal spray processing method on the microstructure, residual stress and properties of coatings: an integrated study for Ni-5 wt.%Al bond coats", Materials Science and Engineering, Vol 364, 2004, pp. 216-231.
- [80] Stokes, J., & Looney, L., "Residual Stress in HVOF Thermally Sprayed Thick Deposits", Surface and Coatings Technology, Vol. 177-178, 2004, pp. 18-23.
- [81] Itoh, A., & Clyne. T. W., "Initiation and Propagation of Interfacial Cracks During Spontaneous Debonding of Thermally Sprayed Coatings", Proceedings of the 8th National Thermal Spray Conference, Texas, USA, 1995, pp. 425-432.
- [82] Vijgen, R. O. E., et al., "Mechanical Measurement of the Residual Stress in Thin PVD Films" Journal of Thin Solid Films, Vol. 270, 1995, pp. 264-269.
- [83] Senderoff, S., et al., Journal of Research, National Bureau of Standards, Vol. 42, Issue 2, 1949, pp. 105-123.
- [84] Tipton, A. A., "The Effect of HVOF Sprayed Coatings on the Elevated Temperature High Cycle Fatigue Behaviour of a Martensitic Stainless Steel", Proceedings of the 8th National Thermal Spray Conference, Texas, USA, 1995, pp. 463-468.
- [85] Shadley, J. R., et al., "Effects of Coating Thickness and Residual Stress on Bond Strength of C633-79 Thermal Spray Coating Test Specimens", Proceedings of the 7th National Thermal Spray Conference, Boston, USA, 1994, pp. 639-645.
- [86] Stokes, J. and Looney, L. "HVOF System Definition to Maximize the Thickness of Formed Components", Surface and Coating Technology., Vol 148 (No. 1) 2001, p. 18-24.

- [87] Sobolev, V. V., et al., "Development of Coating Structure and Adhesion During High Velocity Oxygen-Fuel Spraying of WC-Co Powder on a Copper Substrate", *Journal of Thermal Spray Technology*, Vol. 9, Issue 1, 2000, pp. 100-106.
- [88] Suresh, A., & Mortensen, A., "Fundamentals of Functionally Graded Materials: Processing and Thermomechanical Behaviour of Graded Metals and Metal-Ceramic Composites", The University Press, Cambridge, ISBN No 1861250630, 1998.
- [89] Dussoubs, B., et al., "Modelling of Plasma Spraying of Two Powders", *Journal of Thermal Spray Technology*, Vol. 10, Issue 1, 2001, pp. 105-110.
- [90] Khor, A., et al., "Plasma Sprayed Functionally Graded Thermal Barrier Coatings", *Material Letters*, Vol. 38, Issue 6, 1999, pp. 437-444.
- [91] Khor, K.A., & Gu, W.Y., "Effects of Residual Stress on the Performance of Plasma Sprayed Functionally Graded $\text{ZrO}_2/\text{NiCoCrAlY}$ Coatings", *Journal of Material Science and Engineering A*, Vol. 277, Issue 1-2, 2000, pp. 64-76.
- [92] Celik, E., et al., "Oxidation Behaviour of Functionally Gradient Coatings Including Different Composition of Cermets", *Surface and Coatings Technology*, Vol. 142-144, 2001, pp. 551-556.
- [93] Sampath, S., et al., "Friction and Wear Properties of WC-Co and Mo-Mo₂C Based Functionally Graded Materials", *Wear*, Vol. 249, 2001, pp. 1103-1115.
- [94] Peters, M., et al., "Graded Coatings for Thermal, Wear and Corrosion Barriers", *Materials Science and Engineering A*, Vol. 362, 2003, pp. 61-80.
- [95] Kim, J. H., et al., "Evaluation of Functionally Graded Thermal Barrier Coatings Fabricated by Detonation Gun Spray Technique", *Surface and Coatings Technology*, Vol. 168, 2003, pp. 275-280.

- [96] Sampath, S., et al., "Thermal Spray Processing of FGM", MRS Bulletin, Vol. 20, Issue 1, 1995, pp. 27-31.
- [97] Khor, K. A., et al., "Functionally Graded ZrO_2 -NiCrAlY Coatings Prepared by Plasma Spraying Using Premixed, Spheroidized Powders", Surface and Coatings Technology", Vol. 96, 1997, pp. 305-312.
- [98] Khor, K. A., & Gu, W.Y., "Thermal Properties of Plasma-Sprayed Functionally Graded Thermal Barrier Coatings", Thin Solid Films, Vol. 372, Issue 1-2, 2000, pp. 104-113.
- [99] Khor, K. A., et al., "Mechanical Behaviour of Plasma-sprayed Functionally Graded YSZ/NiCoCrAlY Composite Coatings", Surface and Coatings Technology", Vol. 139, Issue 2-3, 2001, pp. 200-206.
- [100] Walter, L., et al., "Functionally Graded Hardmetals", Journal of Alloys and Compounds", Vol. 338, Issue 1-2, 2002, pp. 194-212.
- [101] Avci, E., et al., "Evaluation of Functionally Graded Coatings Produced by Plasma-Spray Technique", Surface and Coatings Technology, Vol. 116-119, 1999, pp. 292-295.
- [102] Pan, C., et al., "Microstructural Characteristics in Plasma Sprayed Functionally Graded ZrO_2 /NiCrAl Coatings", Surface and Coatings Technology, Vol. 162, 2003, pp. 194-201.
- [103] Voevodin, A. A., et al., "Investigation into Three-Dimensional Laser Processing of Tribological Coatings", Surface and Coatings Technology, Vol. 107, 1998, pp. 12-19.
- [104] ASM Handbook, "Mechanical Testing", Vol. 8 The Materials Information Society, ISBN No 0871700077, 1985.
- [105] PQ Corporation (online), Date of access 12/04/05

- [106] Barrier Group Limited (UK) (Online), <http://www.corrosion.com/thermal.html>, access date 05/03/2007
- [107] P.S. Sidky, and M.G. Hocking, "Review of Inorganic Coatings and Coating Processes For Reducing Wear and Corrosion", Brit. Corros. J., Vol 34 (No. 3), 1999, p. 171-183.
- [108] B.S. Sidhu and S. Parkash, "Degradation behavior of Ni₃Al Plasma-Sprayed Boiler Tube Steels in an Energy Generation System", J. Mat.Engg. Perfor., Vol 14 (No. 3), 2005, p.356-362.
- [109] A. Ul-Hamid, "Diverse Scaling Behavior of the Ni-20Cr Alloy", Maters. Chem. Phys., Vol 80,2003,p. 135-142.
- [110] T. Sundararajan, S. kuroda, T. Itagaki, and F. Abe, "Steam Oxidation Resistance of Ni-Cr Thermal Spray Coatings on 9Cr-1Mo Steel. Part 2: 50 Ni-50Cr", ISIJ Int., Vol 43 (No. 1), 2003, p. 104-111.
- [111] Parker, D. W., "HVOF Moves into the Industrial Mainstream", Journal of Advanced Materials and Processes, Vol. 146, Issue 1, 1994, pp. 31-35.
- [112] G. Davies, M. Breitsameter, Weld. Res. Abroad, Vol. 43, Issue 1, 1997, pp. 5.
- [113] R Thorpe, R. J., & Thorpe, M. L., "High Pressure HVOF: An Update", Proceedings of the 5th National Thermal Spray Conference, California, USA, 1993, pp. 199-204.
- [114] B. Irving, Weld. J. Vol.79, Issue 2, 2000, pp. 42.
- [115] William F.Smith. ,"Structure and Properties of Engineering Alloys",McGraw-Hill Publishing Co.1981.

- [116] C.H. Lee, K.O. Min, "Effects of heat treatment on the microstructure and properties of HVOF-sprayed Ni–Cr–W–Mo–B alloy coatings", *Surf. Coat. Technol.* Vol.132 , Issue 1, 2000, pp. 49.
- [117] J.M. Guilemany, J. Fernánde, J. Delgado, A.V. Benedetti, F. Climent, "Effects of thickness coating on the electrochemical behaviour of thermal spray Cr_3C_2 –NiCr coatings", *Surface and Coating Technology* ,Vol.153, issue 2–3,2002, pp. 107-113.
- [118] L. Gil, M.H. Staia, "Microstructure and properties of HVOF thermal sprayed NiWCrBSi coatings", *Surface and Coating Technology*, Vol. 120, 1999, pp. 423.
- [119] A.H. Dent, A.J. Horlock, D.G. McCartney, S.J. Harris," Microstructure formation in high velocity oxy-fuel thermally sprayed Ni–Cr–Mo–B alloys", *Materials Science and Engineering A*, vol. 283, Issue 1-2, 2000, pp. 242-250
- [120] D. Harvey, O. Lunder, R. Henriksen, in: C.C. Berndt (Ed.), *Proceedings of the 1st International Thermal Spray Conference*, Montreal, Canada, ASM International, Materials Park, OH, 2000 May, p. 991.
- [121] Y.T. Horng, T.C. Chang, J.W. Hsu, H.C. Shih, "The erosive wear and corrosion behavior of zinc- and aluminum-coated steels in simulated coastal environment", *Surface and Coating Technology*, Vol. 168, Issue 2– 3, 2003, pp.209-215.
- [122] E.A. Sacco, N.B. Alvarez, J.D. Culcasi, C.I. Elsner, A.R. Di Sarli, "Effect of the plastic deformation on the electrochemical behavior of metal coated steel sheets", *Surface and Coating Technology*, Vol. 168, Issue 2– 3, 2003, pp.115-122.
- [123] P.R. Sere', M. Zapponi, C.I. Elsner, A.R. Sarli, "Comparative corrosion behaviour of 55Aluminium-zinc alloy and zinc hot-dip coatings deposited on low carbon steel substrates", *Corrosion and. Science*, Vol. 40, Issue 10, 1998, pp. 1711-1723.

- [124] N. Parkansky, R.L. Boxman, S. Goldsmith, Yu. Rosenberg, "Influence of transverse current during In-O vapour deposition", *Surface & coatings technology*, Vol. 76–77, Issue 1– 3, 1995, pp. 197-201.
- [125] S. Kuroda, M. Takemoto, in: C.C. Berndt (Ed.), *Proceedings of the 1st International Thermal Spray Conference*, Montreal, Canada, ASM International, Materials Park, OH, 2000 May, p. 1017.
- [126] M. Knepper, J. Spriestersbach, J. Wisniewski, in: DVS (Ed.), *United Thermal Spray Conference*, Du'sseldorf, ASM Thermal Spray Society, Materials Park, 1999, p. 106.
- [127] J. Hazan, Ch. Coddet, *Materials and Science Forum*, Vol. 289–292, Issue 2, 1997, pp. 719.
- [128] V.A.D. Souza, A. Neville, "Linking electrochemical corrosion behaviour and corrosion mechanisms of thermal spray cermet coatings (WC–CrNi and WC/CrC–CoCr)", *Material Science and Engineering A*, Vol.352, Issue 1– 2, 2003, pp. 202-211.
- [129] Rogne,T.,Solem,T.,and Berget,J., "Effect of Composition and Corrosion Properties of the Metallic Matrix on the Erosion Corrosion Behaviour of HVOF Sprayed WC-Coatings.", *Thermal Spray Technology*, 1992, p.165.
- [130] Al-Fadhli, Hussain Y, "Analysis of the Effect of Bending, Fatigue, Erosion-Corrosion and Tension on HVOF Coating of Metallic Surfaces", *Ph.D.Thesis*, Dublin City University, 2005.
- [131] Berget.J., "Influence of Powder and Spray Parameters on Erosion and Corrosion Properties of HVOF Sprayed WC-Co-Cr Coatings", *Norwegian University of Science and Technology, Norway, Engineering Material Science*, 1998, p.90.
- [132] Wei-Min Zhao, Yong Wang, et al., "Corrosion mechanism of NiCrBSi coatings deposited by HVOF", *Surface & Coatings Technology*, Vol. 190, 2005, p. 293– 298.

- [133] Suman, S., "Corrosion and Erosion-Corrosion of High Velocity Oxy-Fuel (HVOF) Sprayed Coatings", Ph.D. Thesis, University of Glasgow, 2000, p.236-240.
- [134] Evans, H. E., et al., "Smart Overlay Coatings-Concept and Practice", Surface and Coatings Technology, Vol. 149, 2002, pp. 236-244.
- [135] Flexographic Technical Association Document, (Online) <http://www.cellramic.storkgroup.com/thermal.htm>, Date of access 04/01/05.
- [136] Khor, K. A., et al., "Plasma Spraying of Functionally Graded Hydroxyapatite/Ti-6Al-4V Coatings", Surface and Coatings Technology, Vol. 168, 2003, pp. 195-201.
- [137] Shaw, L. L., "Thermal Residual Stresses in Plates and Coatings of Multilayered and Functionally Graded Materials", Composites B, Vol. 29, 1998, pp. 199-210.
- [138] Teixeira, V., "Numerical Analysis of the Influence of Coating Porosity and Substrate Elastic Properties on the Residual Stresses in High Temperature Graded Coatings", Surface and Coatings Technology, Vol. 146-147, 2001, pp. 79-84.
- [139] Ma, F., et al., "Diamond-Like Carbon Gradient Film Prepared by Unbalanced Sputtering and Plasma Immersion Ion Implantation Hybrid Technique", Materials Letters, Vol. 57, 2002, pp. 82-86.
- [140] L. Pawlowski, The Science and Engineering of Thermal Spray Coatings, Wiley, 1995.
- [141] K. Tani, Y. Harada, Y. Kobayashi, in: Proceedings of Fifteenth International Thermal Spray Conference, 1998, pp. 951-956.
- [142] W.J. Brindley, Journal of Thermal Spray Technology, Vol. 6, Issue 1, 1997, pp. 85.
- [143] R.H. Unger, in: Proceedings of National Thermal Spray Conference, ASM International, Materials Park, OH, 1987, pp. 365-370.

- [144] D. Cook, Materials science and engineering, Ph.D. thesis, SUNY, Stony Brook, 2001.
- [145] S. Sampath, G. Bancke, H. Herman, S. Rangaswamy, "Plasma Sprayed Ni--Al Coatings", Surf. Eng., Vol. 5, Issue 4, 1989, pp. 293-298.
- [146] Parks, W. P., et al., "Thermal Barrier Coatings Issues in Advanced Land-Based Gas Turbines", Journal of Thermal Spray Technology, Vol. 6, Issue 2, 1997, pp. 187-192.
- [147] Mutasim, Z., et al., "Thermal Barrier Coatings for Industrial Gas Turbine Applications: An Industrial Note", Journal of Thermal Spray Technology, Vol. 6, Issue 1, 1997, pp. 105-108.
- [148] Yonushonis, T. M., "Overview of Thermal Barrier Coatings in Diesel Engines", Journal of Thermal Spray Technology, Vol. 6, Issue 1, 1997, pp. 50-56.
- [149] Miller, R. A., "Thermal Barrier Coatings for Aircraft Engines: History and Directions", Journal of Thermal Spray Technology, Vol. 6, Issue 1, 1997, pp. 35-42.
- [150] Beele, W., et al., "The Evaluation of Thermal Barrier Coatings-Status and Upcoming Solutions for Today's Key Issues", Surface and Coatings Technology, Vol. 120-121, 1999, pp. 61-67.
- [151] Stover, D., "Effects of Deposition Temperature and Thermal Cycling on Residual Stress State in Zirconia-Based Thermal Barrier Coatings", Surface and Coatings Technology, Vol. 120-121, 1999, pp. 103-111.
- [152] Hongbo, H., et al., "Effect of Thermal Exposure on the Microstructure and Properties of EB-PVD Gradient Thermal Barrier Coatings", Surface and Coatings Technology, Vol. 168, 2003, pp. 23-29.

- [153] Rangraj, S., et al., "Estimating the Fracture Resistance of Functionally Graded Thermal Barrier Coatings from Thermal Shock tests", *Surface and Coatings Technology*, Vol. 173, 2003, pp. 201-212.
- [154] Kon, M., et al., "Development of Calcium Phosphate Based Functional Gradient Bioceramics", *Biomaterials*, Vol. 16, Issue 9 1995, pp. 709-714.
- [155] Kumar, R. R., et al., "Functionally Graded Bioactive Coatings of Hydroxyapatite/Titanium Oxide Composite System", *Materials Letters*, Vol. 55, 2002, pp. 133-137.
- [156] Wang, C. X., "Functionally Graded Calcium Phosphate Coatings Produced by Ion Beam Sputtering/Mixing Deposition", *Biomaterials*, Vol. 22, Issue 12, 2001, pp. 1619-1626.
- [157] Remer, P., et al., "Realisation of Graded Coatings for Biomedical Use", *Materials Science Forum*, Vol. 308-311, 1999, pp. 368-373.
- [158] Liu, G., et al., "Graded Ni-P-PTFE Coatings and Their Potential Applications", *Surface and Coatings Technology*, Vol. 155, 2002, pp. 279-284.
- [159] Verne, E., et al., "Graded Coatings on Ceramic Substrates for Biomedical Applications", *Journal of European Ceramic Society*, Vol. 21, 2001, pp. 2855-2862.
- [160] Park, E., et al., "Graded Coatings of Hydroxyapatite and Titanium by Atmospheric Plasma Spraying", *Material Letters*, Vol. 40, 1999, pp. 228-234.
- [161] Ding, S. J., "Properties and Immersion Behavior of Magnetron-Sputtered Multi-Layered Hydroxyapatite/Titanium Composite Coatings", *Biomaterials*, Vol. 24, Issue 23, 2003, pp. 4233-4238.
- [162] Kumar, R. R., et al., "Functionally Graded Coatings of HA-G-Ti Composites and their in Vivo Studies", *Materials Science and Engineering A*, Vol. 334, 2002, pp. 156-162.

[163] Khor, K. A., et al., "Significance of Melt-Fraction in HVOF Sprayed Hydroxyapatite Particles, Splats and Coatings", *Biomaterials*, Vol. 25, 2004, pp. 1177-1186.

[164] Miller, W. S., et al., "Recent Development in Aluminium Alloys for the Automotive Industry", *Material Science and Engineering A*, Vol. 280, 2000, pp. 37-49.

[165] European Commission White Book, "European Transport Policy for 2010: Time to Decide".

[166] Schumann, S., et al., "Research for a - New Age of Magnesium - in the Automotive Industry", *Journal of Materials Processing Technology*, Vol. 117, 2001, pp. 276-281.

[167] Gray, J. E., et al., "Protective Coatings on Magnesium and its alloys-A Critical Review", *Journal of Alloys and Compounds*, Vol. 336, 2002, pp. 88-113.

[168] Nie, X., et al., "Thickness Effects on the Mechanical Properties of Micro-Arc Discharge Oxide Coatings on Aluminium Alloys", *Surface and Coatings Technology*, Vol. 116-119, 1999, pp. 1055-1060.

[169] Funatani, K., "Emerging Technology in Surface Modification of Light Metals", *Surface and Coatings Technology*, Vol. 133-134, 2000, pp. 264-272.

[170] Edrisy, A., et al., "Wear of Thermal Spray Deposited Low Carbon Steel Coatings on Aluminium Alloys", *Wear*, Vol. 251, 2001, pp. 1023-1033.

[171] Merlo, A. M., "The Contribution of Surface Engineering to the Product Performance in the Automotive Industry", *Surface and Coatings Technology*, Vol. 174-175, 2003, pp. 21-26.

[172] Wenzelburger, M., et al., "Modeling of Thermally Sprayed Coatings on Light Metal Substrates: - Layer Growth and Residual Stress Formation", Surface and Coatings Technology, Vol. 180-181, 2004, pp. 429-435.

[173] Al-Fadhil. HY., "Performance Evaluation of (HVOF) Thermal Spray Coating Using Inconel-625 Powder", M.Sc.Thesis, King Fahd University of Petroleum & Minerals, 2003, p.109.

[174] Aylor; D. M., Hays; R. A., Ferrara; R. J., "Crevice Corrosion Performance of Candidate Naval Ship Seawater Valve Materials in Quiescent and Flowing Natural Seawater", July 1999, p.57, (Online) <http://www.stormingmedia.us>), Access Date-12/08/2005.

[175] Kohler; L. K. Aprigliano; L. F., " Process, Chemistry, and Property Relations for Spray Formed NiCr Alloys", Sept 2002, p.24. (online (<http://www.stormingmedia.us>), Access Date-12/08/2005.)

[176] Kirsten A., Oechsel M., and Moll R.F., "Carbide Containing Materials For Hard Chromium Replacement by HVOF Spraying", ITSC 2005 Proc., Basel, Switzerland, May 2-4,2005, ASM Int., p.957-962.

[177] Bouaricha S., Legoux J.-G. and Marple B.R., " HVOF Coatings Properties of the Newly Thermal Spray Composition WC-WB-Co", ITSC 2005 Proc., Basel, Switzerland, May 2-4,2005, ASM Int., p.981-985.

[178] Piegari, A., et al., "Ultraviolet-Graded Coatings for Lasers: Surface Optical Performance", Thin Solid Films, Vol. 373, 2000, pp. 155-158.

[179] Flame Spray Technology (Online), <http://www.fst.nl/files/fst-thermalspray.pdf>, Date of access 12/05/08

[180] Boy J. H., Kumar A., March P., Willis P., and Herman H., " Cavitation- and Erosion-Resistant Thermal Spray Coatings", (Online)

<http://owwww.cecer.army.mil/techreports/Boycavit/boycavit.jef.pdf> , Access date 11/03/2007

[181] Viking Pump, Inc., (online) <http://www.pumpschool.com/index.htm> Date of access 12/08/06

[182] Berget.J., "Influence of Powder and Spray Parameters on Erosion and Corrosion Properties of HVOF Sprayed WC-Co-Cr Coatings", Norwegian University of Science and Technology, Norway, Engineering Material Science.

[183] Harvey., "The Ultimate Coating-Thermal Spraying at Abington", TWI, Bulletin, 1994, pp.456.

[184] METCO / Perkin Elmer, Diamond Jet: Powder Feed Unit Manual, 1989.

[185] Stokes, J., "Propylene Vaporiser Procedure Manual", DCU, 2006

[186] METCO / Perkin Elmer, METCO Thermal Spraying: General Overview, 1989.

[187] SULZER METCO, "Thermal Spray Safety recommendations", (Online) www.sulzermetco.com, accessed date 12/9/2006.

[188] METCO / Perkin Elmer, "Diamond Jet: Process Manual", 1989.

[189] Stokes, J., "The Theory and Application of the HVOF Spray Process", 2003.

[190] Glancy, S. D., "How Metallographic Preparation Affects the Microstructure of WC/Co Thermal Spray Coatings", Proceedings of the 7th National Thermal Spray Conference, Boston, USA, 1994, pp. 771-777.

[191] Glancy, S. D., "Preserving the Microstructure of Thermal Spray Coatings", Journal of Advanced Materials and Processes, Vol. 148, Issue 1, 1995, pp. 37-40.

[192] Pugh S., Total Design Integrated, Methods for Successful Product Engineering, Pub. Addison-Wesley, 1991.

[193] Material Properties, (Online)

http://www.mcelwee.net/html/densities_of_various_materials.html, Access date: 10/4/2005.

[194] Lyons P., Automation of HVOF Thermal spraying Equipment, Final year Project, Dublin City University, 2000.

[195] Dorf R. C., Bishop, R. H., Modern Control System, 7th edition, Pub. Addison-Wesley, 1995.

[196] Tooley, M., Pc Based Instrumentation and Control, 2nd edition, Pub. Addison-Newnes, 1995.

[197] National Instruments, (Online) www.ni.com, Access date 5/2/2007.

[198] National Instruments, DAQ, AT E Series User Manual, May 2002 edition.

[199] Hyperphysics, (Online) <http://hyperphysics.phy-astr.gsu.edu/Hbase/electronic/opampvar.html#c3>, Access date 5/2/2006.

[200] Wells, L.K., 1995, Lab VIEW Student Edition User's Guide, Pub.Prentic-Hall.

[201] Compumotor Division, Parker Hannifin Corporation, LX Indexer/ Driver User Guide, 1997.

[202] ANSYS Version 8.1 Help menu, 2006.

[203] James, E. A. J., & William, L. H., "Introduction to Fluid Mechanics", Prentice Hall, Englewood Cliffs, New jersey, ISBN No. 0134839412, 1980.

APPENDIX A-Detail Design Drawings

Figure A1: Schematic drawing of the motor holder and bush cover.

Figure A2: Schematic drawing of the needle shaped bolt.

Figure A3: Schematic drawing of the top Plate of the powder holder.

Figure A4: Schematic drawing of the cover plate or base plate of the motor mounting.

Figure A5: Schematic of the individual powder holder [49].

Figure A6: Schematic of the base plate of the powder holder [49].

Figure A7: Sectional assembly drawing of the base plate, the top plate and the individual powder holders [49].

Figure A8: Schematic drawing of the top part of the funnel shaped powder flow path.

Figure A9: Schematic drawing of the bottom part of the funnel shaped mixing zone.

Figure A10: Schematic assembly drawing of the bottom funnel shape design.

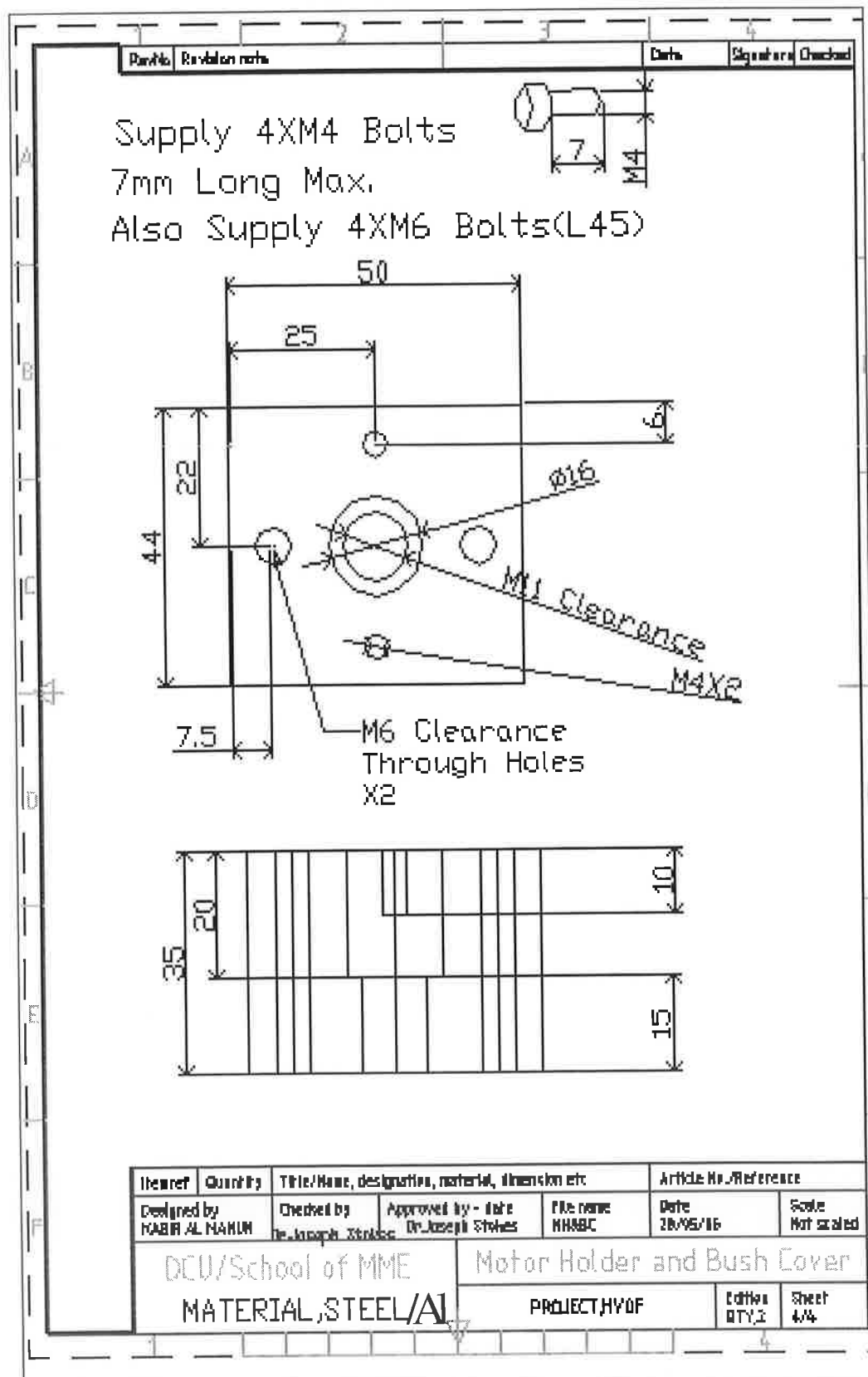


Figure A1: Schematic drawing of the motor holder and bush cover.

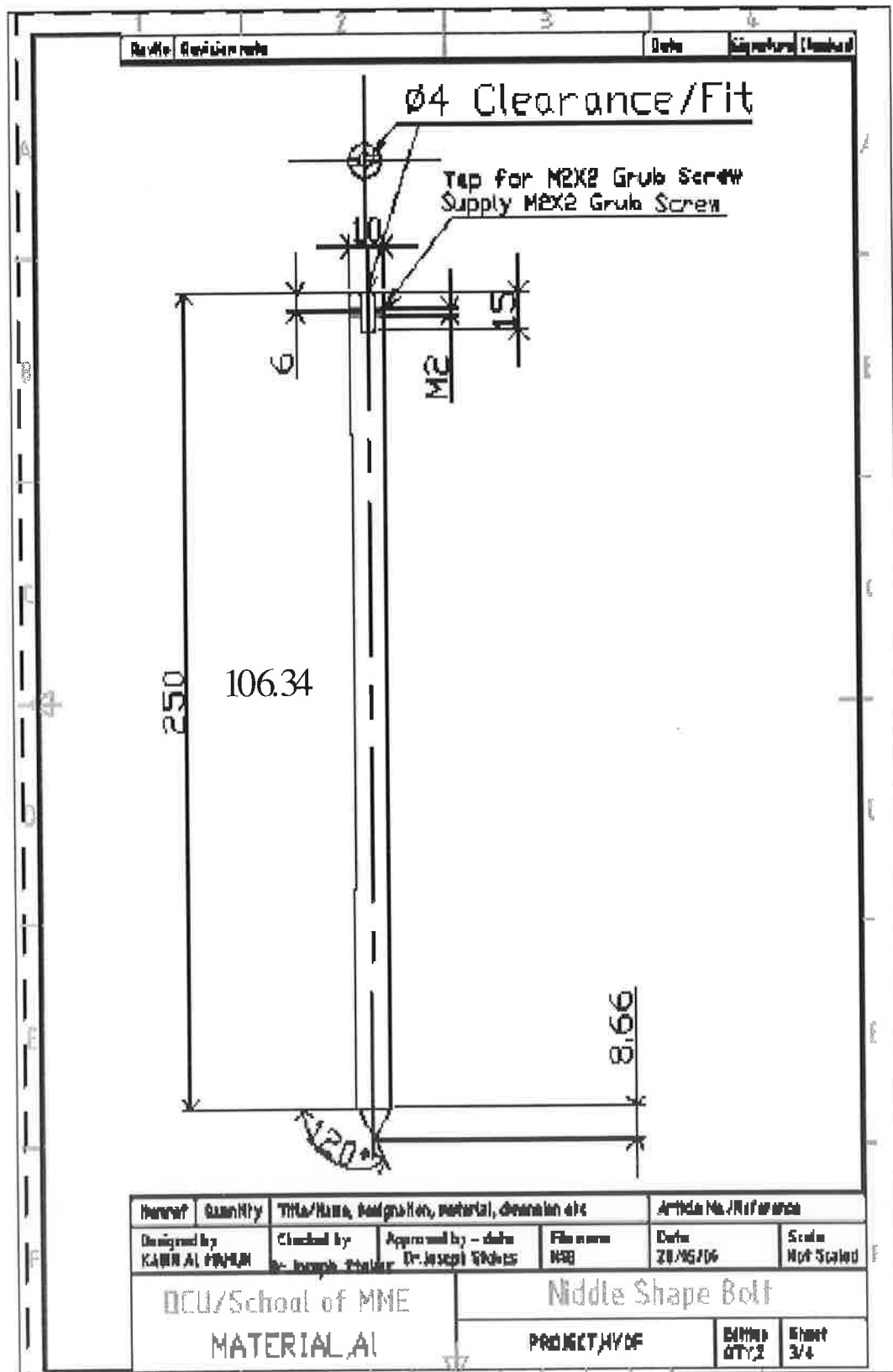


Figure A2: Schematic drawing of the needle shaped bolt.

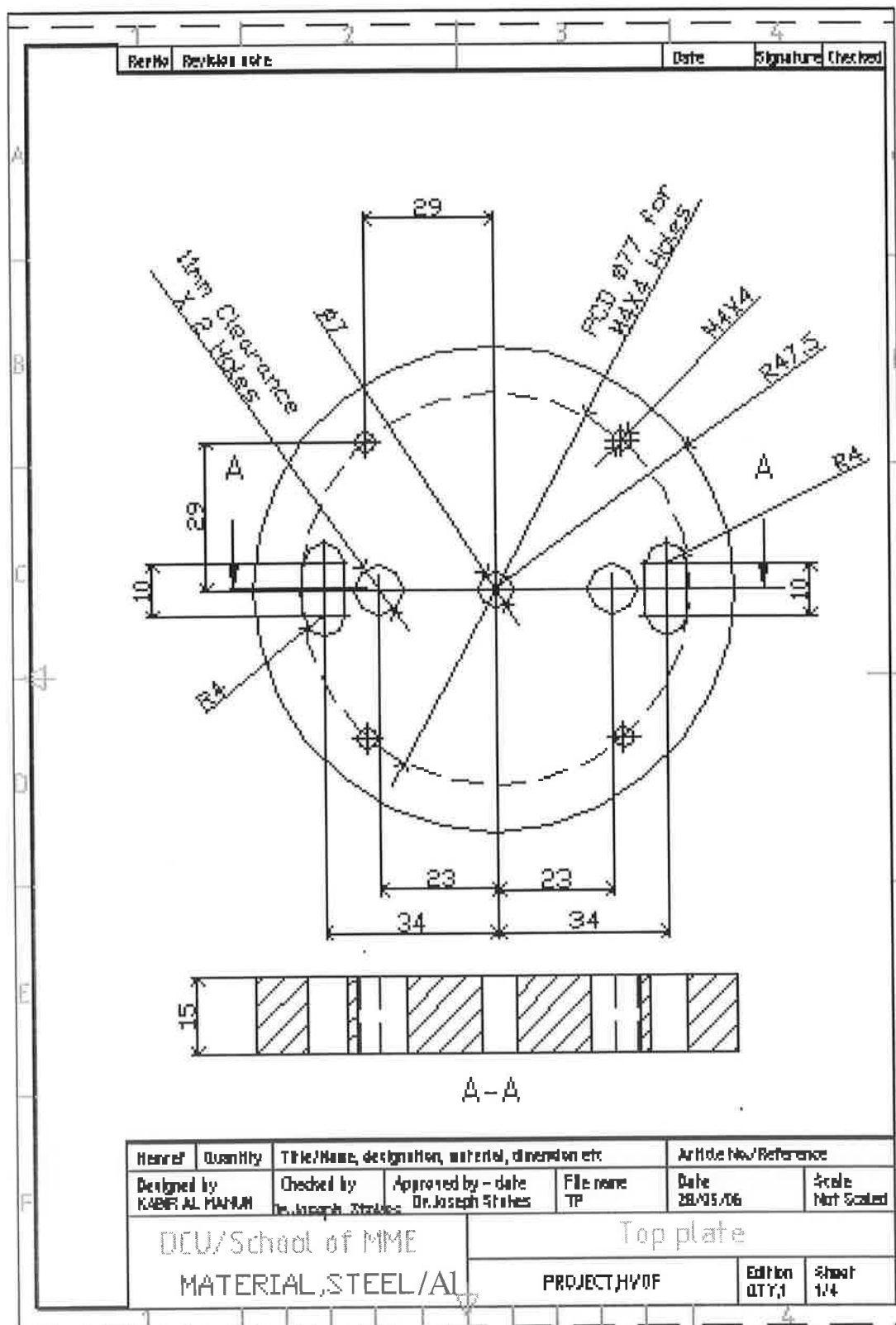


Figure A3: Schematic drawing of the top Plate of the powder holder.

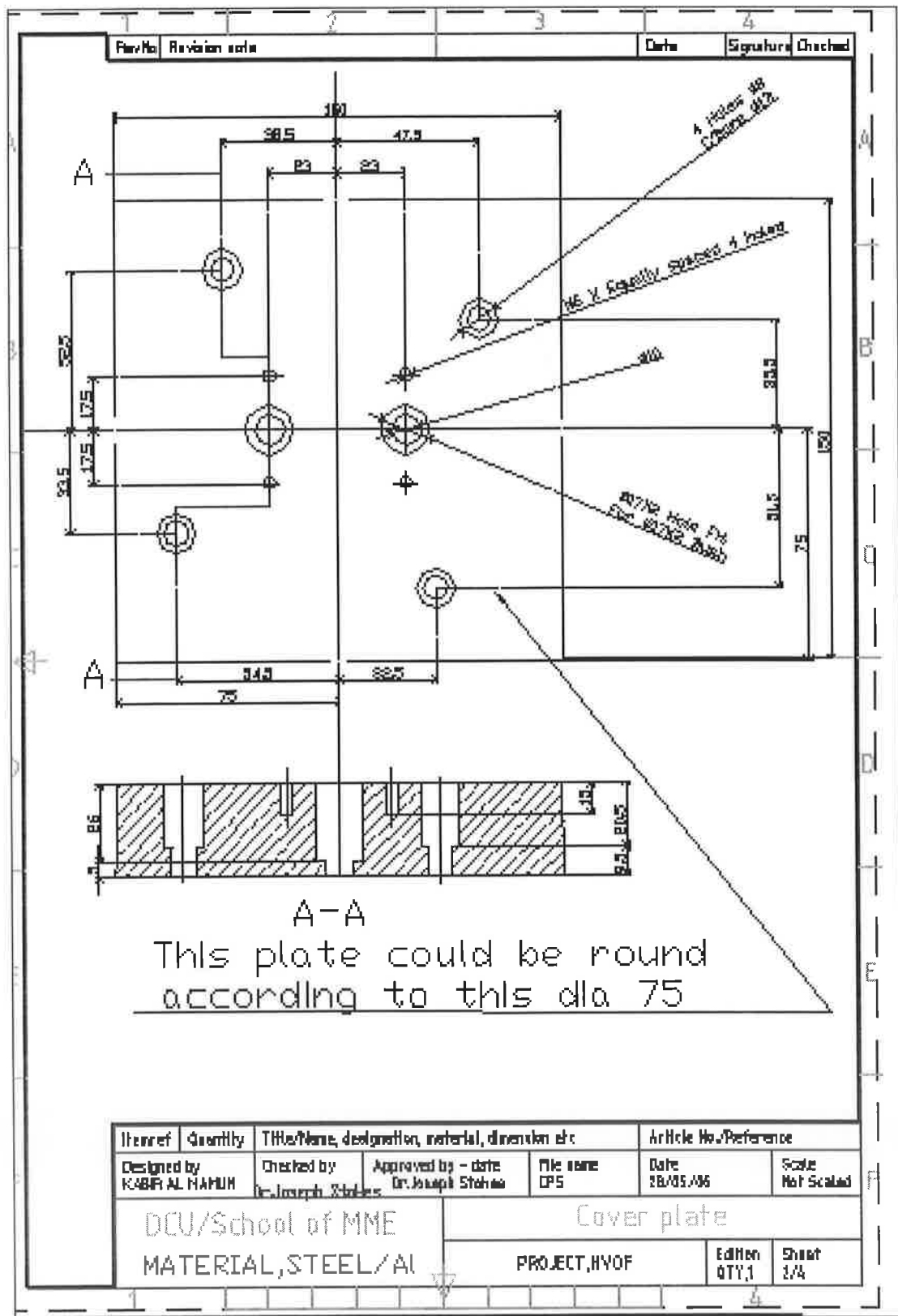
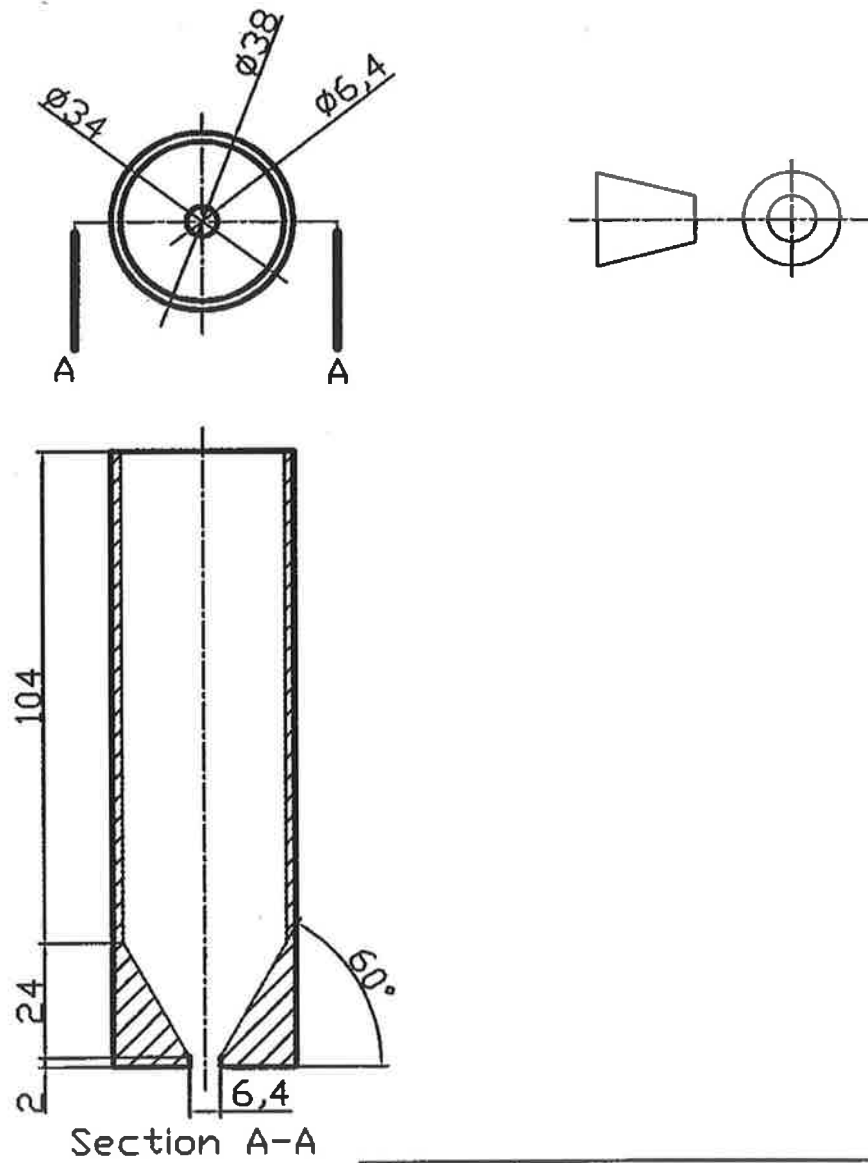


Figure A4: Schematic drawing of the cover plate or base plate of the motor mounting.

All dimension are in mm



THIRD ANGLE PROJECTION	MEng, School of MME		
	POWDER HOLDER		
Modulus Hason	QTY: 2	MATERIAL: STAINLESS STEEL	
DATE: 22/11/01	SCALE: NONE	PROJECT: HVOF	SHEET: 3 OF 5

Figure A5: Schematic of the individual powder holder [49].

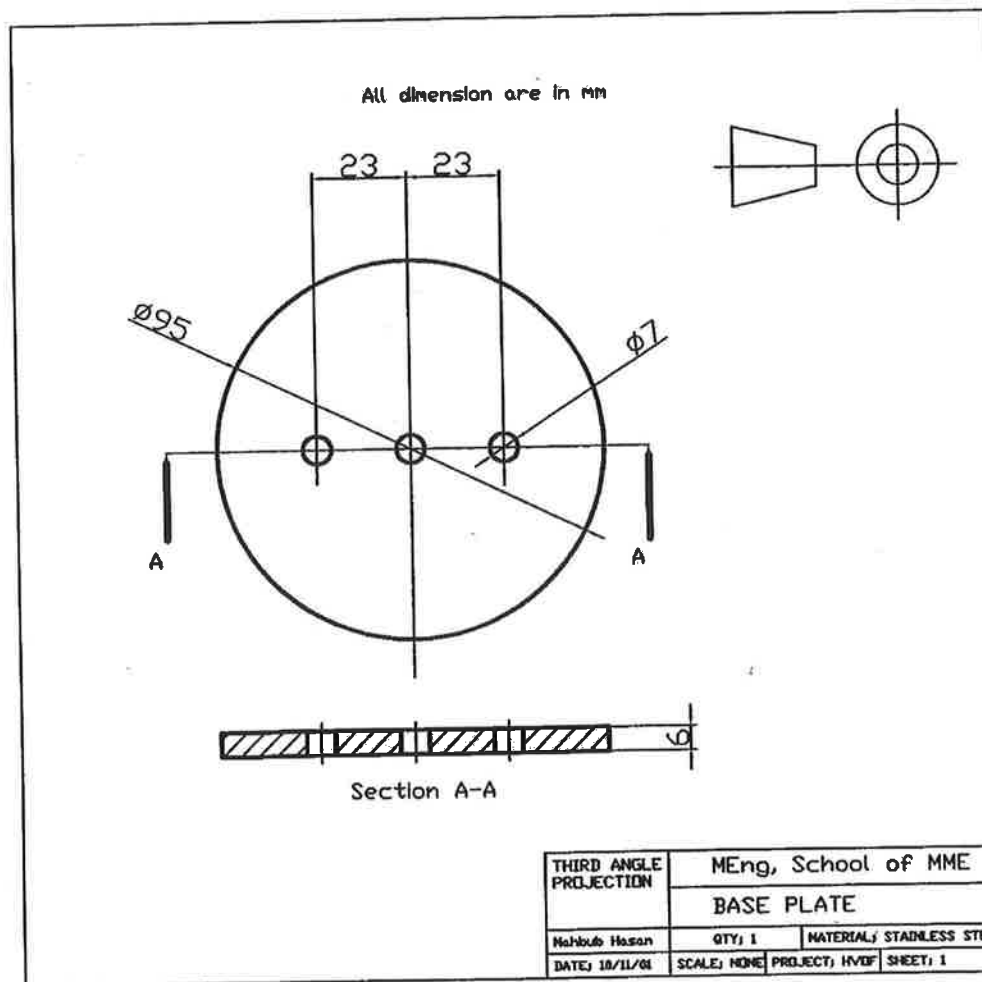


Figure A6: Schematic of the base plate [49].

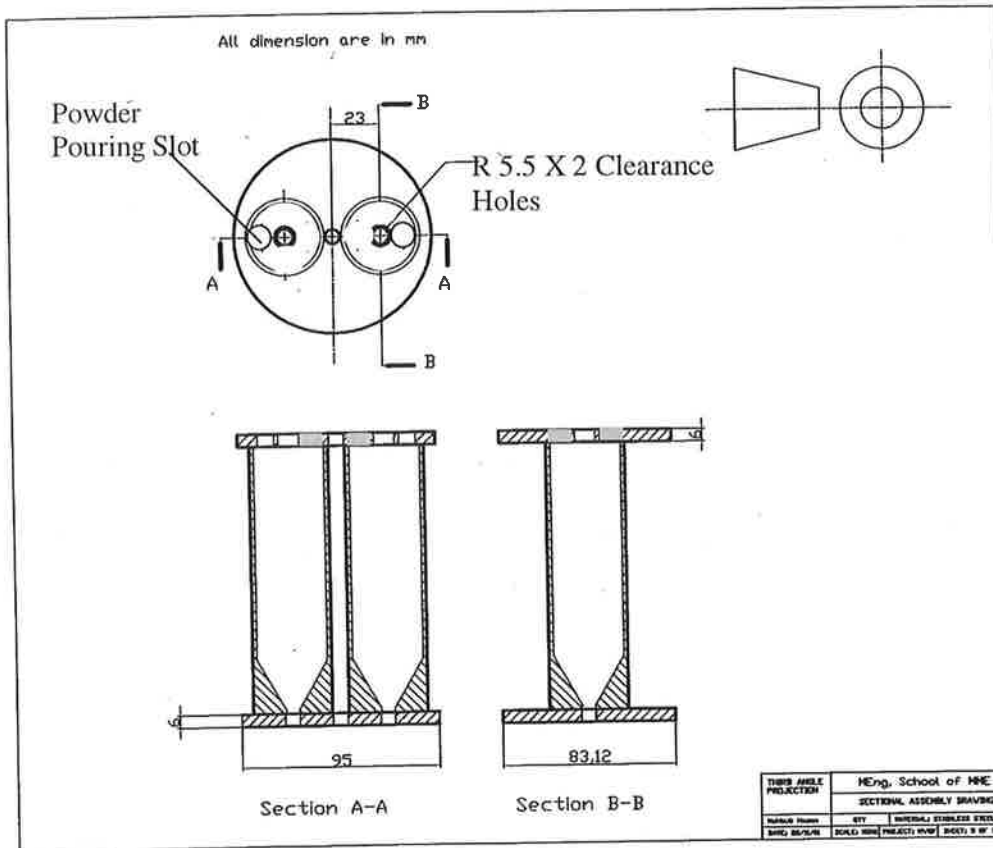


Figure A7: Sectional assembly drawing of the base plate, the top plate and the individual powder holders [49].

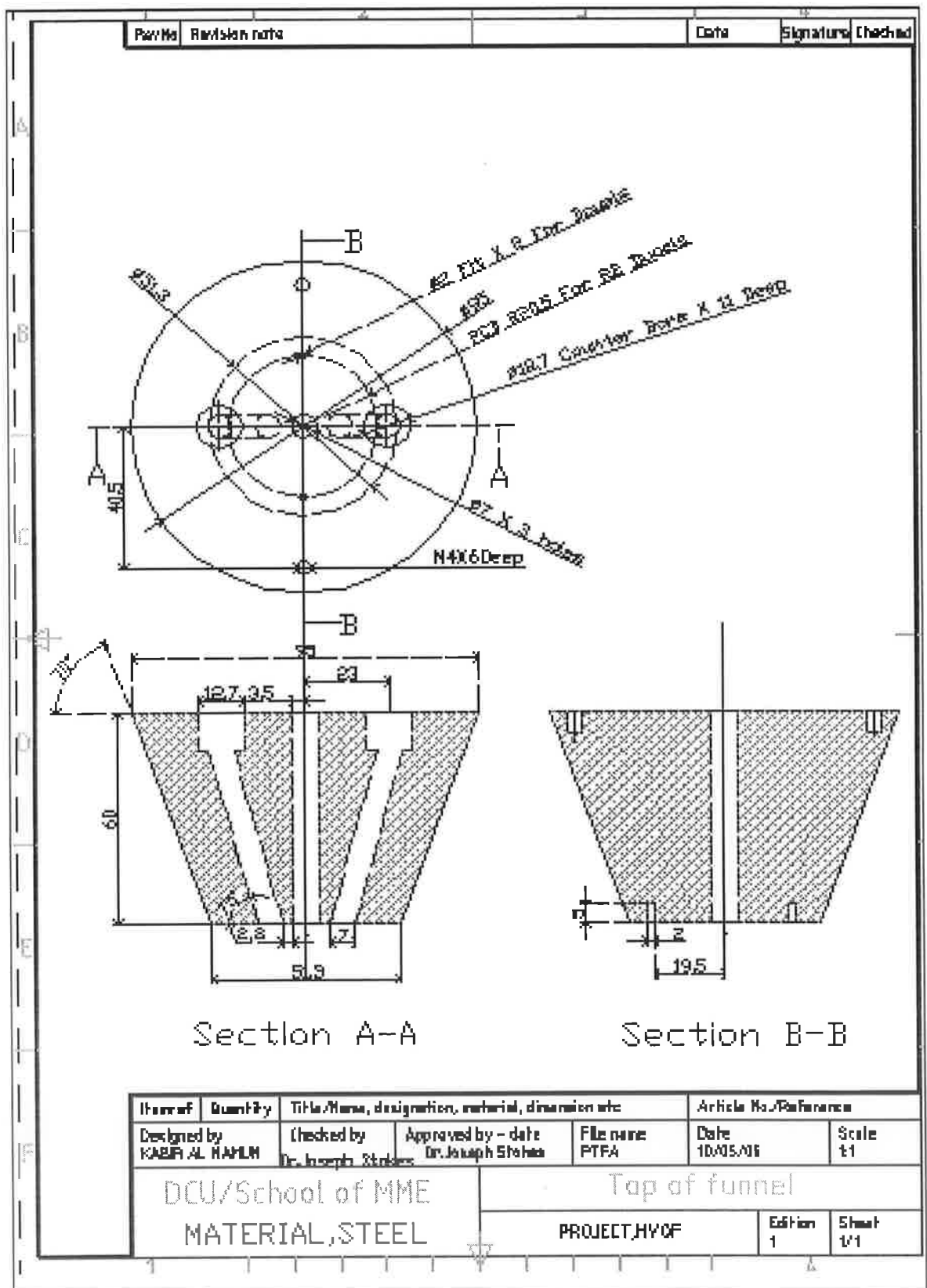


Figure A8: Schematic drawing of the top part of the funnel shaped powder flow path.

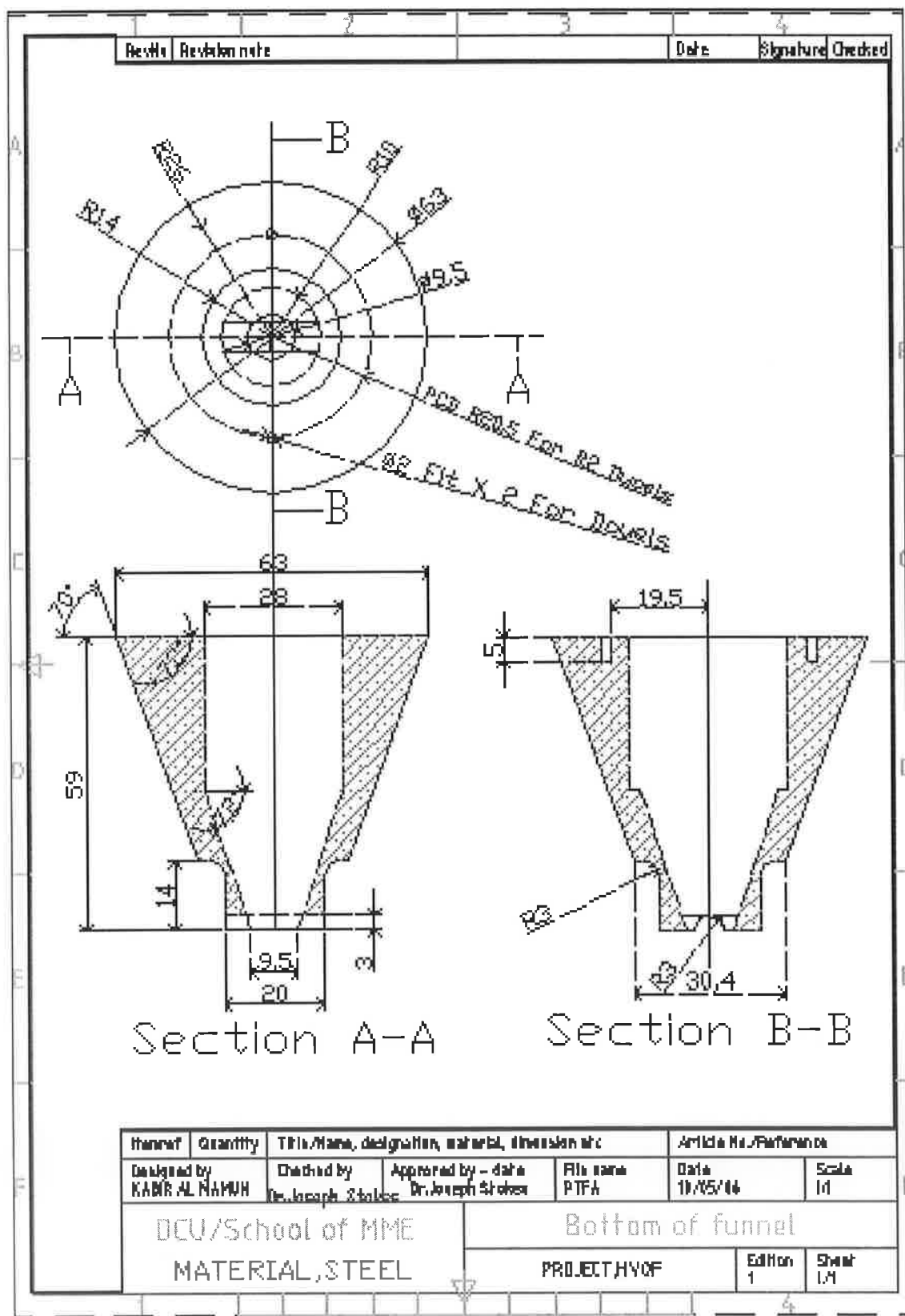


Figure A9: Schematic drawing of the bottom part of the funnel shaped mixing zone.

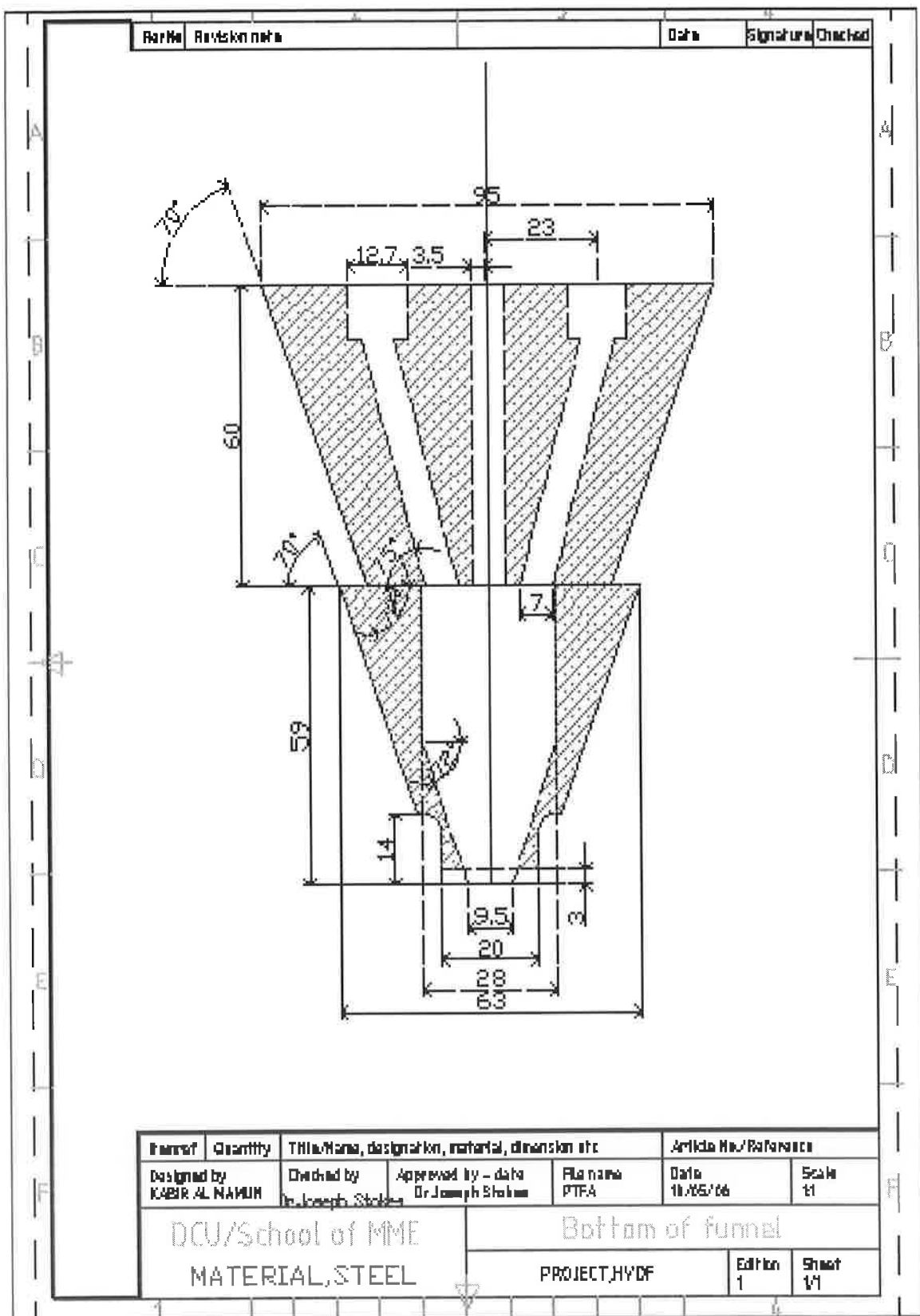


Figure A10: Schematic assembly drawing of the bottom funnel shape design.

APPENDIX B-Data Sheet for the Electrical Components

Appendix B1: Data sheet of the linear actuators (Stock no.: RS 340-6445), actuators wiring instruction and drivers (Stock no.: RS 217-3611)

Appendix B2: Data sheet of AT-MIO-16XE-10 DAQ card

Appendix B3: Data sheet of this 741-type op amp

Digital linear actuators

92000 series DLA's

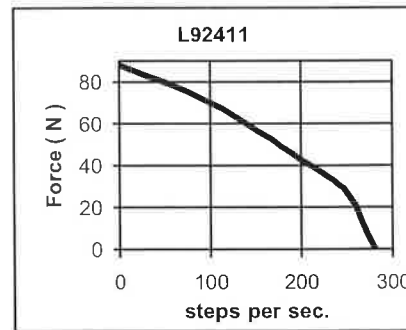
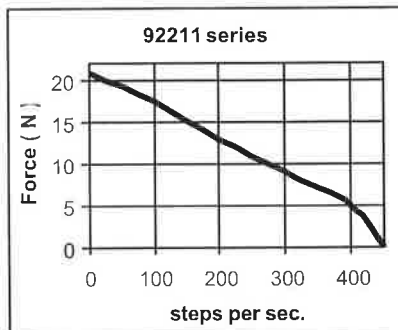
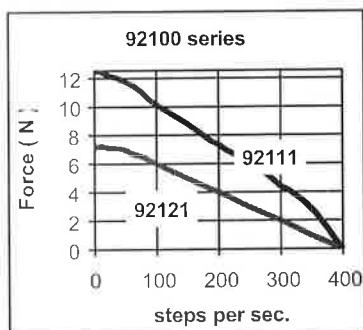
The range of DLA's comprise two versions. Both types are based on 4 phase permanent magnet stepper motor technology and utilise a rotor with an internal thread to provide linear motion via a leadscrew.

The **L92000 series** are provided with a leadscrew which may be attached to the driven mechanism. When the leadscrew is prevented from rotating the operation of the motor imparts linear motion to the screw. The maximum travel of the mechanism is between 47 & 76 mm depending on the model although optional 300 mm long leadscrews may be purchased to increase travel distance if required.

The **K92000 series** incorporate a keyway in the actuator's output slideway thereby providing the spindle with linear motion. This design is ideal for driving spring loaded mechanisms over limited travel.



Typical performance



The above performance describes pull-in (start/stop) operation when the actuators are driven with an L/R drive. Increased performance can be obtained with L/4R drive techniques using drives such as the EM162 series

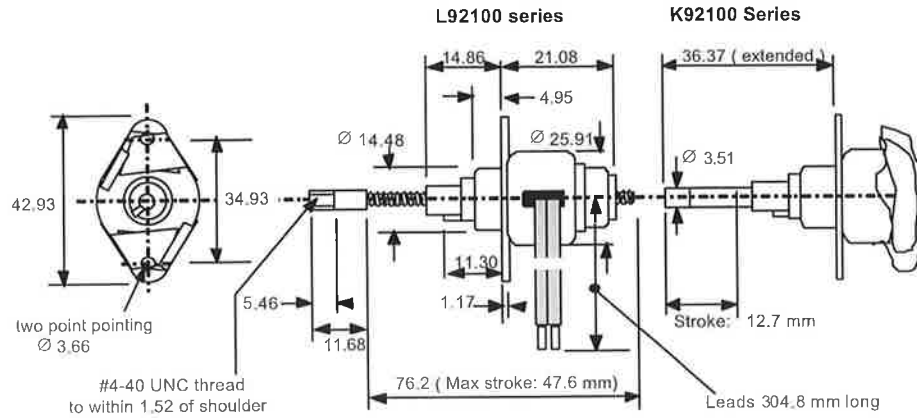
Specification

Standard models		L92121-P2 K92121-P2	L92111-P1	L92211-P2 K92211-P2	L92411-P2
Maximum linear force	N	7.23	12.5	20.9	88
Min. holding force (de-energised)	N	11.13	16.6	11.13	88
Linear travel per step	ins./mm	0.002 / 0.0508	0.001 / 0.0254	0.001 / 0.0254	0.001 / 0.0254
Typical backlash	Steps	2	2	2	2
Maximum linear travel:					
L92000 series using standard screw	mm	47.6	47.6	47.6	76.2
using extended screw	mm	259	259	215	233
K92000 series	mm	12.7	N / A	22.2	N / A
Maximum Pull-in rate	Steps/sec.	380	425	425	275
Maximum Pull-out rate	Steps/sec.	650 *	700 *	700 *	400 *
Bearing construction		Radial Ball	Radial Ball	Radial Ball	Radial Ball
Mass	Kg	0.0425	0.0425	0.198	0.45
Nominal Voltage (L/R Drive)	Vdc	12	5	12	12
Resistance per phase	Ohms	84	15	58	25
Current per phase	Amps	0.146	0.333	0.208	0.453
Inductance per phase	mH	29	5.0	30	25
Suitable drives		SAA 1027 MSE422 EM162	MSE422 EM162 TM162C	SAA 1027 MSE422 EM162	MSE422 MSE542 EM162 TM162C

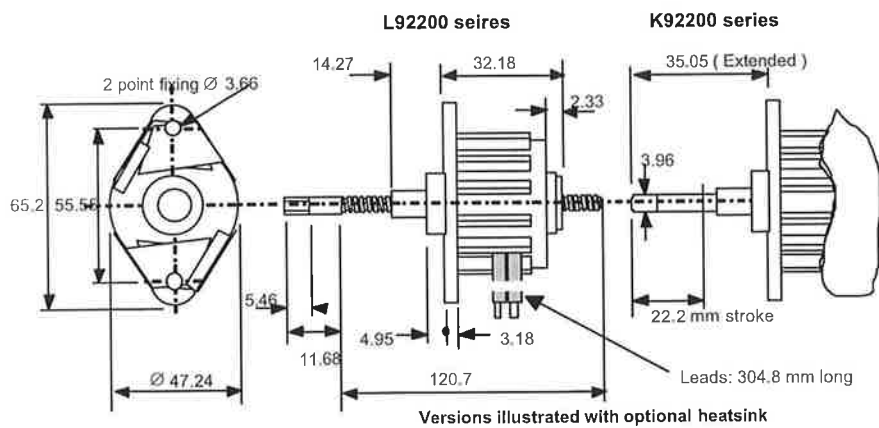
Note* Higher step rates may be achieved using L/4R current forcing techniques.
Alternative low inductance models are available to special order.

Mclennan Servo Supplies Ltd. Tel: +44 (0)8707 700 700 www.mclennan.co.uk

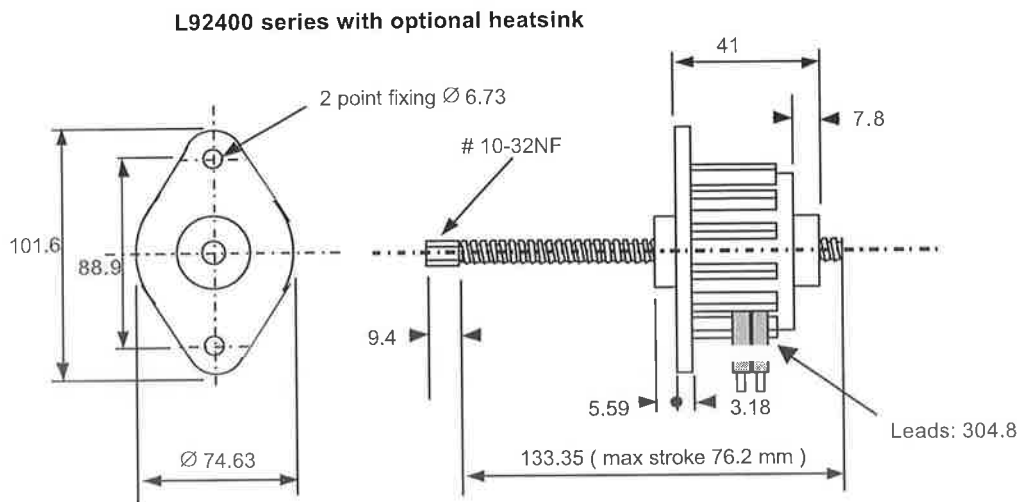




92200 series

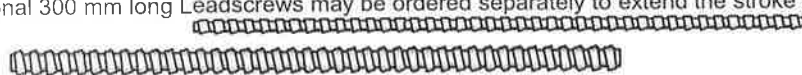


92400 series



Optional Leadscrews for 'L' series actuators:

Optional 300 mm long Leadscrews may be ordered separately to extend the stroke of 'L' series actuators





Instruction Leaflet
Bedienungsanleitung
Hojas de instrucciones
Feuille d'instructions
Foglio d'istruzioni

GB

D

E

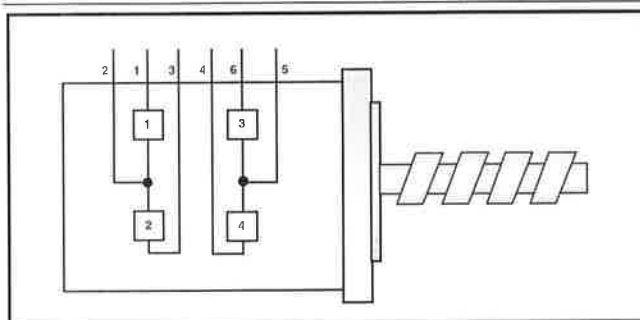
F

I

GB

RS Stock No.

340-6445	7.23 N Linear actuator
340-6467	12.5 N Linear actuator
340-6473	20.9 N Linear actuator
340-6489	88.0 N Linear actuator



		Lead					
RS stock Number	Volts	1	2	3	4	5	6
340-6445	12V	Yellow	Red	Orange	Black	Green	Brown
340-6467	5V	Yellow	Red	Orange	Black	Green	Brown
340-6473	12V	Yellow	Red	Black	Orange	Red	Brown
340-6489	12V	Yellow	Red	Black	Orange	Red	Brown

Also available 305mm (12") long leadscrew, which may be used as a replacement or to increase the length of travel.

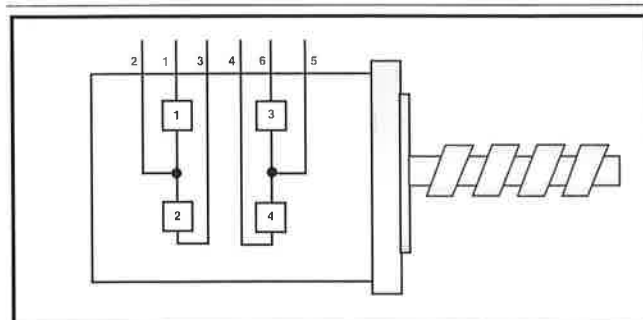
RS stock no.	Linear actuator with Std. leadscrew	Alternative 12 inch leadscrew
	340-6445	340-6495 A
	340-6467	340-6502 B
	340-6473	340-6495 A
	340-6489	340-6524 C

RS Components shall not be liable for any liability or loss of any nature (howsoever caused and whether or not due to RS Components' negligence) which may result from the use of any information provided in RS technical literature.

D

RS Best-Nr.

340-6445	Linearstellglied 7,23 N
340-6467	Linearstellglied 12,5 N
340-6473	Linearstellglied 20,9 N
340-6489	Linearstellglied 88,0 N



		Anschluß					
RS Best.-Nr.	Volt	1	2	3	4	5	6
340-6445	12V	Gelb	Rot	Orange	Schwarz	Grün	Braun
340-6467	5V	Gelb	Rot	Orange	Schwarz	Grün	Braun
340-6473	12V	Gelb	Rot	Schwarz	Orange	Rot	Braun
340-6489	12V	Gelb	Rot	Schwarz	Orange	Rot	Braun

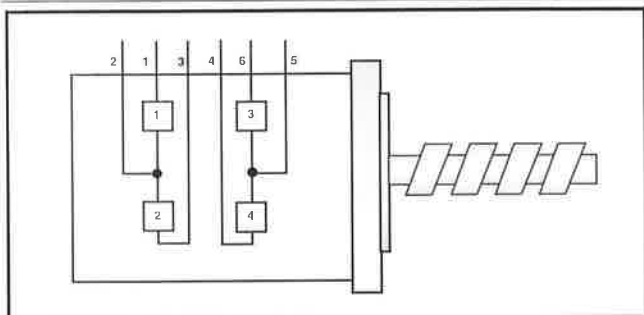
Eine 305mm lange Leitspindel ist ebenfalls lieferbar. Sie kann als Ersatzteil oder zur Verlängerung des Verfahrwegs verwendet werden.

RS Best.-Nr.	Linearstellglied mit Standardleitspindel	Alternative mit 12"-Leitspindel
	340-6445	340-6495 A
	340-6467	340-6502 B
	340-6473	340-6495 A
	340-6489	340-6524 C

RS Components haftet nicht für Verbindlichkeiten oder Schäden jedweder Art (ob auf Fahrlässigkeit von RS Components zurückzuführen oder nicht), die sich aus der Nutzung irgendwelcher der in den technischen Veröffentlichungen von RS enthaltenen Informationen ergeben.

E**Código RS.**

340-6445	Actuador lineal 7,23 N
340-6467	Actuador lineal 12,5 N
340-6473	Actuador lineal 20,9 N
340-6489	Actuador lineal 88,0 N



Cable		1	2	3	4	5	6
Código	Tensión						
340-6445	12V	Amarillo	Rojo	Naranja	Negro	Verde	Marrón
340-6467	5V	Amarillo	Rojo	Naranja	Negro	Verde	Marrón
340-6473	12V	Amarillo	Rojo	Naranja	Negro	Verde	Marrón
340-6489	12V	Amarillo	Rojo	Naranja	Negro	Verde	Marrón

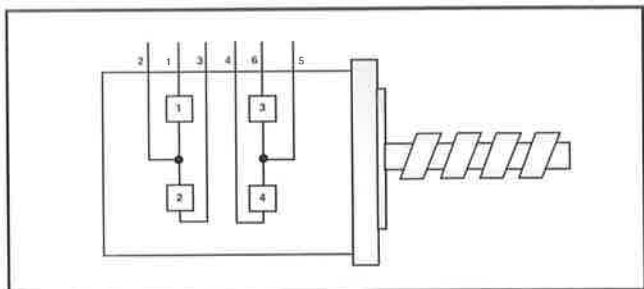
Disponible también husillo de 305 mm (12") de longitud, que puede usarse como repuesto o para aumentar la longitud del recorrido.

	Actuador lineal con husillo estándar	Husillo alternativo de 12"
Código RS	340-6445	340-6495 A
	340-6467	340-6502 B
	340-6473	340-6495 A
	340-6489	340-6524 C

RS Components no será responsable de ningún daño o responsabilidad de cualquier naturaleza (cualquiera que fuese su causa y tanto si hubiese mediado negligencia de RS Components como si no) que pudiese derivar del uso de cualquier información incluida en la documentación técnica de RS.

F**Code commande RS.**

340-6445	Actionneur linéaire 7.23 N
340-6467	Actionneur linéaire 12.5 N
340-6473	Actionneur linéaire 20.9 N
340-6489	Actionneur linéaire 88.0 N



Code commande		Fil					
	Volts	1	2	3	4	5	6
RS							
340-6445	12V	Jaune	Rouge	Orange	Noir	Vert	Marron
340-6467	5V	Jaune	Rouge	Orange	Noir	Vert	Marron
340-6473	12V	Jaune	Rouge	Noir	Orange	Rouge	Marron
340-6489	12V	Jaune	Rouge	Noir	Orange	Rouge	Marron

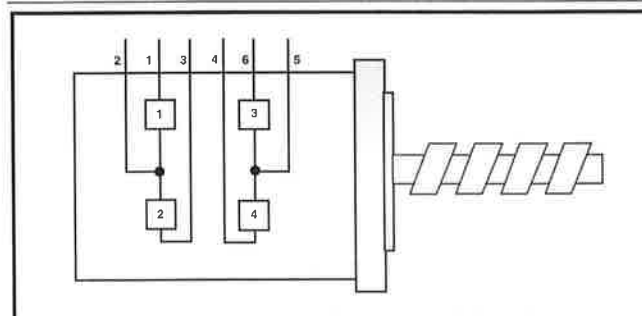
Vis sans fin de 305 mm (12 po) également disponible, qui peut être utilisée comme pièce de rechange, ou pour allonger la course.

	Actionneur linéaire avec vis sans fin standard	Vis sans fin de 12 pouces
Code commande RS	340-6445	340-6495 A
	340-6467	340-6502 B
	340-6473	340-6495 A
	340-6489	340-6524 C

La société RS Components n'est pas responsable des dettes ou pertes de quelque nature que ce soit (quelle qu'en soit la cause ou qu'elle soit due ou non à la négligence de la société RS Components) pouvant résulter de l'utilisation des informations données dans la documentation technique de RS.

I**RS Codici.**

340-6445	7.23 N attuatore lineare
340-6467	12.5 N attuatore lineare
340-6473	20.9 N attuatore lineare
340-6489	88.0 N attuatore lineare



Conduttore		1	2	3	4	5	6
Codice	Volt						
RS							
340-6445	12V	Giallo	Rosso	Arancio	Nero	Verde	Marrone
340-6467	5V	Giallo	Rosso	Arancio	Nero	Verde	Marrone
340-6473	12V	Giallo	Rosso	Nero	Arancio	Rosso	Marrone
340-6489	12V	Giallo	Rosso	Nero	Arancio	Rosso	Marrone

E' disponibile anche una vite madre lunga 305mm (12"), che può essere utilizzata come ricambio o per aumentare la lunghezza di corsa.

	Attuatore lineare con vite madre standard	Vite madre alternativa 12"
Codice RS	340-6445	340-6495 A
	340-6467	340-6502 B
	340-6473	340-6495 A
	340-6489	340-6524 C

La RS Components non si assume alcuna responsabilità in merito a perdite di qualsiasi natura (di qualunque causa e indipendentemente dal fatto che siano dovute alla negligenza della RS Components), che possono risultare dall'uso delle informazioni fornite nella documentazione tecnica.



Instruction Leaflet
Bedienungsanleitung
Hojas de instrucciones
Feuille d'instructions
Foglio d'istruzioni
Betjeningsvejledning
Instructies
Instruktionsfolder

4-Phase Unipolar Stepper Motor Drive Board (GB)

**4-Phasen-Einpol-Schrittmotor-
Antriebsschaltung** (D)

**Tarjeta controladora para motor paso a paso
unipolar de 4 fases** (E)

**Carte d'entraînement de moteur pas-à-pas
unipolaire quadriphasé** (F)

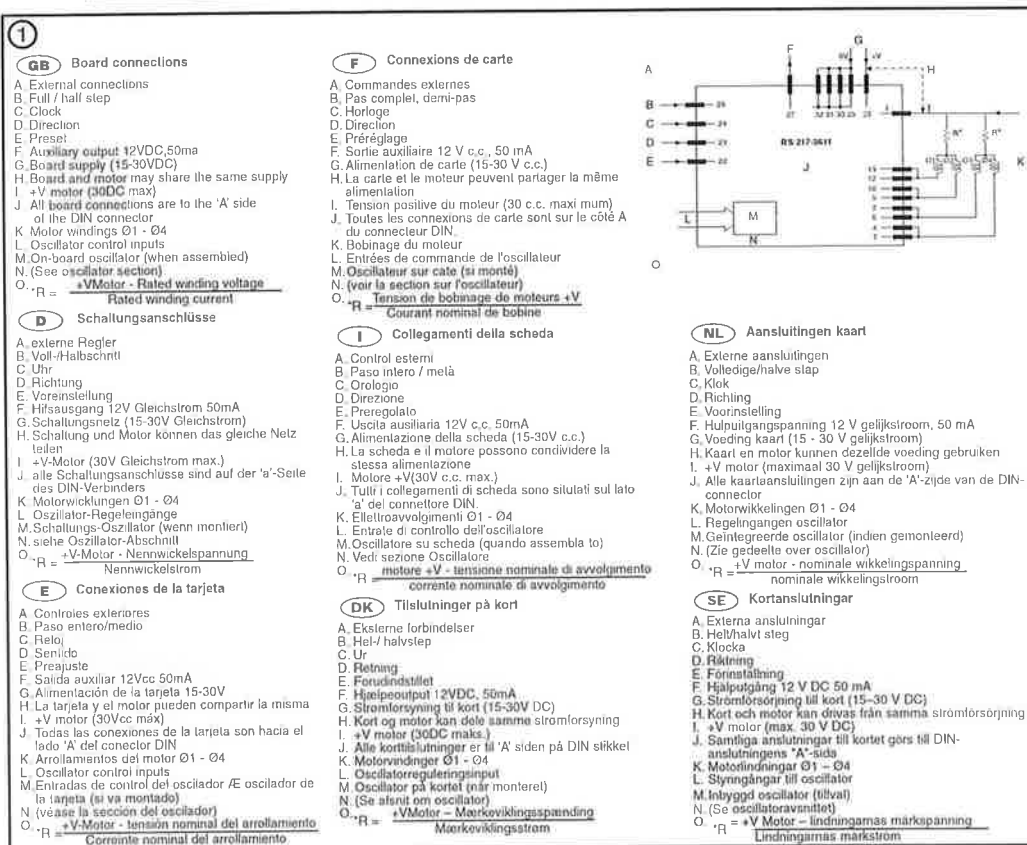
**Scheda di trasmissione per motore passo-
passo unipolare a quattro fasi** (I)

Driverkort til 4 faset, enpolet stepmotor (DK)

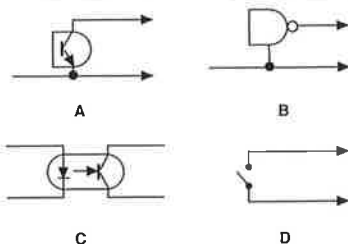
**Besturingskaart voor enkelpolige 4-fasen
stappenmotor** (NL)

Drivkort för 4-fasig unipolär stegmotor (SE)

Figures / Abbildung / Figura / Figurer / Afbeeldingen



②



GB

- A. Open collector T.T.L.
- B. C.M.O.S. (operating @ +12V)
- C. Opto-coupler
- D. Simple switch

E

- A. TTL en colector abierto
- B. CMOS (trabajando a +12V)
- C. Optoacoplador
- D. Interruptor simple

I

- A. TTL a collettore aperto
- B. CMOS (funzionante a+12V)
- C. Isolatore ottico
- D. Commutazione semplice

NL

- A. Open collector TTL
- B. CMOS (functioneert bij +12 V)
- C. Optokoppelaar
- D. Eenvoudige schakelaar

D

- A. Offenkollektor-TTL
- B. CMOS (Betrieb @ +12V)
- C. Optokoppler
- D. Einflachschalter

F

- A. Collecteur ouvert T.T.L
- B. C.M.O.S. (fonctionnant à +12 V)
- C. Photocoupleur
- D. Contacteur simple

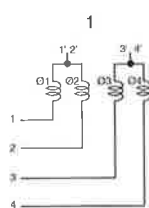
DK

- A. Åben kormmutator TTL
- B. C-MOS, (drift ved +12V)
- C. Optokobler
- D. Simpel bryder

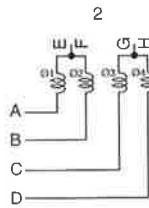
SE

- A. TTL med öppen kollektor
- B. CMOS (driftspänning +12 V)
- C. Optokopplare
- D. Enkel strömbrytare

③



RS 332-947, 332-953



RS 440-464

GB

- 1. 1.75° Stepper motor
- 2. 1.8° Stepper motor

- A. Black
- B. Orange
- C. Red
- D. Yellow
- E. White / Black
- F. White / Orange
- G. Red / White
- H. Yellow / White

E

- 1. Motor a paso de 7,5°
- 2. Motor a paso de 1,8°

- A. Negro
- B. Naranja
- C. Rojo
- D. Amarillo
- E. Blanco / negro
- F. Blanco / naranja
- G. Rojo / blanco
- H. Amarillo / blanco

I

- 1. 1.75° Motore passo-passo
- 2. 1.8° Motore passo-passo

- A. Nero
- B. Arancione
- C. Rosso
- D. Giallo
- E. Bianco / nero
- F. Bianco / arancione
- G. Rosso / bianco
- H. Giallo / bianco

NL

- 1. 1.75° stappenmotor
- 2. 1.8° stappenmotor

- A. Zwart
- B. Oranje
- C. Rood
- D. Geel
- E. Wit/zwart
- F. Wit/oranje
- G. Rood/wit
- H. Geel/wit

D

- 1. 1.75°-Schrittmotoren
- 2. 1.8°-Schrittmotor

- A. Schwarz
- B. Orange
- C. Rot
- D. Gelb
- E. Weiß / Schwarz
- F. Weiß / Orange
- G. Rot / Weiß
- H. Gelb / Weiß

F

- 1. Moteur pas à pas 7,5°
- 2. Moteur pas à pas 1,8°

- A. Noir
- B. Orange
- C. Rouge
- D. Jaune
- E. Blanc/noir
- F. Blanc/orange
- G. Rouge/Blanc
- H. Jaune/Blanc

DK

- 1. 1.75° stepmotor
- 2. 1.8° stepmotor

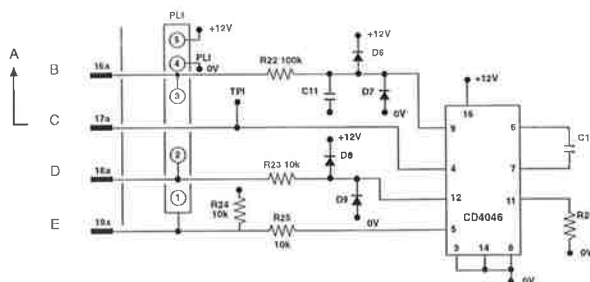
- A. Sort
- B. Orange
- C. Rød
- D. Gul
- E. Hvid / Sort
- F. Hvid / Orange
- G. Rød / Hvid
- H. Gul / Hvid

SE

- 1. 1.75° stegmotor
- 2. 1.8° stegmotor

- A. Svart
- B. Orange
- C. Röd
- D. Gul
- E. Vit/svart
- F. Vit/orange
- G. Röd/vit
- H. Gul/vit

④



GB

- A. To pin 24a
B. Running speed control
C. Clock output
D. Starting (base) speed control
E. Stop / run (12V)/(0V)

R22	100KΩ resistor	RS 131-491	1 off
R23, 24, 25	10KΩ resistor	RS 131-378	3 off
D6, 7, 8, 9	signal diode	RS 271-606	4 off
IC6	CMOS I.C.	RS 306-645	1 off
R26, C11 & C122	(value depends on application)		1 off each

D

- A. An Stift 24a
B. Laufgeschwindigkeitsregelung
C. Uhrenaussgang
D. Start- (Basis-) Geschwindigkeitsregelung
E. Stopp- / Lauf (12V)/(0V)

R22	100kΩ-Widerstand	RS 131-491	1 Stück
R23, 24, 25	10kΩ-Widerstand	RS 131-378	3 Stück
D6, 7, 8, 9	Signaldiode	RS 271-606	4 Stück
IC6	CMOS-IC	RS 306-645	1 Stück
R26, C11 & C12	(Wert hängt von Anwendung ab)		je 1 Stück

E

- A. Al pin 24a
B. Control de la velocidad de funcionamiento
C. Salida de reloj
D. Control de la velocidad inicial (básica)
E. Parada / marcha (12V)/(0V)

R22	Resistencia 100 kΩ	RS 131-491	1 ud.
R23, 24, 25	Resistencia 10 kΩ	RS 131-378	3 ud.
D6, 7, 8, 9	Diode indicador	RS 271-606	4 ud.
IC6	CMOS I.C.	RS 306-645	1 ud.
R26, C11 & C122	(valores según aplicación)		1 de la cada

F

- A. A la liche 24a
B. Commande du régime de fonctionnement
C. Sortie d'horloge
D. Commande de régime de démarrage (base)
E. Marche/arrêt (12 V)/(0 V)

R22	Résistance 100 KΩ	RS 131-491	1
R23, 24, 25	Résistance 10 KΩ	RS 131-378	3
D6, 7, 8, 9	Diode de signal	RS 271-606	4
IC6	CMOS I.C.	RS 306-645	1
R26, C11 et C122	(la valeur dépend de l'application)		1 chac.

I

- A. Al piedino 24a
B. Controllo velocità di esecuzione
C. Uscita orologio
D. Controllo velocità di partenza (di base)
E. Arresto / esecuzione (12V)/(0V)

R22	resistore 100kΩ	RS 131-491	n.1
R23, 24, 25	resistore 10kΩ	RS 131-378	n.3
D6, 7, 8, 9	diode di segnale	RS 271-606	n.4
IC6	ciruito integrato CMOS	RS 306-645	n.1
R26, C11 e C12	(il valore dipende dall'applicazione)		n.1 ciascuno

DK

- A. Til ben 24a
B. Regulering af kørehastighed
C. Ur - output
D. Regulering af start-hastighed (basis)
E. Stop / kø (12V)/(0V)

R22	100KOhm modstand	RS 131-491	1 slukket
R23, 24, 25	10kOhm modstand	RS 131-378	3 slukket
D6, 7, 8, 9	signaldiode	RS 271-606	4 slukket
IC6	CMOS-IC	RS 306-645	1 slukket
R26, C11 og C122	(værdien afhænger af anvendelsen)		1 fra hver

NL

- A. Naar pen 24a
B. Bedrijfstoeentalregeling
C. Uitgang klok
D. Basisoeentalregeling
E. Uit bedrijf/in bedrijf (12 V)/(0 V)

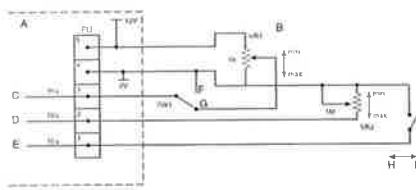
R22	100KΩ weerstand	RS 131-491	1 stuk
R23, 24, 25	10KΩ weerstand	RS 131-378	3 stuk
D6, 7, 8, 9	signaaldiode	RS 271-606	4 stuk
IC6	CMOS IC	RS 306-645	1 stuk
R26, C11 & C122	(waarde hangt van toepassing af)		ieder 1 stuk

SE

- A. Till stift 24a
B. Varvtalsreglering
C. Klockutgång
D. Start(grund)varvtalsreglering
E. Stopp/kör (12 V/0 V)

R22	Resistor 100 kΩ	RS 131-491	1 st.
R23, 24, 25	Resistor 10 kΩ	RS 131-378	3 st.
D6, 7, 8, 9	Signaldiod	RS 271-606	4 st.
IC6	CMOS IC	RS 306-645	1 st.
R26, C11 och C122	(värdet beror på tillämpningen)		1 st. av varje

⑤



GB

- A Drive board
B Use multi-turn potentiometers (VR1 & VR2)
C Running speed control
D Base speed control
E Stop / run
F OFF
G ON
H Run
I Stop

D

- A Antriebsschaltung
B Benutzen Sie mehrgängige Potentiometer (VR1 & VR2)
C Laufgeschwindigkeitsregelung
D Grundgeschwindigkeits-Regelung
E Stopp / Lauf
F EIN
G AUS
H Lauf
I Stopp

E

- A Tarjeta controladora
B Utilización de potenciómetros de vueltas múltiples (VR1 y VR2)
C Control de velocidad de marcha
D Control de la velocidad básica
E Parada / marcha
F OFF
G ON
H Marcha
I Parada

F

- A Carte d'entraînement
B Utiliser des potentiomètres à plusieurs tours (VR1 et VR2)
C Commande du régime de fonctionnement
D Commande du régime de base
E Arrêt/marche
F ARRÊT
G MARCHÉ
H Marche
I Arrêt

I

- A. Scheda di trasmissione
B. Usare potenziometri multigiri (VR1 & VR2)
C. Controllo della velocità di esecuzione
D. Controllo della velocità di base
E. Arresto / esecuzione
F. ON
G. OFF
H. Esecuzione
I. Arresto

DK

- A. Driverkort
B. Anvend potentiometre, der kan køre flere omgange (VR1 og VR2)
C. Regulering af kørehastighed
D. Regulering af basisstarthastighed
E. Stop / køre
F. Slukket
G. Tændt
H. Køre
I. Stop

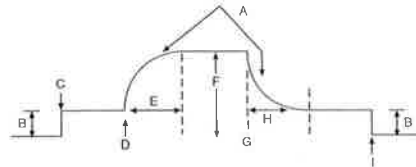
NL

- A. Bestuurskaart
B. Gebruik meergangenpotentiometers (VR1 & VR2)
C. Bedrijfsstoerentalregeling
D. Basisstoerentalregeling
E. Uit bedrijf in bedrijf
F. Uit
G. Aan
H. In bedrijf
I. Uit bedrijf

SE

- A. Drivkort
B. Använd flervarvspotentiometrar (VR1 och VR2)
C. Varvstörreglering
D. Grundvarvstörreglering
E. Stopp/kör (12 V/0 V)
F. Från
G. Till
H. Kör
I. Stopp

⑥



GB

- A. R22 x C11 time constant (typically 50ms)
B. Base speed
C. Switch On
D. SW1 On
E. Ramp-up
F. Running speed
G. SW1 Off
H. Decay
I. Switch Off

DK

- A. R22 x C11-Zeiskonstante (typisch 50ms)
B. Grundgeschwindigkeit
C. AUSschalten
D. SW1 AUS
E. Abfall
F. Laufgeschwindigkeit
G. SW1 EIN
H. Anstieg
I. EINschalten

E

- A. R22 x C11 constante de tiempo (normal 50ms)
B. Velocidad base
C. Interruptor Conectado
D. Interruptor 1
E. Rampa de aceleración
F. Velocidad de marcha
G. Interruptor 1 Desconectado
H. Deceleración
I. Interruptor Desconectado

F

- A. Temps de mise en fonctionnement R22 x C11 (habituellement 50 ms)
B. Régime de base
C. Accélération
D. Contacteur 1 allumé
E. Mise en marche
F. Régime de fonctionnement
G. Contacteur 1 éteint
H. Extinction
I. Ralentissement

I

- A. Caratteristica di progressione-velocità del motore
B. Costante di tempo R22 x C11 (tipicamente 50ms)
C. Velocità di base
D. Accensione
E. Progressione
F. Velocità di esecuzione
G. INT1 OFF
H. Smorzamento
I. Spegnimento

DK

- A. Motorhastighed - accelerationsgenskaber
B. R22 x C11 tidskonstant (typisk 50ms)
C. Grundhastighed
D. Bryder tændt
E. Br. 1 lændt
F. Acceleration
G. Kørehastighed
H. Br. 1 slukket
I. Henfald

NL

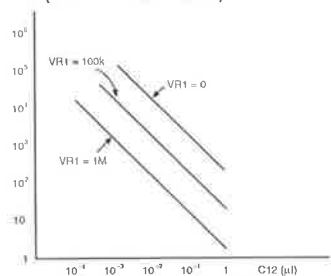
- A. Karakteristiek van de oploopsnelheid van het motortoerental
B. R22 x C11 tijdconstante (standaard 50 ms)
C. Basisstoerental
D. Inschakelen
E. Oploop
F. Bedrijfsstoerental
G. Schak1 uit
H. Verval
I. Uitschakelen

SE

- A. Motorvarvtal, rampkaraktäristik
B. R22 x C11 tidkonstant (typiskt 50 ms)
C. Grundvarvtal
D. Strömbrytare till
E. Uppramp
F. Driftvarvtal
G. Brytare 1 från
H. Avklingning
I. Strömbrytare från

⑦

A (R26 = ∞ VR2 = min.)



GB

- A. Base frequency

D

- A. Grundfrequenz

E

- A. Frecuencia base

F

- A. Fréquence de base

I

- A. Frequenza di base

DK

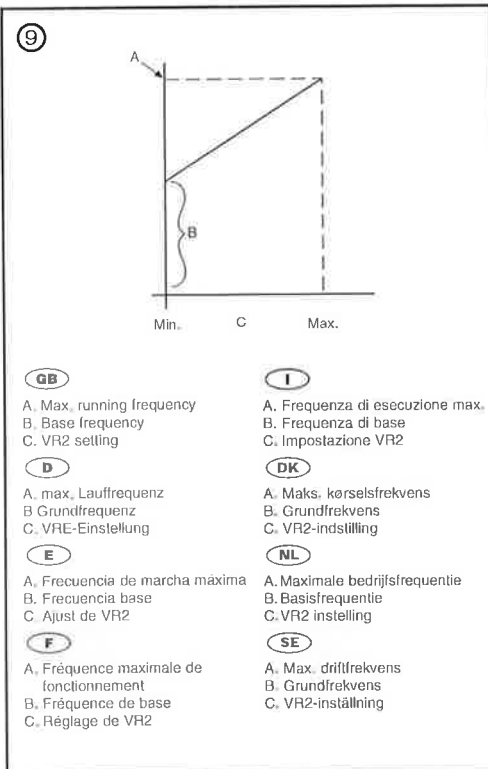
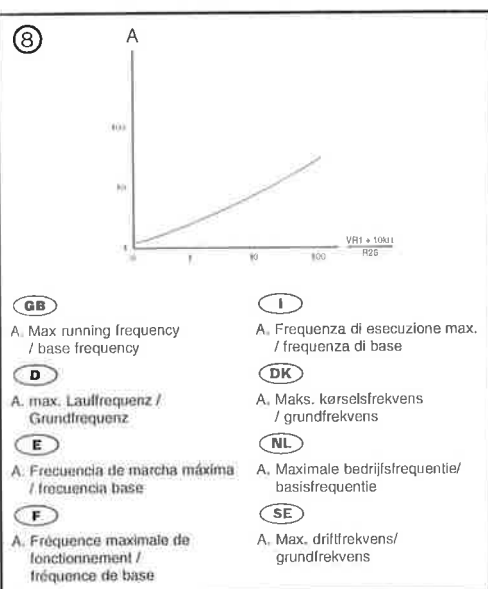
- A. Grundfrekvens

NL

- A. Basisfrequentie

SE

- A. Grundfrekvens



RS Stock No.

217-3611

Max. power dissipated through R = (rated motor current) $2 \times R$. If the power dissipation is high it is advisable to arrive at the required value of 'R' by using a network of series or parallel resistors. (The use of higher wattage resistors and heat sinks may be required).

Max. current consumption (motor & board) = $2 \times$ (current per phase) + 60mA. Thus ensure power supply cables used are sufficiently rated.

External control signals e.g. full/half step, direction etc. as well as the oscillator (if fitted) stop/run signal can be applied to the circuit in any of the methods of Figure 2.

Connection to RS stepper motors

When the winding of the RS stepper motors are assigned (Ø1 - Ø4) as shown in Figure 3, they can be connected to the board according to Figure 1.

If the supply voltage is set to 24Vdc then 'R' values for use with the RS motors are given in table 1 below.

Table 1

Motor	Rated Current (A)	Rated Winding Voltage (V)	R (Ω)	Power Dissipation through R (W)
332-947	0.1	12	120	1.2
332-953	0.24	12	47	3
440-464	2	3	10.5	5

For other details and motors performance refer to RS data sheet on stepper motors.

On-board oscillator assembly

If external clock source is not available, on-board oscillator can be assembled simply by soldering into place the required RS Components listed below.

Note : the oscillator clock output must be externally wired to the clock, input-pin 24a.

If oscillator remote controls are required (e.g. front panel controls) then plug PLI (5-way inter p.c.b. RS stock no.467-576) can be added together with mating cable shell (RS stock no. 467-627) and crimp terminals (RS stock no.467-598)

Starting (base) and running speed control

The on-board oscillator can be arranged to start at a fixed frequency (thus a fixed motor speed) and then ramp up to a final value (the running motor speed). This facility is available to start the motor within its pull-in performance region and then accelerate the motor through so that it can operate within the pull-out mode. On switch-off the motor decelerates automatically.

Three parameters need to be determined for any application :

- The starting speed: this should be below the pull-in speed for the motor (with any additional load).
- The running (final) speed: this should be within the pull-out capability of the motor (with any additional load).
- The acceleration and deceleration rate between starting and running speeds: this is limited by motor capability to accelerate through its own (plus any load) inertia.

Oscillator controls (external)

Note : Oscillator frequency corresponds directly to motor speed in step/s or half step/s depending on motor drive mode.

For a 1.8° stepper motor :

$$\text{speed in revs / min} = \frac{60}{200} \times \text{speed in step/s}$$

or

$$\text{speed in revs / min} = \frac{60}{400} \times \text{speed in 'half' step/s}$$

For a 7.5° stepper motor :

$$\text{speed in revs / min} = \frac{60}{48} \times \text{speed in step/s}$$

or

$$\text{speed in revs / min} = \frac{60}{96} \times \text{speed in 'half' step/s}$$

V6771

Oscillator frequency setting

Recommended component values :

VR1	0 - 1M Ω
VR2	0 - 1k Ω
R26	0 - 10k Ω
C12	greater than 100pF

Determine the base frequency and maximum running frequency. Using Fig 7 and the base frequency value choose a value for C12 and VR1. Calculate the ratio max. running frequency/base frequency to determine the ratio :

$$\frac{VR1 + R23 \text{ (fixed at } 10k\Omega\text{)}}{R26}$$

and thus using Figure 8 establish the required value for R26.

Once all component values are established and assembled the oscillator frequency range is as shown in Figure 9. If SW1 is 'OFF' the oscillator runs at base frequency. When SW1 in 'ON' the oscillator builds up (at a rate depending on R22 x C11 time constant) to a frequency determined by VR2 setting.

WARNINGS: Turn OFF power supply before connecting or disconnecting any wiring, circuitry, motor etc., to the board.
DISCONNECTING THE MOTOR WITH THE POWER ON WILL DESTROY THE RSAT134. Motor windings can generate very high discharge voltages.

Technical specification

Size _____ standard Euro card (168 x 100 x 15)
Mating edge connector _____ standard 32-way DIN 41612 socket e.g. _____ (RS stock no. 471-503 or 467-453)
Supply (board and motor) _____ 15-30Vdc + 10% max, unregulated smoothed
Current consumption:
Board only _____ 60mA
Motor winding _____ dependent on the motor _____ used-up to 2A per phase max.
On-board auxiliary output _____ 12Vdc 50mA max, regulated
Switching logic control (CMOS and open collector T.T.L. compatible):
Level '0' _____ 0V
Level '1' _____ 12V
Inputs pins:
25, Full / half step _____ Level '1' full step / Level '0' half step
23, Direction _____ Connecting this pin to Zero volts will change the direction of the motor.
24, Clock _____ 1Hz-25kHz, 10 μ s min. pulse width negative edge triggered.
22, Preset _____ Active Level '0' set motor drive states to Q1, & Q3 'OFF', Q2 & Q4 'ON' (full step mode) Q1, Q2 & Q3 'OFF', Q4 'ON' (Half step mode)-see Figure 1.
Automatic preset at switch-on

RS Components shall not be liable for any liability or loss of any nature (howsoever caused and whether or not due to RS Components' negligence) which may result from the use of any information provided in RS technical literature.



Maximale durch R verlorene Leistung = (Motornennstrom)² x R. Wenn die Verlustleistung hoch ist, ist es ratsam, zum erforderlichen Wert von R durch Verwendung eines Netzes von Reihen- oder Parallelwiderständen zu gelangen. (Der Gebrauch von Widerständen höherer Wattzahl und Wärmesenken kann nötig sein).
Maximaler Stromverbrauch (Motor & Schaltung) = 2 x (Strom pro Phase) + 60mA. Vergewissern Sie sich daher, daß benutzte Leistungsnetzwerkable ausreichende Nennleistung haben.
Externe Regelsignale, z. B. Voll-/Halbschritt, Richtung usw., und auch das Oszillator- (wenn eingebaut)
Stopp-/Laufsignal können auf den Schaltkreis durch jegliche der Methoden in Abb. 2 angewendet werden.

Anschluß an RS-Schrittmotoren

Wenn die Wicklungen der RS-Schrittmotoren zugewiesen sind (Ø1 - Ø4), wie in Abb. 3 gezeigt, können sie gemäß Abb. 1 an die Schaltung angeschlossen werden.
Wenn die Netzspannung auf 24V Gleichstrom eingestellt ist, dann sind R-Werte zum Gebrauch mit den RS-Motoren in untenstehender Tabelle 1 angegeben:

6

Tabelle 1

Motor	Nennstrom (A)	Nennwicklungs-spannung (V)	R (Ω)	Verlustleistung durch R (W)
332-947	0,1	12	120	1,2
332-953	0,24	12	47	3
440-464	2	3	10,5	5

Für andere Konstruktionseinzelheiten und Motorenleistung beziehen Sie sich auf RS-Datenblatt über Schrittmotoren.

Montage des Schaltungsoszillators

Wenn externe Uhrenquelle nicht verfügbar ist, kann ein Schaltungs-Oszillator einfach montiert werden, indem die unten angegebenen RS-Bauteile einfach in Stellung gelötet werden.

Hinweis: der Oszillator-Uhrenaussgang muß extern an die Uhr verdrahtet werden, Eingangs-Stift 24a).

Wenn Oszillator-Fernsteuerungen erforderlich sind (z. B. Vordertafelsteuerungen), dann kann Stecker-PLI (5-Wege-RS-Zwischenschaltung 467-576) hinzugefügt werden, zusammen mit passendem Kabelgehäuse RS 467-627 und Quetschanschlüssen RS 467-598.

Start- (Basis-) und Laufgeschwindigkeits-Regelung

Der Schaltungs-Oszillator kann angeordnet werden, um bei einer festen Frequenz (daher einer festen Motorgeschwindigkeit) zu starten und dann auf einen Endwert zu steigen (die Motor-Laufgeschwindigkeit). Diese Einrichtung ist verfügbar, um den Motor innerhalb seines Milnahme-Leistungsbereiches zu starten und dann den Motor durchzubeschleunigen, sodaß er innerhalb des Außertrittfall-Modus arbeiten kann. Beim Ausschalten verzögert der Motor automatisch.

Drei Parameter müssen für jede Anwendung bestimmt werden:

- Die Startgeschwindigkeit: diese sollte unterhalb der Milnahme-geschwindigkeit für den Motor (mit jeglicher Zusatzlast) liegen.
- Die Lauf- (End-) Geschwindigkeit: diese sollte innerhalb der Außertrittfallleistung des Motors (mit jeglicher Zusatzlast) liegen.
- Die Beschleunigungs- und Verzögerungsrate zwischen Start- und Laufgeschwindigkeiten: dies wird durch die Fähigkeit des Motors, durch seine eigene (plus jegliche Last)-Trägheit durchzubeschleunigen, begrenzt.

Oszillatorsteuerungen (extern)

Hinweis: Oszillatorfrequenz entspricht direkt der Motorgeschwindigkeit in Schritt(en) oder Halbschritt(en), abhängig vom Motor-Antriebsmodus.

Für einen 1,80-Schrittmotor

$$\text{Geschwindigkeit in U/min} = \frac{60}{200} \times \text{Geschwindigkeit in Schritten/s}$$

oder

$$\text{Geschwindigkeit in U/min} = \frac{60}{400} \times \text{Geschwindigkeit in Halbschritten/s}$$

Für einen 7,50-Schrittmotor

$$\text{Geschwindigkeit in U/min} = \frac{60}{48} \times \text{Geschwindigkeit in Schritten/s}$$

oder

$$\text{Geschwindigkeit in U/min} = \frac{60}{96} \times \text{Geschwindigkeit in Halbschritten/s}$$

Oszillator-Frequenzeinstellung

Empfohlene Bauteilewerte

VR1	0 - 1 M Ω
VR2	1 k Ω
R26	10 k Ω - 1 M Ω
C12	größer als 100 pF

Bestimmen Sie die Grundfrequenz und maximale Lauf Frequenz. Abb. 7 und den Grundfrequenzwert benutzend, wählen Sie einen Wert für C12 und VR1. Berechnen Sie das Verhältnis max. Laufgeschwindigkeit/Grundfrequenz, um das Verhältnis von

$$\frac{VR1 + R23 \text{ (fixed at } 10k\Omega\text{)}}{R26}$$

zu bestimmen und daher, Abb. 8 benutzend, den erforderlichen Wert für R26 zu ermitteln.

Sobald alle Bauteilewerte bestimmt und zusammengetragen sind, ist der Oszillator-Frequenzbereich wie in Abb. 9 gezeigt. Wenn SW1 AUS ist, läuft der Oszillator mit Grundfrequenz. Wenn SW1 EIN ist, dann baut der Oszillator (in einem Maße, das von der Zeitkonstante R22 x C11 abhängt) auf eine durch VR2-Einstellung bestimmte Frequenz auf.

ACHTUNG: Stromversorgung ausschalten, bevor Schaltungen, Verdrahtungen, Motoren u.ä. an die R5AIT134-Treiberplatine angeschlossen werden, ABTRENKEN DES MOTORS BEI EINGESCHALTETER VERSORGUNG FÜHRT ZUR ZERSTÖRUNG DER R5AIT134-TREIBERPLATINE. Die Wicklungen können hohe Entladespannungen erzeugen.

Technische Daten:

Größe _____ Standard-Eurocard 168 x 100 x 15
 Passender Kantenstecker _____ Standard-32-Pol DIN 41612-Buchse,
 z. B. RS 471-503 oder 467-453
 Netz (Schaltung und Motor) _____ 15-30V Gleichstrom +10% max.,
 unregelmäßig geglättet
 Stromverbrauch:
 a) nur Schaltung _____ 60mA
 b) Motorwicklungen _____ abhängig von verwendetem Motor -
 bis zu 2A/Phase max.
 Schaltungs-Hilfsausgang _____ 12V Gleichstrom 50mA max. **geregelt**
Schaltlogikregelung _____ **Niveau 0** OV
 CMOS- und Offenkollektor - TTL-kompatibel
 Eingangsstile:
 25. Voll-/Halbschritt _____ Pegel „1“ - Vollschritt / Pegel „0“ - Halbschritt
 Wird dieser Stift an 0 Volt gelegt,
 23. Drehrichtung _____ ändert sich die Drehrichtung des Motors,
 1Hz bis 25kHz, 10µs min., Impulsbreite,
 24. Takt _____ Auslösung auf negative Flanke
 22. Voreinstellung _____ Aktiver Pegel „0“ setzt Motorantriebszustände auf
 Q1 & Q3 OFF (Aus)
 Q2 & Q4 ON [EIN] (Vollschrittmodus),
 Q1, Q2 & Q3 OFF [AUS],
 Q4 ON [EIN] (Halbschrittmodus) - siehe Abb.4.
 Automatische Voreinstellung beim Einschalten

RS Components haftet nicht für Verbindlichkeiten oder Schäden jedweder Art (ob auf Fahrlässigkeit von RS Components zurückzuführen oder nicht), die sich aus der Nutzung irgendwelcher der in den technischen Veröffentlichungen von RS enthaltenen Informationen ergeben.



Código RS.

217-3611

Potencia máxima disipada a través de R = (corriente nominal del motor) 2 x R. Si hay una disipación de potencia elevada es aconsejable llegar al valor requerido de "R" utilizando una red de resistencias en serie o en paralelo (puede ser necesario utilizar resistencias con un wataje superior, así como disipadores de calor).

Consumo máximo de corriente (motor y tarjeta) = 2 x (corriente por fase) + 60mA. Por ello es necesario cerciorarse de que los cables de alimentación tengan capacidad suficiente.

Pueden aplicarse al circuito en cualquiera de los métodos de la figura 2 señales de control exteriores, por ejemplo, paso entero/medio, sentido de giro, etc., así como la señal de marcha/parada del oscilador (si lo lleva).

Conexión con los motores paso a paso RS

Cuando están asignados los arrollamientos de los motores paso a paso RS (Ø1 - Ø 4) tal como se indica en la figura 3, se pueden conectar a la tarjeta según la figura 1.

Si la tensión de alimentación está fijada a 24Vcc, entonces los valores de "R" que han de utilizarse con los motores RS figuran en la tabla 1 siguiente.

Tabla 1.

Motor	Corriente nominal (A)	Tensión nominal por arrollamiento	R (Ω)	Potencia disipada a través de R (W)
332-947	0,1	12	120	1,2
332-953	0,24	12	47	3
440-464	2	3	10,5	5

Para los demás detalles y prestaciones del motor véase la hoja de características RS de los motores paso a paso.

Montaje del oscilador en la tarjeta

Si no se dispone de una fuente de reloj exterior, se puede montar un oscilador en la tarjeta, simplemente soldando en su lugar los componentes RS necesarios que se indican a continuación.

Nota: la salida del reloj del oscilador debe cablearse externamente con el reloj, pin de entrada 24a.

Si se requieren controles remotos para el oscilador (por ejemplo, controles en el panel frontal), entonces puede añadir la clavija PLI (de 5 vías entre PCBs, código RS 467-576), junto con la correspondiente carcasa de cable (código RS 467-627) y terminales de engarzar (código RS 467-598).

Control de la velocidad inicial (básica) y de marcha

El oscilador de la tarjeta se puede disponer de manera que arranque a una frecuencia fija (por lo tanto, una velocidad de motor fija) y a continuación, suba hasta un valor final (la velocidad de marcha del motor). Esta posibilidad tiene el fin de arrancar el motor dentro de su zona de prestaciones de arranque, acelerando a continuación el motor hasta que pueda funcionar dentro de su régimen de par máximo en servicio continuo. Al desconectar, el motor decelera automáticamente.

Para cualquier aplicación es necesario determinar tres parámetros:

- La velocidad de arranque: debe ser inferior a la velocidad de sincronización del motor (con cualquier carga adicional).
- La velocidad de marcha final: debe estar dentro de las posibilidades de funcionamiento continuado y sincronizado a par máximo del motor (con cualquier carga adicional).
- La tasa de aceleración y deceleración entre las velocidades inicial y de marcha: viene limitada por la posibilidad que tiene el motor de acelerar por su propia inercia (con cualquier carga).

Controles del oscilador (exteriores)

Nota: La frecuencia del oscilador se corresponde directamente con la velocidad del motor en pasos o medios pasos, según el modo de accionamiento del motor.

Para un motor paso a paso de 1,8°

$$\text{Velocidad en r.p.m.} = \frac{60}{200} \times \text{velocidad en pasos}$$

o

$$\text{Velocidad en r.p.m.} = \frac{60}{400} \times \text{velocidad en "medios pasos"}$$

Para un motor paso a paso de 7,5°

$$\text{Velocidad en r.p.m.} = \frac{60}{48} \times \text{velocidad en pasos}$$

o

$$\text{Velocidad en r.p.m.} = \frac{60}{96} \times \text{velocidad en "medios pasos"}$$

Ajuste de la frecuencia del oscilador

Valores recomendados para los componentes:

VR1	0-1 MΩ
VR2	0-1 kΩ
R26	0-10 kΩ
C12	mayor que 100 pF

Determine la frecuencia base y la frecuencia de funcionamiento máxima. Utilizando la figura 7 y el valor de la frecuencia base, elija un valor para C12 y VR1. Calcule la proporción máxima entre frecuencia de marcha/frecuencia base para determinar la relación:

$$\frac{\text{VR1} + \text{R23 (fijada a 10 kΩ)}}{\text{R26}}$$

y de esa manera utilizando la figura 8, determine el valor necesario para R26. Una vez que se hayan determinado los valores de todos los componentes y se hayan montado éstos, el margen de frecuencia del oscilador es el indicado en la figura 9. Si SW1 está "DESCONECTADO", el oscilador funciona a la frecuencia base. Cuando SW1 está "CONECTADO", el oscilador va acelerando (a una razón que depende de la constante de tiempo R22 x C11) hasta una frecuencia determinada por el ajuste de VR2.

V6771

ADVERTENCIAS: Desconecte la fuente de alimentación antes de conectar o desconectar cualquier bobinado, circuitería, motor, etc. a la tarjeta R5AIT134. DESCONECTAR EL MOTOR CUANDO HAY ALIMENTACIÓN, DESTRUIRÁ LA R5AIT134. Los bobinados del motor pueden generar alta tensión.

Especificaciones técnicas

Dimensiones Tarjeta Eurocard-estándar (168 x 100 x 15)
 Conector de borde correspondiente Estándar 32 vías DIN 41612
 Alimentación (tarjeta y motor) zócalo estándar, etc. p.e. (Código RS 471-503 ó 467-453)
 15-30Vcc + 10% máx.
 sin regular filtrada
 Consumo de corriente:
 Tarjeta sola 60mA
 Arrollamientos del motor según el motor utilizado
 - hasta 2A/lase máx.
 Salida auxiliar en la tarjeta 12Vcc, 50mA máx. regulada
 Control de la lógica de conmutación
 (compatible con CMOS y T.T.L. de colector abierto):
 Nivel "0" 0V
 Nivel "1" 12V
 Terminales de entrada:
 25. Paso completo / medio Nivel "1" paso completo/ Nivel "0" medio paso
 23. Sentido Si se conecta este terminal a cero voltios, se cambiará el sentido de giro del motor.
 24. Reloj 1 Hz - 25 kHz, impulso mínimo de 10µs con activación por flanco negativo
 22. Preajuste El nivel activo "0" fija los estados del motor en Q1 y Q3 DESCONECTADO, Q4 "CONECTADO" (modo de medio paso - ver Fig. 1)
 Prefijado automático al conectar los interruptores.

RS Components no será responsable de ningún daño o responsabilidad de cualquier naturaleza (cualquiera que fuese su causa y tanto si hubiese mediado negligencia de RS Components como si no) que pudiese derivar del uso de cualquier información incluida en la documentación técnica de RS.



Code commande RS

217-3611

Puissance maximale dissipée par R = (courant nominal du moteur) $2 \times R$. Si la dissipation de puissance est élevée, on recommande d'atteindre la valeur voulue de R en utilisant un réseau de résistances en série ou en parallèle. (des résistances de puissance supérieure et des dissipateurs de chaleur peuvent être nécessaires).

Consommation maximale de courant (moteur et carte) = $2 \times$ (courant par phase) + 60 mA. Ceci assure que les câbles d'alimentation utilisés ont une capacité suffisante.

On peut transmettre des signaux de commande, par exemple pas complet, demi-pas, direction, etc., ainsi que le signal marche/arrêt de l'oscillateur (le cas échéant) au circuit dans une des méthodes quelconques de la figure 2.

Connexion aux moteurs pas-à-pas RS

Quand les bobines des moteurs pas-à-pas RS sont affectées (Ø1 - Ø4), tel qu'illustré à la figure 3, on peut les raccorder à la carte, conformément à la figure 1.

Si la tension d'alimentation est réglée à 24 Vcc, les valeurs R à utiliser avec les moteurs RS sont données dans le tableau 1 ci-dessous.

Tableau 1

Moteur	Courant nominal (A)	Tension nominale de bobine (V)	R (Ω)	Dissipation de puissance par R (W)
332-947	0,1	12	120	1,2
332-953	0,24	12	47	3
440-464	2	3	10,5	5

Pour d'autres détails et connaître la performance des moteurs, se reporter à la fiche technique de RS sur les moteurs pas-à-pas.

Ensemble oscillateur intégré

Si on ne dispose pas d'une horloge externe, on peut monter un oscillateur intégré simplement en soudant en place les composants RS nécessaires énumérés ci-dessous.

Nota : La sortie d'horloge de l'oscillateur doit être raccordée extérieurement à l'horloge, fiche d'entrée 24 a.

Si des commandes à distance de l'oscillateur sont nécessaires (par exemple, commandes du panneau avant), la prise PL1 (carte de circuits imprimés intermédiaire à 5 fiches, Code commande RS 467-576) peut alors être ajoutée avec l'isolant de câble correspondant (Code commande RS 467-627) et des bornes serties (Code commande RS 467-598).

Commande de régime de démarrage (base) et de fonctionnement

On peut prévoir de faire démarrer l'oscillateur intégré à une fréquence fixe (donc à un régime de moteur fixe), puis de le faire accélérer à une valeur finale (le régime de fonctionnement du moteur). Cette caractéristique est disponible pour faire démarrer le moteur dans la plage de synchronisation, puis le faire accélérer afin qu'il puisse fonctionner dans le mode de désynchronisation. A la coupure, le moteur décélère automatiquement.

Il faut déterminer trois paramètres pour une application quelconque.

- Le régime de démarrage : il doit être inférieur au régime de synchronisation pour le moteur (avec une charge supplémentaire quelconque).
- Le régime de fonctionnement (final) : il doit être conforme à la capacité de désynchronisation du moteur (avec une charge supplémentaire quelconque).
- Le taux d'accélération et de décélération entre les régimes de démarrage et de fonctionnement : il est limité par la capacité du moteur d'accélérer par sa propre inertie (plus une charge quelconque).

Commandes de l'oscillateur (externe)

Nota : La fréquence de l'oscillateur correspond directement au régime du moteur en pas/seconde ou en demi-pas/seconde, selon le mode d'entraînement du moteur.

Pour un moteur pas-à-pas de 1,8° :

Régime en tours/minute = $\frac{60}{200} \times$ régime en pas/seconde

ou
 régime en tours/minute = $\frac{60}{400} \times$ régime en demi-pas/seconde

Pour un moteur pas-à-pas de 7,5° :

Régime en tours/minute = $\frac{60}{48} \times$ régime en pas/seconde

ou
 régime en tours/minute = $\frac{60}{96} \times$ régime en demi-pas/seconde

Réglage de la fréquence de l'oscillateur

Valeur de composant recommandé :

VR1	0 - 1 MΩ
VR2	0 - 1 kΩ
R26	0 - 10 kΩ
C12	supérieur à 100 pF

Déterminer la fréquence de base et la fréquence maximale de fonctionnement. En utilisant la figure 7 et la fréquence de base, choisir une valeur pour C12 et VR1. Calculer le rapport fréquence maximale de fonctionnement/fréquence de base pour déterminer le rapport :

$$\frac{VR1 + R23 \text{ (fixé à } 10 \text{ k}\Omega\text{)}}{R26}$$

et ainsi, en utilisant la figure 8, établir la valeur nécessaire de R26.

Une fois toutes les valeurs de composants établies et ceux-ci montés, la plage de fréquence est telle qu'indiquée à la figure 9. Si SW1 est à la position OFF, l'oscillateur fonctionne à la fréquence de base. Si SW1 est à ON, l'oscillateur accélère (à un taux qui dépend de la constante de temps R22 x C11) à une fréquence déterminée par le réglage de VR2.

AVERTISSEMENTS : ETEINDRE l'alimentation électrique avant de brancher ou de débrancher un fil, un circuit, le moteur, etc., à la carte R5AIT134. LE DEBRANCHEMENT DU MOTEUR SOUS TENSION DETRUIRA LA CARTE R5AIT134. Les bobinages du moteur peuvent produire des tensions de décharge très élevées.

Caractéristiques techniques

Dimensions _____ carte Euro standard (168 x 100 x 15)
 Connecteur de bord correspondant _____ standard DIN 41612
 à 32 fiches douille, exemple
 (Code commande RS 471-503 ou 467-453)
 Alimentation (carte et moteur) _____ 15-30 Vcc + 10 % maximum
 non régulé, adouci

Consommation de courant :

Carte seulement _____ 60 mA
 Bobinage du moteur _____ selon le moteur jusqu'à 2A/phase maximale
 Sortie auxiliaire intégrée _____ 12 Vcc 50 mA maximum, régulée
 Commande logique de commutation

(CMOS et collecteur ouvert compatible T.T.L.) :

Niveau 0 _____ 0 V
 Niveau 1 _____ 12 V

Broches d'entrée :

25. Pas complet/demi-pas _____ Pas complet niveau « 1 » /
 Demi-pas niveau « 0 »
 23. Sens : _____ Si cette broche est connectée sur 0 V,
 le sens de rotation du moteur est modifié.
 24. Horloge _____ 1 Hz-25 kHz, amplitude d'impulsion
 min. 10 µs déclenchée par le flanc négatif.
 22. Présélection _____ Niveau actif « 0 » règle les états d'entraînement
 du moteur à Q1 et Q3 « OFF »
 Q2 et Q4 ON (mode de pas complet) Q1
 Q2 et Q3 OFF, Q4 ON (mode de demi-pas) - voir figure 1.
 Préréglage automatique à la mise en marche

La société RS Components n'est pas responsable des pertes ou dommages de quelque nature que ce soit (celle qu'en soit la cause ou qu'elle soit due ou non à la négligence de la société RS Components) pouvant résulter de l'utilisation des informations données dans la documentation technique de RS.



RS Codici.

217-3611

Dissipazione max. di potenza attraverso R = (corrente nominale del motore)² x R. In caso di elevata dissipazione di potenza, si consiglia di raggiungere il valore richiesto di R usando una rete di resistori seriali o paralleli. (Può essere necessario l'uso di dissipatori di calore e resistori più potenti).
 Corrente assorbibile max. (motore e scheda) = 2 x (corrente per fase) + 60mA.
 Assicurarsi pertanto che i cavi di alimentazione utilizzati siano adeguati.
 I segnali di controllo esterni (per es. passo intero/metà, direzione ecc.) e il segnale di arresto/esecuzione dell'oscillatore (se montato) possono essere applicati in uno qualsiasi dei metodi di Fig. 2.

Collegamento ai motori passo-passo RS

Quando gli avvolgimenti dei motori passo-passo RS vengono predisposti (ø/1 - ø/4) secondo lo schema di Fig. 3, è possibile collegarli alla scheda secondo la Fig. 1.

Se la tensione di alimentazione è impostata su 24V c.c., i valori R da usare con i motori RS sono quelli riportati nella seguente tabella:

motore	corrente nominale (A)	tensione di avvolgimento nominale (V)	R (Ω)	Dissipazione di potenza attraverso R (W)
332-947	0,1	12	120	1,2
332-953	0,24	12	47	3
440-464	2	3	10,5	5

Per ulteriori informazioni sui dettagli di progettazione e sulle prestazioni dei motori, consultare il foglio specifiche tecniche RS relativo ai motori passo-passo.

Assemblaggio dell'oscillatore su scheda

Se non è disponibile un orologio esterno, è possibile assemblare un oscillatore su scheda semplicemente saldando in posizione i componenti RS elencati di seguito.

Nota: l'uscita dell'orologio dell'oscillatore deve essere collegata esternamente all'orologio; piedino di ingresso: 24a).

Se l'oscillatore richiede dei comandi a distanza (per es. comandi sul pannello anteriore) si può usare la spina PLI (inter-pcb a 5 vie RS 467-576) insieme al guscio dei cavi di accoppiamento RS 467-627 e ai terminali aggraffati RS 467-598.

Controllo della velocità di partenza (di base) e di esecuzione

L'oscillatore su scheda può essere impostato per l'avvio ad una frequenza predeterminata (velocità di motore predeterminata) per poi progredire ad un valore finale (velocità di esecuzione del motore). Questa funzione consente di avviare il motore dalla propria modalità di trazione e di accelerare quindi la corsa fino a quando è in grado di funzionare allo stato inerziale. Allo spegnimento, il motore decelererà automaticamente.

Per qualsiasi applicazione bisogna determinare tre parametri:

- La velocità di partenza: deve essere inferiore alla velocità di trazione del motore (con eventuale carico aggiuntivo).
- La velocità di esecuzione (finale): deve essere compresa nella capacità inerziale del motore (con eventuale carico aggiuntivo).
- Il tasso di accelerazione e decelerazione compreso tra le velocità di partenza e di esecuzione: è limitato dalla capacità del motore di accelerare per inerzia propria (con eventuale carico).

Controlli dell'oscillatore (esterni)

Nota: La frequenza dell'oscillatore corrisponde direttamente alla velocità del motore in passi/s o mezzi passi/s, a seconda della modalità di trasmissione del motore.

Per una velocità di motore passo-passo di 1,8°

in giri / min = $\frac{60}{200} \times \text{velocità in passi/s}$

o in giri / min = $\frac{60}{400} \times \text{velocità in mezzi passi/s}$

Per una velocità di 7,5° di motore passo-passo

in giri / min = $\frac{60}{48} \times \text{velocità in passi/s}$

o in giri / min = $\frac{60}{96} \times \text{velocità in mezzi passi/s}$

Impostazione della frequenza dell'oscillatore

Valori raccomandati dei componenti

VR1	0 - 1MΩ
VR2	0 - 1kΩ
R26	0 - 10kΩ
C12	maggiore di 100pF

Determinare la frequenza di base e la frequenza di esecuzione massima. Usando la Fig. 7 e il valore di frequenza di base, scegliere un valore per C12 e VR1. Calcolare il rapporto frequenza di esecuzione max/frequenza di base per determinare il rapporto:

$$\frac{\text{VR1} + \text{R23 (fissato a } 10\text{k}\Omega)}{\text{R26}}$$

quindi, usando la Fig. 8, stabilire il valore necessario per R26.

Una volta stabiliti e assemblati tutti i valori dei componenti, la gamma di frequenze dell'oscillatore è quella mostrata in Fig. 9. Se INT1 è OFF, l'oscillatore funziona alla frequenza di base. Quando INT1 è ON l'oscillatore arriverà ad una frequenza determinata dall'impostazione VR2 (ad una velocità dettata dalla costante di tempo R22 x C11).

Avvertenza: Spegnerne l'alimentazione prima di collegare o scollegare fili, circuiterie, motori etc., alla scheda R5AIT134. SCOLLEGARE IL MOTORE MENTRE SI TROVA COLLEGATO ALLA CORRENTE PUÒ DANNEGGIARE LA SCHEDA R5AIT134. Gli avvolgimenti del motore possono generare tensioni di scarica molto elevate.

Specifiche tecniche:

Dimensioni _____ scheda Euro standard 168 x 100 x 15
 Connettore per scheda di accoppiamento _____ presa standard DIN 41612
 a 32 vie (per es. RS 471-503 o RS 467-453)
 Tensione di alimentazione (scheda e monitor) _____ 15-30V c.c. + 10% max.
 non regolata e filtrata

Corrente assorbita:

solo scheda _____ 60mA
 elettroavvolgimento _____ dipende dal motore

uscita _____ usato - fino a 2A/fase max.

Uscita ausiliaria su scheda _____ 12V c.c. 50mA max, regolata

Controllo logico di commutazione

Livello "0" _____ 0V

Livello "1" _____ 12V

V6771

Pin ingressi:

25. Passo intero / mezzo passo _____ Livello '1' passo intero / Livello '0' mezzo passo
23. Direzione _____ Collegando questo pin a zero volt si cambia la direzione del motore.
24. Orologio _____ 1Hz-25kHz, 10µs ampiezza min. impulsi connettore negativo attivato.
22. Preregolato _____ Il livello attivo '0' imposta gli stati della scheda di trasmissione su Q1, e Q3 'OFF'; Q2 & Q4 ON (modalità passo intero); Q1, Q2 & Q3 OFF, Q4 ON (modalità mezzo passo) - vedi Fig. 1. Predisposto automaticamente per l'accensione;

La RS Components non si assume alcuna responsabilità in merito a perdite di qualsiasi natura (di qualunque causa e indipendentemente dal fatto che siano dovute alla negligenza della RS Components), che possono risultare dall'uso delle informazioni fornite nella documentazione tecnica.



RS Varenr

217-3611

Maks. effekttab gennem R = (mærkemotorstrøm) 2 x R. Hvis effekttabet er højt, tilrådes det at opnå den krævede værdi på 'R' ved hjælp af et net af serielle eller parallelle modstande. (Anvendelse af modstande med højere effekt kan være påkrævet).

Maks. strømforbrug (motor og kort) = 2 x (strøm pr. fase) + 60mA. Sørg derfor for, at strømforsyningskablerne er tilstrækkeligt dimensioneret.

Eksterne regulerings signaler, f.eks., hel/halvstep, retning mm, samt oscilatoren (hvis monteret) stop/kør-signal, kan føjes til kredsen med en af metoderne i figur 2.

Tilslutning til RS stepmotorer

Når viklingen på RS stepmotorerne er koblet (Ø1 - Ø4) som vist på figur 3, kan de kobles til kortet som på figur 1.

Hvis forsyningsspændingen er sat til 24V DC, er 'R'-værdierne til anvendelse med RS motorene som givet i tabel 1 nedenfor.

Tabel 1

Motor	Mærkestrøm (A)	Mærkeviklings spænding (V)	R (Ω)	Effekttab gennem R (W)
332-947	0,1	12	120	1,2
332-953	0,24	12	47	3
440-464	2	3	10,5	5

Yderligere detaljer og motorkarakteristik findes i RS datablad om stepmotorer.

Montering af oscilator på kortet

Hvis et eksternt takt-ur ikke findes, kan en oscilator monteres på kortet ved palodning af de påkrævede RS-komponenter, der vises nedenfor.

Bemærk: Oscilator takt-uret skal kobles eksternt til takt-urets, input-ben 24a.

Hvis der kræves fjernstyring af oscilatoren, (f.eks., regulering fra frontpanelet,) kan stikket PLI (5-polet stikket for printkort. RS varenr. 467-576) sættes sammen ved hjælp afatningshuset (RS varenr. 467-627) og crimp kontakter (RS varenr. 467-598)

Regulering af start- (grund) og kørselshastighed

Den påmonterede oscilator kan bringes til at starte ved en fast frekvens (og derfor en fast motorhastighed) og derefter accelerere op til en slutværdi (motorens kørehastighed). Denne funktion er der for at kunne starte motoren inden for dens synkroniseringsområde og derefter accelerere den igennem, så den kan fungere inden for vippeområdet. Ved brydning decelererer motoren automatisk.

Tre parametre skal fastlægges før anvendelse:

- Starthastighed: Skal være under motorens synkroniseringshastighed (med evt. ekstra belastning).
- Korehastigheden (sluthastigheden): Skal være inden for motorens vippehastighed (med evt. ekstra belastning).
- Accelerations- og decelerationshastigheden mellem start- og korehastighed: Begrænses af motorens evne til at accelerere mod sin egeninerti (plus inerti fra evt. ekstra belastning).

Oscillatorregulering (ekstern)

Bemærk: Oscillatorfrekvensen svarer direkte til motorhastigheden i step eller halvstep afhængigt af motorens drift.

For en 1,8° stepmotor:

Hastighed i o./min = 60 x hastighed i step/sek.
200

eller

Hastighed i o./min = 60 x hastighed i 'halv' step/sek.
400

For en 7,5° stepmotor:

Hastighed i o./min = 60 x hastighed i step/sek.
48

eller

Hastighed i o./min = 60 x hastighed i 'halv' step/sek.
96

Indstilling af oscilatorfrekvens

Anbefalede komponentværdier:

VR1	0 - 1MΩ
VR2	0 - 1kΩ
R26	0 - 10kΩ
C12	Større end 100pf

Bestem grundfrekvensen og den maksimale kørselsfrekvens. Væg en værdi for C12 og VR1 ved hjælp af fig 7 og værdien for grundfrekvensen. Beregn forholdet maks. kørselsfrekvens/grundfrekvens for at bestemme forholdet:

$$VR1 + R23 \text{ (fast ved } 10k\Omega)$$

R26

og derved fastlægge den krævede værdi for R26 ved hjælp af figur 8.

Når alle komponentværdier er fastlagt og samlet, er oscilatorfrekvensen som vist på figur 9. Hvis SW1 er 'OFF', kører oscilatoren ved grundfrekvensen. Når SW1 er 'ON', accelererer oscilatoren til en frekvens, der bestemmes af VR2-indstillingen (med en hastighed, der afhænger af R22 x C11 tidskonstant).

ADVARSEL: Sørg for at afbryde strømforsyningen inden du tilslutter eller frakobler ledninger, kredsløb, motor osv. med R5AIT134 kortet. FRAKOBLES MOTOREN VED TILKOBLET STRØMTILFØRSEL, ØDELÆGGES R5AIT134. Motorviklingerne kan generere meget høje afledningsspændinger.

Tekniske data

Størrelse: _____ standard Eurokort (168 x 100 x 15)

Kantstik _____ standard 32-bens DIN 41612-stik, f.eks.

(RS varenr. 471-503 eller 467-453)

Strømforsyning (kort og motor) _____ 15-30V DC + 10% max.

ureguleret, udjævnet

Strømforbrug:

Kun kort _____ 60mA

Motorvikling _____ afhængig af den anvendte

motor - op til maks. 2A pr. fase.

Påloddet hjælpeudstyr output _____ 12V DC 50mA maks. reguleret

Logisk omkoblingskredsløb (kompatibelt med C-MOS og åben kommutator

TTL):

Niveau '0' _____ 0V

Niveau '1' _____ 12V

Input-ben:

25. Hel/halvstep _____ Niveau '1' helstop/niveau '0' halvstep

23. Retning _____ Hvis dette ben forbindes til 0 volt,

ændres motorens retning.

24. Ur _____ 1Hz-25kHz, 10µs min. impuls med negativ kant udløst.

22. Forudindstillet _____ Aktivt niveau '0' sætter motorens

kørselsstand til Q1 & Q3 'OFF'.

Q2 og Q4 'ON' (helstepdrift) Q1, Q2 og

Q3 'OFF', Q4 'ON' (halvstepdrift) - se figur 1.

Automatisk forudindstilling ved indkobling

RS Components frasiger sig ethvert ansvar eller økonomisk tab (uanset årsag og uanset, om dette måtte skyldes RS Components' uagtsomhed), der opstår, som følge af brugen af oplysningerne i RS' tekniske materiale



RS Voorraadnummer

217-3611

Het maximale gedissipeerde vermogen door R = (nominale motorstroom) 2 x R. Als het gedissipeerde vermogen hoog is, is het aan te bevelen de benodigde waarde van 'R' te bereiken door een netwerk van serie- of parallelweerstand te gebruiken. (Het kan nodig zijn weerstanden en koellichamen met een hoger vermogen te gebruiken). Het maximale stroomverbruik (motor & kaart) = 2 x (stroom per fase) + 60 mA. Zorg er dus voor dat de gebruikte voedingskabels voldoende nominaal vermogen hebben.

De externe besturingssignalen, bv. volledige/halve stap, richting etc en het uit bedrijf/in bedrijf-sigitaal van de oscillator (indien gemonteerd) kunnen op het circuit worden aangesloten op één van de manieren van afbeelding 2.

Aansluiting op de RS stappenmotoren

Als de wikkeling van de RS stappenmotoren zijn toegewezen (Ø1 - Ø4) als aangegeven in afbeelding 3 kunnen zij op de printplaat worden aangesloten als in afbeelding 1.

De 'R'-waarden die voor de RS motoren dienen te worden gebruikt als de voedingsspanning is ingesteld op 24 V gelijkstroom worden in tabel 1 hieronder weergegeven.

Tabel 1

Motor	Nominale stroomsterkte (A)	Nominale wikkelingspanning (V)	R (Ω)	Gedissipeerd vermogen door R (W)
332-947	0.1	12	120	1.2
332-953	0.24	12	47	3
440-464	2	3	10.5	5

Raadvleeg voor meer gegevens en vermogens van motoren het RS gegevensblad over stappenmotoren.

Montage van geïntegreerde oscillator

Als de externe bron van de klok niet beschikbaar is, kan de geïntegreerde oscillator eenvoudig worden gemonteerd door de hieronder aangegeven benodigde RS componenten op hun plaats te solderen.

Opmerking: de uitgang van de klok van de oscillator dient met externe kabels op de klok te worden aangesloten, ingangspan 24a.

Als de oscillator op afstand moet kunnen worden bediend (bv. frontpaneelregelingen), kan stekker PLI (5-weg, in de printplaat, RS voorraadnummer 467-576) worden toegevoegd samen met een bijpassend kabelomhulsel (RS voorraadnummer 467-627) en krullemmen (RS voorraadnummer 467-598)

Basis- en bedrijfstoerentalregeling

De geïntegreerde oscillator kan worden afgesteld om met een vaste frequentie (en dus een vast motortoerental) te beginnen en daarna op te lopen tot een uiteindelijke waarde (het bedrijfstoerental). Met deze voorziening kan de motor starten binnen het vangvermogengebied en dan versnellen zodat deze kan werken binnen de inzetmodus. Na uitschakeling remt de motor automatisch af.

Voor elke toepassing dienen drie parameters te worden geconfigureerd:

- Het basistoerental: deze dient onder de vangsnellheid van de motor te liggen (ook met extra belasting).
- Het (uiteindelijke) bedrijfstoerental: deze dient binnen het inzetgebied van de motor te liggen (ook met extra belasting).
- De versnellings- en vertragingstijd tussen de basis- en bedrijfstoerentalen: deze wordt beperkt door het vermogen van de motor om door diens eigen massa traagheid (plus die van de extra belasting) te versnellen.

Besturingen van de oscillator (extern)

Opmerking: De frequentie van de oscillator komt direct overeen met het motortoerental in stap(pen) of halve stap(pen), afhankelijk van de motoraandrijvingsmodus.

Voor een 1,8° stappenmotor:

$$\text{toerental in omw./min} = \frac{60 \times \text{toerental in stappen/s}}{200}$$

of

$$\text{toerental in omw./min} = \frac{60 \times \text{toerental in 'halve' stappen/s}}{400}$$

Voor een 7,5° stappenmotor:

$$\text{toerental in omw./min} = \frac{60 \times \text{toerental in stappen/s}}{48}$$

of

$$\text{toerental in omw./min} = \frac{60 \times \text{toerental in 'halve' stappen/s}}{96}$$

Instelling frequentie oscillator

Aanbevolen waarden componenten:

VR1	0-1 MΩ
VR2	0-1 kΩ
R26	0-10 kΩ
C12	groter dan 100 pF

Bepaal de basisfrequentie en de maximale bedrijfsfrequentie. Gebruik afbeelding 7 en de waarde van de basisfrequentie om een waarde voor C12 en VR1 te kiezen. Bereken de verhouding maximaal bedrijfsvermogen/basisvermogen om de verhouding

$$\frac{\text{VR1} + \text{R23 (vastgelegd op 10 kΩ)}}{\text{R26}}$$

te berekenen en gebruik vervolgens afbeelding 8 om de benodigde waarde van R26 te bepalen.

Als alle waarden van de componenten zijn bepaald en samengebracht ziet het frequentiebereik van de oscillator eruit als aangegeven in afbeelding 9. Als Schak1 'UIT' staat loopt de oscillator op de basisfrequentie. Als Schak1 'AAN' staat, versnelt de oscillator (de snelheid waarmee hangt af van R22 x C11 tijdconstante) tot een frequentie bepaald door de VR2 instelling.

WAARSCHUWINGEN: Schakel de voeding UIT voordat u bedrading, circuits, motor enz. op de RSALT134-kaart aansluit of daarvan losmaakt. WANNEER DE MOTOR WORDT LOSGEKOPPELD TERWIJL DE VOEDING IS INGESCRAKELD, ZAL DE RSALT134 ONHERSTELBAAR BESCHADIGD WORDEN. Motorwikkelingen kunnen zeer hoge ontladingsspanningen genereren.

Technische gegevens

Alfmeting _____ standaard Europese kaart (168 x 100 x 15)
Connector aansluitende randen _____ standaard 32-weg
DIN-houder 41612, bv.
(RS voorraadnummer 471-503 of 467-453)

Voeding (kaart en motor) _____ 15-30 V gelijkstroom + maximaal 10%,
afgevlakt en niet gestabiliseerd

Stroomverbruik:

Alleen kaart _____ 60 mA
Motorwikkeling _____ afhankelijk van de gebruikte motor,
tot maximaal 2 A per fase.

Geïntegreerde hulpuitgangspanning _____ 12 V gelijkstroom,
maximaal 50 mA, gestabiliseerd

Schakellogicaregeling (compatibel met CMOS en open collector TTL):

Niveau '0' _____ 0 V
Niveau '1' _____ 12 V

Ingangen:

25. Volledige/halve stap _____ niveau '1' volledige stap / niveau '0' halve stap
23. Richting _____ Als deze pen op nul volt wordt aangesloten,
keert de draairichting van de motor om.

24. Klok _____ 1 Hz-25 kHz, minimaal 10 μs,
pulsbreedte getriggert op negatieve rand

22. Voorinstelling _____ Actief niveau '0' zet de motoraandrijfsstatus op
Q1, & Q3 'OFF',
Q2 & Q4 'AAN' (modus volledige stap) Q1, Q2 &
Q3 'UIT', Q4 'AAN' (modus halve stap) - zie afbeelding 1.
Automatische voorinstelling bij inschakeling

RS Components accepteert geen aansprakelijkheid met betrekking tot enige verantwoordelijkheid of enig verlies (door welke oorzaak dan ook en al of niet te wijten aan nalatigheid van de zijde van RS Components) die zou kunnen ontstaan in verband met het gebruik van gegevens die in de technische documentatie van RS Components zijn opgenomen.

V6771



RS Lagernummer

217-3611

Max. effekt bortkyld genom $R = (\text{motorns märkström})^2 \times R$. Om bortkyld effekt är hög, rekommenderas att man bygger upp erforderligt värde på "R" med ett nät av serie- eller parallellkopplade resistorer. (Effektmotstånd och kylflansar kan vara nödvändigt.)

Max. strömförbrukning (motor och kort) $= 2 \times (\text{strömmen i varje fas}) + 60 \text{ mA}$. Se till att strömförsörjningskablarna är avsedda för denna ström.

Externa styrsignaler, Lex, helt/halvt steg eller riktning liksom oscillaions (om sådan är installerad) stopp/körsignal kan kopplas in direkt i kretsen i samtliga de i fig. 2 visade fallen.

Anslutning till RS stegmotorer

När lindningarna i RS stegmotorer är betecknade ($\emptyset 1 - \emptyset 4$) så som visas i fig. 3, kan de anslutas till kortet så som visas i fig. 1.

Om matningsspänningen är inställd till 24 V DC, är "R"-värdena för RS stegmotorer de i tabell 1 nedan givna.

Tabell 1

Motor	Märkström (A)	Lindningarnas märkspänning (V)	R (Ω)	Genom R bortkyld effekt (W)
332-947	0,1	12	120	1,2
332-953	0,24	12	47	3
440-464	2	3	10,5	5

Ytterligare information om motorprestanda finns i RS datablad för stegmotorer.

Inbyggd oscillator

Om det inte finns någon extern klocksignal att tillgå, kan en inbyggd oscillator skapas genom att man på kortet löder in de erforderliga, nedan förtecknade komponenterna från RS.

Obs: Oscillatorns klocksignal måste kopplas externt till klockan, ingångsstilt 24 a.

Om fjärrstyrning av oscilatorn krävs (Lex, från en frontpanel), kan man använda en PLI-anslutning (5-polig kretskortsförbindning, RS largernr 467-576) och till denna passande kabelhölje (RS largernr 467-627) och krympanslutningar (RS largernr 467-598).

Start(grund)varvtalsreglering och

driftvarvtalsreglering

Den inbyggda oscilatorn kan kopplas så att den startar vid en fast frekvens (och därmed ett fast motorvarvtal) och därefter rampar upp till slutvarvtalet (motorns driftvarvtal). Denna funktion finns för att man ska kunna starta motorn utan att överskrida dess startmoment och accelerera den så att dess maximala driftmoment inte överskrids. Vid avstängning retarderar motorn automatiskt.

De tre parametrarna nedan måste fastställas för alla tillämpningar.

- Startvarvtal, som måste vara lägre än motorns startvarvtal (med eventuell extra last).
- Driftvarvtal (slutvarvtal) som måste ligga inom motorns driftprestanda (med eventuell extra last).
- Lutningen för accelerations- och retardationsramperna mellan start- och driftvarvtal. Ramplutningen begränsas av motorns förmåga att övervinna sitt eget plus eventuell lasts masströghetsmoment.

Oscillatorstyrning (extern)

Obs: Oscillatorfrekvensen är motsvarar direkt motorns varvtal uttryckt i steg/sekund eller halvsteg/sekund beroende på driftläge.

1,8° stegmotor:

$$\text{varvtal i varv/min} = \frac{60 \times \text{varvtalet i steg/sekund}}{200}$$

eller

$$\text{varvtal i varv/min} = \frac{60 \times \text{varvtalet i "halvsteg"/sekund}}{400}$$

7,5° stegmotor:

$$\text{varvtal i varv/min} = \frac{60 \times \text{varvtalet i steg/sekund}}{48}$$

eller

$$\text{varvtal i varv/min} = \frac{60 \times \text{varvtalet i "halvsteg"/sekund}}{96}$$

Inställning av oscillatorfrekvensen

Rekommenderade värden:

VR1	0-1 M Ω
VR2	0-1 k Ω
R26	0-10 k Ω
C12	större än 100 pF

Fastställ grundfrekvensen och max. driftfrekvens. Välj lämpliga värden för C 12 och VR 1 med hjälp av fig. 7 och basfrekvens. Beräkna kvoten max. driftfrekvens/grundfrekvens för att kunna fastställa förhållandet:

$$\frac{VR1 + R23 \text{ (fast vid } 10k\Omega)}{R26}$$

och använd fig. 8 för att fastställa erforderligt värde på R 26.

När alla komponentvärden fastställts och komponenterna monterats, är oscillatorfrekvensen den i fig. 9 visade. Om strömbrytare 1 (SW1) är avstängd, svänger oscilatorn med grundfrekvens. När strömbrytare 1 (SW 1) är tillslagen ökar oscilatorns frekvens gradvis (med en hastighet som beror på tidskonstanten R 22 x C 11) till en frekvens bestämd av VR 2-inställningen.

VARNINGAR: Stäng av strömförsörjningen innan du ansluter till eller kopplar bort någon som helst kabel, krets, motor etc, till RSAIT134 -tavlans, ATT STÄNGA AV MOTORN MED STRÖMMEN PÅ KOMMER ATT FÖRSTÖRA RSAIT134. Motorlindningarna kan avge mycket höga urladdningsspänningar.

Tekniska data

Storlek _____ standard Europakort (168 x 100 x 15)

Bottenkontakt _____ standard 32-polig kontakt DIN 41612, Lex.

RS largernr 471-503 eller 467-453

Strömförsörjning (kort och motor) _____ 15-30 V DC +10 % max., oreglerad, glättad

Strömförbrukning:

Enbart kort _____ 60 mA

Motorlindning _____ beror på motortyp - upp till 2 A per fas

Hjälputgång på kortet _____ 12 V DC 50 mA max. reglerad

Logikstyrning (kompatibel med CMOS och TTL med öppen kollektor):

Nivå "0" _____ 0 V

Nivå "1" _____ 12 V

Ingångar:

25. Helt/halvt steg _____ Nivå "1" helt steg / Nivå "0" halvt steg

23. Riktning Genom att ansluta stiftet till noll volt ändras motorns riktning.

24. Klocka _____ 1-25 000 Hz, minsta pulsvidd 10 μ s, triggnings

22. Förinställning _____ Förinställd aktiv nivå

"0"sätter motorstyrstatus till Q1, och Q3 "OFF"

Q2 och Q4 "ON" (halvstegsläge)

Q1, Q2 och Q3 "OFF", Q4 "ON" (halvstegsläge) - se fig. 1.

Automatisk förinställning vid tillslagning

RS Components ska inte vara ansvarigt för någon som helst skuld eller förlust av vilken art det vara må (hur denna än har orsakats och om den är orsakad av försumlighet från RS Components eller ej) som kan resultera från användning av någons som helst information som tillhandahålls i tekniska skriftler från RS Components.

E Series Multifunction DAQ – 100 kS/s, 16-Bit, 16 or 64 Analog Inputs

NI 6030E, NI 6031E, NI 6032E, NI 6033E

- 100 kS/s, 16-bit resolution, up to 64 single-ended analog inputs
- Two 16-bit analog outputs
- 8 digital I/O lines (5 V/TTL); two 24-bit counter/timers
- Analog and digital triggering
- Available for PCI, PXI/CompactPCI, and ISA
- NI DAQ driver software simplifies configuration and measurements

Models

NI 6030E

- PCI-MIO-16XE-10
- PXI-6030E
- AT-MIO-16XE-10

NI 6031E

- PCI-6031E
- PXI-6031E

NI 6032E

- PCI-6032E
- AT-AI-16XE-10

NI 6033E

- PCI-6033E

Real-Time

See page 142

NI Application Software

- LabVIEW
- Measurement Studio
- VI Logger

Operating System Compatibility

- Windows 2000/NT/Me/9x*
- Mac OS – not for all hardware

Accessories

See page 256

Calibration Certificate Included

See page 24.

*Visit ni.com/info and enter winxp for the latest operation system information.

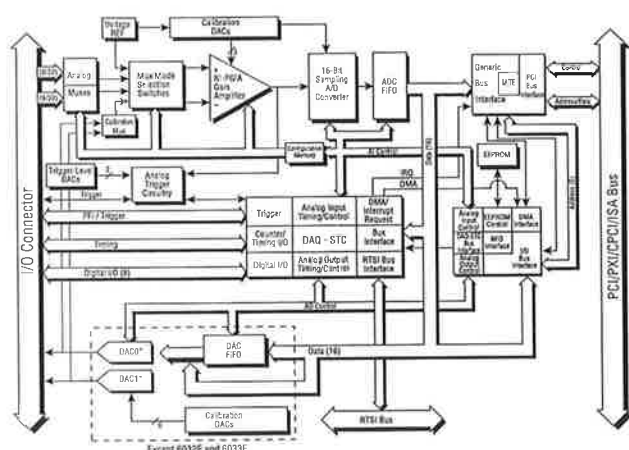
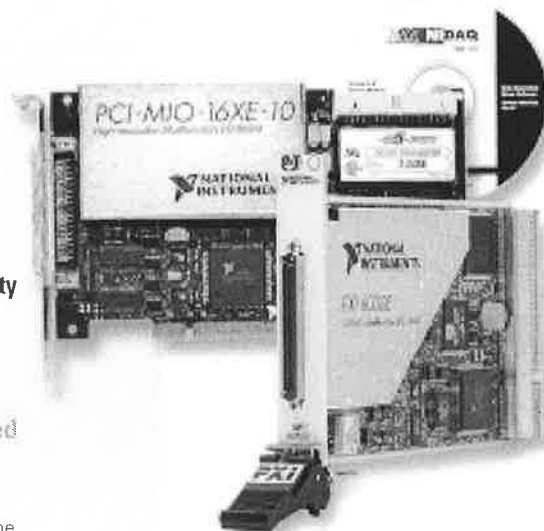


Figure 1. NI 6030E, NI 6031E, NI 6032E, and NI 6033E Hardware Block Diagram

See the E Series Multifunction DAQ Overview on page 230 for a more detailed hardware overview.

Overview

The NI 6030E, NI 6031E, NI 6032E, and NI 6033E DAQ devices use E Series technology to deliver high performance and reliable data acquisition capabilities to meet a wide range of application requirements. You get up to 100 kS/s, 16-bit performance, with a choice of either 16 or 64 single-ended analog inputs. Depending on your hard drive, these devices can stream to disk at rates up to 100 kS/s.

These E Series DAQ devices feature analog and digital triggering capability, as well as two 24-bit, 20 MHz counter/timers; and eight digital I/O lines. The NI 6030E and NI 6031E also feature two 16-bit analog outputs.

INFO CODES

For more information or to order products online, visit mccominfo and enter:

pcimio16xe10
pxi6030e
atmio16xe10
pci6031e
pxi6031e
pci6032e
atai16xe10
pci6033e

BUY ONLINE!

Consider our NI 6052E high-speed, 16-bit products. See page 241.

Family	Bus	Analog Inputs	Resolution	Sampling Rate S/s	Input Range	Analog Outputs	Resolution	Output Rate	Output Range	Digital I/O	Counter/Timers	Triggers
NI 6030E	PCI, PXI/CPCI, AT	16 SE/8 DI	16 bits	100 kS/s	±0.1 to ±10 V	2	16 bits	100 kS/s	±10 V	8	2, 24-bit	Analog and Digital
NI 6031E	PCI, PXI/CPCI	64 SE/32 DI	16 bits	100 kS/s	±0.1 to ±10 V	2	16 bits	100 kS/s	±10 V	8	2, 24-bit	Analog and Digital
NI 6032E	PCI, ISA	16 SE/8 DI	16 bits	100 kS/s	±0.1 to ±10 V	—	—	—	—	8	2, 24-bit	Analog and Digital
NI 6033E	PCI	64 SE/32 DI	16 bits	100 kS/s	±0.1 to ±10 V	—	—	—	—	8	2, 24-bit	Analog and Digital

Table 1. NI 6030E, NI 6031E, NI 6032E, and NI 6033E Channel, Speed, and Resolution Specifications (See page 271 for detailed specifications.)

E Series Multifunction DAQ – 100 kS/s, 16-Bit, 16 or 64 Analog Inputs

Nominal Range (V)		Absolute Accuracy							Relative Accuracy	
		% of Reading		Offset (µV)	Noise + Quantization (µV)		Temp Drift (%/°C)	Absolute Accuracy at Full Scale (mV)	Resolution (µV)	
		24 Hrs	1 Year		Single Pt.	Averaged			Single Pt.	Averaged
Positive FS	Negative FS									
±10.0	-10.0	0.0044	0.0061	479.2	634.1	54.9	0.0001	1.147	723.3	72.3
±5.0	-5.0	0.0344	0.0361	243.6	317.1	27.5	0.0006	2.077	361.6	36.2
±2.0	-2.0	0.0344	0.0361	102.2	126.8	11.0	0.0006	0.836	144.7	14.5
±1.0	-1.0	0.0344	0.0361	55.1	63.4	5.5	0.0006	0.422	72.3	7.2
±0.5	-0.5	0.0344	0.0361	31.6	36.8	3.2	0.0006	0.215	42.2	4.2
±0.2	-0.2	0.0394	0.0411	17.4	22.5	2.0	0.0006	0.102	26.5	2.7
±0.1	-0.1	0.0444	0.0461	12.7	19.6	1.8	0.0006	0.061	24.1	2.4
10.0	0.0	0.0044	0.0061	326.6	417.8	36.6	0.0001	0.976	482.2	48.2
5.0	0.0	0.0344	0.0361	167.3	208.9	18.3	0.0006	1.992	241.1	24.1
2.0	0.0	0.0344	0.0361	71.7	83.6	7.3	0.0006	0.802	96.4	9.6
1.0	0.0	0.0344	0.0361	39.9	41.8	3.7	0.0006	0.405	48.2	4.8
0.5	0.0	0.0344	0.0361	23.9	28.1	2.5	0.0006	0.207	33.1	3.3
0.2	0.0	0.0394	0.0411	14.4	19.6	1.8	0.0006	0.098	24.1	2.4
0.1	0.0	0.0444	0.0461	11.2	18.1	1.7	0.0006	0.059	22.9	2.3

Note: Accuracies are valid for measurements following an internal E Series Calibration. Averaged numbers assume dithering and averaging of 100 single-channel readings. Measurement accuracies are listed for operational temperatures within ±1 °C of internal calibration temperature and ±10 °C of external or factory calibration temperature. One-year calibration interval recommended. The Absolute Accuracy at Full Scale calculations were performed for a maximum range input voltage (for example, 10 V for the ±10 V range) after one year, assuming 100 pt averaging of data. See overview on page 234 for an example calculations.

Table 2. NI 6030E, NI 6031E, NI 6032E, and NI 6033E Analog Input Accuracy Specifications

Nominal Range (V)		Absolute Accuracy					Absolute Accuracy at Full Scale (mV)
		% of Reading			Offset (µV)	Temp Drift (%/°C)	
Positive FS	Negative FS	24 Hrs	90 Days	1 Year			
10	-10	0.0045	0.0053	0.0062	812.8	0.0001	1.430
10	0	0.0045	0.0053	0.0062	583.9	0.0001	1.201

Note: Temp Drift applies only if ambient is greater than $\pm 10^{\circ}\text{C}$ of previous external calibration. See page 234 for example calculations.

Table 3. NI 6030E, NI 6031E, NI 6032E, and NI 6033E Analog Output Accuracy Specifications.

Ordering Information

NI 6030E	
PCI-MIO-16XE-10	777384-01
PXI-6030E	777555-01
AT-MIO-16XE-10*	777181-01
NI 6031E	
PCI-6031E	777514-01
PXI-6031E	777636-01
NI 6032E	
PCI-6032E	777422-01
AT-AI-16XE-10*	777279-01
NI 6033E	
PCI-6033E	777516-01

Includes NI-DAQ driver software.

*Windows only

For information on extended warranty and value added services, see page 22.

Recommended Configurations

Family	DAQ Device	Accessory	Cable
NI 6030E	PCI-MIO-16XE-10	SCB-68 (776844-01)	SH6868-EP (184749-01)
	PXI-6030E	TB-2705 (778241-01)	—
	AT-MIO-16XE-10	SCB-68 (776844-01)	SH6868-EP (184749-01)
NI 6031E	PCI-6031E	SCB-100 (776990-01)	SH100100 (182853-01)
	PXI-6031E	Two TBX-68s (777141-01)	SH100686B (182849-01)
NI 6032E	PCI-6032E	SCB-68 (776844-01)	SH6868-EP (184749-01)
	AT-AI-16XE-10	SCB-68 (776844-01)	SH6868-EP (184749-01)
NI 6033E	PCI-6033E	SCB-100 (776990-01)	SH100100 (182853-01)

For E Series accessory and cable information, see page 256.

See page 233 in the E Series Multifunction DAQ Overview for I/O connector diagrams.

See page 271 for detailed specifications.

E Series Multifunction DAQ Accessories

Selection Guide

Step 1. Select your E Series device.

Step 2. Using Tables 1 and 2 as a guide, determine which accessories are appropriate for that device. Select an accessory. Table 3 provides descriptions for E Series device accessories.

Step 3. Using Tables 1 and 2, determine which cable is required to connect your selected device and accessory.

Device	Accessory			
	TBX-68, CB-68LP, CB-68LPR, DAQ Signal Accessory, CA-1000, BNC-2110, BNC-2120, BNC-2090, SCB-68	TB-2705	SCXI Signal Conditioning	SCC Modular
Cables				
68-pin E Series (except DAQCard)	SH68-68-EP (shielded)	Connects directly to the device (PXI only)	See page 385 for SCXI Signal Conditioning details	See page 461 for SCC Modular Signal Conditioning details
Latching DAQCards	R6868 (unshielded)	N/A	See page 385 for SCXI Signal Conditioning details	See page 461 for SCC Modular Signal Conditioning details
NI 6024E, NI 6062E	SHC68-68-EP (shielded)	N/A	See page 385 for SCXI Signal Conditioning details	See page 461 for SCC Modular Signal Conditioning details
Nonlatching DAQCards	RC68-68 (unshielded)	N/A	See page 385 for SCXI Signal Conditioning details	See page 461 for SCC Modular Signal Conditioning details
AI-16E-4, AI-16XE-50	PSH68-68 (shielded)	N/A	See page 385 for SCXI Signal Conditioning details	See page 461 for SCC Modular Signal Conditioning details
	PR68-68F (unshielded)			

Table 1. Accessories and Cables for 68-Pin and DAQCard E Series Devices

Device	Accessory					
	TBX-68, CB-68LP, CB-68LPR, DAQ Signal Accessory, CA-1000, BNC-2110, BNC-2120, BNC-2090, SCB-68	BNC-2115	TBX-68, CB-68LP, CB-68LPR, CA-1000, SCB-68	SCB-100	SCXI Signal Conditioning	SCC Modular Signal Conditioning
Cables						
100-pin E Series with 64 AI channels NI 6071E, NI 6031E, NI 6033E AT-MIO-64E-3	SH1006868 (shielded); splits into two 68-pin connectors; these accessories are used with the first 68-pin connector. See Figure 16 on page 260.	SH1006868 (shielded); splits into two 68-pin connectors; these accessories are used with the second 68-pin connector.	SH1006868 (shielded); splits into two 68-pin connectors; these accessories are used with the second 68-pin connector.	SH100100 (shielded)	See page 385 for SCXI Signal Conditioning details	See page 461 for SCC Modular Signal Conditioning details
100-pin E Series with 16 AI channels and 32 DIO lines PCI-6025E, AT-6021E	SH1006868 (shielded); splits into two 68-pin connectors; these accessories are used with the first 68-pin connector. See Figure 16 on page 260.	SH1006868 (shielded); splits into two 68-pin connectors; these accessories are used with the second 68-pin connector.	SH1006868 (shielded); splits into two 68-pin connectors; these accessories are used with the second 68-pin connector.	SH100100 (shielded)	See page 385 for SCXI Signal Conditioning details	See page 461 for SCC Modular Signal Conditioning details

Table 2. Accessories and Cables for 100-Pin and DAQCard E Series Devices

Accessory	Description	Page
SCXI Signal Conditioning	High channel-count signal conditioning platform	385
SCC Modular Signal Conditioning	Single or dual channel signal conditioning modules	461
AMUX-64T, 5B, SSR, ER, and SC-204x Signal Conditioning	External signal conditioning accessories	478
BNC-2110	BNC accessory for 68-pin E Series devices	257
BNC-2115	BNC accessory for extended I/O on 100-pin E Series devices	257
BNC-2120	BNC accessory with function generator (for 68-pin E Series devices)	257
BNC-2090	Rack-mountable BNC accessory (for 68-pin E Series devices)	257
CA-1000 enclosure	Configurable connectivity enclosure	257
TB-2705	Latching screw terminal block for PXI E Series modules	258
SCB-100	100-pin, shielded screw terminal block with breadboard areas	258
SCB-68	68-pin, shielded screw terminal block with breadboard areas	258
TBX-68	68-pin, DIN rail-mountable screw terminal block	258
CB-68LP, CB-68LPR	68-pin, low-cost screw terminal block	258
Signal Source and Demo Accessory	DAQ signal accessory to demo and test analog, digital and counter/timer functions	259

For complete and up-to-date information about accessories, visit ni.com/catching

Table 3. Overview of E Series DAQ Accessories

E Series Multifunction DAQ Accessories

SCXI High-Performance Signal Conditioning (see Figure 1)

SCXI is a modular high-performance signal conditioning platform that you use as a front end to your E Series DAQ device. With the SCXI multiplexing architecture, you can expand your analog inputs to 3,072 channels. Additionally, SCXI offers a variety of modules for connecting to thermocouples, RTDs, strain gauge transducers, LVDT position sensors, ICP-compatible accelerometers/microphones, thermistors, millivolt inputs, voltage inputs up to 1000 V, current inputs (0-20mA), frequency inputs or dynamic signals.

See page 385 for details on SCXI Signal Conditioning.

SCC Series – Modular Signal Conditioning for Low-Channel Count Applications (see Figure 2)

The SCC Series modular signal conditioning system consists of SCC modules that plug into a low-profile SC-2345 shielded carrier. SCC modules give you single or dual-channel signal conditioning for up to 16 analog input channels and eight digital I/O lines of your plug-in E Series DAQ device. The SCC Series offers signal conditioning for a variety of inputs, including thermocouples, RTDs, strain gauges, ICP-compatible accelerometers, accelerators, analog inputs requiring isolation, high voltage (up to 100 V), current (0-20mA), and optically isolated digital I/O. Lowpass filtering and bread boarding modules are also available.

See page 461 for details on SCC Signal Conditioning.

Connector Blocks

BNC-2100 Series Connector Blocks (see Figure 3)

Shielded connector blocks with signal-labeled BNC connectors for easy connectivity of your analog input, analog output, digital I/O and counter/timer signals to your E Series device. The BNC-2110 and BNC-2120 work with all E Series devices. The BNC-2120 also provides a function generator, quadrature encoder, temperature reference, thermocouple connector and LED so that you can test the functionality of your hardware. The BNC-2115 has 24 BNC inputs for connecting to the extended I/O channels of our 100-pin E Series DAQ devices.

BNC-2110.....	777643-01
Dimensions – 20.3 by 11.2 by 5.5 cm (8.0 by 4.4 by 2.2 in.)	
BNC-2115.....	777807-01
Dimensions – 20.3 by 11.2 by 5.5 cm (8.0 by 4.4 by 2.2 in.)	
BNC-2120.....	777960-01
Dimensions – 26.7 by 11.2 by 6.0 cm (10.5 by 4.4 by 2.4 in.)	

BNC-2090 Shielded BNC Adapter Chassis (see Figure 4)

Shielded, rack-mountable adapter with signal-labeled BNC connectors, spring terminal blocks, and component locations for passive signal conditioning. Consists of 22 BNC connectors and 28 spring terminals to simplify connection to your analog, digital, trigger and counter/timer signals. The BNC-2090 has silk-screened component locations that you use to develop simple signal conditioning circuits. For added flexibility, you can connect any E Series DAQ device to the BNC-2090 from the front or rear through dual 68-pin connectors.

BNC-2090.....	777270-01
Dimensions – 48.3 by 4.4 by 18.8 cm (19.0 by 1.7 by 7.4 in.)	



Figure 1. SCXI High-Performance Signal Conditioning

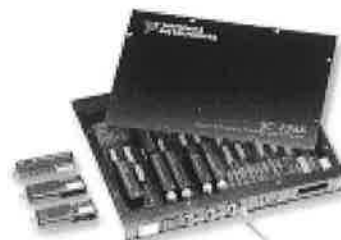


Figure 2. SCC Portable, Modular Signal Conditioning

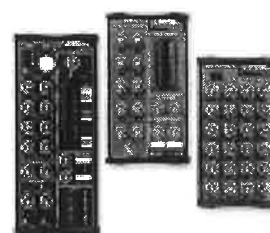


Figure 3. BNC-2100 Series Connector Blocks

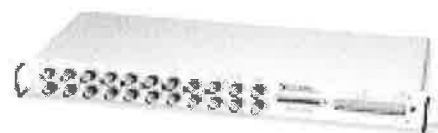


Figure 4. BNC-2090 Shielded BNC Adapter Chassis



Figure 5. CA-1000 Configurable Signal Conditioning Enclosure



Figure 6. TB-2705 Terminal Block



Figure 7. SCB-68 and SCB-100 Shielded I/O Connector Blocks

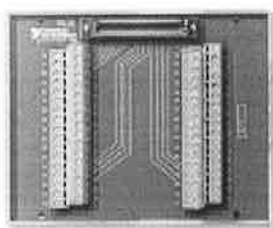


Figure 8. TBX-68 I/O Connector Block

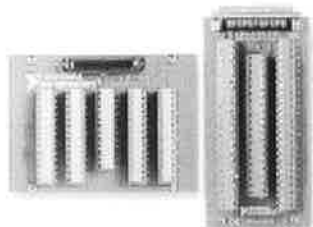


Figure 9. CB-68LP and CB-68LPR I/O Connector Blocks



Figure 10. DAQ Signal Accessory

E Series Multifunction DAQ Accessories

CA-1000 Configurable Signal Conditioning Enclosure (see Figure 5)

Configurable enclosure that gives you maximum user-defined connectivity and flexibility through customized panelettes. Each enclosure can accommodate up to 9 panelettes.

Dimensions – 30.7 by 25.4 by 4.3 cm (21.1 by 10 by 1.7 in.)

See page 263 for more information about the CA-1000.

TB-2705 Terminal Block for 68-pin PXI E Series Devices (see Figure 6)

Screw terminal block for PXI that works with your PXI E Series DAQ devices. Latches to the front of your PXI module with locking screws and provides strain relief as well as easy access to your analog, digital, trigger and counter/timer signals through screw terminals.

TB-2705778241-01

Dimensions – 8.43 by 10.41 by 2.03 cm (3.32 by 4.1 by 0.8 in.)

SCB-68 and SCB-100 Shielded I/O Connector Blocks (see Figure 7)

Shielded I/O connector blocks for rugged, very low-noise signal termination for connecting to 68-pin or 100-pin E Series DAQ devices, respectively. Silk-screened component locations for easy addition of simple signal-conditioning circuitry for your analog input channels. They also include general-purpose breadboard areas (two on the SCB-68; three on the SCB-100) as well as an IC temperature sensor for cold-junction compensation in temperature measurements.

SCB-68776844-01

Dimensions – 19.5 by 15.2 by 4.5 cm (7.7 by 6.0 by 1.8 in.)

SCB-100776990-01

Dimensions – 19.5 by 15.2 by 4.5 cm (7.7 by 6.0 by 1.8 in.)

TBX-68 I/O Connector Block with DIN-Rail Mounting (see Figure 8)

Termination accessory with 68 screw terminals for easy connection of field I/O signals to 68-pin DAQ devices. Includes one 68-pin male connector for direct connection to 68-pin cables. The TBX-68 is mounted in a protective plastic base with hardware for mounting on a standard DIN rail.

TBX-68777141-01

Dimensions – 12.50 by 10.74 cm (4.92 by 4.23 in.)

CB-68LP and CB-68LPR I/O Connector Blocks (see Figure 9)

Low-cost termination accessory with 68 screw terminals for easy connection of field I/O signals to 68-pin E Series DAQ devices. Includes one 68-pin male connector for direct connection to 68-pin cables. The connector blocks include standoffs for use on a desktop or for mounting in a custom panel. The CB-68LP has a vertical-mounted 68-pin connector. The CB-68LPR has a right-angle mounted connector, and is used with the CA-1000 (see page 263).

CB-68LP777145-01

Dimensions – 14.35 by 10.74 cm (5.65 by 4.23 in.)

CB-68LPR777145-02

Dimensions – 7.62 by 16.19 cm (3.00 by 6.36 in.)

E Series Multifunction DAQ Accessories and Cables

Signal Source and Demo Accessory (see Figure 10)

The DAQ Signal Accessory demonstrates and tests the use of analog, digital, and counter/timer functions of DAQ devices. You can connect the DAQ Signal Accessory directly to your DAQ device. It features a built-in function generator, quadrature encoder, solid-state relay, IC temperature sensor, noise generator, microphone jack, thermocouple jack, four LEDs, and a digital trigger button. The DAQ Signal Accessory works with all E Series DAQ devices.

DAQ Signal Accessory777382-01
Dimensions – 12.7 by 12.7 cm (5.0 by 5.0 in.)

RTSI Bus Cables (see Figures 11 and 12)

Use RTSI bus cables to connect timing and synchronization signals among Measurement, Vision, Motion, and Controller Area Network (CAN) boards for PCI and ISA and DAQPad 6070E boards. For systems using long and short boards order the extended RTSI cable.

2 boards776249-02
3 boards776249-03
4 boards776249-04
5 boards776249-05
Extended, 5 boards777562-05
3 external boards186464-01

Shielded I/O Cables

SH68-68-EP Shielded Cable (see Figure 13)

Shielded 68-conductor cable terminated with two 68-pin female 0.050 series D-type connectors. Features individually-shielded analog twisted pairs for reduced crosstalk with high-speed devices. This cable works with all 68-pin E Series devices (except latching DAQCards). If you need a right-angle connector, the SH68-68R1-EP shielded cable is fully compatible.

1 m184749-01
2 m184749-02

SH68-68R1-EP Shielded Cable (see Figure 14)

Shielded 68-conductor cable; one end terminates with a 68-pin female 0.050 series D-type connector and the other end terminates with a right-angle 68-pin female 0.050 series D-type connector.

1 m187051-01

SH100100 Shielded Cable (see Figure 15)

Shielded 100-conductor cable terminated with 100-pin male 0.050 series D-type connectors. This cable connects the 100-pin E Series devices to 100-pin accessories.

1 m182853-01
2 m182853-02



Figure 11. RTSI Bus Cable



Figure 12. Extended RTSI Bus Cable



Figure 13. SH68-68-EP Shielded Cable



Figure 14. SH68-68R1-EP Shielded Cable



Figure 15. SH100100 Shielded Cable

E Series Multifunction DAQ Accessories and Cables



Figure 16. SH1006868 Shielded Cable



Figure 17. SHC68-68-EP Shielded Cable



Figure 18. PSHR68-68 Shielded Cable Kit



Figure 19. PSHR68-68M Shielded Cable



Figure 20. R6868 Ribbon Cable

SH1006868 Shielded Cable (see Figure 16)

Shielded cable that connects to 100-pin E Series devices and terminates with two female 68-pin 0.050 series D-type connectors. See Table 2 on page 256 for accessories compatible with each 68-pin connector.

1 m	182849-01
2 m	182849-02

SHC68-68-EP and SHC68U-68-EP Shielded Cables for Latching E Series DAQCards (see Figure 17)

These cables connect a latching E Series DAQCard (NI 6062E and NI 6024E) to standard 68-pin accessories. Latching screws secure the shielded connector to the PCMCIA DAQCard. The SHC68-68-EP is a shielded 68-conductor cable terminated with a VHDCI 68-pin male connector at one end and a 68-pin female 0.050 series D-type connector at the other. The SHC68U-68-EP is identical to the SHC68-68-EP except it uses an inverted VHDCI 68-pin male connector. Use the SHC68U-68-EP for a DAQCard located in the bottom PCMCIA slot in your laptop. Use the SHC68-68-EP cable with a DAQCard inserted in the upper PCMCIA slot in your laptop. When using two E Series DAQCard PCMCIA devices in adjacent slots, you must use one SHC68-68-EP and one SHC68U-68-EP.

SHC68-68-EP	
0.5 m	186838-0R5
1 m	186838-01
SHC68U-68-EP	
0.5 m	187406-0R5
1 m	187406-01

PSHR68-68 Shielded Cable Kit for Nonlatching DAQCards (see Figure 18)

Shielded cable for use in connecting non-latching E Series DAQCards (AI-16E-4 and AI-16XE-50) with 68-pin accessories. The kit contains the PSHR68-68M, the PCMCIA Strain-Relief Adapter and a 1 m SH68-68-EP cable.

1 m	777293-01
-----------	-----------

PSHR68-68M Shielded Cable for Nonlatching DAQCards (see Figure 19)

Shielded cable for use in connecting non-latching E Series DAQCards (AI-16E-4 and AI-16XE-50) with custom cables and other 68-pin cable assemblies.

0.1 m	183569-01
-------------	-----------

E Series Multifunction DAQ Accessories and Cables

Ribbon I/O Cables

R6868 Ribbon Cable for E Series Devices (see Figure 20)

68-conductor flat ribbon cable terminated with two 68-pin connectors. Use this cable to connect a 68-pin E Series device to 68-pin accessories.

1 m182482-01

RC68-68 Ribbon Cable for Latching DAQCards (see Figure 21)

Ribbon cable that connects to a latching E Series DAQCard (NI 6062E, NI 6024E) and is terminated with a 68-pin female connector that attaches directly to 68-pin accessories. Two RC68-68 cables can be used together in adjacent PCMCIA slots.

0.25 m187252-0R25

1 m187252-01

PR68-68F for Non-Latching DAQCards (see Figure 22)

Ribbon cable that connects to a non-latching E Series DAQCard (AI-16E-4, AI-16XE-50) and is terminated with a 68-pin female connector that attaches directly to 68-pin accessories.

0.2 m183646-0R2

1 m183646-01

Custom Connectivity Components

68-Pin Custom Cable Connector/Backshell Kit (see Figure 23)

68-pin female mating connector and backshell kit for use in making custom cables. Solder-cup contacts are available for soldering of cable wires to the connector.

68-pin connector/backshell kit776832-01

PCB Mounting Connectors for Custom Accessories (see Figure 24)

PCB connectors for use in building custom accessories that connect to 68-conductor or 100-conductor shielded and ribbon cables. Two connectors are available, one for right-angle and one for vertical mounting onto a PCB.

68-position, male, right-angle mounting777600-01

68-position, male, vertical mounting777601-01

100-position, female, right-angle mounting777778-01

100-position, female, vertical mounting.....777779-01

PCMCIA Strain-Relief Accessory (see Figure 25)

Accessory that attaches to the bottom of your notebook computer and provides adjustable strain relief for one or two PCMCIA cables attached to the installed PCMCIA card(s). Used with non-latching E Series DAQCards (AI-16E-4, AI-16XE-50).

PCMCIA Strain-Relief Accessory777550-01



Figure 21. RC68-68 Ribbon Cable



Figure 22. PR68-68F Ribbon Cable

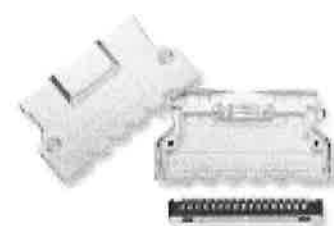


Figure 23. 68-Pin Custom Cable Connector/Backshell Kit



Figure 24. PCB Mounting Connectors for Custom Accessories



Figure 25. PCMCIA Strain-Relief Accessory

E Series Multifunction DAQ Accessories and Cables



Figure 26. USB Cable



Figure 27. IEEE 1394 Cable

USB Cable (see Figure 26)

Cable that connects DAQPad devices for the Universal Serial Bus (USB) to a USB port. The USB cables have a USB B-type connector and a USB A-type connector.

1 m	184125-01
2 m	184125-02

IEEE 1394 Cable (see Figure 27)

Cable that connects DAQPad devices for IEEE 1394 (FireWire) to an IEEE 1394 port.

1 m (latching)	185798-01
2 m (latching)	185798-02

Use Interactive Online Catalog Configurator for Quick Product Selection

You can now easily configure NI multifunction data acquisition (DAQ) measurement systems using a new, interactive feature of our online catalog. The interactive online catalog offers a better, easier way to select and purchase measurement solutions from National Instruments. Based on user input, the interactive online catalog suggests products and then suggests the appropriate cables and accessories for those products. This new automated tool helps eliminate ordering mistakes and product-compatibility errors.

To take advantage of the online catalog for multifunction DAQ devices, visit ni.com/catalog.

From the Products and Services menu, select Data Acquisition, then select Multifunction I/O. The online catalog prompts you with a series of questions regarding preferences for operating system, computer bus, number of channels, and maximum sampling rate. The online catalog then recommends several appropriate DAQ devices. You can review specifications on each device and select your preferred product. Next, the catalog suggests the preferred accessory and cable solution designed to work with the selected DAQ device. You have the option of choosing the preferred configuration or choosing from a separate list of accessories and cables that also work with the selected DAQ device. You can purchase the selected items online.



Figure 28. Use the interactive configuration tool in the NI online catalog to select and purchase multifunction DAQ solutions.

Configurable Signal Conditioning Enclosure

CA-1000

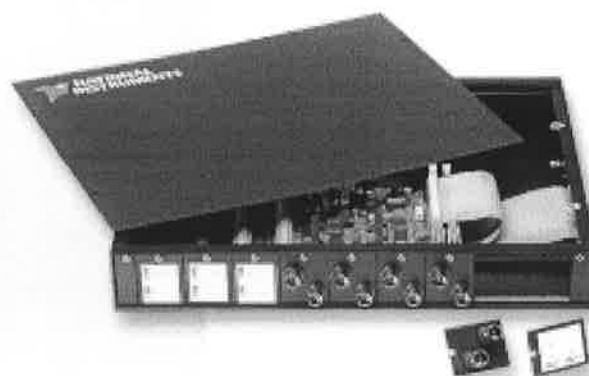
- Versatile connector/enclosure system
- Houses signal conditioning and connector block accessories
- Wide variety of I/O connectivity and panelette options
- Holds maximum of 18 connectivity/interface panelettes
- Low profile enclosure
- Rack-mount and stacking kits available

I/O Connectivity

- BNC
- Thermocouple
- Banana jack
- LEMO® connector (B-Series)
- MIL-Spec
- SMB
- Dual 9-pin D-Sub
- Strain relief

Interface Panelettes

- Momentary pushbutton switch
- Potentiometer
- Toggle switch
- Rocker switch
- LED



Overview

The National Instruments CA-1000 is a configurable signal conditioning enclosure designed for maximum user-defined I/O connectivity and flexibility. The CA-1000 is a portable enclosure for laptop, desktop, and rack-mount applications. In the CA-1000, you can install many NI signal conditioning accessories, such as the SC-204x signal conditioning products, and the SCB-68, CB-68LPR, and CB-50LP terminal blocks. The result is a compact, portable, flexible, and comprehensive signal conditioning/interconnection system. The CA-1000 also facilitates quick connection and disconnection with standard I/O connectors for easy system integration and reconfiguration. By adding interface panelettes, such as toggle switches, potentiometers, and LEDs, you can locally control and verify system operation.

Description

The CA-1000 system includes four components: 1) CA-1000 enclosure, 2) I/O and interface panelettes, 3) signal conditioning or measurement accessories installed in the CA-1000, and 4) for 50-pin accessories, an internal cable adapter to connect the signal conditioning accessory to the cable attached to the CA-1000.

CA-1000 Enclosure

The metal enclosure provides a low-profile, portable housing for signal conditioning and connector accessories. You can place the enclosure under a laptop PC, on a benchtop, or in a 19 in. rack. You can also stack two or more enclosures with the stacking kit. The CA-1000 enclosure includes five cable entry locations, so you can place the 68-pin or 50-pin connector that you cable to your measurement device on either the side or the rear of the CA-1000

enclosure. Please note, the CA-1000 is shipped without any panelettes, signal conditioning accessories, connector blocks, or cables. Order all of these components separately.

Internal Accessories

The CA-1000 houses a variety of signal conditioning and data acquisition accessories, including the SC-204x, SCB-68, CB-68LPR, and CB-50LP (Table 1 on page 264). You mount these accessories to the bottom panel of the CA-1000 enclosure.

I/O Panelettes

The CA-1000 includes a user-configurable signal connection scheme. This connectivity flexibility is achieved with interchangeable panelettes. The panelettes, which come with standard signal connectors – for example, BNC, SMB, banana jack, thermocouple plugs, and LEMO, MIL-Spec, and 9-pin D-Sub connectors – mount in the front of the CA-1000 enclosure. The CA-1000 front panel offers nine panelette slots. The rear panel can also be removed offering nine more panelette slots. However, this option is not available if you are using the SCB-68 inside the CA-1000. You can mix and match different types of panelettes. Each panelette (except for the strain-relief panel) includes lead wires that you connect to the screw terminals of the accessory mounted inside the CA-1000. You can therefore connect the panelettes to any I/O signal available on the accessory.

INFO CODES
For more information
or to order products
online, visit ni.com/info
and enter:

ca1000

BUY ONLINE!

Configurable Signal Conditioning Enclosure

Interface Panelettes

National Instruments also offers interface panelettes, which expand the functionality of the CA-1000. Interface panelettes include traditional interface controls and displays, such as rocker switches, toggle switches, momentary switches, potentiometers, and LEDs. Using interface panelettes, which are mounted alongside I/O panelettes, you can change hardware inputs, trigger events, or verify operational status. Each interface panelette includes lead wires for connection to the screw terminals of the accessory mounted inside the CA-1000.

Cabling

The cabling needed to connect the CA-1000 to the measurement device depends on the accessories installed in the CA-1000 and the

measurement device used. Some accessories installed in the CA-1000 require internal cabling to connect the accessory to the CA-1000 wall. Use Table 1 to determine what cabling components you need, including the cable to your measurement device.

The CA-1000 also provides the flexibility of five external interconnection locations, giving convenient cabling for laptop applications by aligning the I/O connector with the location of the PCMCIA slots on laptop computers. With the five external interconnection locations, you can also customize desktop and rack-mount applications for added convenience.

Devices	SC-204x Series	Connector Blocks	
		CB-50LP	CB-68LPR or SCB-68
68-pin E Series DAQ Devices (except DAQCards)	R68M-50F and SH68-68-EP ¹	N/A	SH68-68-EP ¹
100-pin E Series DAQ Devices ²	Applicable for one leg	N/A	SH1006868
Latching E Series DAQCards:	R68M-50F and SHC68-68-EP	N/A	SHC68-68-EP
DAQCard-6062E, DAQCard-6024E	—	—	—
Nonlatching E Series DAQCards:	R68M-50F and PSHR68-68 Shielded Cable Kit ²	N/A	PSHR68-68 Shielded Cable Kit ²
DAQCard-AI-16E-4, DAQCard-AI-16XE-50	—	—	—
68-pin Digital I/O and Counter/Timer Devices (except DAQCards)	N/A	N/A	SH68-68-D1
PCI-DIO-32HS, PXI-6533, AT-DIO-32HS,	—	—	—
NI 6534, NI 660x	—	—	—
Nonlatching 68-pin Digital I/O DAQCards:	N/A	N/A	PSHR68-68-D1 Shielded Cable Kit
DAQCard-6533	—	—	—
Simultaneous Sampling Multifunction DAQ Devices	N/A	N/A	SH68-68-EP ¹
PCI-6503	N/A	R50M-50F and SH50-50	N/A
PC-DIO-24	—	—	—
DAQCard-DIO-24	N/A	R50M-50F and PSH27-50F-D1	N/A
NI 6527 ³ , PCI-DIO-96 ³ , PXI-6508 ³ , DAQPad-6508 ³	N/A	Two R50M-50F and R1005050 ⁴	N/A
PC-DIO-96 ³	N/A	Two R50M-50F and NB5 ⁴	N/A

¹You can also use the SH68-68R1-EP or R6868. ²You can also use the PR68-68F. ³You can use two CA-1000 enclosures with one of these devices. Please note: If you are using a NI 435x series data logger, please see Figure 1 on page 298 for information on cabling to a CB-68T and CA-1000. ⁴Splits into two 50-pin connectors. See page 319 for information on using the CA-1000 with signal source products.

Table 1 CA-1000 Cabling

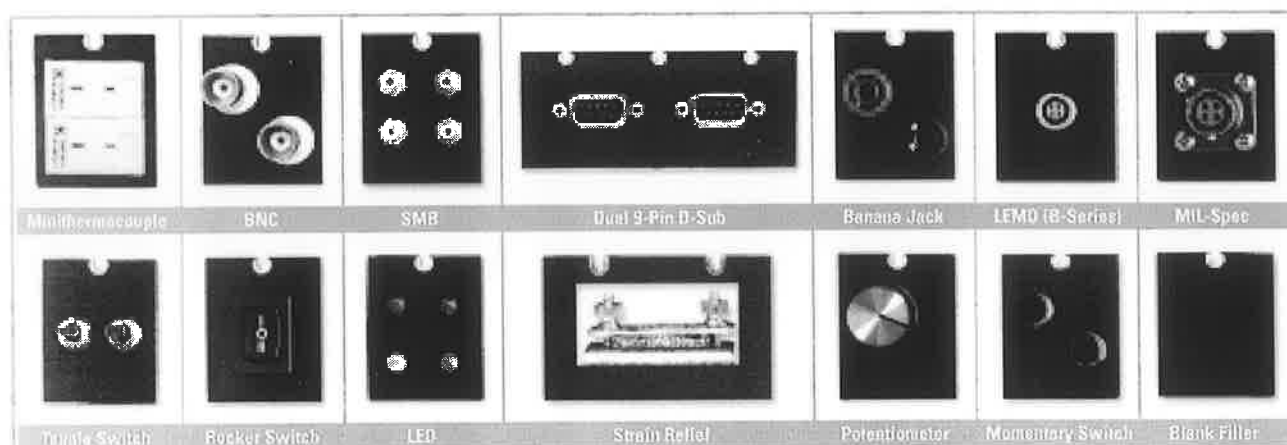


Table 2 CA-1000 Panelette Options

Configurable Signal Conditioning Enclosure

Panelmate	Description	Connectors/Units per Panelmate	Slot Width
Minithermocouple Jack	J-type	2	1
	K-type	2	1
	Uncompensated	2	1
Thermocouple Jack	J-type	1	1
	K-type	1	1
	Uncompensated	1	1
BNC	BNC connector	2	1
SMB	SMB connector	4	1
Banana Jack	Banana Jack	2	1
LEMO	2-pin female	2	1
	4, 6-pin female	1	1
MIL-Spec	2, 4, 6-pin female	1	1
9-pin D-sub	Single (male)	1	2
	Single (female)	1	2
	Dual (male)	2	3
	Dual (female)	2	3
Momentary Pushbutton Switch	On – off	2	1
Toggle Switch	(On – off – on)	2	1
Rocker Switch	(On – off – on)	1	1
LED	A red, green, yellow, and orange LED	4	1
Potentiometer	1 turn, 10 kW	1	1
Strain Relief	Screw clamp	1	2
Blank	Filler panel	—	1

Table 3 CA-1000 Panelette descriptions

Ordering Information

CA-1000 (enclosure only)777664-01
 Dimensions – 30.7 by 25.4 by 4.3 cm (21.1 by 10.3 by 1.7 in.)

I/O Connector Panelettes

Minithermocouple, J-type (2 included)184736-01
 Minithermocouple, K-type (2 included)184736-02
 Minithermocouple, uncompensated (2 included)184736-03
 Thermocouple, J-type187597-01
 Thermocouple, K-type187597-02
 Thermocouple, uncompensated187597-03
 BNC (2 included)184737-01
 Banana jack (2 included)186405-01
 LEMO connector (B-Series)
 Dual 2-pin, female187585-01
 4-pin, female187585-02
 6-pin, female187585-03
 MIL-C-26482 (Series 1)
 MS3112E8-2 S187591-01
 MS3112E8-4 S187591-02
 MS3112E10-6 S187591-03
 SMB (4 included)185505-01

Ordering Information (continued)

Strain relief184721-01
 9-Pin D-Sub
 Single male184738-01
 Dual male184738-02
 Single female184738-03
 Dual female184738-04
 Blank184483-01

Interface Panelettes

Momentary pushbutton switch (2 included)185380-01
 Rocker switch (on/off/on)185379-01
 Toggle switch (on/off/on – 2 included)185378-01
 Potentiometer (10 k Ω , single turn)185377-01
 LED 4 – (Includes: 1 green,
 1 red, 1 orange, 1 yellow)185376-01

External Cables

SH68-68-EP, 1 m182419-01
 SH68-68-D1, 1 m183432-01
 SH68-68R1-EP, 1 m187051-01
 SH50-50, 1 m777720-01
 R6868, 1 m182482-01
 R1005050, 1 m182762-01
 NB5, 1 m181304-10
 SH1006868, 1 m182849-01
 PSHR68-68 Shielded Cable Kit777293-01
 PSHR68-68-D1 Shielded Cable Kit777420-01
 PR68-68F, 1 m183646-01
 PSH27-50F-D1, 1 m776989-01
 SHC68-68-EP, 1 m186838-01

Internal Cables

R50M-50F ribbon cable184526-0R3
 R68M-50F MIO bulkhead ribbon cable777660-0R3

Accessories

CA-1000 Rack-Mount Kit (1U)777665-01
 CA-1000 Stacking Kit777666-01
 CA-1000 Panel Mount Kit187243-01
 Strain Relief Kit¹187407-01
¹You cannot use the Strain Relief Kit in conjunction with the rack-mount, panel-mount, or stacking kits.

For information on extended warranty and value added services, see page 22.

E Series Multifunction DAQ Overview

Self-Calibration Using an Internal Reference

The E Series analog inputs and outputs have calibration circuitry to correct gain and offset errors. You can calibrate the device in software to avoid analog I/O errors caused by time and temperature drift at run time. No external circuitry is necessary; an internal reference ensures high accuracy and stability over time and temperature. Factory-calibration constants are permanently stored in an onboard EEPROM and cannot be modified. A modifiable section of the EEPROM stores user-modifiable constants. You can return the devices to their initial factory calibration by accessing the unmodified factory constants. Included with all E Series devices is an NIST-traceable and ISO-9002 certified calibration certificate. Visit ni.com/calibration for more information.

I/O Interface – MITE and DAQ-PnP

All of the PCI and PXI E Series use the MITE ASIC as a bus master interface to the PCI bus. The E Series products for ISA use an ASIC that fully implements the Plug and Play ISA Specification, so that the DMA level, interrupt channels, and base I/O address are all software configurable. All other E Series devices are inherently Plug and Play compatible. Visit ni.com/info and enter *exniev* to download a technical paper on bus mastering.

RTSI Bus Interface

All E Series devices except DAQCards, USB DAQ Pads, and PXI modules are interfaced to the National Instruments RTSI bus with an embedded cross-matrix switch in the DAQ-STC. This switch synchronizes several DAQ devices by sending timing signals to them on the RTSI bus. Using RTSI bus, a single master device can control one or more slave devices for both single and multiple A/D conversions. The PXI Trigger bus serves the same purpose for PXI systems as RTSI bus.

E Series Multifunction DAQ Software NI-DAQ

NI-DAQ, our driver software bundled with every E Series multifunction DAQ device, provides access to the features of your DAQ hardware, so that you can easily develop powerful measurement solutions.

You can use NI-DAQ to perform single-point and buffered analog I/O, digital I/O, and counter/timer input operations. You can perform those operations individually, or program your device to perform multiple operations simultaneously. To facilitate integration of signal conditioning in your system, NI-DAQ provides you with a single interface for programming both the E Series device and signal conditioning modules. Using NI-DAQ, you can also synchronize your E Series multifunction DAQ device with other measurement devices, to build measurement systems customized to your particular needs.

Measurement & Automation Explorer

NI Measurement & Automation Explorer (MAX) software, which is

bundled with every E Series multifunction DAQ device, guides you through hardware configuration, channel scaling, and sensor set-up. You can also test the basic operation of your E Series device and signal connections using a test panel.

What About Signal Conditioning?

Signal conditioning is one of the most important, and most overlooked, components of a data acquisition system. Many sensors require special signal conditioning technology, and no DAQ device has the capability to provide all types of signal conditioning to all sensors. Using NI signal conditioning products, you can measure a wide variety of signals and sensors. These modular conditioning devices come in a range of sizes, from rack-mountable SCXI systems to portable SCC systems.

See page 383 for more information on Signal Conditioning.

ACH8	34	58	ACH0
ACH1	33	67	AIGND
AIGND	32	66	ACH9
ACH10	31	65	ACH2
ACH3	30	64	AIGND
AIGND	29	63	ACH11
ACH4	28	62	AISENSE
AIGND	27	61	ACH12
ACH13	26	60	ACH5
ACH6	25	59	AIGND
AIGND	24	58	ACH14
ACH15	23	57	ACH7
DAC0OUT ¹	22	56	AIGND
DAC1OUT ¹	21	55	ADGND ¹
EXTREF ¹	20	54	ADGND ¹
DIO4	19	53	DGND
DIO6	18	52	DIO0
DIO1	17	51	DIO5
DIO8	16	50	DGND
DGND	15	49	DIO2
+5 V	14	48	DIO7
DGND	13	47	DIO3
DGND	12	46	SCANCLK
PF12/TRIG1	11	45	EXTSTROBE*
PF11/TRIG2	10	44	DGND
DGND	9	43	PF12/CONVERT*
+5 V	8	42	PF13/GPCTR1_SOURCE
DGND	7	41	PF14/GPCTR1_GATE
PF15/UPDATE*	6	40	GPCTR1_OUT
PF16/WFTRIG	5	39	DGND
DGND	4	38	PF17/STARTSCAN
PF18/GPCTR0_GATE	3	37	PF18/GPCTR0_SOURCE
GPCTR0_OUT	2	36	DGND
FREQ_OUT	1	35	DGND

¹ Not available on AT-AI-16XE-10, PCI-6032E, DAQCard-AI-16E-4, DAQCard-AI-16XE-50

Figure 3. 68-Pin I/O Connector for NI 6070E, NI 6060E, NI 6062E, NI 6052E, NI 6041E, NI 6040E, NI 6036E, NI 6035E, NI 6034E, NI 6032E, NI 6030E, NI 6024E, NI 6023E, NI 6020E, NI 6012E and NI 6011E Devices

AIGND	1	51	ACH16
AIGND	2	52	ACH24
ACH0	3	53	ACH17
ACH9	4	54	ACH25
ACH1	5	55	ACH18
ACH8	6	56	ACH26
ACH2	7	57	ACH19
ACH10	8	58	ACH27
ACH3	9	59	ACH20
ACH11	10	60	ACH28
ACH4	11	61	ACH21
ACH12	12	62	ACH29
ACH5	13	63	ACH22
ACH13	14	64	ACH30
ACH6	15	65	ACH31
ACH14	16	66	ACH32
ACH7	17	67	ACH40
ACH15	18	68	ACH33
AISENSE	19	69	ACH34
DAC0OUT ¹	20	70	ACH35
DAC1OUT ¹	21	71	ACH43
EXTREF ¹	22	72	AISENSE2
ADGND ¹	23	73	ACH36
DGND	24	74	ACH37
DIO0	25	75	ACH45
DIO4	26	76	ACH38
DIO1	27	77	ACH39
DIO5	28	78	ACH47
DIO2	29	79	ACH48
DIO6	30	80	ACH56
DIO3	31	81	ACH49
DIO7	32	82	ACH57
DGND	33	83	ACH50
+5 V	34	84	ACH58
+5 V	35	85	ACH51
SCANCLK	36	86	ACH59
EXTSTROBE*	37	87	ACH60
PF10/TRIG1	38	88	ACH53
PF11/TRIG2	39	89	ACH61
PF12/CONVERT*	40	90	ACH54
PF13/GPCTR1_SOURCE	41	91	ACH62
PF14/GPCTR1_GATE	42	92	ACH63
GPCTR1_OUT	43	93	
PF15/UPDATE*	44	94	
PF16/WFTRIG	45	95	
PF17/STARTSCAN	46	96	
PF18/GPCTR0_SOURCE	47	97	
PF19/GPCTR0_GATE	48	98	
GPCTR0_OUT	49	99	
FREQ_OUT	50	100	

¹ Not available on PCI-6033E

Figure 2. 100-Pin I/O Connector for NI 6071E, NI 6061E, NI 6031E, NI 6033E Devices

AIGND	1	51	PC7
AIGND	2	52	GND
ACH0	3	53	PC6
ACH8	4	54	GND
ACH1	5	55	PC5
ACH9	6	56	GND
ACH2	7	57	PC4
ACH10	8	58	GND
ACH3	9	59	PC3
ACH11	10	60	GND
ACH4	11	61	PC2
ACH12	12	62	GND
ACH5	13	63	PC1
ACH13	14	64	GND
ACH6	15	65	PC0
ACH14	16	66	GND
ACH7	17	67	PB7
ACH15	18	68	GND
AISENSE	19	69	PB6
DAC0OUT	20	70	GND
DAC1OUT	21	71	PB5
RESERVED	22	72	GND
ADGND	23	73	PB4
DGND	24	74	PB3
DIO0	25	75	PB2
DIO4	26	76	GND
DIO1	27	77	PB1
DIO5	28	78	GND
DIO2	29	79	PB0
DIO6	30	80	GND
DIO3	31	81	PA7
DGND	32	82	GND
+5 V	33	83	PA6
+5 V	34	84	GND
SCANCLK	35	85	PA5
EXTSTROBE*	36	86	GND
PF10/TRIG1	37	87	PA4
PF11/TRIG2	38	88	GND
PF12/CONVERT*	39	89	PA3
PF13/GPCTR1_SOURCE	40	90	GND
PF14/GPCTR1_GATE	41	91	PA2
GPCTR1_OUT	42	92	GND
PF15/UPDATE*	43	93	PA1
PF16/WFTRIG	44	94	GND
PF17/STARTSCAN	45	95	PA0
GPCTR0_SOURCE	46	96	GND
GPCTR0_GATE	47	97	GND
GPCTR0_OUT	48	98	GND
FREQ_OUT	49	99	GND
	50	100	GND

Figure 4. 100-Pin I/O Connector for NI 6021E and NI 6025E Devices

E Series Multifunction DAQ Specifications

Specifications – 16-Bit E Series NI 6052E, NI 603xE, and NI 601xE

These specifications are typical for 25 °C unless otherwise noted.

Analog Input

Accuracy specifications See tables in E Series product pages

Input Characteristics

Number of channels

6052E	16 single-ended or 8 differential (software selectable per channel)
6030E	
6032E	
6034E	
6035E	
6036E	64 single-ended or 32 differential (software selectable per channel)
601xE	
6031E	
6033E	

Type of ADC Successive approximation
Resolution 16 bits, 1 in 65,536

Maximum sampling rate

6052E	333 kS/s
6034E	200 kS/s
6035E	
6036E	
6030E	100 kS/s
6031E	
6032E	
6033E	
601xE	20 kS/s; 200 kS/s single-channel sampling with the DAQCard™-AI-16XE-50

Streaming-to-disk rate (system dependent)¹

6052E	333 kS/s
6034E	200 kS/s
6035E	
6036E	
6030E	100 kS/s
6031E	
6032E	
6033E	
601xE	20 kS/s

¹Streaming-to-disk rates do not apply to RT Series devices

Input signal ranges

Device	Range Software Selectable	Dipolar Input Range	Unipolar Input Range
6052E	20 V	±10 V	—
	10 V	±5 V	0 to 10 V
	5 V	±2.5 V	0 to 5 V
	2 V	±1 V	0 to 2 V
	1 V	±500 mV	0 to 1 V
	500 mV	±250 mV	0 to 500 mV
	200 mV	±100 mV	0 to 200 mV
6030E 6031E 6032E 6033E	100 mV	±50 mV	0 to 100 mV
	20 V	±10 V	—
	10 V	±5 V	0 to 10 V
	5 V	—	0 to 5 V
	4 V	±2 V	—
	2 V	±1 V	0 to 2 V
	1 V	±500 mV	0 to 1 V
6034E 6035E 6036E	500 mV	—	0 to 500 mV
	400 mV	±200 mV	—
	200 mV	±100 mV	0 to 200 mV
	100 mV	—	0 to 100 mV
	20 V	±10 V	—
	10 V	±5 V	—
	1 V	±500 mV	—
601xE	100 mV	±50 mV	—
	20 V	±10 V	—
	10 V	±5 V	0 to 10 V
	5 V	—	0 to 5 V
	2 V	±1 V	—
	1 V	—	0 to 1 V
	200 mV	±100 mV	—
	100 mV	—	0 to 100 mV

Input coupling DC

Maximum working voltage
(signal + common mode) Each input should remain within
±11 V of ground

Oversoltage protection

Powered on ±25 V
Powered off ±15 V

Inputs protected

6052E	ACH<0..15>, AISENSE
6030E	
6032E	
6034E	
6035E	
6036E	ACH<0..63>, AISENSE, AISENSE2
601xE	
6031E	
6033E	

FIFO buffer size 512 samples, (1024 samples for
DAQCard; 2048 for PCI-MIO-16XE-50)

Data transfers

PCI, PXI, AT DMA, interrupts, programmed I/O
DAQCard Interrupts, programmed I/O

DMA modes

PCI, PXI Scatter-gather (single transfer,
demand transfer)

AT Single transfer, demand transfer

Configuration memory size 512 words

E Series Multifunction DAQ Specifications

16-Bit E Series NI 6052E, NI 603xE, and NI 601xE (continued)

Transfer Characteristics

Relative accuracy (dithered)

Device	Typical	Maximum
6052E	± 1.5 LSB	± 3 LSB
6034E		
6035E		
6036E		
6030E	± 0.75 LSB	± 1 LSB
6031E		
6032E		
6033E		
6011E	± 0.5 LSB	± 1 LSB
6012E	± 1.5 LSB	± 2 LSB

DNL

Device	Typical	Maximum
6052E	± 0.5 LSB	± 1 LSB
603xE		
6011E		
6012E		
6012E	$+1.5$ to -0.75 LSB	$+2.25$ to -1.0 LSB

No missing codes 16 bits, guaranteed

Amplifier Characteristics

Input impedance

Device	Normal Powered On	Powered Off	Overload
6052E	100 G Ω in parallel with 100 pF	820 Ω	820 Ω
603xE			
601xE			
601xE	7 G Ω in parallel with 100 pF	820 Ω ; 1 k Ω for DAQCard	820 Ω ; 1 k Ω for DAQCard

Input bias and offset current

Device	Bias Current	Offset Current
6052E	± 200 pA	± 100 pA
6034E		
6035E		
6036E		
6030E	± 1 nA	± 2 nA
6031E		
6032E		
6033E		
6011E	± 10 nA	± 20 nA
6012E	± 10 nA	± 14 nA

CMRR, DC to 60 Hz

Device	Range	CMRR	
		Bipolar	Unipolar
6052E	20 V	92 dB	—
	10 V	97 dB	97 dB
	5 V	101 dB	101 dB
	2 V	104 dB	104 dB
	100 mV to 1 V	105 dB	105 dB
6030E	20 V	92 dB	—
	10 V	97 dB	92 dB
	5 V	—	97 dB
	2 V	101 dB	—
	100 mV to 500 mV	105 dB	105 dB
6034E	20 V	85 dB	—
	10 V	85 dB	—
	5 V	96 dB	—
	2 V	96 dB	—
	100 mV	96 dB	—
601xE	20 V	80 dB	—
	10 V	85 dB	80 dB
	5 V	—	86 dB
	2 V	100 dB	—
	1 V	—	100 dB
	200 mV	120 dB	—
	100 mV	—	120 dB

Dynamic Characteristics

Bandwidth

Device	Range	Small Signal (-3 dB)
6052E	All ranges	480 kHz
6030E	All ranges	255 kHz
6031E		
6032E		
6033E		
6034E	All ranges	413 kHz
6035E		
6036E		
6011E	5 to 20 V	63 kHz
	1 to 2 V	57 kHz
	100 to 200 mV	33 kHz
	1 to 2 V	66 kHz
6012E	5 to 20 V	69 kHz
	100 to 200 mV	39 kHz

System noise (LSB_{rms}, including quantization)

Device	Range	Bipolar	Unipolar
6052E	2 to 20 V	0.95	0.95
	1 V	1.1	1.1
	500 mV	1.3	1.3
	200 mV	2.3	2.3
6030E	2 to 20 V	0.6	0.8
	1 V	0.7	0.8
	400 to 500 mV	1.1	1.1
	200 mV	2.0	2.0
6034E	10 to 20 V	0.8	—
	1 V	1.0	—
	100 mV	5.6	—
	100 mV	—	3.8
6011E	1 to 20 V	0.5	0.5
	100 to 200 mV	0.8	1.4
	1 to 20 V	1.0	1.0
	100 to 200 mV	1.2	1.6

Settling time to full-scale step

Device	Range	Accuracy				
		$\pm 0.00070\%$ (± 0.5 LSB)	$\pm 0.0015\%$ (± 1 LSB)	$\pm 0.0031\%$ (± 2 LSB)	$\pm 0.0061\%$ (± 4 LSB)	$\pm 0.024\%$ (± 16 LSB)
6052E	2 to 20 V	20 μ s typical	10 μ s max	5 μ s max	4 μ s max	3 μ s typical
	1 V	20 μ s typical	15 μ s max	8 μ s max	4 μ s max	3 μ s typical
	200 to 500 mV	20 μ s typical	15 μ s max	8 μ s max	4 μ s max	3 μ s typical
	100 mV	20 μ s typical	15 μ s max	10 μ s max	4 μ s max	3 μ s typical
6030E	All	40 μ s max	20 μ s max	—	10 μ s max	—
6032E	All	—	—	—	—	—
6031E	All	50 μ s max	25 μ s max	—	10 μ s max	—
6033E	All	—	—	—	—	—
6034E	1 to 20 V	—	—	5 μ s max	—	—
6035E	100 mV	—	—	—	5 μ s typical	—
6036E	—	—	—	—	—	—
6011E	1 to 20 V	—	50 μ s max	—	50 μ s max	—
	200 mV (bipolar), 100 mV (unipolar)	—	75 μ s max	—	50 μ s max	—
	100 mV (unipolar)	—	75 μ s max	—	50 μ s max	—
6012E	1 to 20 V	—	—	50 μ s max	50 μ s max	—
	200 mV (bipolar), 100 mV (unipolar)	—	—	60 μ s max	50 μ s typical	—
	100 mV (unipolar)	—	—	60 μ s max	50 μ s typical	—

Crosstalk

Device	Adjacent Channels	All Other Channels
6052E	-75 dB	-90 dB
603xE	—	—
601xE	-85 dB	>100 dB

E Series Multifunction DAQ Specifications

16-Bit E Series NI 6052E, NI 603xE, and NI 601xE (continued)

Analog Output

Output Characteristics

Number of channels

6052E	2 voltage outputs
6030E	
6031E	
6035E	
6036E	
6011E	
6032E	None
6033E	
6034E	
6012E	

Resolution

6052E	16 bits, 1 in 65,536
6036E	
6030E	
6031E	
6035E	12 bits, 1 in 4,096
6011E	

Maximum update rate

6052E	333 kS/s
6036E	10 kS/s, system dependent
6030E	
6031E	100 kS/s
6035E	
6011E	20 kS/s, system dependent

Type of DAC Double buffered, multiplying

FIFO buffer size

6052E	2,048 samples
6030E	
6031E	
6035E	None
6036E	
6011E	

Data transfers

PCI, PXI, AT DMA, interrupts, programmed I/O
DAQCard Interrupts, programmed I/O

DMA modes

PCI, PXI Scatter-gather (single transfer, demand transfer)
AT Single transfer, demand transfer

Transfer Characteristics

Relative accuracy

6052E	±0.35 LSB typical, ±1 LSB max
6030E	±0.5 LSB typical, ±1 LSB max
6031E	
6035E	±0.3 LSB typical, ±0.5 LSB max
6036E	±2 LSB max
6011E	±0.5 LSB max

DNL ±1.0 LSB max

Monotonicity

6052E	16 bits, guaranteed
6036E	
6030E	
6031E	
6035E	12 bits, guaranteed
6011E	

Voltage Output

Ranges

6052E	±10 V, 0 to 10 V, ±EXTREF, 0 to EXTREF, software selectable
6030E	±10 V, 0 to 10 V; software selectable
6031E	
6035E	±10 V
6036E	
6011E	

Output coupling DC
Output impedance 0.1 Ω max
Current drive ±5 mA max
Protection Short-circuit to ground
Power-on state

6052E	0 V (±20 mV)
6030E	
6031E	
6035E	0 V (±200 mV)
6036E	0 V (±21 mV)
6011E	0 V (±85 mV)

External reference input (6052E only)

Range ±11 V
Overvoltage protection ±25 V powered on, ±15 V powered off
Input impedance 10 kΩ
Bandwidth (-3 dB) 3 kHz
Slew rate 0.3 V/μs

Dynamic Characteristics

Settling time and slew rate

Device	Settling time for full-scale step	Slew rate
6052E	3.5 μs to ±1 LSB accuracy	15 V/μs
6030E	10 μs to ±1 LSB accuracy	5 V/μs
6031E		
6035E	10 μs to ±0.5 LSB accuracy	10 V/μs
6036E	5 μs to ±1 LSB accuracy	15 V/μs
6011E	50 μs to ±0.5 LSB accuracy	2 V/μs

Noise

6052E	60 μV _{rms} , DC to 1 MHz
6030E	
6031E	
6035E	200 μV _{rms} , DC to 1 MHz
6036E	110 μV _{rms} , DC to 400 kHz
6011E	40 μV _{rms} , DC to 1 MHz

Glitch energy (at mid-scale transition)

Digital I/O

Number of channels 8 input/output

Compatibility 5 V/TTL

Device	Amplitude	Duration
6052E	±10 mV	1 μs
6030E	N/A	N/A
6031E		
6035E	±12 mV	2 μs
6036E	±10 mV	1 μs
6011E	±30 mV	10 μs

Power-on state Input (high impedance)

Data transfers Programmed I/O

Digital logic levels

Level	Minimum	Maximum
Input low voltage	0 V	0.8 V
Input high voltage	2 V	5 V
Output low voltage (I _{out} = 24 mA)	—	0.4 V
Output high voltage (I _{out} = 13 mA)	4.35 V	—

E Series Multifunction DAQ Specifications

Specifications – 16-Bit E Series NI 6052E, NI 603xE, and NI 601xE (continued)

Timing I/O

General-Purpose Up/Down Counter/Timers

Number of channels	2
Resolution	24 bits (1 in 16, 777, 216)
Compatibility	5 V/TTL

Digital logic levels

Signal	Minimum	Max
Input low voltage	0.0 V	0.8 V
Input high voltage	2.0 V	5.0 V
Output low voltage (I _{out} = 5 mA)	—	0.4 V
Output high voltage (I _{out} = 3.5 mA)	4.35 V	—

Base clocks available	20 MHz and 100 kHz
Base clock accuracy	±0.01%
Maximum source frequency	20 MHz
External source selections	PFI0..PFI9, RTSI0..RTSI6, analog trigger; software selectable
External gate selections	PFI0..PFI9, RTSI0..RTSI6, analog trigger; software selectable
Minimum source pulse duration	10 ns
Minimum gate pulse duration	10 ns, edge-detect mode
Data transfers	
PCI, PXI, AT	DMA, interrupts, programmed I/O
DAQCard	Interrupts, programmed I/O
DMA modes	
PCI, PXI	Scatter-gather (single transfer, demand transfer)
AT	Single transfer, demand transfer

Frequency Scaler

Number of channels	1
Resolution	4 bits
Compatibility	5 V/TTL

Digital logic levels

Signal	Minimum	Max
Input low voltage	0.0 V	0.8 V
Input high voltage	2.0 V	5.0 V
Output low voltage (I _{out} = 5 mA)	—	0.4 V
Output high voltage (I _{out} = 3.5 mA)	4.35 V	—

Base clocks available	10 MHz, 100 kHz
Base clock accuracy	±0.01%
Data transfers	Programmed I/O

Triggers

Analog Triggers

Number of triggers

6052E	1
6030E	
6031E	
6032E	
6033E	
6034E	None
6035E	
6036E	
601xE	

Purpose

Analog input	Start and stop trigger, gate, clock
Analog output	Start trigger, gate, clock
General-purpose counter/timers	Source, gate

Source

6052E	ACH<0..15>, PFI0/TRIG1
6030E	
6032E	
6031E	ACH<0..63>, PFI0/TRIG1
6033E	

Level

Internal source, ACH<0..15/63>	±Full-scale
External source, PFI0/TRIG1	±10 V

Slope Positive or negative; software selectable

Resolution 12 bits, 1 in 4,096

Hysteresis Programmable

Bandwidth (-3 dB)

Accuracy ±1% of full-scale range max

Device	Internal Source ACH<0..63>	External Source PFI0/TRIG1
6052E	700 kHz	700 kHz
6030E, 6031E, 6032E, 6033E	255 kHz	4 MHz

Digital Triggers (all devices)

Number of triggers 2

Purpose

Analog input	Start and stop trigger, gate, clock
Analog output	Start trigger, gate, clock
General-purpose counter/timers	Source, gate

Source PFI0..PFI9, RTSI0..RTSI6

Slope Positive or negative; software selectable

Compatibility 5 V/TTL

Response Rising or falling edge

Pulse width 10 ns minimum

E Series Multifunction DAQ Specifications

16-Bit E Series NI 6052E, NI 603xE, and NI 601xE (continued)

External Input for Digital or Analog Trigger (PFI0/TRIG1)

Impedance	10 k Ω
Coupling	DC
Protection	
Digital trigger	-0.5 to (V _{CC} + 0.5) V
Analog trigger	
On/Off/Disabled	± 35 V

Calibration

Recommended warm-up time	15 minutes; 30 minutes for DAQCard
Calibration interval	1 year
Onboard calibration reference	
DC Level	

6052E	5.000 V (± 1.0 mV)	Over full operating temperature, actual value stored in EEPROM
6030E		
6031E		
6032E		
6033E		
6012E		5.000 V (± 3.5 mV)
6034E		
6035E		
6036E		
6011E	5.000 V (± 3.0 mV)	

Temperature coefficient

6052E	± 0.6 ppm/ $^{\circ}$ C max
6030E	
6031E	
6032E	
6033E	
6012E	± 5.0 ppm/ $^{\circ}$ C max
6034E	
6035E	
6036E	
6011E	

Long-term stability

6052E	± 6.0 ppm/ $\sqrt{1000$ h
6030E	
6031E	
6032E	
6033E	
6034E	± 15.0 ppm/ $\sqrt{1000$ h
6035E	
6036E	
601xE	

RTSI (PCI and ISA only)

Trigger lines	7
---------------	---

PXI Trigger Bus (PXI only)

Trigger lines	6
Star Trigger	1

Bus Interface

PCI, PXI	Master, slave
AT, DAQCard	Slave

Power Requirements¹

Device	+5 VDC ($\pm 5\%$)	Power Available at I/O Connector
6052E	1.3 A	+4.65 to +5.25 VDC, 1 A
603xE (PCI, PXI), except 6034E/6035E	1.5 A	+4.65 to +5.25 VDC, 1 A
6034E	0.9 A	+4.65 to +5.25 VDC, 1 A
6035E		
6036E		
603xE (AT)	1.2 A	+4.65 to +5.25 VDC, 1 A
PCI-MIO-16XE-50	1.1 A	+4.65 to +5.25 VDC, 1 A
DAQCard-A1-16XE-50	230 mA	+4.65 to +5.25 VDC, 250 mA
AT-MIO-16XE-50	750 mA	+4.65 to +5.25 VDC, 1 A

Physical¹

Dimensions (not including connectors)¹

PCI	17.5 by 10.6 cm (6.9 by 4.2 in.)
PXI	16.0 by 10.0 cm (6.3 by 3.9 in.)
ISA (long)	33.8 by 9.9 cm (13.3 by 3.9 in.)
ISA (short)	17.5 by 9.9 cm (6.9 by 4.2 in.)
DAQCard	Type II PC Card

I/O connectors

6052E	68-pin male SCSI-II type
6030E	
6032E	
6034E	
6035E	
6036E	100-pin female 0.050 D-type
6011E	
6031E	
6033E	68-pin female PCMCIA
6012E	

Environment

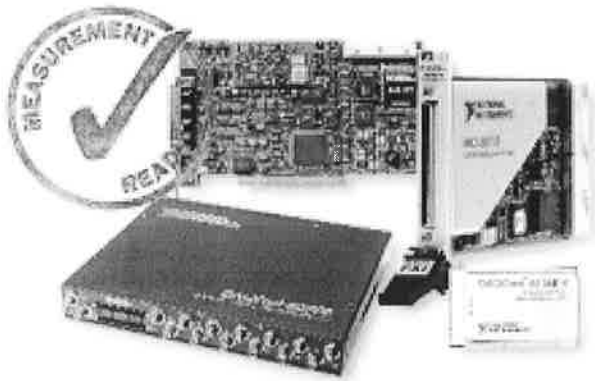
Operating temperature	0 to 55 $^{\circ}$ C; DAQCards should not exceed 55 $^{\circ}$ C while in PCMCIA slot
Storage temperature	-20 to 70 $^{\circ}$ C
Relative humidity	10 to 90%, noncondensing

Certifications and Compliances

CE Mark Compliance CE

¹See page 148 for RT Series devices power requirements and physical parameters.

E Series DAQ Accuracy Specifications



Every Measurement Counts

There is no room for error in your measurements. From sensor to software, your system must deliver accurate results. NI provides detailed specifications for our products so that you do not have to guess how they will perform. Along with traditional data acquisition specifications, our E Series multifunction data acquisition (DAQ) devices also include accuracy tables to assist you in selecting the appropriate hardware for your application. These tables are found on the product pages and include specifications for both absolute and relative accuracy.

Absolute Accuracy

Absolute accuracy is the specification you use to determine the overall maximum error of your measurement. Absolute accuracy specifications apply only to a successfully calibrated DAQ device. There are four components of an absolute accuracy specification:

Percent of Reading is a percent of the actual input voltage.

Offset is a constant offset applied to all measurements.

Noise + Quantization is based on noise and depends on the number of points averaged for each measurement.

Drift is based on variations in your ambient temperature.

Based on these components, the formula for calculating absolute accuracy is:

$$\text{Absolute Accuracy} = \pm[(\text{Input Voltage} \times \% \text{ of Reading}) + (\text{Offset} + \text{Noise} + \text{Quantization} + \text{Drift})]$$

Drift is already accounted for unless your ambient temperature is outside +15 to +35 °C. For instance, if your ambient temperature is at 45 °C, you must account for 10 °C of drift. This is calculated by:

$$\text{Drift} = \text{Temperature Difference} \times \% \text{ Drift per } ^\circ\text{C} \times \text{Input Voltage}$$

Absolute Accuracy at Full Scale is a calculation of absolute accuracy for a specific voltage range using the maximum voltage within that range taken one year after calibration, the Accuracy Drift Reading, and the Noise + Quantization averaged value.

Below is the **Absolute Accuracy at Full Scale** calculation for the PCI-MIO-16XE-50 after one year using the ± 10 V input range while averaging 100 samples of a 10 V input signal. In all the Absolute Accuracy at Full Scale calculations, we assume that the ambient temperature is between 15 and 35 °C. You can see on the next page that the calculation for the ± 10 V input range for Absolute Accuracy at Full Scale yields 1.443 mV. This calculation is done using the parameters in the same row for one year Absolute Accuracy Reading, Offset and Noise + Quantization as well as a value of 10 V for the input voltage value. You can then see that the calculation is as follows:

$$\text{Absolute Accuracy} = \pm[(10 \times 0.0001) + 397.2 \mu\text{V} + 45.8 \mu\text{V}] = \pm 1.443 \text{ mV}$$

The following example assumes the same conditions except that the ambient temperature is 45 °C. You can begin with the calculation above and add in the Drift calculation using the % Drift per °C from the table on the next page (see Table 1).

$$\text{Absolute Accuracy} = 1.443 \text{ mV} + [(45 ^\circ\text{C} - 35 ^\circ\text{C}) \times 0.000002 / ^\circ\text{C} \times 10 \text{ V}] = \pm 1.643 \text{ mV}$$

If you are making single-point measurements, use the Single-Point Noise + Quantization specification from the accuracy tables. If you are averaging multiple points for each measurement, the value for Noise + Quantization changes. The Averaged Noise + Quantization in the accuracy tables assumes that you average 100 points per measurement. If you are averaging a different number of points, use the following equation to determine your Noise + Quantization:

$$\text{Noise + Quantization for } x \text{ averaged points} = \frac{\text{Averaged Noise + Quantization from table} \times \sqrt{100/X}}$$

For example, if you are averaging 1000 points per measurement with the PCI-MIO-16XE-50 in the ± 10 V input range, the Noise + Quantization is determined by:

$$\text{Noise + Quantization} = 45.7 \mu\text{V} \times \sqrt{100/1000} = 14.5 \mu\text{V}$$

The Noise + Quantization specifications assume that dithering is disabled for single-point measurements and enabled for averaged measurements.

See page 24 or visit ni.com/calibration for more information on the importance of calibration on DAQ device accuracy.

To calculate the accuracy of NI measurement products, visit ni.com/measurements/accuracy

E Series DAQ Accuracy Specifications

Relative Accuracy

Relative accuracy is the specification that compares the difference between two or more measurements. It indicates the degree to which two or more measurements can be distinguished from each other. The two major contributors to relative accuracy are the resolution of the device's analog-to-digital Converter (ADC) and the system noise. The accuracy tables show both single-point and averaged relative accuracy, which include both ADC resolution and system noise effects. Averaging will improve your relative accuracy for DC measurements.

As an example, assume you are monitoring a voltage once per second using the ± 10 V range on the PCI-MIO-16XE-50 and averaging 100 points for each measurement. Using the accuracy table on page 255 (reprinted below for your convenience), we find:

$$\text{Averaged Relative Accuracy} = 60.3 \mu\text{V}$$

This means that a measurement taken at time t_2 would have to be 60.3 μV greater or less than the measurement taken at time t_1 in order to detect a difference in the input voltage. Relative accuracy does not depend on DAQ device calibration.

Detailed Specifications

The pages starting at page 266 contain detailed specifications for all National Instruments E Series multifunction devices. Devices can be identified by their family number. For instance, if you want to determine the common-mode rejection ratio (CMRR) in the 10 V range for the PCI-6052E in unipolar range, you would look at the 16-bit E Series Multifunction DAQ specification on page 272. For the 10 V range, the CMRR specification for the NI 6052E devices is 97 dB.

	Nominal Range (V)	Absolute Accuracy							Relative Accuracy	
		% of Reading			Offset (pV)	Noise + Quantization (pV)		Temp. Drift (%/°C)	Resolution (pV)	
		24 Hrs.	90 Days	1 Year		Single Pt.	Averaged		Single Pt.	Averaged
Analog Input	± 10	0.0058%	0.0078%	0.0100%	397.2	526.4	45.8	0.0002	1.443	602.7
	± 5	0.0208%	0.0228%	0.0250%	200.6	263.2	22.9	0.0007	1.474	301.4
	± 1	0.0208%	0.0228%	0.0250%	43.3	52.6	4.6	0.0007	0.298	60.3
	± 0.1	0.0408%	0.0428%	0.0450%	7.9	8.4	0.7	0.0012	0.054	9.6
	0 to 10	0.0058%	0.0078%	0.0100%	244.6	263.2	22.9	0.0002	1.268	301.4
	0 to 5	0.0208%	0.0228%	0.0250%	124.3	131.6	11.4	0.0007	1.386	150.7
	0 to 1	0.0208%	0.0228%	0.0250%	28.1	26.3	2.3	0.0007	0.280	30.1
	0 to 0.1	0.0408%	0.0428%	0.0450%	6.4	7.0	0.6	0.0012	0.052	8.4
Analog Output	± 10	0.0075%	0.0095%	0.0117%	815.4	1029.1	91.6	0.0005	2.077	1205.4
	± 5	0.0225%	0.0245%	0.0267%	409.7	514.6	45.8	0.0010	1.791	602.7
	± 1	0.0225%	0.0245%	0.0267%	85.1	102.9	9.2	0.0010	0.361	120.5
	± 0.1	0.0425%	0.0445%	0.0467%	12.1	12.2	1.1	0.0015	0.060	14.5
	0 to 10	0.0075%	0.0095%	0.0117%	591.2	514.6	45.8	0.0005	1.807	602.7
	0 to 5	0.0225%	0.0245%	0.0267%	297.6	257.3	22.9	0.0010	1.656	301.4
	0 to 1	0.0225%	0.0245%	0.0267%	62.7	51.5	4.6	0.0010	0.334	60.3
	0 to 0.1	0.0425%	0.0445%	0.0467%	9.9	8.0	0.7	0.0015	0.057	9.6

Note: Accuracies are valid for measurements following an internal E Series Calibration. Averaged numbers assume dithering and averaging of 100 single-channel readings. Measurement accuracies are listed for operational temperatures within ± 1 °C of internal calibration temperature and ± 10 °C of external or factory-calibration temperature. One-year calibration interval recommended. The Absolute Accuracy at Full Scale calculations were performed for a maximum range input voltage (for example, 10 V for the ± 10 V range) after one year, assuming 100 pt averaging of data. See Overview on page 234 for an example calculation of this type.

Table 1. NI 601xE Analog Input Accuracy Specifications

LM741 Operational Amplifier

General Description

The LM741 series are general purpose operational amplifiers which feature improved performance over industry standards like the LM709. They are direct, plug-in replacements for the 709C, LM201, MC1439 and 748 in most applications.

The amplifiers offer many features which make their application nearly foolproof: overload protection on the input and

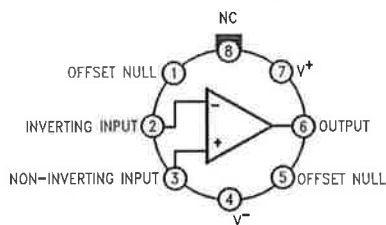
output, no latch-up when the common mode range is exceeded, as well as freedom from oscillations.

The LM741C is identical to the LM741/LM741A except that the LM741C has their performance guaranteed over a 0°C to +70°C temperature range, instead of -55°C to +125°C.

Features

Connection Diagrams

Metal Can Package

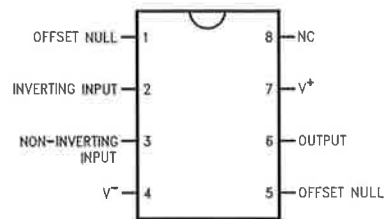


00934102

Note 1: LM741H is available per JM38510/10101

Order Number LM741H, LM741H/883 (Note 1),
LM741AH/883 or LM741CH
See NS Package Number H08C

Dual-In-Line or S.O. Package



00934103

Order Number LM741J, LM741J/883, LM741CN
See NS Package Number J08A, M08A or N08E

Ceramic Flatpak

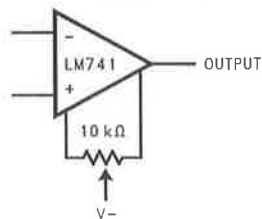


00934105

Order Number LM741W/883
See NS Package Number W10A

Typical Application

Offset Nulling Circuit



00934107

Absolute Maximum Ratings (Note 2)

If Military/Aerospace specified devices are required, please contact the National Semiconductor Sales Office/ Distributors for availability and specifications.

(Note 7)

	LM741A	LM741	LM741C
Supply Voltage	±22V	±22V	±18V
Power Dissipation (Note 3)	500 mW	500 mW	500 mW
Differential Input Voltage	±30V	±30V	±30V
Input Voltage (Note 4)	±15V	±15V	±15V
Output Short Circuit Duration	Continuous	Continuous	Continuous
Operating Temperature Range	–55°C to +125°C	–55°C to +125°C	0°C to +70°C
Storage Temperature Range	–65°C to +150°C	–65°C to +150°C	–65°C to +150°C
Junction Temperature	150°C	150°C	100°C
Soldering Information			
N-Package (10 seconds)	260°C	260°C	260°C
J- or H-Package (10 seconds)	300°C	300°C	300°C
M-Package			
Vapor Phase (60 seconds)	215°C	215°C	215°C
Infrared (15 seconds)	215°C	215°C	215°C

See AN-450 "Surface Mounting Methods and Their Effect on Product Reliability" for other methods of soldering

surface mount devices.

ESD Tolerance (Note 8)	400V	400V	400V
------------------------	------	------	------

Electrical Characteristics (Note 5)

Parameter	Conditions	LM741A			LM741			LM741C			Units
		Min	Typ	Max	Min	Typ	Max	Min	Typ	Max	
Input Offset Voltage	$T_A = 25^\circ\text{C}$ $R_S \leq 10\text{ k}\Omega$ $R_S \leq 50\Omega$		0.8	3.0		1.0	5.0		2.0	6.0	mV
	$T_{AMIN} \leq T_A \leq T_{AMAX}$ $R_S \leq 50\Omega$ $R_S \leq 10\text{ k}\Omega$			4.0			6.0			7.5	mV
											mV
Average Input Offset Voltage Drift				15							$\mu\text{V}/^\circ\text{C}$
Input Offset Voltage Adjustment Range	$T_A = 25^\circ\text{C}$, $V_S = \pm 20\text{V}$	±10				±15			±15		mV
Input Offset Current	$T_A = 25^\circ\text{C}$		3.0	30		20	200		20	200	nA
	$T_{AMIN} \leq T_A \leq T_{AMAX}$			70		85	500			300	nA
Average Input Offset Current Drift				0.5							nA/°C
Input Bias Current	$T_A = 25^\circ\text{C}$		30	80		80	500		80	500	nA
	$T_{AMIN} \leq T_A \leq T_{AMAX}$			0.210			1.5			0.8	μA
Input Resistance	$T_A = 25^\circ\text{C}$, $V_S = \pm 20\text{V}$	1.0	6.0		0.3	2.0		0.3	2.0		M Ω
	$T_{AMIN} \leq T_A \leq T_{AMAX}$, $V_S = \pm 20\text{V}$	0.5									M Ω
Input Voltage Range	$T_A = 25^\circ\text{C}$							±12	±13		V
	$T_{AMIN} \leq T_A \leq T_{AMAX}$				±12	±13					V

Electrical Characteristics (Note 5) (Continued)

Parameter	Conditions	LM741A			LM741			LM741C			Units
		Min	Typ	Max	Min	Typ	Max	Min	Typ	Max	
Large Signal Voltage Gain	$T_A = 25^\circ\text{C}$, $R_L \geq 2\text{ k}\Omega$ $V_S = \pm 20\text{V}$, $V_O = \pm 15\text{V}$ $V_S = \pm 15\text{V}$, $V_O = \pm 10\text{V}$	50			50	200		20	200		V/mV V/mV
	$T_{AMIN} \leq T_A \leq T_{AMAX}$, $R_L \geq 2\text{ k}\Omega$, $V_S = \pm 20\text{V}$, $V_O = \pm 15\text{V}$ $V_S = \pm 15\text{V}$, $V_O = \pm 10\text{V}$	32			25			15			V/mV V/mV V/mV
	$V_S = \pm 5\text{V}$, $V_O = \pm 2\text{V}$	10									V/mV
Output Voltage Swing	$V_S = \pm 20\text{V}$ $R_L \geq 10\text{ k}\Omega$ $R_L \geq 2\text{ k}\Omega$	± 16 ± 15									V V
	$V_S = \pm 15\text{V}$ $R_L \geq 10\text{ k}\Omega$ $R_L \geq 2\text{ k}\Omega$				± 12 ± 10	± 14 ± 13		± 12 ± 10	± 14 ± 13		V V
Output Short Circuit Current	$T_A = 25^\circ\text{C}$	10	25	35		25			25		mA
	$T_{AMIN} \leq T_A \leq T_{AMAX}$	10		40							mA
Common-Mode Rejection Ratio	$T_{AMIN} \leq T_A \leq T_{AMAX}$ $R_S \leq 10\text{ k}\Omega$, $V_{CM} = \pm 12\text{V}$ $R_S \leq 50\Omega$, $V_{CM} = \pm 12\text{V}$	80	95		70	90		70	90		dB dB
Supply Voltage Rejection Ratio	$T_{AMIN} \leq T_A \leq T_{AMAX}$, $V_S = \pm 20\text{V}$ to $V_S = \pm 5\text{V}$ $R_S \leq 50\Omega$ $R_S \leq 10\text{ k}\Omega$	86	96		77	96		77	96		dB dB
Transient Response	$T_A = 25^\circ\text{C}$, Unity Gain		0.25	0.8		0.3			0.3		μs
			6.0	20		5			5		%
Bandwidth (Note 6)	$T_A = 25^\circ\text{C}$	0.437	1.5								MHz
Slew Rate	$T_A = 25^\circ\text{C}$, Unity Gain	0.3	0.7			0.5			0.5		V/ μs
Supply Current	$T_A = 25^\circ\text{C}$					1.7	2.8		1.7	2.8	mA
Power Consumption	$T_A = 25^\circ\text{C}$										
	$V_S = \pm 20\text{V}$		80	150							mW
	$V_S = \pm 15\text{V}$					50	85		50	85	mW
	$V_S = \pm 20\text{V}$										
	$T_A = T_{AMIN}$			165							mW
	$T_A = T_{AMAX}$			135							mW
LM741	$V_S = \pm 15\text{V}$										
	$T_A = T_{AMIN}$					60	100				mW
	$T_A = T_{AMAX}$					45	75				mW

Note 2: "Absolute Maximum Ratings" indicate limits beyond which damage to the device may occur. Operating Ratings indicate conditions for which the device is functional, but do not guarantee specific performance limits.

Electrical Characteristics (Note 5) (Continued)

Note 3: For operation at elevated temperatures, these devices must be derated based on thermal resistance, and T_j max. (listed under "Absolute Maximum Ratings"). $T_j = T_A + (\theta_{JA} P_D)$

Thermal Resistance	Cerdip (J)	DIP (N)	HO8 (H)	SO-8 (M)
θ_{JA} (Junction to Ambient)	100°C/W	100°C/W	170°C/W	195°C/W
θ_{JC} (Junction to Case)	N/A	N/A	25°C/W	N/A

Note 4: For supply voltages less than $\pm 15V$, the absolute maximum input voltage is equal to the supply voltage.

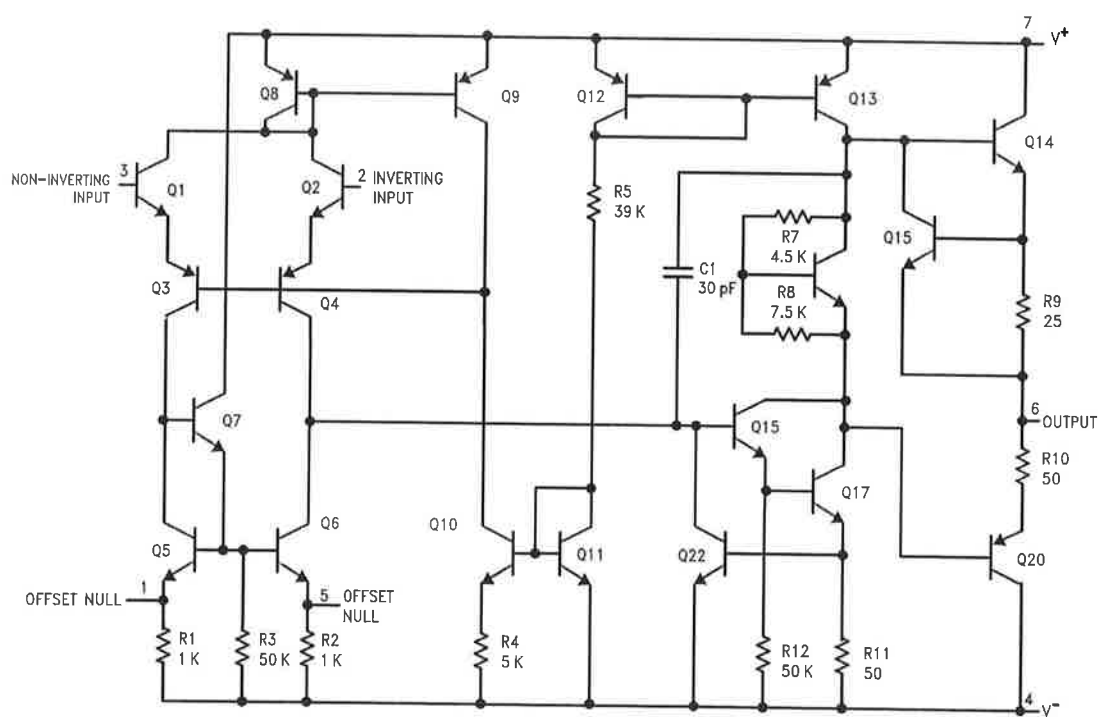
Note 5: Unless otherwise specified, these specifications apply for $V_S = \pm 15V$, $-55^\circ C \leq T_A \leq +125^\circ C$ (LM741/LM741A). For the LM741C/LM741E, these specifications are limited to $0^\circ C \leq T_A \leq +70^\circ C$.

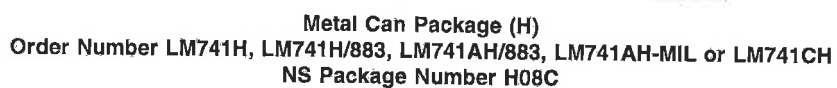
Note 6: Calculated value from: BW (MHz) = $0.35/\text{Rise Time}(\mu s)$.

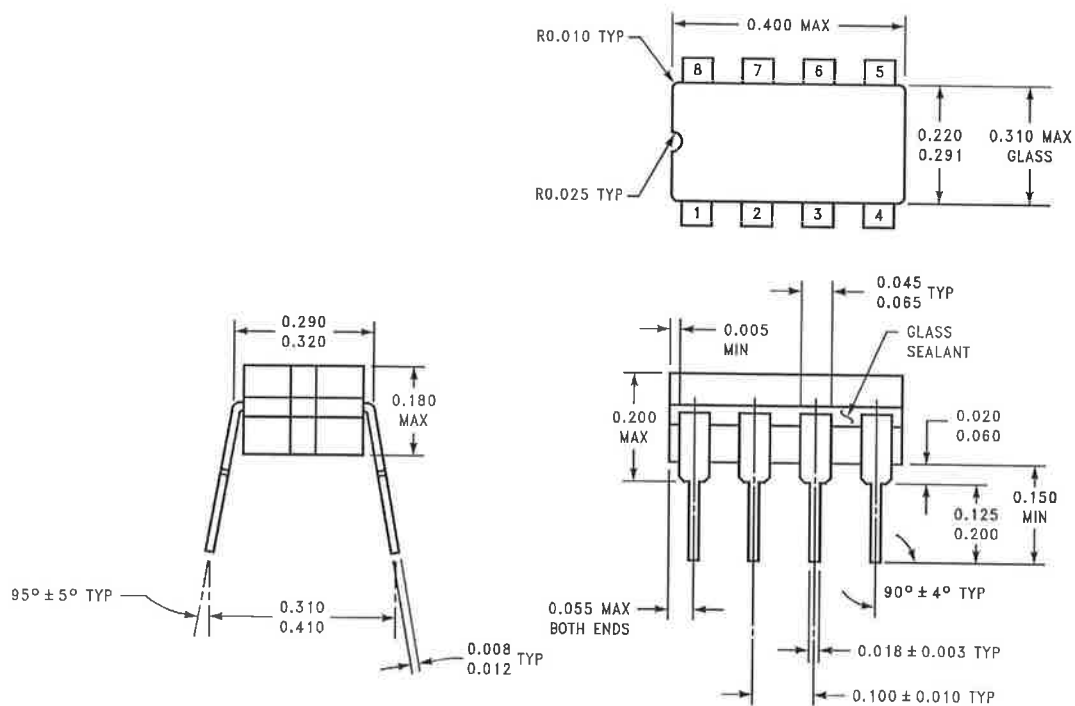
Note 7: For military specifications see RETS741X for LM741 and RETS741AX for LM741A.

Note 8: Human body model, $1.5\text{ k}\Omega$ in series with 100 pF .

Schematic Diagram

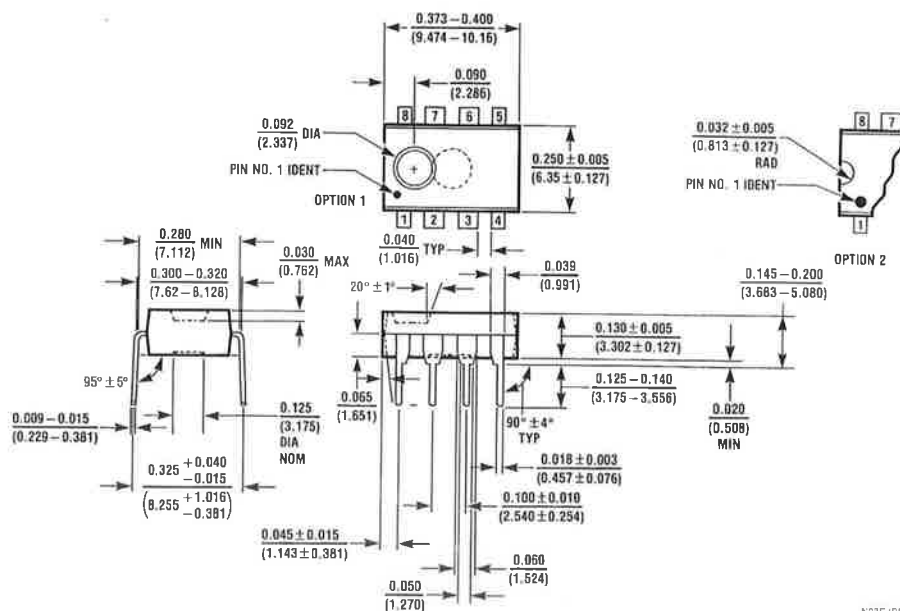




Physical Dimensions inches (millimeters) unless otherwise noted (Continued)

JOB A (REV K)

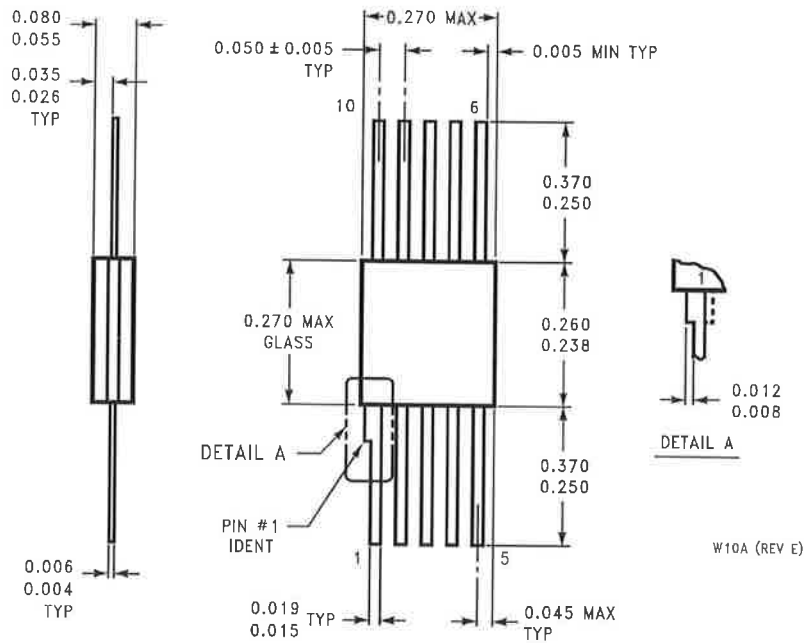
Ceramic Dual-In-Line Package (J)
Order Number LM741J/883
NS Package Number J08A



NO3E (REV F)

Dual-In-Line Package (N)
Order Number LM741CN
NS Package Number N08E

Physical Dimensions inches (millimeters) unless otherwise noted (Continued)



10-Lead Ceramic Flatpak (W)
Order Number LM741W/883, LM741WG-MPR or LM741WG/883
NS Package Number W10A

National does not assume any responsibility for use of any circuitry described, no circuit patent licenses are implied and National reserves the right at any time without notice to change said circuitry and specifications.

For the most current product information visit us at www.national.com.

LIFE SUPPORT POLICY

NATIONAL'S PRODUCTS ARE NOT AUTHORIZED FOR USE AS CRITICAL COMPONENTS IN LIFE SUPPORT DEVICES OR SYSTEMS WITHOUT THE EXPRESS WRITTEN APPROVAL OF THE PRESIDENT AND GENERAL COUNSEL OF NATIONAL SEMICONDUCTOR CORPORATION. As used herein:

1. Life support devices or systems are devices or systems which, (a) are intended for surgical implant into the body, or (b) support or sustain life, and whose failure to perform when properly used in accordance with instructions for use provided in the labeling, can be reasonably expected to result in a significant injury to the user.
2. A critical component is any component of a life support device or system whose failure to perform can be reasonably expected to cause the failure of the life support device or system, or to affect its safety or effectiveness.

BANNED SUBSTANCE COMPLIANCE

National Semiconductor certifies that the products and packing materials meet the provisions of the Customer Products Stewardship Specification (CSP-9-111C2) and the Banned Substances and Materials of Interest Specification (CSP-9-111S2) and contain no "Banned Substances" as defined in CSP-9-111S2.



National Semiconductor
Americas Customer
Support Center
 Email: new.feedback@nsc.com
 Tel: 1-800-272-9959

www.national.com

National Semiconductor
Europe Customer Support Center
 Fax: +49 (0) 180-530 85 86
 Email: europa.support@nsc.com
 Deutsch Tel: +49 (0) 69 9508 6208
 English Tel: +44 (0) 870 24 0 2171
 Français Tel: +33 (0) 1 41 91 8790

National Semiconductor
Asia Pacific Customer
Support Center
 Email: ap.support@nsc.com

National Semiconductor
Japan Customer Support Center
 Fax: 81-3-5639-7507
 Email: jpn.feedback@nsc.com
 Tel: 81-3-5639-7560

Appendix – C

Post processes ANSYS simulation results

- **Post process results of ANSYS modelling at 1:1 nitrogen gas pressure ratio on the inlet pressure tube to pick up shaft (obtain from pressure plot of ANSYS result)**
- **Post process results of ANSYS modelling at 1.8:1 nitrogen gas pressure ratio on the inlet pressure tube to pick up shaft (obtain from pressure plot of ANSYS result)**

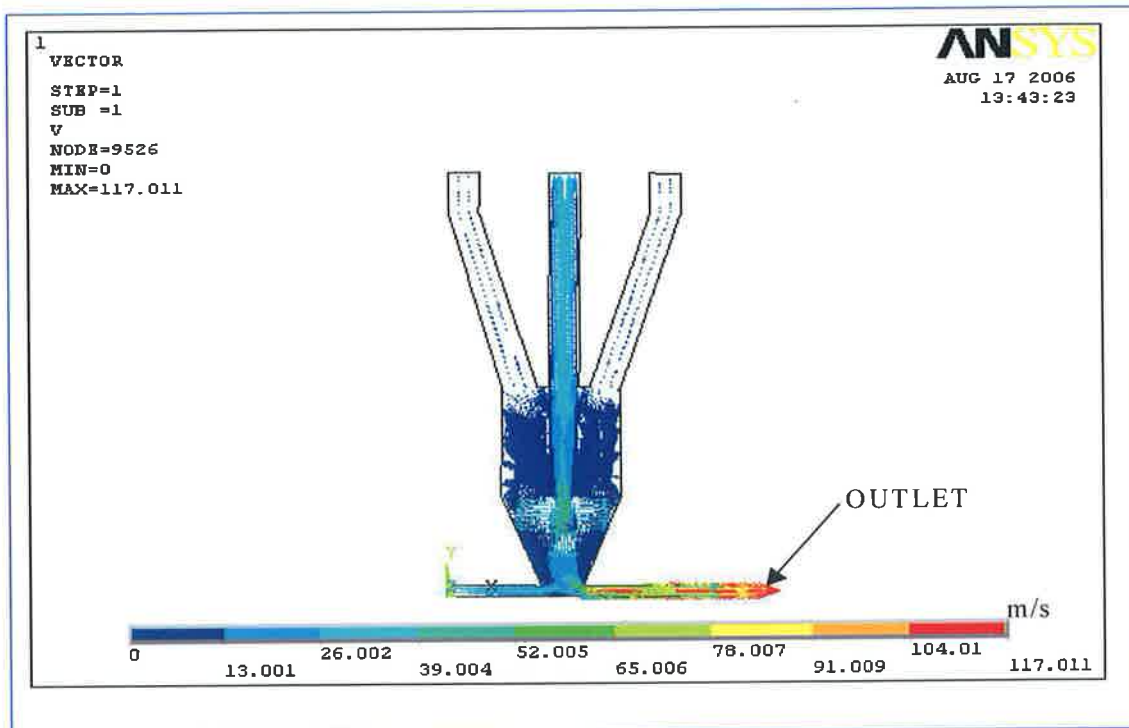


Figure C1: Vector plot showing the path of the velocity particles at 1:1 nitrogen gas pressure ratio on the inlet pressure tube to pick up shaft (obtain from pressure plot of ANSYS result).

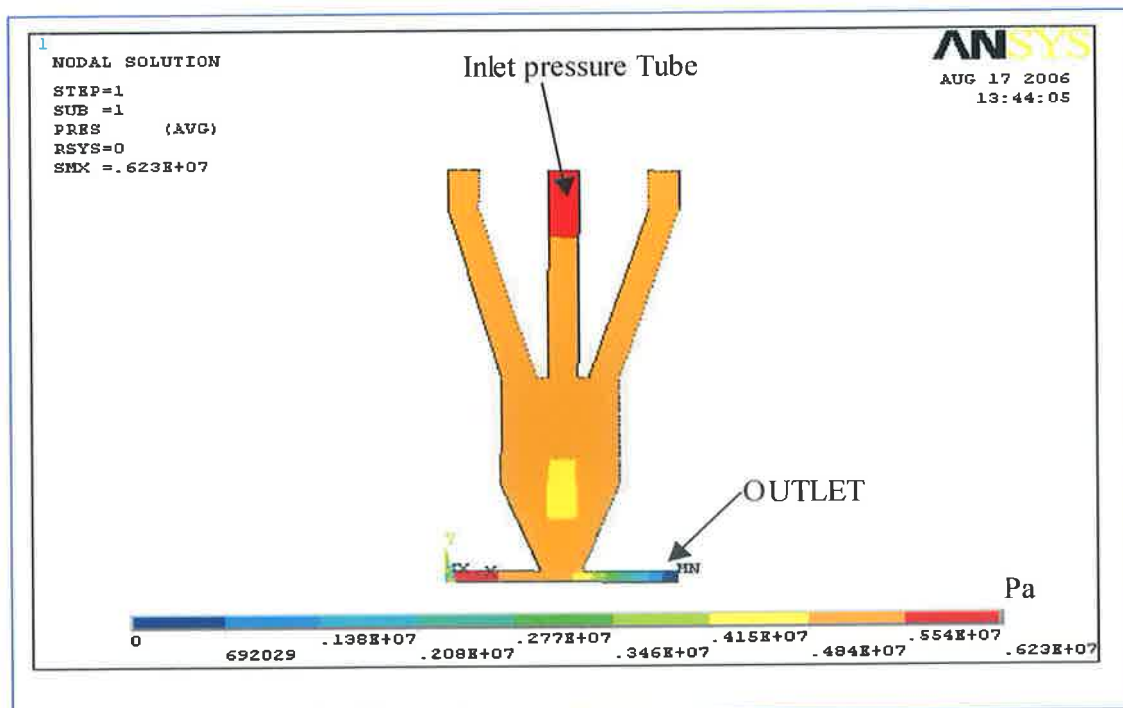


Figure C2: Pressure plot from nodal solution shows the pressure of inlet tube and pick up shaft inlet are same means 1:1.

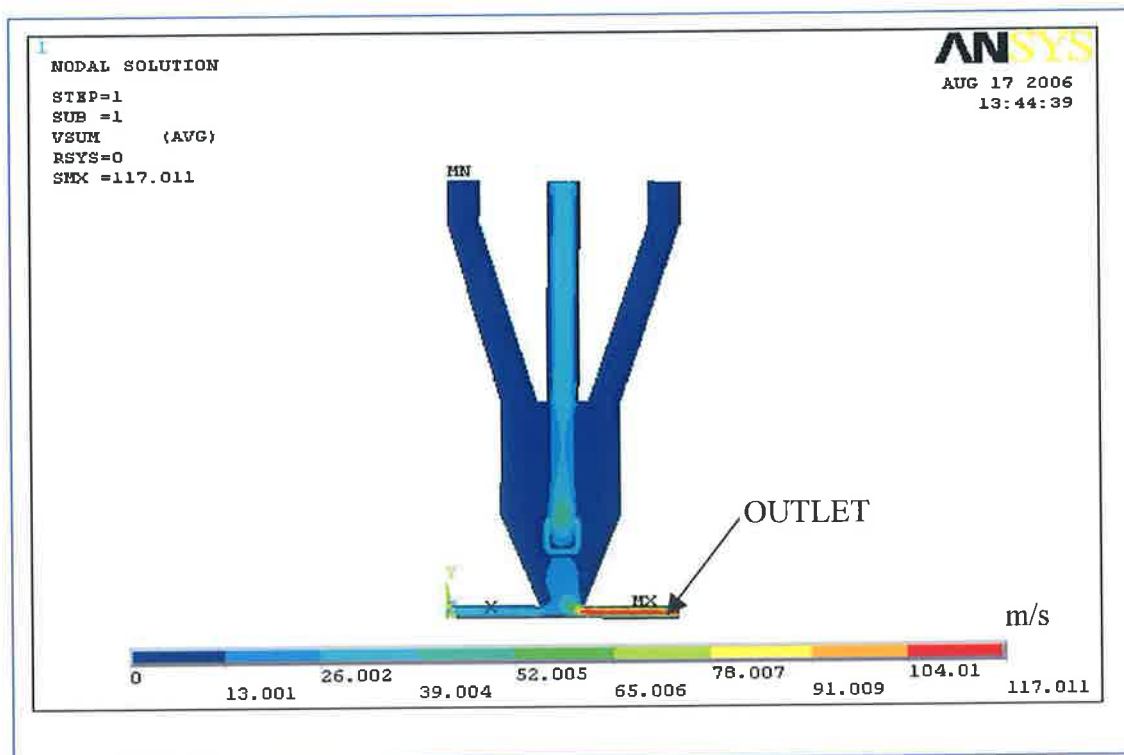


Figure C3: Velocity plot of the modelling from the nodal solution at 1:1 pressure ratio.

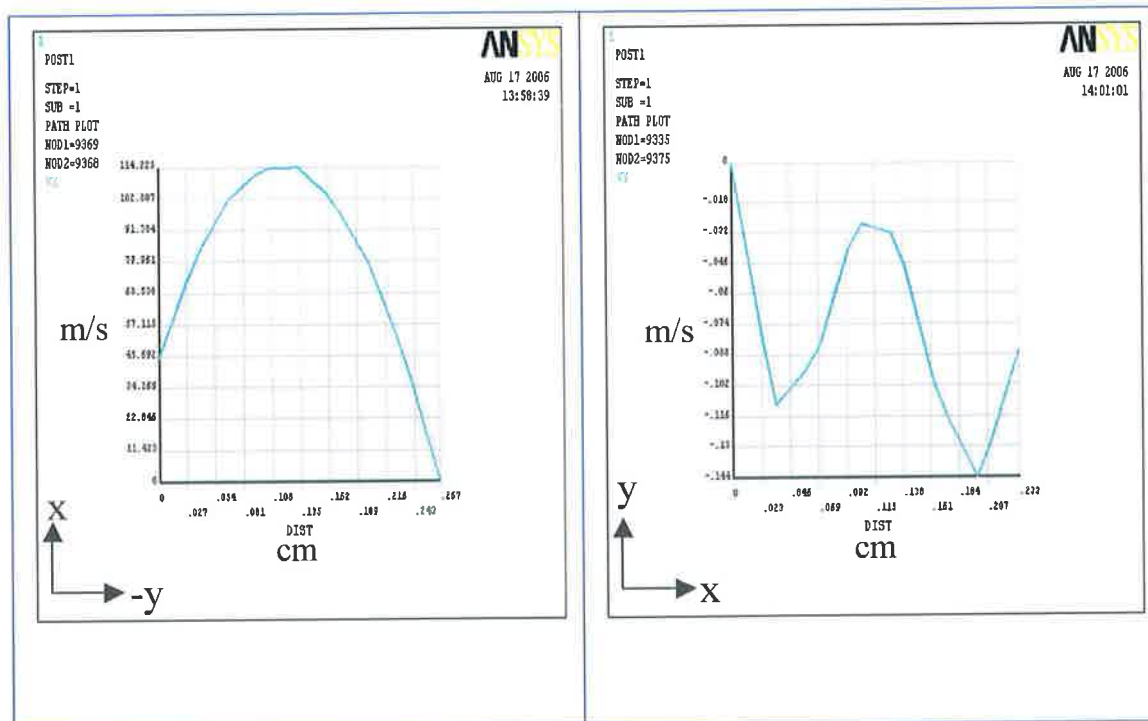


Figure C4: Velocity profile at outlet at 1:1 pressure ratio (left VX and right VY).

Velocity values are in m/s.

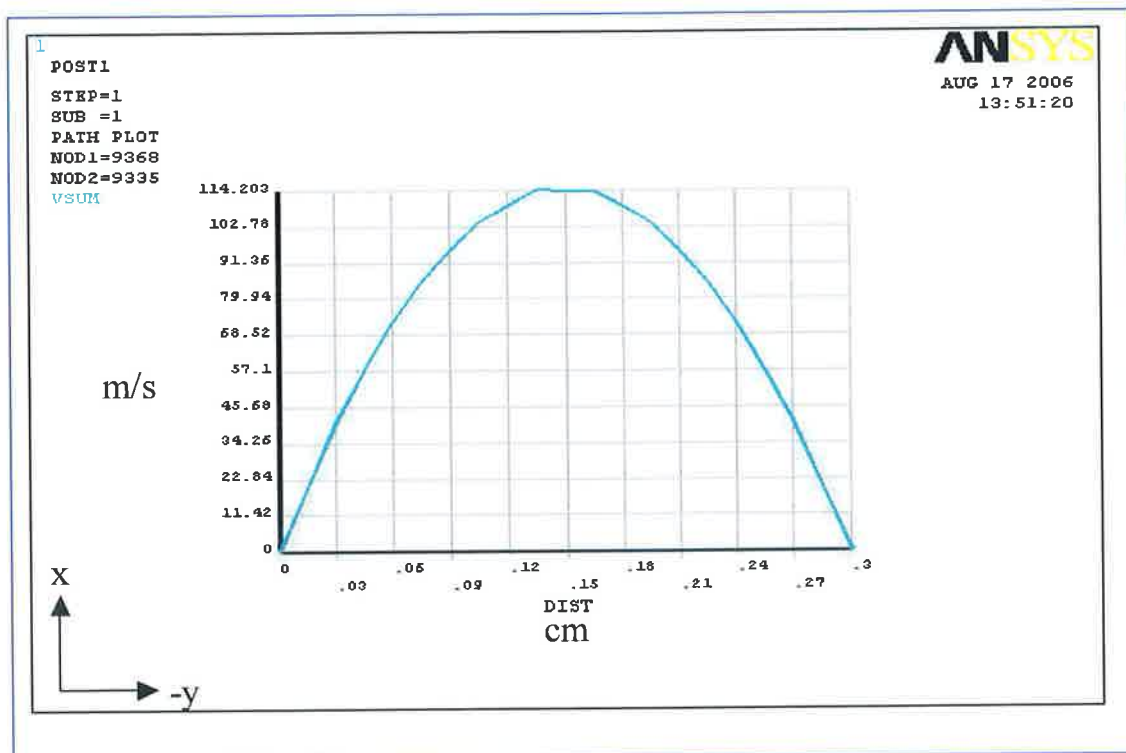


Figure C5: VSUM at outlet when pressure ratio is 1:1. Velocity values are in m/s.

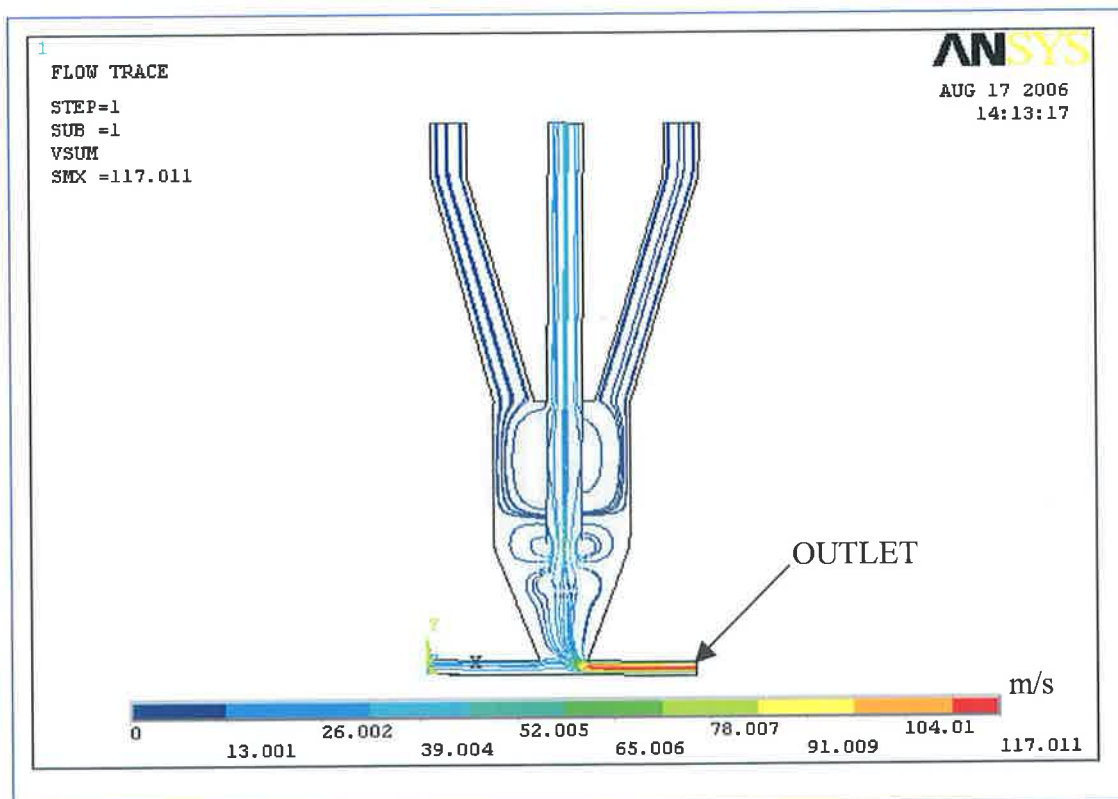


Figure C6: Particle flow lines for nitrogen gas and powders for a pressure ratio of 1:1.

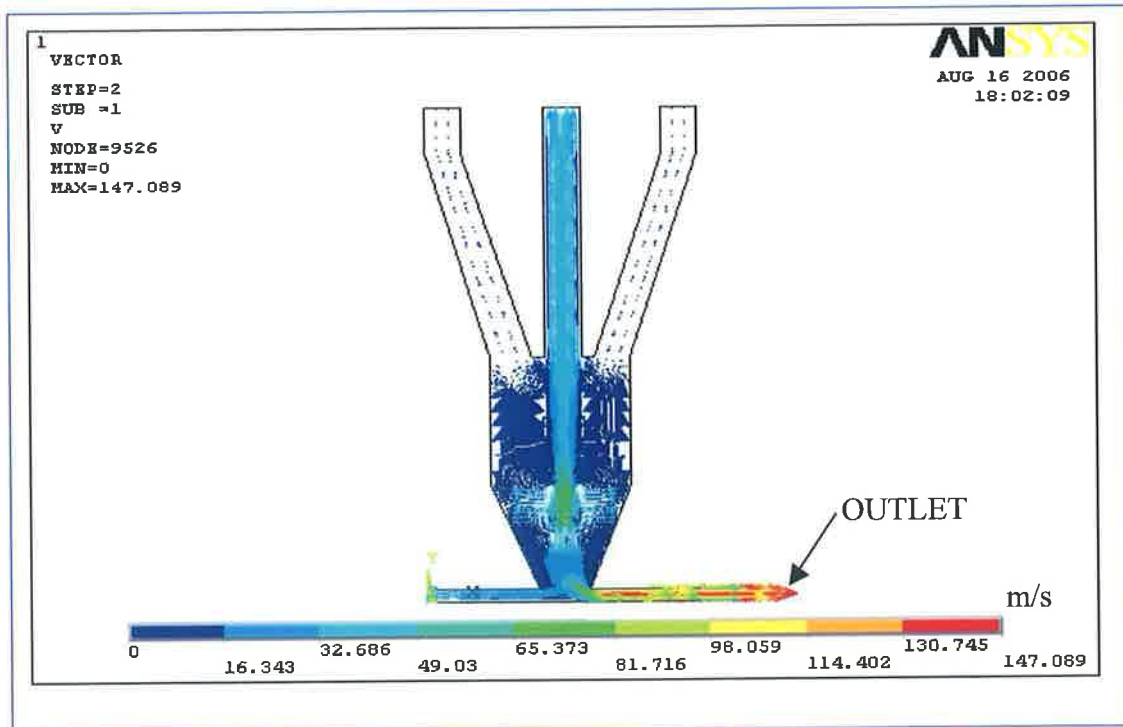


Figure C7: Vector plot showing the path of the velocity particles at 1.8:1 nitrogen gas pressure ratio on the inlet pressure tube to pick up shaft (obtain from pressure plot of ANSYS result).

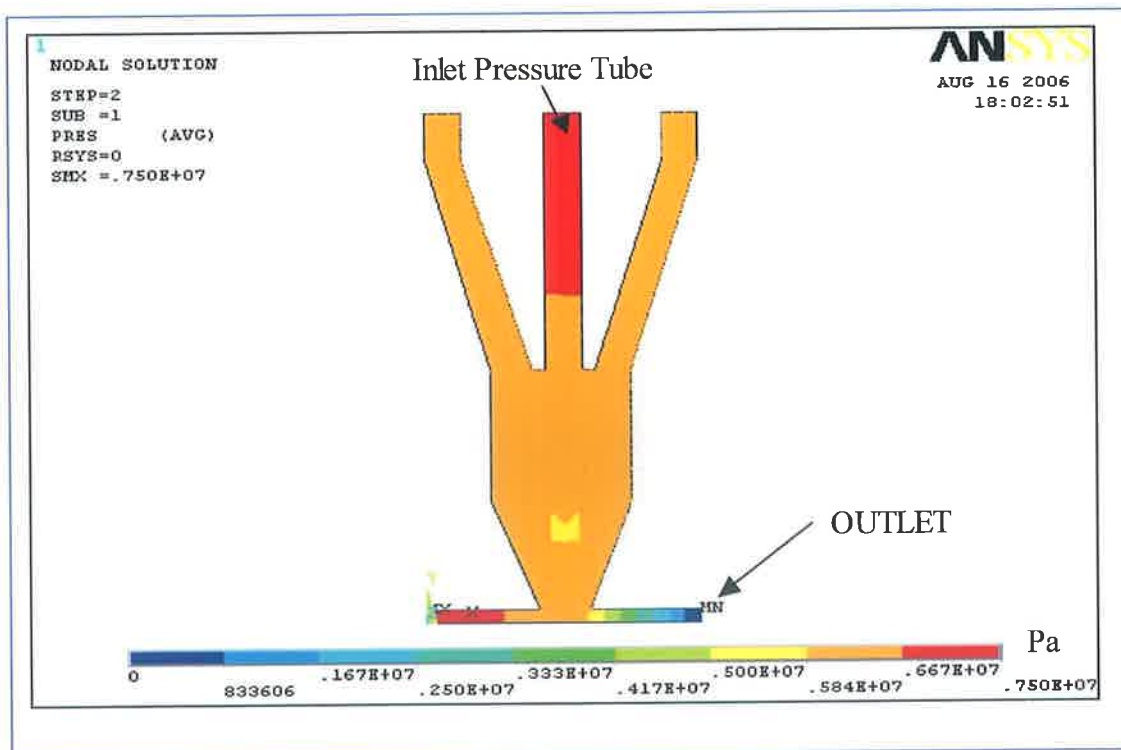


Figure C8: Pressure plot from nodal solution shows the pressure of inlet tube and pick up shaft inlet are same means 1.8:1.

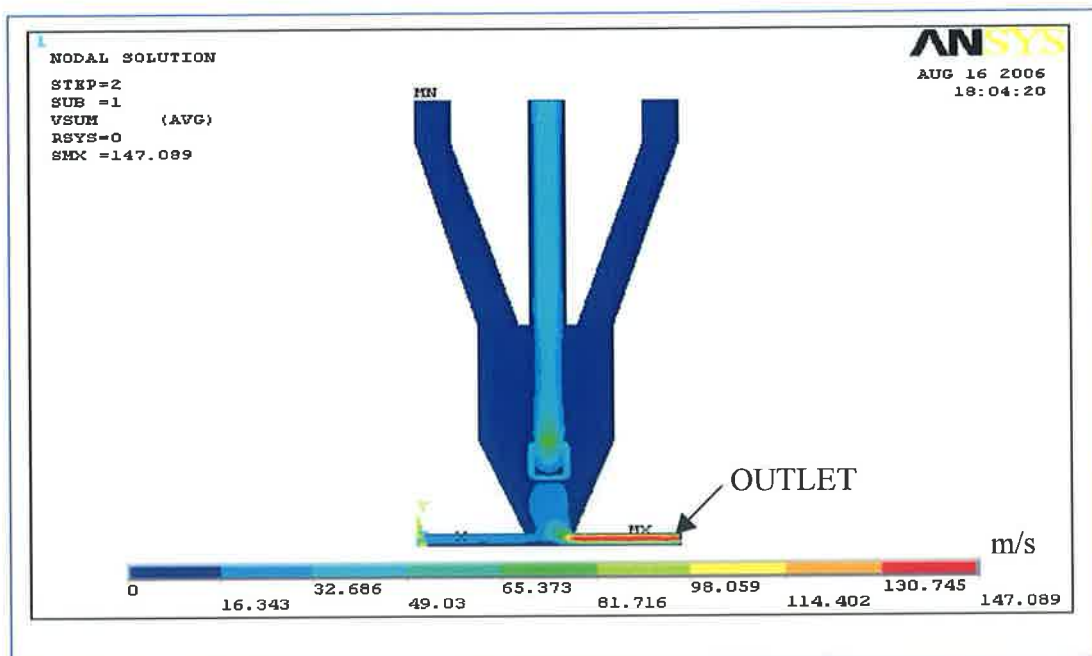


Figure C9: Velocity plot of the modelling from the nodal solution at 1.8:1 pressure ratio.

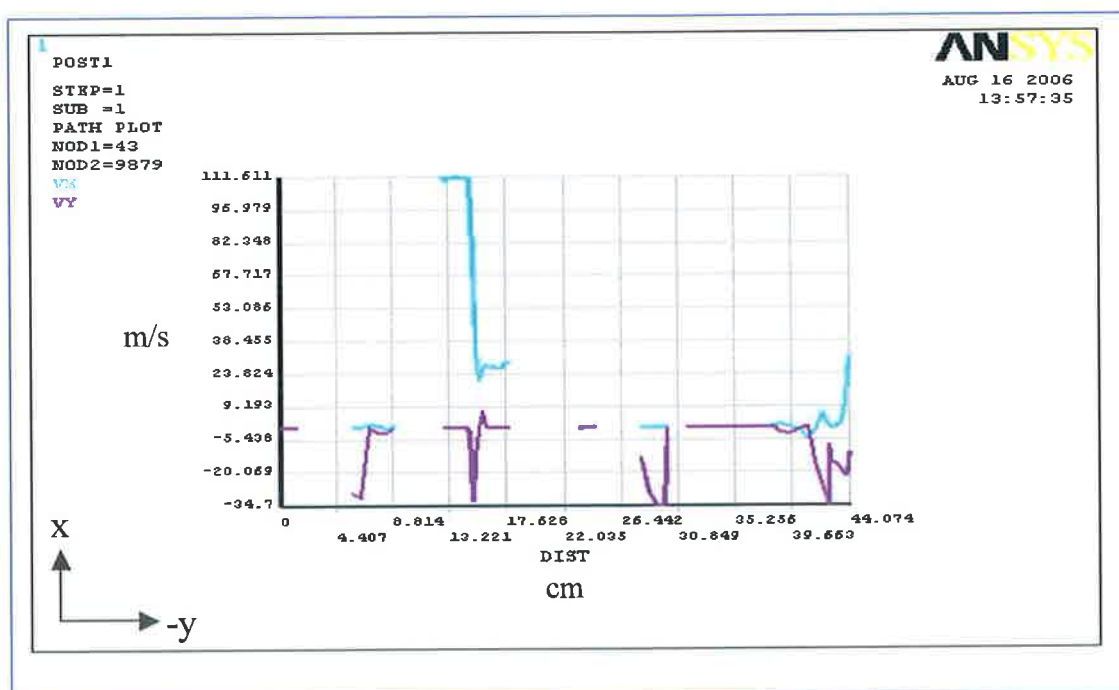


Figure C10: VSUM at outlet when pressure ratio is 1:1. Velocity values are in m/s.

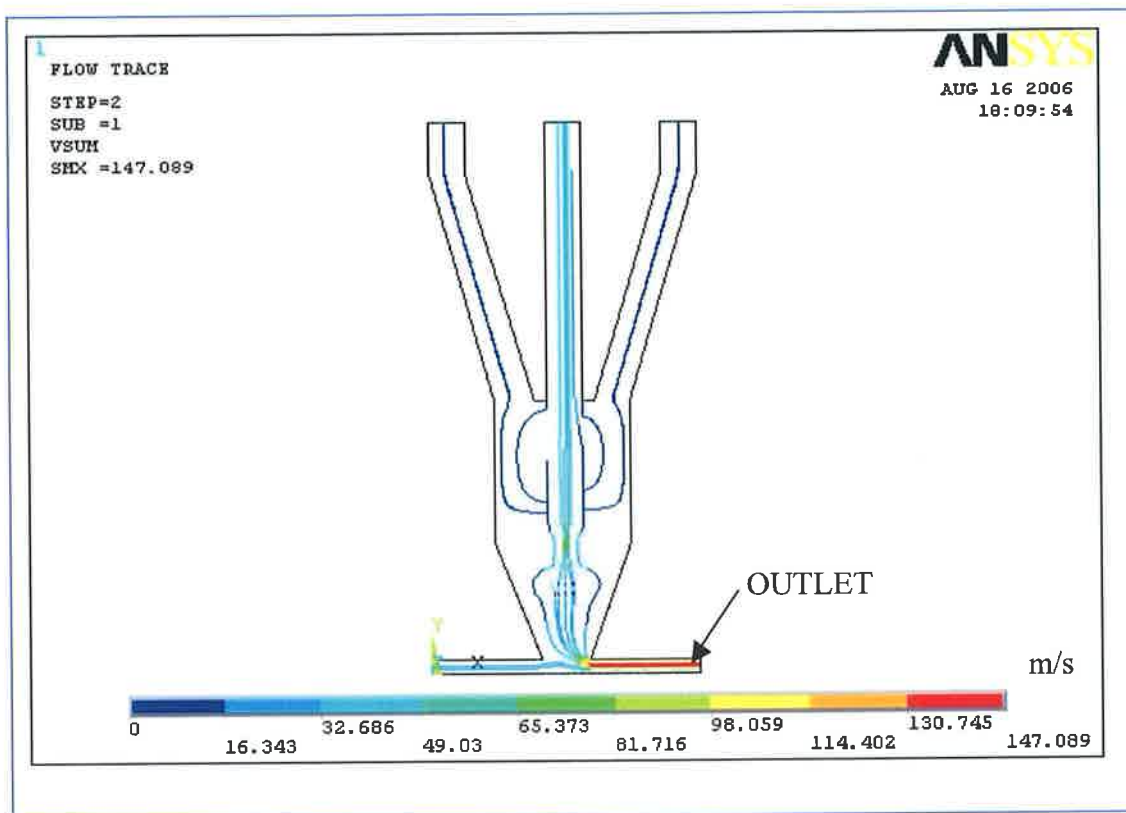


Figure C11: Particle flow lines for nitrogen gas and powders for a pressure ratio of 1.8:1.

Appendix – D

- **Results of powder flow bench tests using chamber ‘B’ when chamber ‘A’ was empty (0 mm to 4 mm).**
- **Results of powder flow bench tests using chamber ‘A’ when chamber ‘B’ was empty for reverse direction (4 mm to 0 mm).**
- **Results of powder flow bench tests using chamber ‘B’ when chamber ‘A’ was empty for reverse direction (4 mm to 0 mm).**

Table D1: Weight of stainless steel (Diamalloy 1003) from Chamber 'B' for various increments of its associated Needle.

Experiment Number	Vertical Increment of the Needle (mm)	Weight of the container (gm)	Total weight (Container + Powder) (gm)	Powder weight (gm)	Average weight (gm)
D1	1.00	8.41	10.44	2.03	2.09
D2			11.04	2.63	
D3			10.01	1.60	
D4	2.00	8.41	20.32	11.91	10.50
D5			17.78	9.37	
D6			18.63	10.22	
D7	2.50	8.41	26.91	18.50	18.95
D8			25.52	17.11	
D9			29.64	21.23	
D10	3.00	8.41	34.32	25.91	24.50
D11			31.87	23.46	
D12			32.53	24.12	
D13	4.00	8.41	91.01	82.60	81.40
D14			89.41	81.00	
D15			89.00	80.59	
D16	4.50	8.41	91.07	82.66	82.36
D17			91.02	82.61	
D18			90.21	81.80	
D19	5.00	8.41	90.50	82.09	82.39
D20			90.59	82.18	
D21			91.32	82.91	

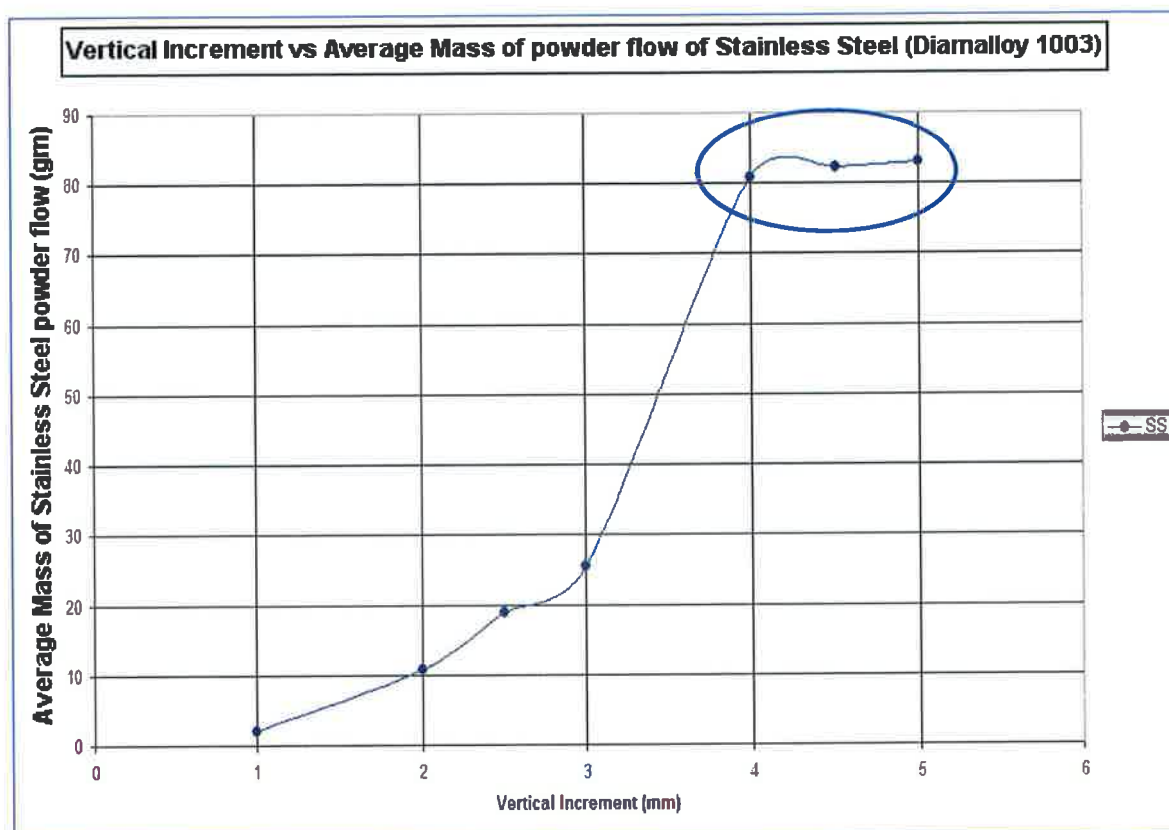


Figure D1: Average mass of stainless steel (Diamalloy 1003) powder flow with vertical increment of the needle shaped bolt controlled via Lab VIEW programming and data obtained from Table D1.

Table D2: Weight of Nickel alloy¹ (Diamalloy 1005) from Chamber 'B' for various increments of its associated Needle.

Experiment Number	Vertical Increment of the Needle (mm)	Weight of the container (gm)	Total weight (Container + Powder) (gm)	Powder weight (gm)	Average weight (gm)
E1	1.00	8.41	10.11	1.70	1.56
E2			10.07	1.66	
E3			9.72	1.31	
E4	2.00	8.41	21.01	12.60	11.91
E5			19.65	11.24	
E6			20.31	11.90	
E7	2.50	8.41	28.74	20.33	18.69
E8			26.04	17.63	
E9			26.52	18.11	
E10	3.00	8.41	39.67	31.26	34.88
E11			46.32	37.91	
E12			43.87	35.46	
E13	4.00	8.41	87.91	79.50	80.40
E14			86.88	78.47	
E15			91.63	83.22	
E16	4.50	8.41	91.69	83.28	83.80
E17			92.17	82.76	
E18			90.78	82.37	
E19	5.00	8.41	91.53	83.12	83.16
E20			91.02	82.61	
E21			92.17	83.76	

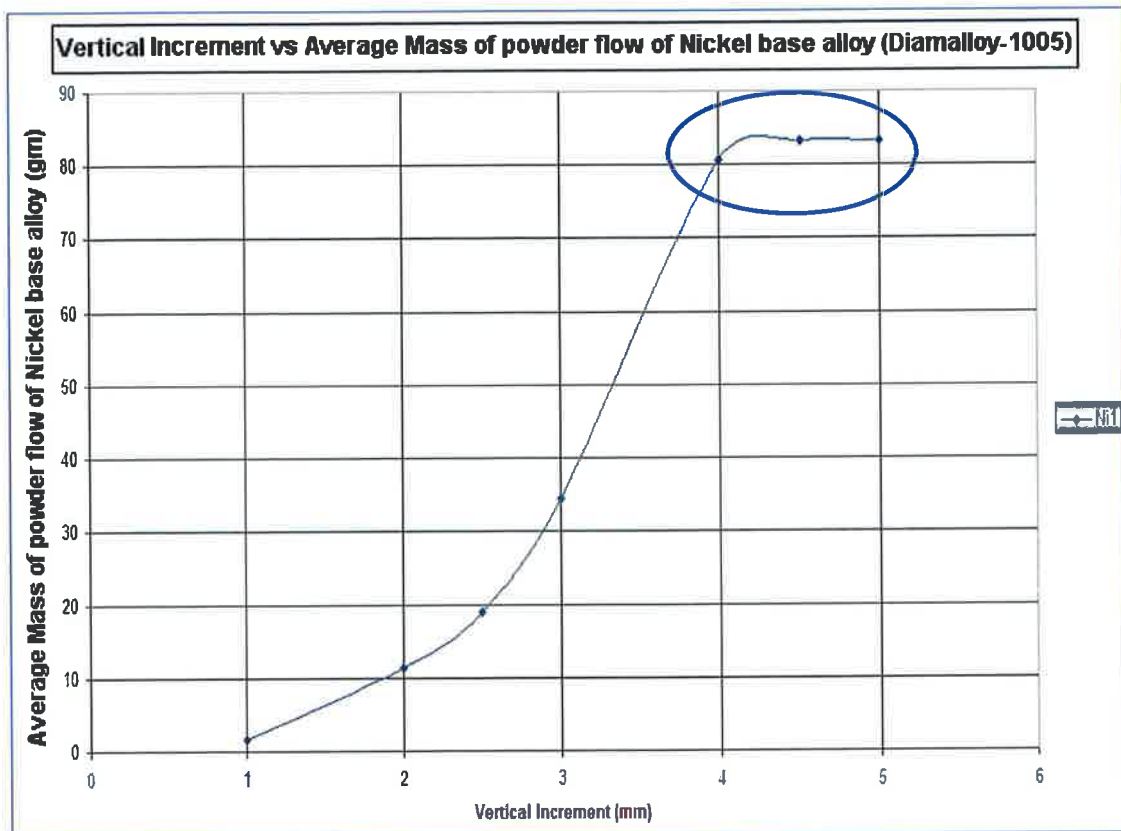


Figure D2: Average mass of nickel base alloy1 (Diamalloy 1005) powder flow with vertical increment of the needle shaped bolt controlled via Lab VIEW programming and data obtained from Table D2.

Table D3: Weight of Nickel alloy² (Diamalloy 2001) from Chamber 'B' for various increments of its associated Needle.

Experiment Number	Vertical Increment of the Needle (mm)	Weight of the container (gm)	Total weight (Container + Powder) (gm)	Powder weight (gm)	Average weight (gm)
F1	1.00	8.41	20.89	12.48	9.78
F2			17.68	9.27	
F3			15.99	7.58	
F4	2.00	8.41	48.31	39.90	40.23
F5			49.12	40.71	
F6			48.51	40.10	
F7	2.50	8.41	58.82	50.41	50.91
F8			60.84	52.43	
F9			58.31	49.90	
F10	3.00	8.41	71.13	62.72	62.58
F11			71.76	63.35	
F12			70.08	61.67	
F13	4.00	8.41	101.51	93.10	93.34
F14			101.83	92.96	
F15			102.37	93.96	
F16	4.50	8.41	103.87	95.46	94.89
F17			103.46	95.05	
F18			102.59	94.18	
F19	5.00	8.41	104.03	95.62	95.88
F20			104.89	96.48	
F21			103.95	95.54	

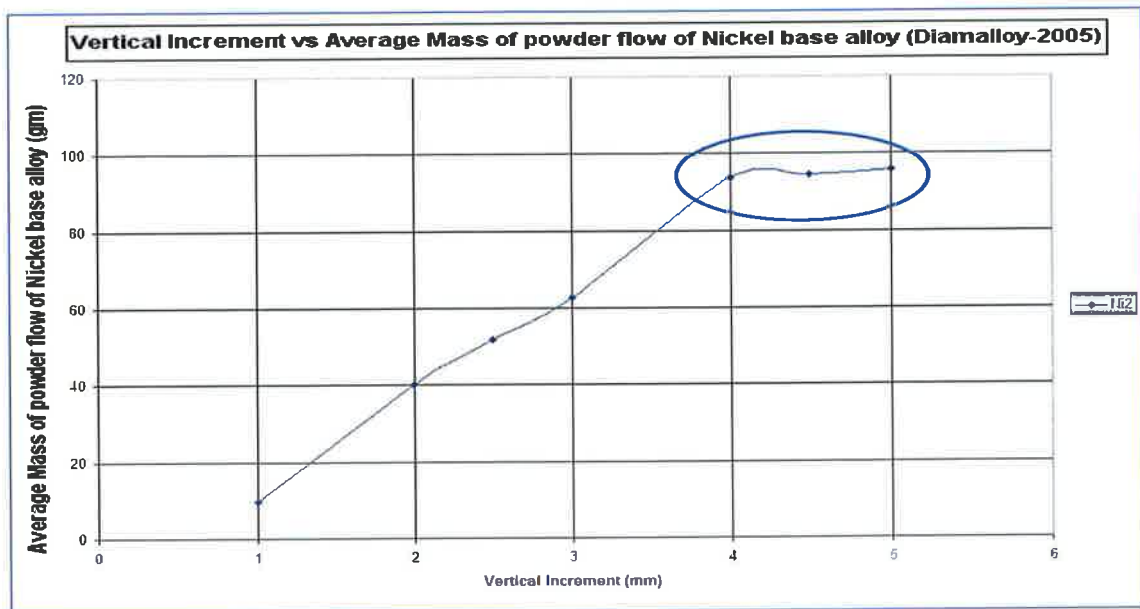


Figure D3: Average mass of nickel base alloy² (Diamalloy 2001) powder flow with vertical increment of the needle shaped bolt controlled via Lab VIEW programming and data obtained from Table D3.

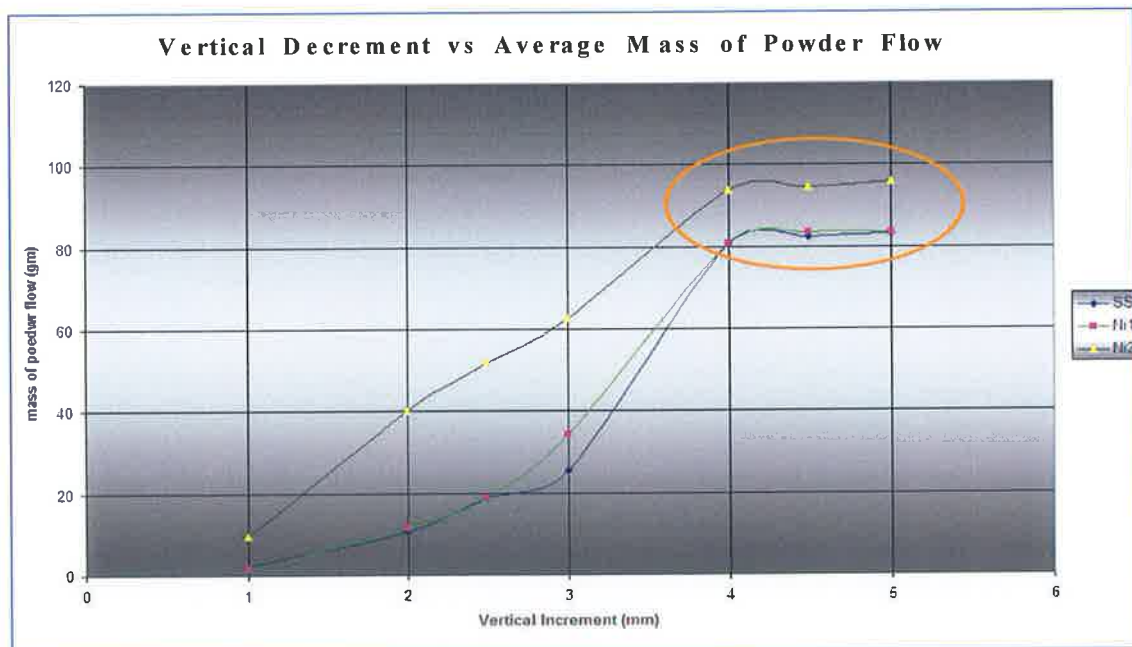


Figure D4: Comparison of average mass of stainless steel (Diamalloy 1003), nickel base alloy¹ (Diamalloy 1005) and nickel base alloy² (Diamalloy 2001) powder flow with vertical increment of the needle shaped bolt controlled via Lab VIEW programming. The combine graphical representation of figure D1, D2 and D3 and data obtained from Table D1, D2 and D3 respectively.

Table D4: Weight of stainless steel (Diamalloy 1003) from Chamber 'A' for various decrements of its associated Needle.

Experiment Number	Vertical Decrement of the Needle (mm)	Weight of the container (gm)	Total weight (Container + Powder) (gm)	Powder weight (gm)	Average weight (gm)
G1	5.00	8.41	91.33	82.92	82.31
G2			89.97	81.56	
G3			90.87	82.46	
G4	4.50	8.41	90.95	82.54	82.40
G5			91.28	82.87	
G6			90.20	81.79	
G7	4.00	8.41	89.88	81.47	81.99
G8			89.97	81.56	
G9			91.35	82.94	
G10	3.0	8.41	33.85	25.44	24.69
G11			32.79	24.38	
G12			32.65	24.24	
G13	2.50	8.41	25.95	17.54	18.19
G14			25.35	16.94	
G15			28.49	20.08	
G16	2.00	8.41	17.96	9.55	10.19
G17			17.89	9.48	
G18			19.95	11.54	
G19	1.00	8.41	11.40	2.99	2.55
G20			11.15	2.74	
G21			10.34	1.93	

Table D5: Weight of Nickel alloy¹ (Diamalloy 1005) from Chamber 'A' for various decrements of its associated Needle.

Experiment Number	Vertical Decrement of the Needle (mm)	Weight of the container (gm)	Total weight (Container + Powder) (gm)	Powder weight (gm)	Average weight (gm)
H1	5.00	8.41	92.09	83.68	83.32
H2			90.98	82.57	
H3			92.12	83.71	
H4	4.50	8.41	91.09	82.68	82.99
H5			91.87	83.46	
H6			91.24	82.83	
H7	4.00	8.41	88.23	79.82	80.54
H8			88.54	80.13	
H9			90.07	81.66	
H10	3.0	8.41	40.34	31.93	35.25
H11			45.66	37.25	
H12			44.98	36.57	
H13	2.50	8.41	28.55	20.14	19.09
H14			27.08	18.67	
H15			26.89	18.48	
H16	2.00	8.41	20.12	12.02	12.24
H17			21.09	12.68	
H18			20.43	12.02	
H19	1.00	8.41	9.96	1.55	1.74
H20			10.23	1.82	
H21			10.27	1.86	

Table D6: Weight of Nickel alloy² (Diamalloy 2001) from Chamber 'A' for various decrements of its associated Needle.

Experiment Number	Vertical Decrement of the Needle (mm)	Weight of the container (gm)	Total weight (Container + Powder) (gm)	Powder weight (gm)	Average weight (gm)
I1	5.00	8.41	103.12	94.71	95.19
I2			104.04	95.63	
I3			103.63	95.22	
I4	4.50	8.41	102.53	94.12	93.53
I5			101.21	92.80	
I6			102.09	93.68	
I7	4.00	8.41	100.87	92.46	92.94
I8			101.65	93.24	
I9			101.53	93.12	
I10	3.0	8.41	71.56	63.15	62.59
I11			70.98	62.57	
I12			70.45	62.04	
I13	2.50	8.41	59.07	50.66	51.35
I14			59.88	51.47	
I15			60.32	51.91	
I16	2.00	8.41	48.56	40.15	40.06
I17			47.99	39.58	
I18			48.87	40.46	
I19	1.00	8.41	18.15	9.74	9.64
I20			17.78	9.37	
I21			18.23	9.82	

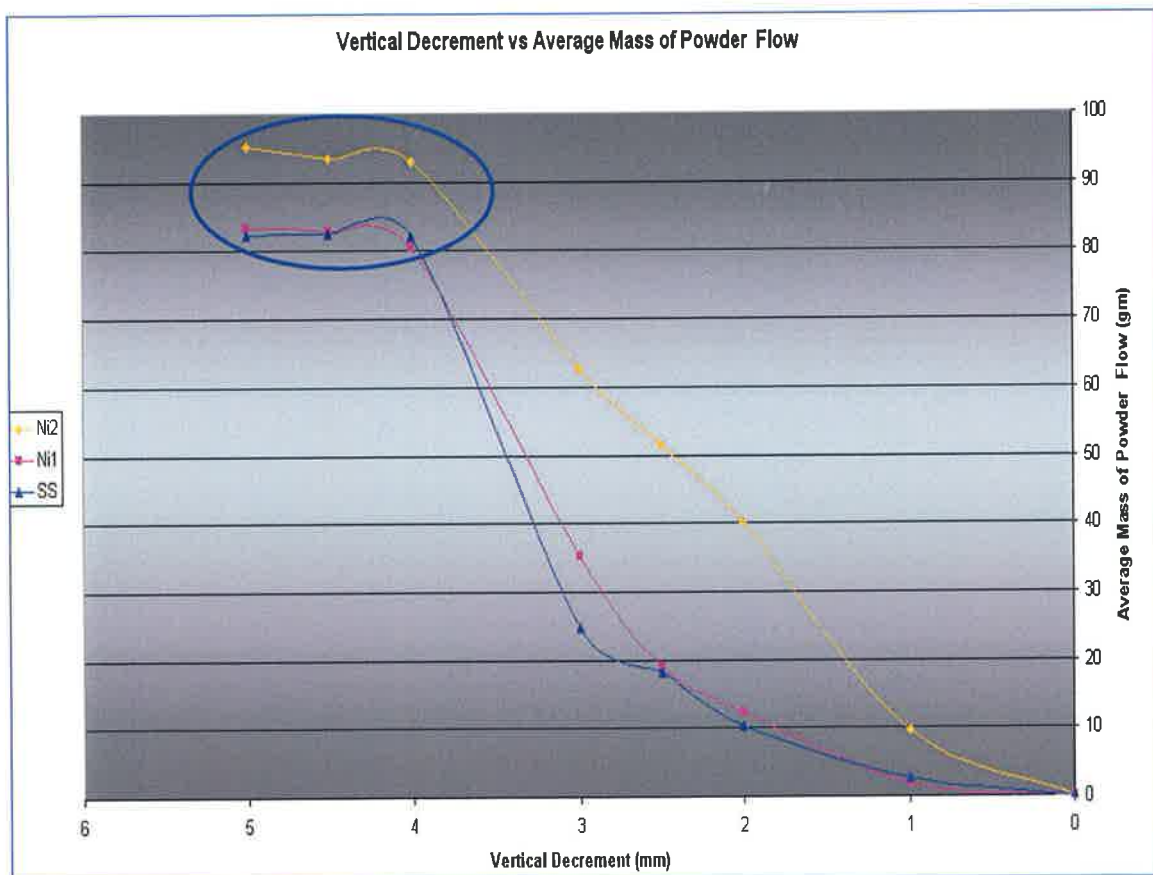


Figure D5: Comparison of average mass of stainless steel (Diamalloy 1003), nickel base alloy¹ (Diamalloy 1005) and nickel base alloy² (Diamalloy 2001) powder flow from Chamber 'A' with vertical decrement of the needle shaped bolt controlled via LabVIEW programming. Data obtained from Table D4, D5 and D6 respectively.

Table D7: Weight of stainless steel (Diamalloy 1003) from Chamber 'B' for various decrements of its associated Needle.

Experiment Number	Vertical Decrement of the Needle (mm)	Weight of the container (gm)	Total weight (Container + Powder) (gm)	Powder weight (gm)	Average weight (gm)
J1	5.00	8.41	89.91	81.50	81.81
J2			90.53	82.12	
J3			90.23	81.82	
J4	4.50	8.41	91.37	82.96	82.42
J5			90.23	81.82	
J6			90.89	82.48	
J7	4.00	8.41	91.00	82.59	82.31
J8			90.11	81.70	
J9			91.05	82.64	
J10	3.0	8.41	34.12	25.71	24.88
J11			32.79	24.38	
J12			32.95	24.54	
J13	2.50	8.41	26.17	17.76	18.56
J14			26.25	17.84	
J15			28.49	20.08	
J16	2.00	8.41	20.96	12.55	11.14
J17			18.75	10.34	
J18			18.93	10.52	
J19	1.00	8.41	10.87	2.46	2.42
J20			10.95	2.54	
J21			10.67	2.26	

Table D8: Weight of Nickel alloy¹ (Diamalloy 1005) from Chamber 'B' for various decrements of its associated Needle.

Experiment Number	Vertical Decrement of the Needle (mm)	Weight of the container (gm)	Total weight (Container + Powder) (gm)	Powder weight (gm)	Average weight (gm)
K1	5.00	8.41	92.17	83.76	83.25
K2			91.23	82.82	
K3			91.59	83.18	
K4	4.50	8.41	90.89	82.48	83.09
K5			91.57	83.16	
K6			92.04	83.63	
K7	4.00	8.41	89.65	81.24	81.06
K8			88.09	79.68	
K9			90.67	82.26	
K10	3.0	8.41	42.09	33.68	35.09
K11			43.34	34.93	
K12			45.08	36.67	
K13	2.50	8.41	27.95	19.54	18.94
K14			27.32	18.91	
K15			26.79	18.38	
K16	2.00	8.41	20.05	11.64	12.13
K17			21.34	12.93	
K18			20.23	11.82	
K19	1.00	8.41	10.56	2.15	2.15
K20			10.34	1.93	
K21			10.78	2.37	

Table D9: Weight of Nickel alloy² (Diamalloy 2001) from Chamber 'B' for various decrements of its associated Needle.

Experiment Number	Vertical Decrement of the Needle (mm)	Weight of the container (gm)	Total weight (Container + Powder) (gm)	Powder weight (gm)	Average weight (gm)
L1	5.00	8.41	102.79	94.38	94.89
L2			103.14	94.73	
L3			103.98	95.57	
L4	4.50	8.41	101.41	93.00	93.44
L5			101.76	93.35	
L6			102.37	93.96	
L7	4.00	8.41	101.23	92.82	92.69
L8			101.76	93.35	
L9			100.31	91.90	
L10	3.0	8.41	72.07	63.66	63.41
L11			71.78	63.37	
L12			71.62	63.21	
L13	2.50	8.41	59.07	50.66	51.39
L14			59.31	50.90	
L15			61.02	52.61	
L16	2.00	8.41	47.23	38.82	39.37
L17			47.43	39.02	
L18			48.67	40.26	
L19	1.00	8.41	17.98	9.57	9.74
L20			17.76	9.35	
L21			18.71	10.30	

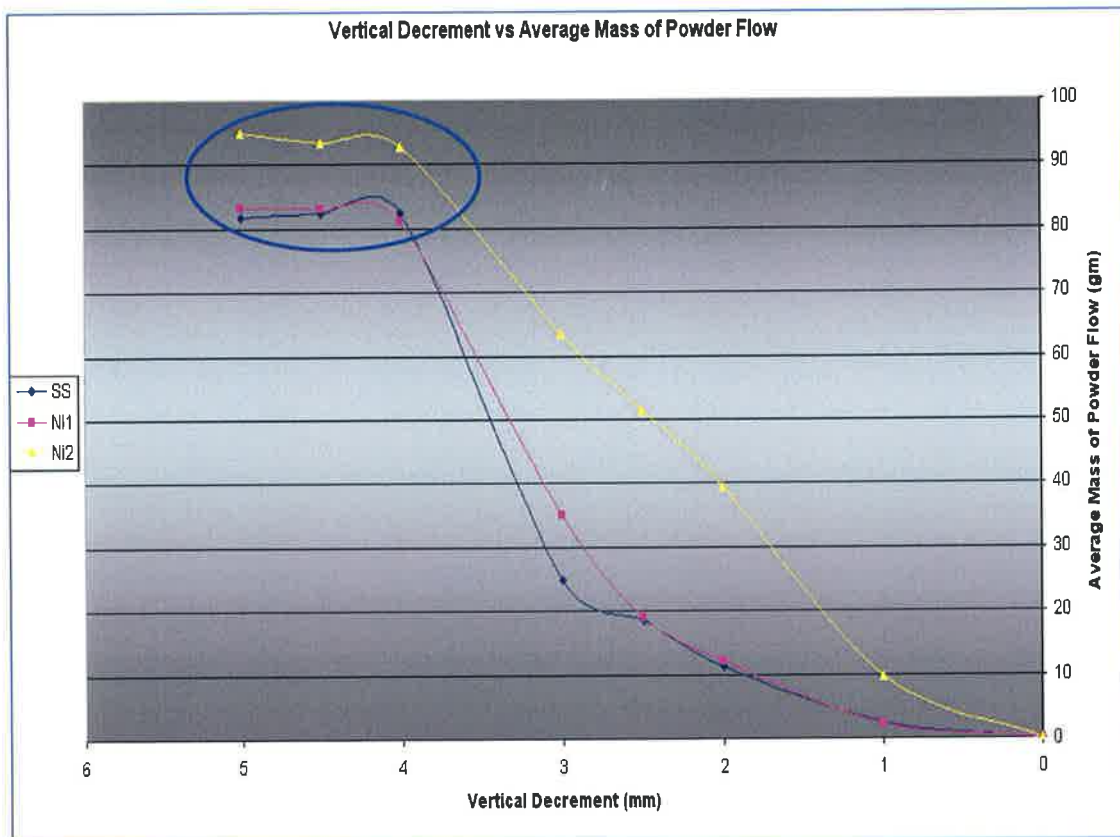


Figure D6: Comparison of average mass of stainless steel (Diamalloy 1003), nickel base alloy¹ (Diamalloy 1005) and nickel base alloy² (Diamalloy 2001) powder flow from Chamber 'B' with vertical decrement of the needle shaped bolt controlled via LabVIEW programming. Data obtained from Table D7, D8 and D9 respectively.

Appendix-E

Procedure of Standard Test Method for Flow Rate of Metal Powders



Standard Test Method for Flow Rate of Metal Powders¹

This standard is issued under the fixed designation B 213; the number immediately following the designation indicates the year of original adoption or, in the case of revision, the year of last revision. A number in parentheses indicates the year of last reapproval. A superscript epsilon (ϵ) indicates an editorial change since the last revision or reapproval.

1. Scope

1.1 This test method covers the determination of the flow rate of metal powders and is suitable only for those powders that will flow unaided through the specified apparatus.

1.2 The values stated in SI units are to be regarded as the standard (except for the flowmeter funnel, which is fabricated in inch-pound units). The values given in parentheses are for information only.

1.3 *This standard does not purport to address all of the safety concerns, if any, associated with its use. It is the responsibility of the user of this standard to establish appropriate safety and health practices and determine the applicability of regulatory limitations prior to use.*

2. Referenced Documents

2.1 ASTM Standards:

B 215 Practices for Sampling Finished Lots of Metal Powders²

B 243 Terminology of Powder Metallurgy²

3. Terminology

3.1 **Definitions**—Definitions of powder metallurgy terms can be found in Terminology B 243.

3.2 Definitions of Terms Specific to This Standard:

3.2.1 **flow rate, n** —the time required for a powder sample of standard mass to flow through an orifice in a standard instrument according to a specified procedure.

4. Summary of Test Method

4.1 A weighed mass (50.0 g) of metal powder is timed as it flows through the calibrated orifice of a funnel.

5. Significance and Use

5.1 The rate and uniformity of die cavity filling are related to flow properties, which thus influence production rates and uniformity of compacted parts.

5.2 The ability of a powder to flow is a function of interparticle friction. As interparticle friction increases, flow is slowed. Fine powders may not flow.

5.3 Humidity and moisture content influence flow rate. Wet or moist powders may not flow.

5.4 This test method may be part of the purchase agreement between powder manufacturers and powder metallurgy (P/M) part producers, or it can be an internal quality control test by either the producer or the end user.

6. Apparatus

6.1 **Powder Flowmeter Funnel³**—A flowmeter funnel (Fig. 1) having a calibrated orifice of 0.10 in. (2.54 mm) in diameter.

NOTE 1—The dimensions shown for the flowmeter funnel, including the orifice, are not to be considered controlling factors. Calibration with emery, as specified in Section 9, determines the working flow rate of the funnel.

6.2 **Stand³**—A stand (Fig. 2) to support the powder flowmeter funnel.

6.3 **Base**—A level, vibration free base to support the powder flowmeter stand.

6.4 **Timing Device**—A stopwatch or other suitable device capable of measuring to the nearest 0.1 s.

6.5 **Chinese Emery³**—An emery powder used to calibrate the flowmeter funnel.

6.6 **Balance**—A balance suitable for weighing at least 50.0 g to the nearest 0.1 g.

7. Sampling

7.1 A quantity of powder sufficient to run the desired number of flow tests shall be obtained in accordance with Practice B 215.

8. Preparation of Apparatus

8.1 Clean the funnel with clean dry toweling paper.

8.2 Clean the funnel orifice with a clean dry pipe cleaner.

9. Calibration of Apparatus

9.1 The manufacturer supplies the powder flowmeter funnel calibrated as follows:

9.1.1 Heat an open glass jar of Chinese emery in a drying oven at a temperature of 102° to 107°C (215° to 225°F) for 1 h.

9.1.2 Cool the emery to room temperature in a desiccator.

9.1.3 Follow the procedure outlined in steps 10.1.1–10.1.8.

¹ This test method is under the jurisdiction of ASTM Committee B-9 on Metal Powders and Metal Powder Products and is the direct responsibility of B09.02 on Base Metal Products.

Current edition approved Sept. 10, 1997. Published March 1998. Originally published as B 213 – 46T. Last previous edition B 213 – 90.

² Annual Book of ASTM Standards, Vol. 02.05.

³ The flowmeter funnel, stand, and Chinese emery are available from AcidPowder International, LLC.

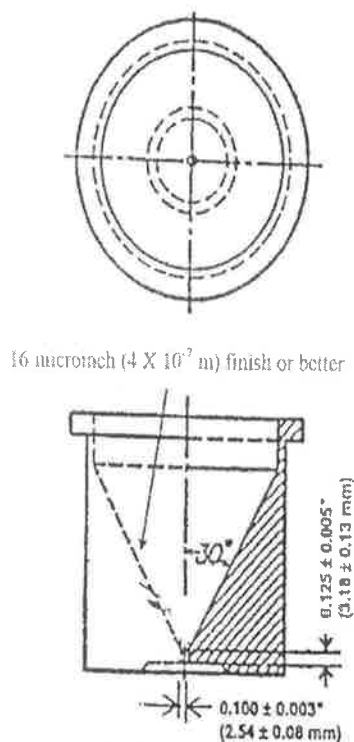


FIG. 1 Flowmeter Funnel

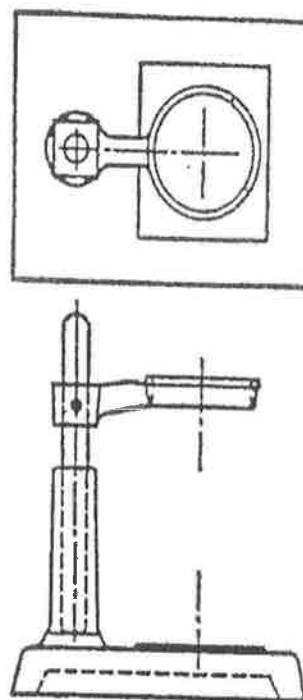


FIG. 2 Stand

9.1.4 Repeat steps 10.1.2-10.1.8 using the identical 50.0 g mass of emery for all the tests until 5 flow times, the extremes of which shall not differ by more than 0.4 s, have been recorded.

9.1.5 The average of these five flow times is stamped on the bottom of the funnel.

9.2 The flow rate of Chinese emery powder was established by an interlaboratory study conducted by Subcommittee B09.02 in 1995.⁴ It represents the flow rate through the master flowmeter funnel that had been used in a previous interlaboratory study with the former Turkish emery calibration powder, which is no longer available.

9.3 It is recommended that the flow rate be checked periodically, at least every six months, using the procedure outlined in steps 9.1.1-9.1.5. If the flow rate has changed from that stamped on the instrument, the new correction factor will be 40.0 divided by this new flow rate. Before adopting the new correction factor, however, it is recommended that the cause of the change be investigated. If the flow rate has increased (faster flow), it is probable that repeated use has burnished the orifice and the new correction factor may be used. A decrease in flow rate (slower flow) may indicate a plating of soft powder upon the orifice. This should be removed carefully with the aid of a pipe cleaner and the calibration test rerun, the new correction factor being calculated if required. It is recommended that the use of a funnel be discontinued after the flow rate of the emery has increased such that the time of flow is less than 37 s.

⁴ Supporting data is available from ASTM Headquarters.

10. Procedure

10.1 Method 1—Stationary Powder Start to Flow Measurement:

10.1.1 Weigh out a 50.0 g mass of powder, as sampled, into a clean weighing dish.

10.1.2 Block the discharge orifice at the bottom of the funnel with a dry finger.

10.1.3 Carefully pour the 50.0 g sample of powder into the center of the flowmeter funnel without any tapping, vibration or movement of the funnel.

10.1.4 Place the emptied weighing dish on the flowmeter stand directly under the funnel orifice.

10.1.5 Simultaneously start the stopwatch and remove your finger from the discharge orifice.

10.1.6 If the powder fails to start flowing, one light tap on the funnel rim is permitted. Further tapping of the funnel, however, or poking or stirring of the powder in the funnel with a wire or any other implement is not permitted.

10.1.7 Stop the stopwatch the instant the last of the powder exits the orifice.

10.1.8 Record the elapsed time to the nearest 0.1 s.

10.1.9 More than one flow may be run if desired. Use a fresh 50.0 g quantity of powder for each flow test. Average the flow times.

10.2 Method 2—Moving Powder Start to Flow Measurement:

10.2.1 Place an empty receptacle directly under the discharge orifice.

10.2.2 Weigh out a 50.0 g mass of powder, as sampled, into a clean weighing dish.

10.2.3 Pour the 50.0 g powder specimen into the center of

the funnel and start the stopwatch the instant the powder exits the orifice.

10.2.4 Stop the stopwatch the instant the last of the powder exits the orifice.

10.2.5 Record the elapsed time to the nearest 0.1 s.

10.2.6 More than one flow may be run if desired. Use a fresh 50.0 g quantity of powder for each flow test. Average the flow times.

11. Calculation

11.1 Calculate the correction factor by dividing 40.0 by either the flow rate stamped on the bottom of the funnel, or the new calibration flow rate established in 9.3.

11.2 Multiply the elapsed time (see 10.1.9 or 10.2.6) by the desired correction factor (see 11.1).

12. Report

12.1 Report the corrected flow rate in seconds to the nearest second.

13. Precision and Bias

13.1 *Precision*—Precision has been determined from an interlaboratory study performed by seven laboratories of Subcommittee B09.02.⁴

13.1.1 Repeatability intervals, r , are listed in Table 1. In 95 % of flow rate determinations, on the basis of test error

TABLE 1 Precision of Flow Rate Measurements of Metal Powders

Powder	Apparent Density (g/cm ³)	Flow Rate \times Avg. (s/50 g)	Repeatability (r) Avg. 3 Flows (s)	Reproducibility (R) Avg. 3 Flows (s)
Sphencol bronze	5.04	12	0.1	0.8
Iron #1	2.46	31	0.7	2.5
Iron #2	3.03	26	1.0	2.1
Iron (lubricated)	3.18	26	1.3	2.2
Bronze premix (lubricated)	3.31	31	1.7	2.6
Brass (lubricated)	3.51	42	4.1	9.7

alone, duplicate tests in the same laboratory by the same operator on one homogeneous lot of powder will differ by no more than the stated amount in seconds.

13.1.2 Reproducibility intervals, R , are listed in Table 1. For 95 % of comparative trials done in two different laboratories, and on the basis of test error alone, single tests on the same homogeneous lot of powder will differ by no more than the stated amount in seconds.

13.2 *Bias*—No statement can be made about bias, because there is no standard reference material for flow rate measurement.

14. Keywords

14.1 flow rate; metal powder flow; powder flow

The American Society for Testing and Materials takes no position respecting the validity of any patent rights asserted in connection with any item mentioned in this standard. Users of this standard are expressly advised that determination of the validity of any such patent rights, and the risk of infringement of such rights, are entirely their own responsibility.

This standard is subject to revision at any time by the responsible technical committee and must be reviewed every five years and if not revised, either reapproved or withdrawn. Your comments are invited either for revision of this standard or for additional standards and should be addressed to ASTM Headquarters. Your comments will receive careful consideration at a meeting of the responsible technical committee, which you may attend. If you feel that your comments have not received a fair hearing you should make your views known to the ASTM Committee on Standards, 100 Barr Harbor Drive, West Conshohocken, PA 19428.

Appendix F- SEM Analysis Results

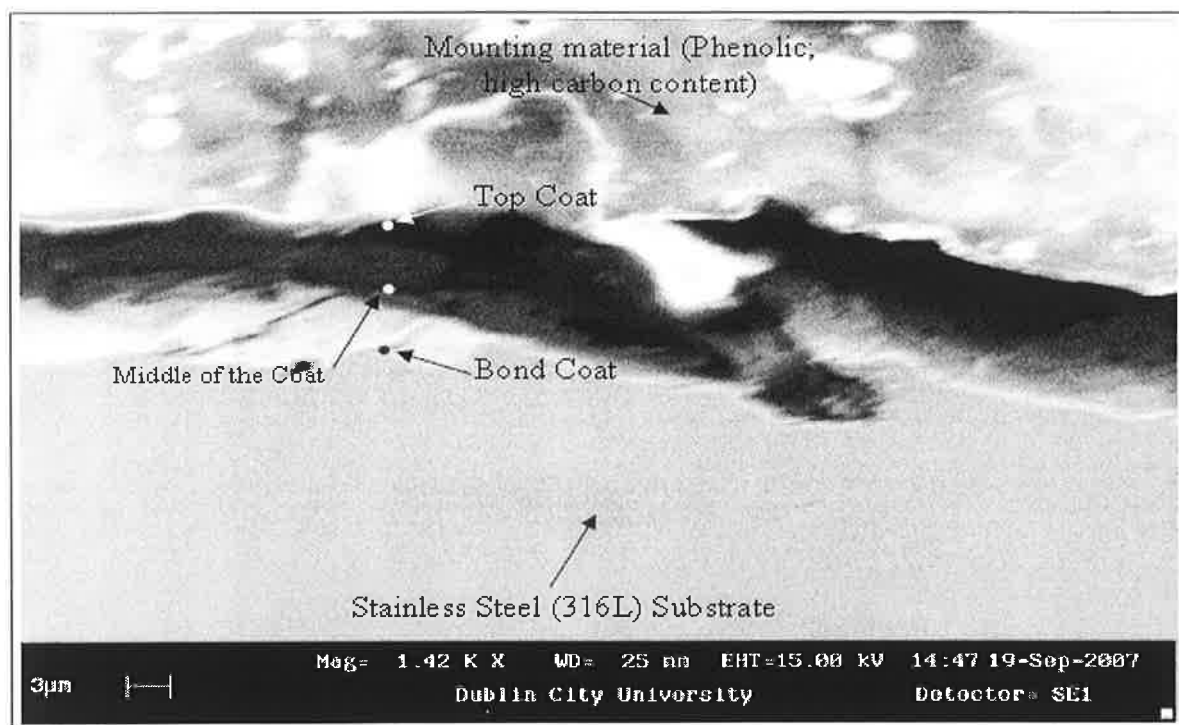


Figure F1: A SEM image of the functionally graded coating sample 1 (Diamalloy 1003 and Diamalloy 2001) (Represent of Figure 6.17 for the 2nd and 3rd set of point analysis).

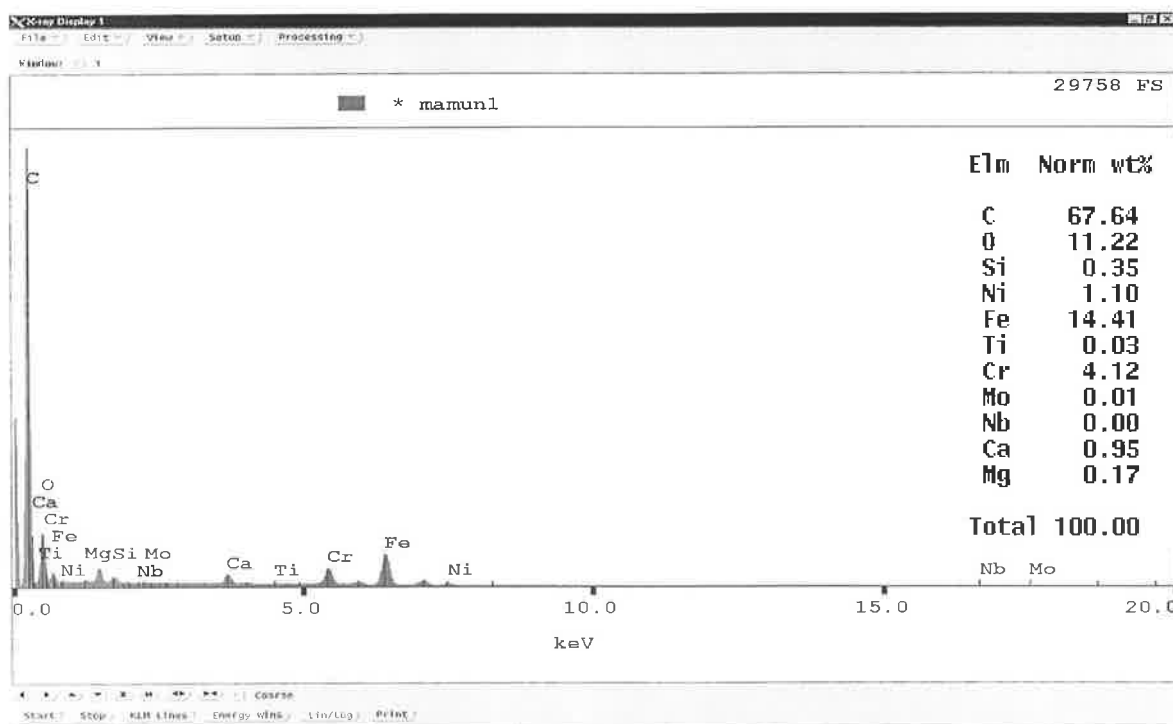


Figure F2: Chemical composition of the final coat or the Top Coat/Service Coat of Sample 1 (2nd set of point analysis).

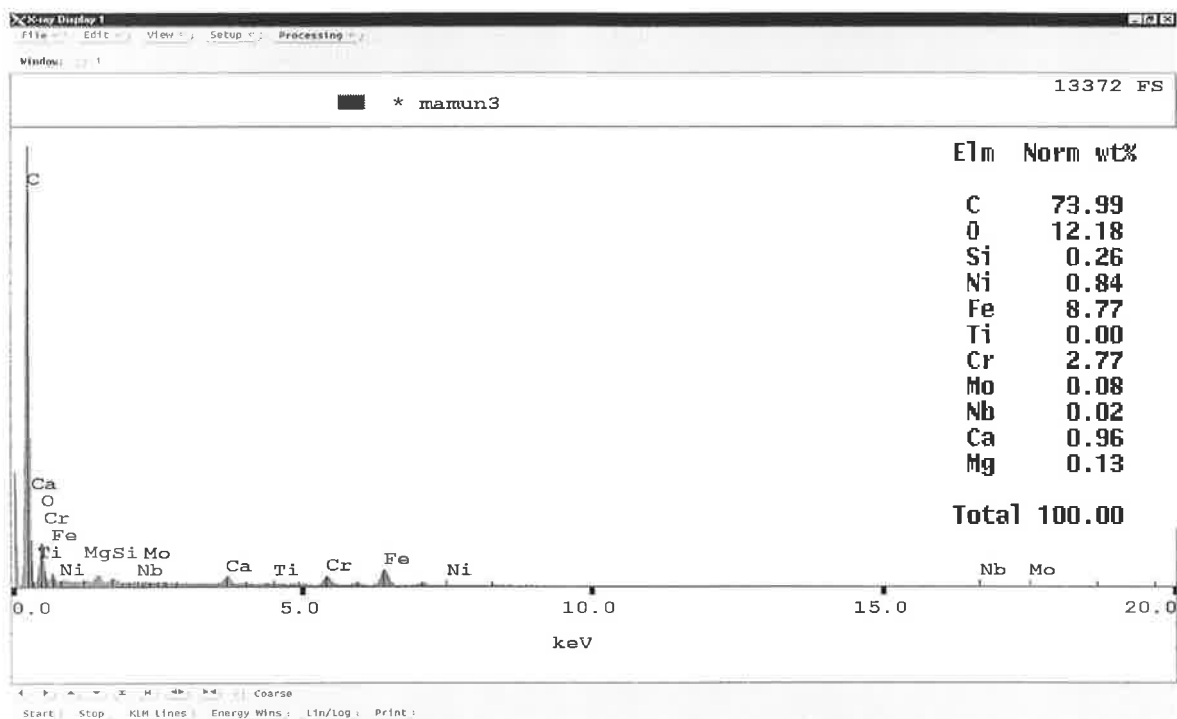


Figure F3: Chemical composition of the final coat or the Top Coat/Service Coat of Sample 1 (3rd set of point analysis).

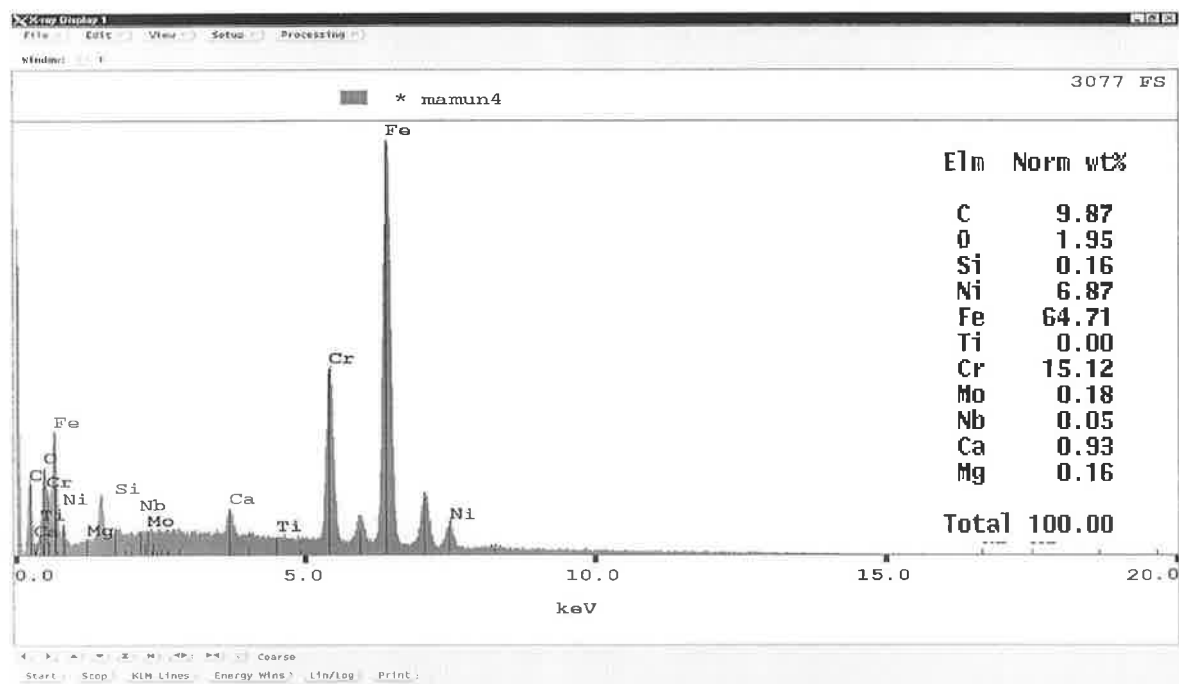


Figure F4: Chemical composition of the middle layer or Middle of the Coat of Sample 1 (2nd set of point analysis).

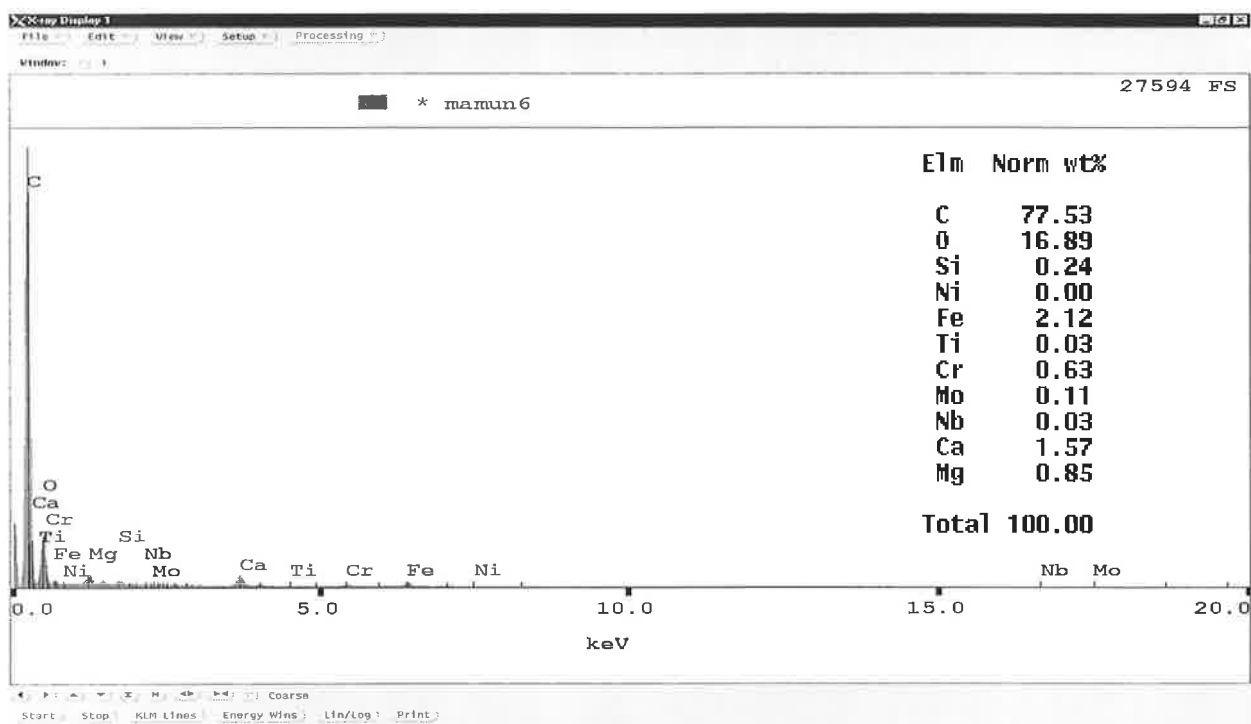


Figure F5: Chemical composition of the middle layer or Middle of the Coat of Sample 1 (3rd set of point analysis).

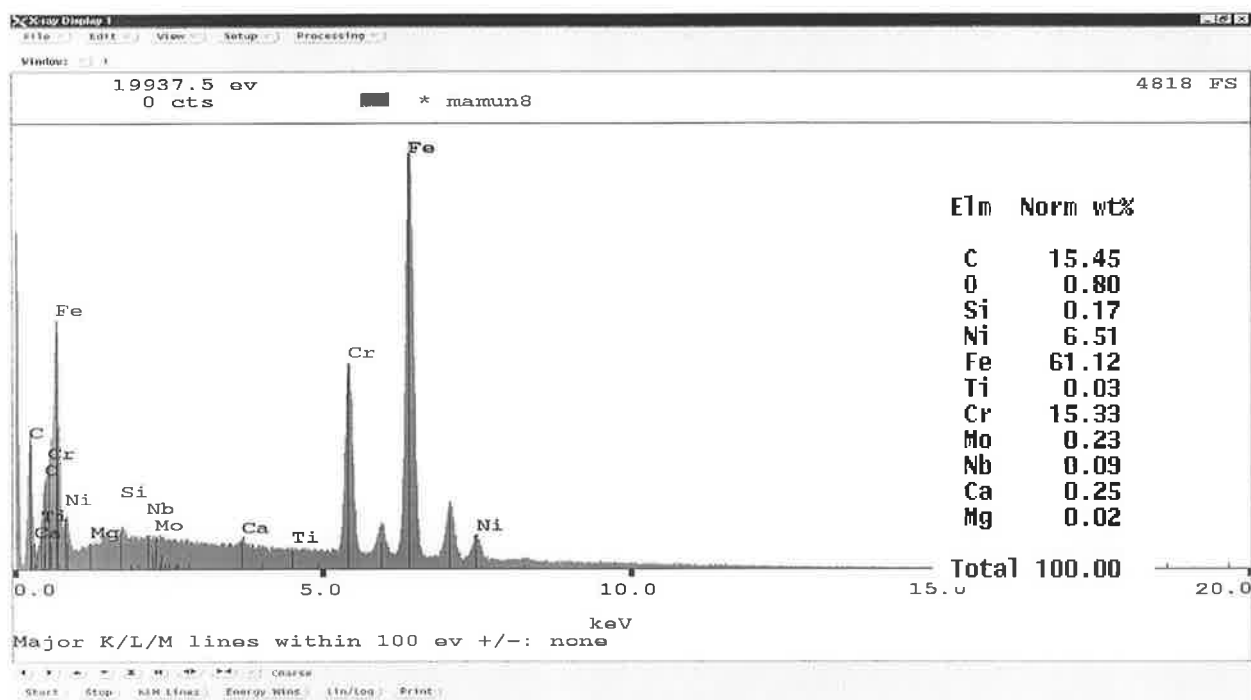


Figure F6: Chemical composition of the first coat or the Bond coat of Sample 1 (2nd set of point analysis).

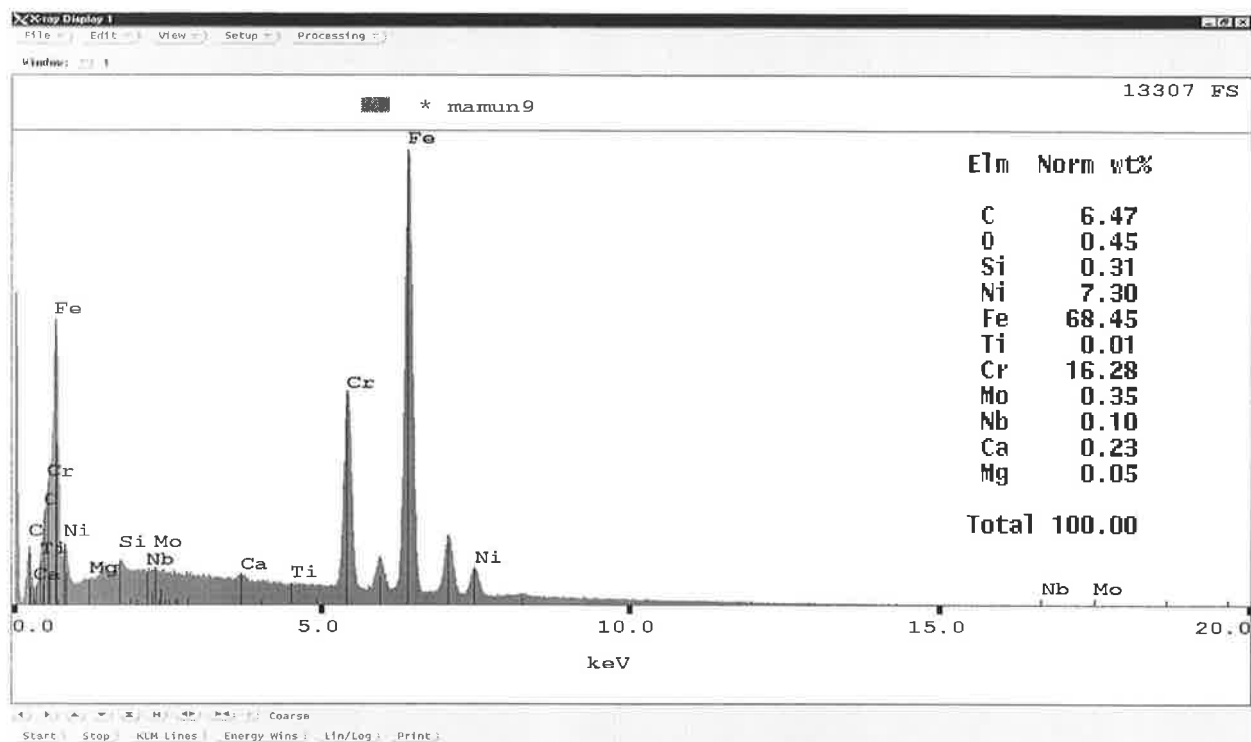


Figure F7: Chemical composition of the first coat or the Bond coat of Sample 1 (3rd set of point analysis).

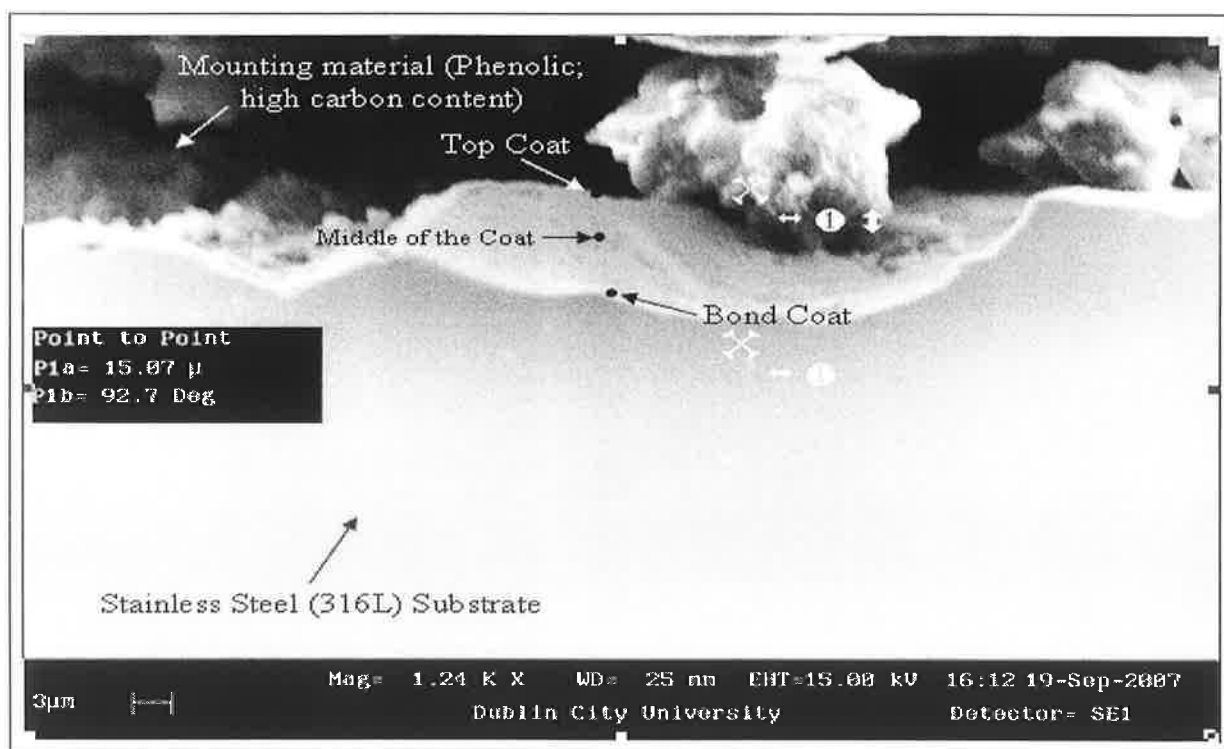


Figure F8: A SEM image of the functionally graded coating sample 2 (Diamalloy 1003 and Diamalloy 1005) (Represent of Figure 6.21 for the 2nd and 3rd set of point analysis).

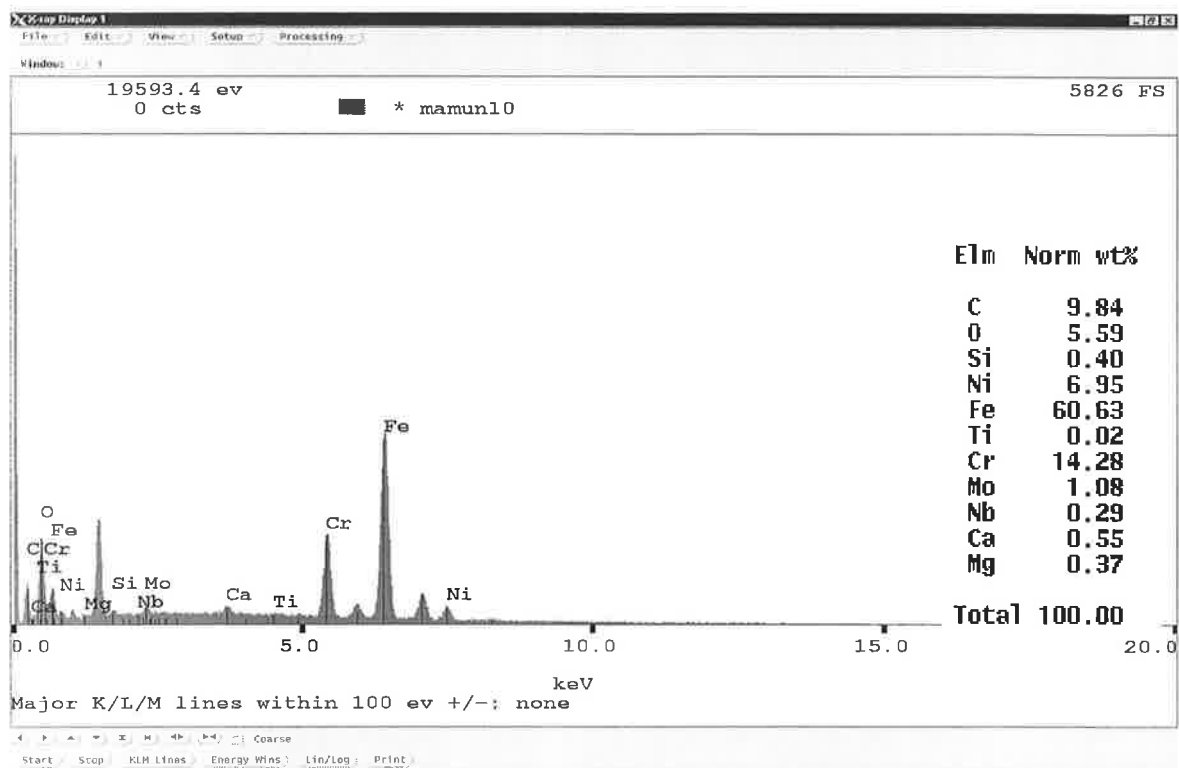


Figure F9: Chemical composition of the final coat or the Top Coat/Service Coat of Sample 2 (3rd set of point analysis).

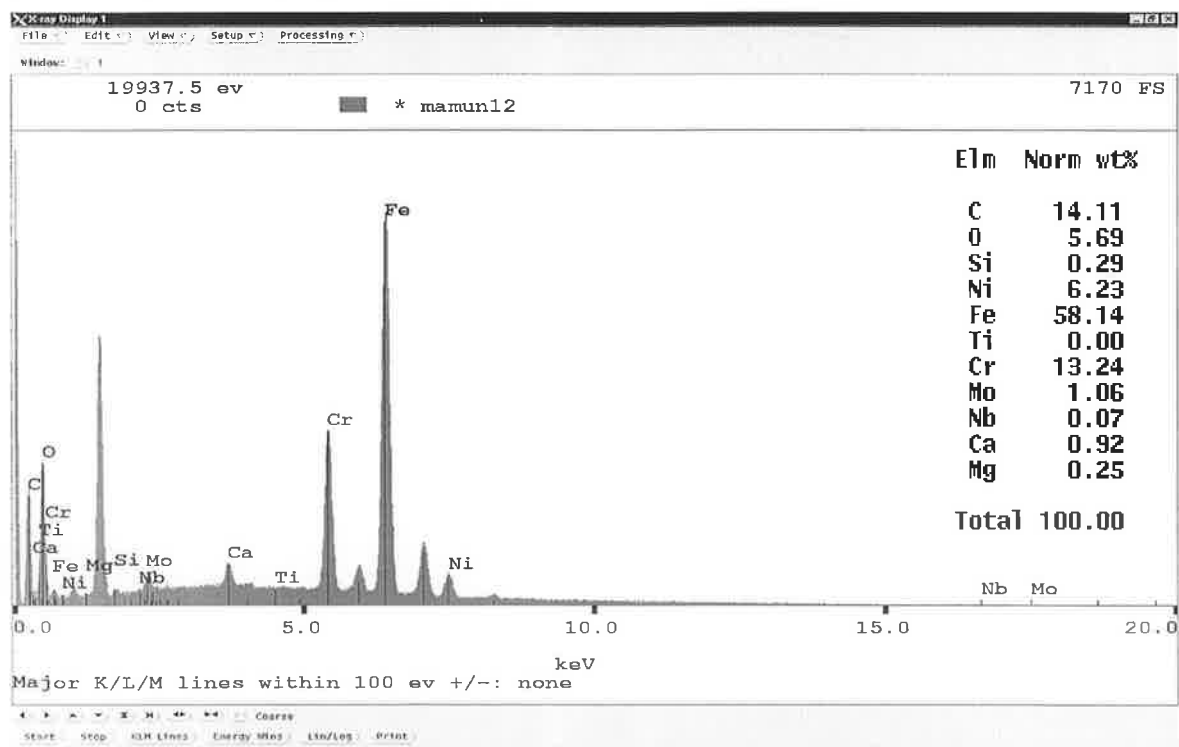


Figure F10: Chemical composition of the final coat or the Top Coat/Service Coat of Sample 2 (3rd set of point analysis).

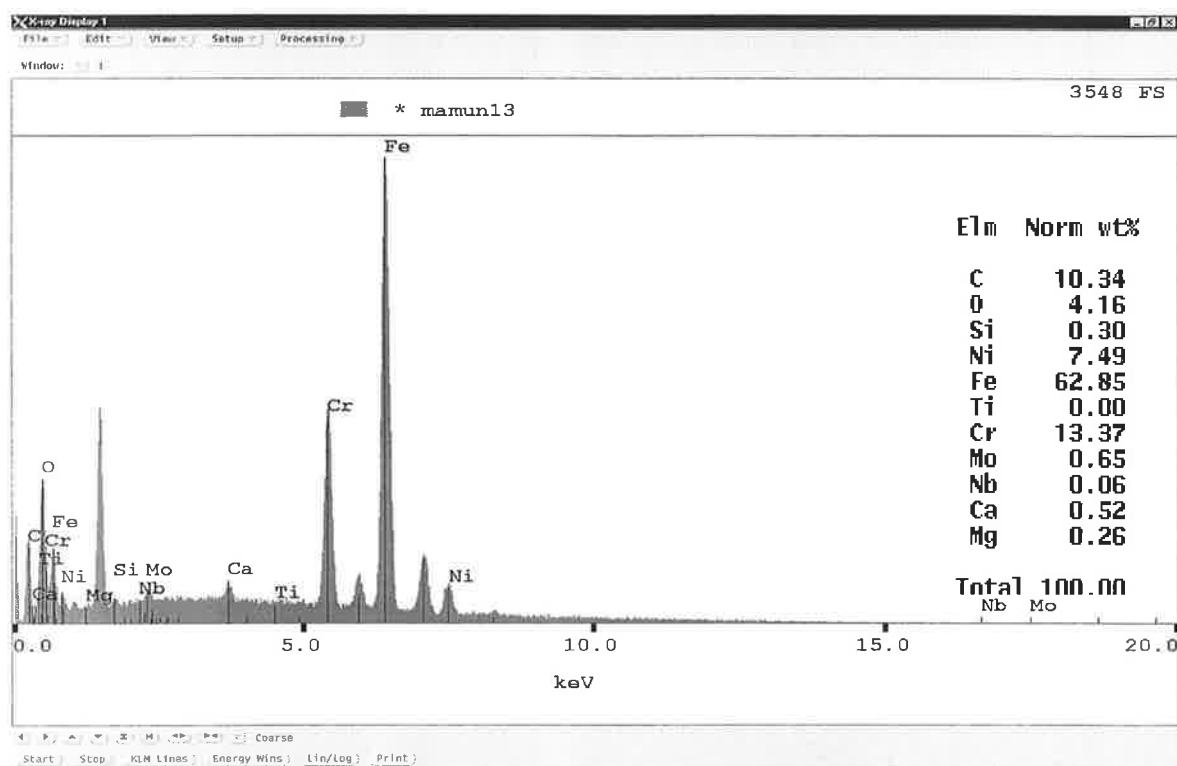


Figure F11: Chemical composition of the middle layer or Middle of the Coat of Sample 2 (2nd set of point analysis).

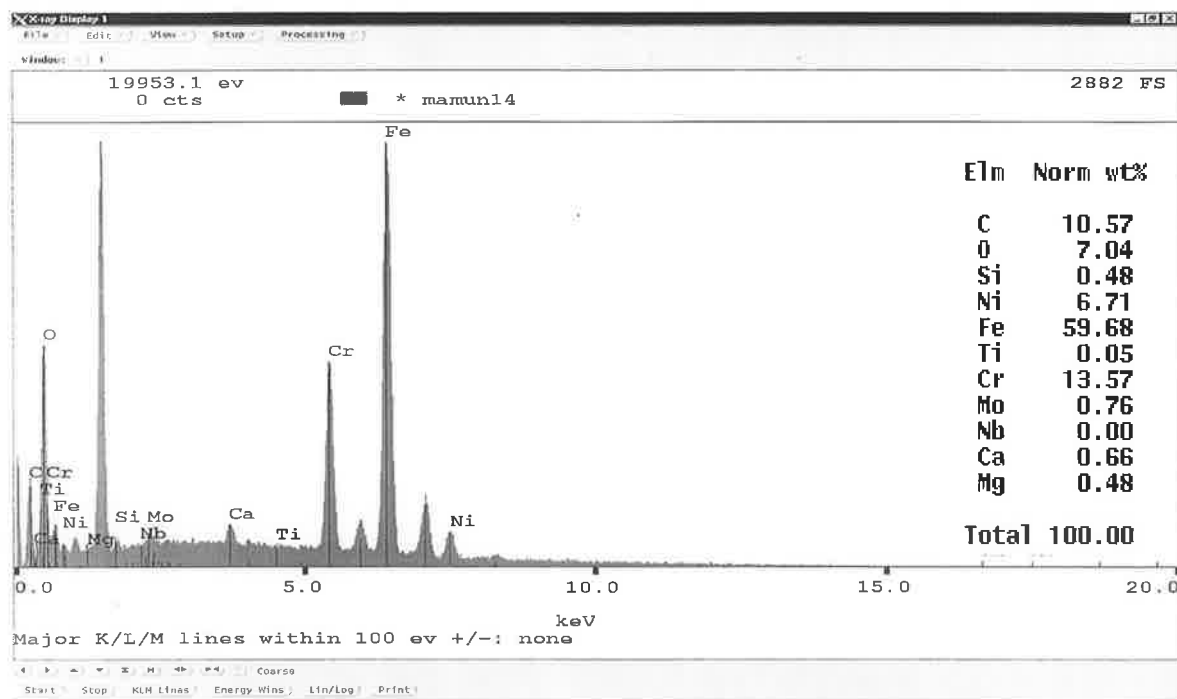


Figure F12: Chemical composition of the middle layer or Middle of the Coat of Sample 2 (3rd set of point analysis).

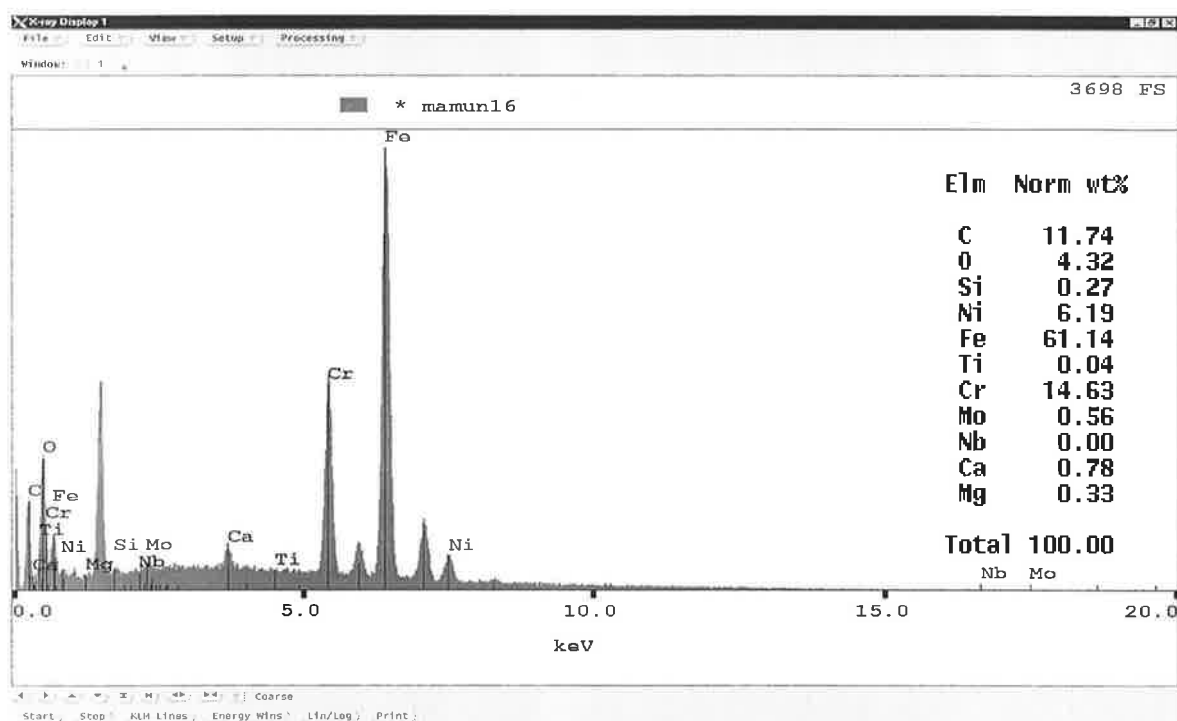


Figure F13: Chemical composition of the first coat or the Bond coat of Sample 2 (2nd set of point analysis).

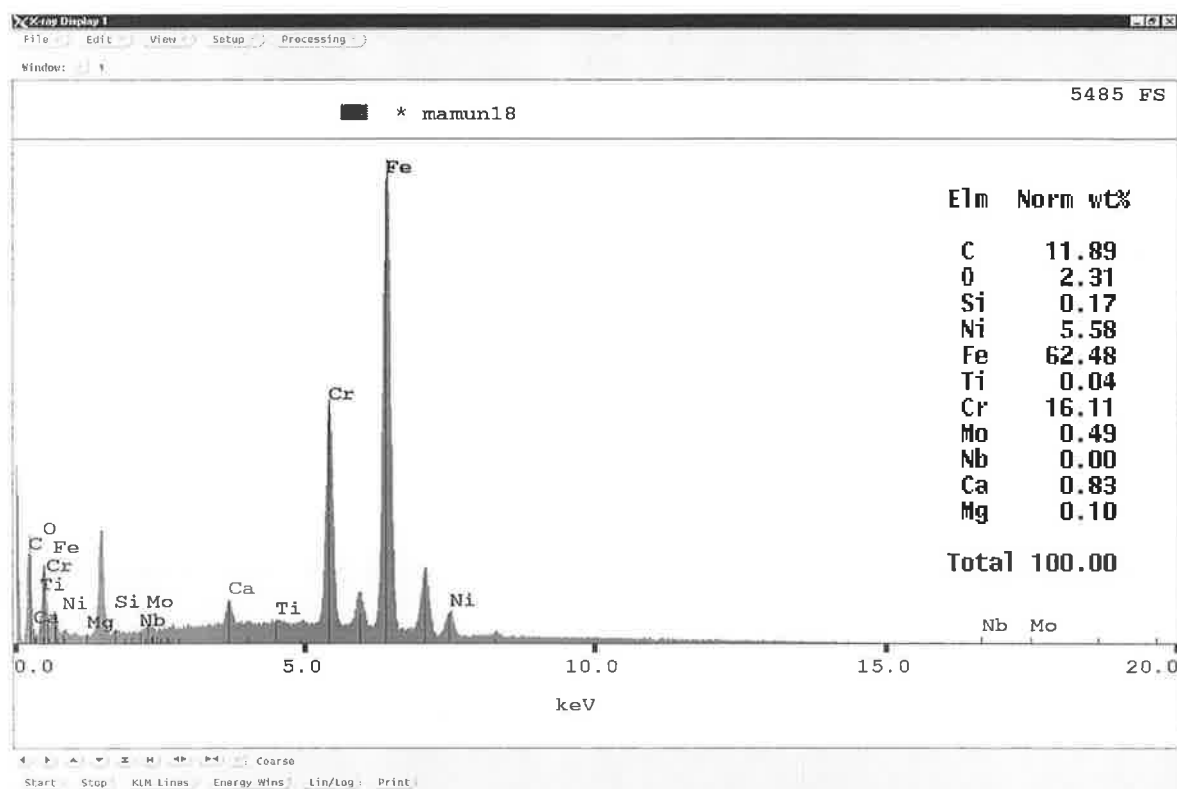
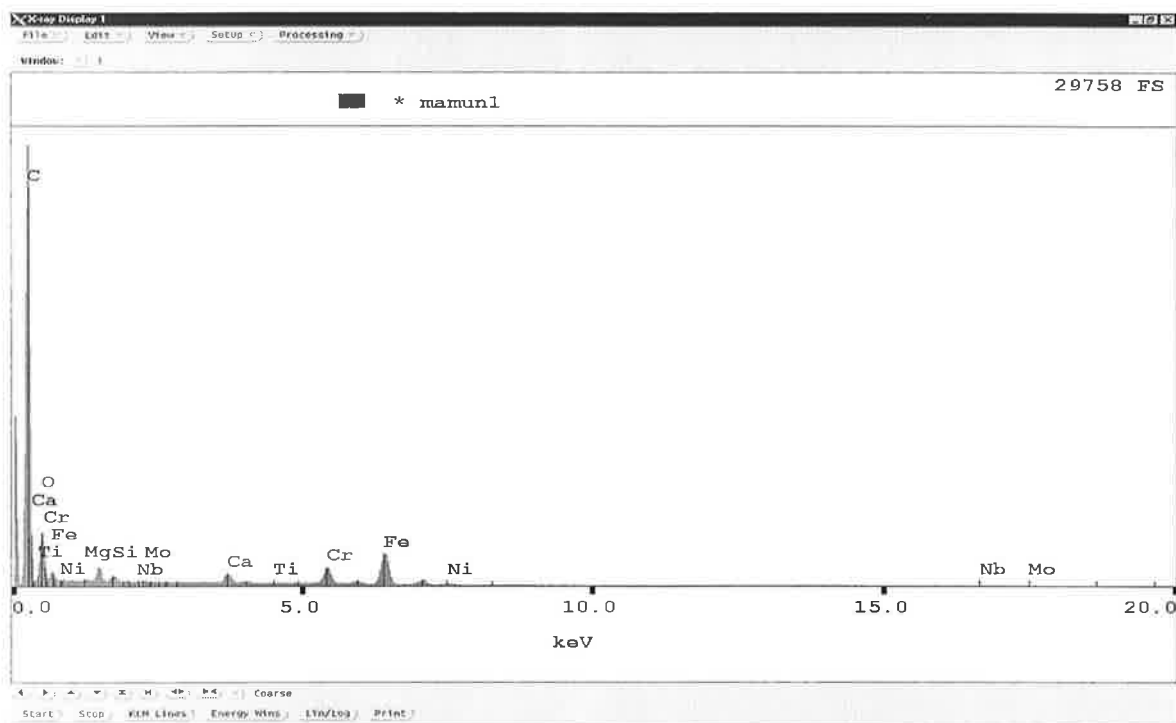


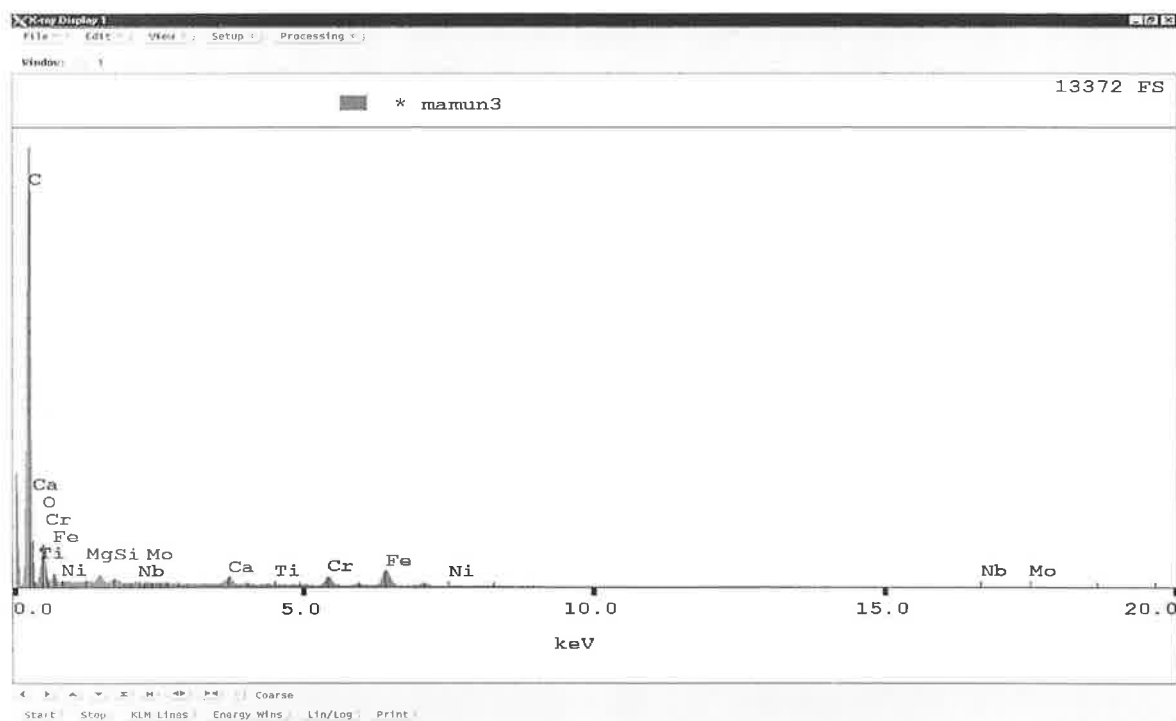
Figure F14: Chemical composition of the first coat or the Bond coat of Sample 2 (3rd set of point analysis).

Figure F1: A SEM image of the functionally graded coating sample 1 (Diamalloy 1003 and Diamalloy 2001) (Represent of Figure 6.17 for the 2nd and 3rd set of point analysis). lxxxiii



lxxxiii

Figure F2: Chemical composition of the final coat or the Top Coat/Service Coat of Sample 1 (2nd set of point analysis). lxxxiii



lxxxiv

lxxxii